Optical and Electro-optical Properties of Nematic Liquid Crystals with Nanoparticle Additives

By

Javad Mirzaei

A Thesis submitted to the Faculty of Graduate Studies of
The University of Manitoba
in partial fulfilment of the requirements of the degree of

DOCTOR OF PHILOSOPHY

Department of Chemistry
Faculty of Science
University of Manitoba
Winnipeg, MB, Canada

Abstract

Liquid crystals (LCs) are an interesting class of materials that are attracting significant attention due to their ever-growing applications in a wide variety of fields such as liquid crystal display (LCD) technology, materials science and bioscience. In recent years, along with the developments of materials at the nanoscale, doping LCs with nanoparticles (NPs) has emerged as a very promising approach for improving LC properties. Nanoparticle additives can introduce novel effects on optical and electro-optical properties of nematic liquid crystals (N-LCs), such as altered molecular alignment, faster response time and increased efficiency.

This thesis studies the impacts that the inclusion of metallic NPs made of gold or semiconductor CdSe quantum dots (QDs), have on optical and electro-optical properties of N-LCs. Using polarized optical microscopy and detailed capacitance and transmittance measurements of nematic mixtures in electro-optic test cells, characteristics such as optical texture, phase transition temperatures, switching voltages and dielectric anisotropy are investigated in pure as well as doped samples. Surface ligands in NPs and their chemical functionalization play an important role in the LC-NP interactions, largely by determining the dispersibility of NPs and stability of the nanocomposites. One important objective of this thesis is to investigate and prepare a series of gold nanoparticles (Au NPs) with specially formulated robust coatings that maximizes solubility and stability in LC medium. Silanization of NPs is developed as a method to overcome the stability challenge. The functionalization of silanized NPs with aliphatic ligands or liquid crystalline molecules, provides chemically and thermally stable NPs with hydrophobic and structurally compatible surfaces required for dispersion in N-LCs. After complete characterization the synthesized particles are used to make the new nematic nanocomposites.

By analysis of the structure-property relationships governing LC-nanomaterial composites and by comparison of new results and data from previous studies on other types of NPs, this thesis will further reveal the mechanism of the interrelations between host LC molecules and NP, considering the role of variables such as core composition, size and surface chemistry of NPs (e.g. siloxane shell, aliphatic ligand *vs*. liquid crystalline ligand) in achieving stable LC composites with desired optical and electro-optical properties.

Acknowledgments

This work could not have happened without the help of those dozen and more, for which I am incredibly grateful. First and foremost, I sincerely extend my deepest gratitude to my advisor, Prof. Torsten Hegmann, for his guidance, support and kind mentoring during my Ph.D. program. He always believed in my capacity to investigate new research problems and made sure I had the resources needed to succeed. I greatly thank my co-advisor, Prof. Michael Freund, for his support and scientific guidance.

I am most grateful to the members of my advisory and internal examining committee (Profs. Torsten Hegmann, Michael Freund, Mario Bieringer, Georg Schreckenbach and Douglas Thomson) for their time, expertise at various stages of my Ph.D. studies and careful evaluation of my thesis. Special thanks to Prof. Linda Reven (McGill University), the external examiner of my thesis, for her time in reviewing and providing valuable comments.

I would like to thank our collaborators, many research groups and individuals who have contributed their expertise to this work and/or assisted with facilities in their labs. Dr. Martin Urbanski and Prof. Heinz Kitzerow (Department of Chemistry, University of Paderborn, Germany) for their excellent work with electro-optical characterization (dynamic and transmittance measurements) of liquid crystal nanocomposites and numerical simulation; Prof. Kui Yu (Steacie Institute for Molecular Sciences, Canada) and

her group members for providing magic-sized quantum dots; Dr. Michael Wand (LC Vision Inc., USA) for generously providing update software and advice on LCAS instrument; Prof. Freund for access to XPS instrument; Dr. Kevin McEleny for XPS and SAXS measurements; Prof. Bieringer's research group (group member: Mr. Joey Lussier) for access to TGA and XRD instruments; Dr. Abdul Khan and Mr. Andre Dufresne for HR-TEM and TEM analyses; Dr. Bangar Balajepalli (Nikon Canada) for training in FCPM; Dr. Tom Ward for his assistance with the equipment of the MCAL; Dr. Kirk Mart and Mr. Terry Wolowiec for their assistance with NMR experiments, and finally Prof. Qingjin Peng (Department of Mechanical Engineering, University of Manitoba) and Mr. Murray Waldman (Sunnex Biotechnologies Co., Canada) for all their support and guidance throughout an additional research project funded by NSERC Engage Grant.

I would like to thank all the former and current members of both Prof. Hegmann's and Prof. Freund's research groups for all their help and the enthusiasm they brought to the lab. My special thanks go to Mr. Xiang Feng, Drs. Vinith Yathindranath, Mitya Reznikov, Oana Stamatoiu, Ms. Anshul Sharma, Mr. Mattew Worden, Drs. Hao Qi, Brandy Kinkead, Michael MacDonald and Iman Yahyaie.

I thank Prof. Peter Budzelaar, head and the office staff members (Mr. Keith Travis, Ms. Sharon Mullen and Ms. Tricia Lewis) of the Department of Chemistry for all their help. My studies at the University of Manitoba were supported in part by the scholarships, bursaries and travel awards from the Department of Chemistry, Faculty of Science and Faculty of Graduate Studies for which I am very thankful. Financial support for the projects from the agencies including the University of Manitoba, NSERC-CRSNG, the Government of Manitoba and Canada Foundation for Innovation are greatly appreciated.

There are people in everyone's personal lives who make success both possible and rewarding. I would like to thank my parents, Mr. Gholamreza Mirzaei and Ms. Nahid Hamidipour, my brothers, Jafar, Alireza, and all my friends for their love, support and encouragement throughout the years. Last but definitely not least, I greatly thank my lovely wife, Mehrsima Ashkannejad, and her parents Mehdi Ashkannejad and Mina Jabarouti for their never-ending support and encouragement. Thank you, Mehrsima, now and always. I could not have done this without you.

This dissertation is lovingly dedicated to my parents and my wife, Mehrsima.

Their support, encouragement, and constant love have sustained me throughout my life.

Contents

List of Tables

List of Figures

List of Copyrighted Material*

Figure 1.1 Typical examples (and molecular shapes) of the main types of molecules forming LC phases. Reproduced with permission from Ref. 18 - Copyright: Springer Science.

Figure 1.4 Temperature dependence of dielectric permittivity in liquid crystals with $\Delta\varepsilon > 0$; Tc and εiso are clearing temperature and permittivity of isotropic liquid, respectively. Reproduced from Ref. 21 - Open Access Journal

Figure 1.5 Schematic representation of unidirectional deformations; a) bend, b) splay, and c) twist imposed on the system. Images represent the director field in a two dimensional slice of a three dimensional sample. Director n is set to be aligned with the *z*-axis. Reproduced with permission from Ref. 23 – Copyright: The Royal Society of Chemistry.

Figure 1.12 Schematic drawings representing the principle of FCPM technique. Reproduced with permission from Ref. 28 - Copyright: Elsevier Science.

Figure 1.19 Schematic representation of the major optical and electrical components of a liquid crystal display. Reproduced with permission from Ref. 36 - Copyright: Academic Press.

Figure 1.20 Schematic drawing of operating principle of the TN mode; a) OFF-state, b) ON-state. Reproduced with permission from Ref. 165 – Copyright: The Royal Society of Chemistry.

Figure 1.21 Flowchart of the development of LCDs highlighting the advantage of each mode, starting with the dynamic scattering mode to the new Blue Phase concept. Reproduced with permission from Ref. 5 – Copyright: Taylor & Francis.

Figure 1.23 Various ligand exchange and modifications of hydrophobic nanoparticles. Reproduced with permission from Ref. 63 – Copyright: The American Chemical Society.

Figure 1.24 Schematic diagram of surface functionalization of a NP with mesogens, dendrimers or pyridine in alkyl thiol-for-alkyl thiol exchange. Adapted from Ref. 75 – Copyright: Elsevier.

Figure 1.25 Schematic reaction of DMAP to thiol exchange. X moiety may introduce new surface chemistry on the NPs. Reproduced with permission from Ref. 80 – Copyright: Springer-Verlag.

Figure 1.28 (a) Schematic illustration of the origin of the SPR in quasi-spherical Au NPs. (b) Optical absorption spectra of 22, 48 and 99 nm spherical Au NPs. The broad absorption band corresponds to the surface plasmon resonance. Reproduced with permission from Ref. 94 – Copyright: Taylor & Francis.

Figure 1.29 Typical defects created by spherical particles in N-LCs. (a) hyperbolic hedgehog, (b) Saturn ring and (c) boojums defect with two surface defects forming around particles with planar boundary conditions. (d) A chain of droplets formed by interaction between the topological dipoles with hedgehog-type defects. (e) Optical microscope picture of several water droplets forming a long chain with hedgehog type of defects. Reproduced with permission from Ref. 117 – Copyright: The American Physical Society.

Figure 1.30 a) Structure and phase transition temperatures (°C) of nematic LC1 (top) and its POM photomicrographs taken on cooling just below the Iso–N phase transition (crossed polarisers) showing Schlieren texture of the N phase (bottom). b) Structure of truncated cuboctahedral shape of the Au NP capped with (S)-naproxen-end thiol (top) and fingerprint POM texture of the N^* phase of LC1 doped with 5wt% (S)-naproxen-capped Au NP at 44

°C (bottom). c) Structure of truncated cuboctahedral shape of the Au NP capped with dodecanethiolate (top), and stripe texture of the N phase with coexisting areas of homeotropic alignment of 5wt% dodecyl thiol-capped Au NP in LC1 at 64 °C (bottom). Reproduced with permission from Ref. 10 – Copyright: The Royal Society of Chemistry.

Figure 1.31 a) Schematic image of the substrate design of an LC cell with ITO electrodes and alignment layers comprised of continuous layer of 30° SiOx and patterned printed layer of gold NPs. b) POM image of the LC texture and alignment pattern in cells (bare ITO and cell gap: 5 μm) created by printed NPs in the nematic mixture MLC-6610 (Reproduced with permission from Ref. 107 – Copyright: WILEY-VCH.

Figure 1.32 Schematic representation of synthesis of LC-functionalized Au NP using LC thiols exchange reaction (top). (a) TEM micrograph (scale bar: 5 nm) of the Au NP (b) POM texture of the LC ligand (c) POM texture of the LC-functionalized Au NP showing the typical nematic Schlieren texture. Reproduced with permission from Ref. 157 – Copyright: The American Chemical Society.

Figure 2.1 Size-dependent PL colors of semiconductor QDs. Electronic structure of QDs correlated with the QD radius and resulting 'blue shift' due to quantum confinement. Reproduced with permission from Ref. 41 – Copyright: Wiley VCH.

Figure 2.2 (a) Schematic representation of surface trap sites and their effect on quenching PL. Adapted from Ref. 50 – Copyright: American Chemical Society. (b) Electronic structure of a core-shell quantum dot made of two semiconductors forming a heterojunction (core surrounded by the shell of a wider bandgap). Adapted from Ref. 41 – Wiley VCH.

Figure 2.3 Exchange of dodecylamine with 3-mercaptopropionic acid and its effect on charge recombination dynamics of TOPO-capped CdSe QDs. Reproduced with permission from Ref. 50 - Copyright: American Chemical Society.

Figure 2.5 Self-assembly of CdS QDs in the 5CB nematic host as a function of applied electric field: (a) symmetry of the QDs chain aggregates in the nematic phase; (b) QD aggregates in the nematic host below the Fréedericksz transition; (c) switching of the QDs aggregates by the electric field above the Fréedericksz transition. Reproduced with permission from Ref. 109 – Copyright: American Physical Society.

Figure 2.6 (a) Comparison of normalized photoluminescence spectra of QDs in toluene and in N-LC matrix. The emission of the latter is red-shifted by $\Delta\lambda = 37$ nm. Optical texture of the nematic phase imaged with polarized optical microscopy for (b) unaligned pure N-LC, (c) unaligned mixture of N-LC with QDs 30:1 by volume confirming the nematic phase in the mixture by showing typical Schlieren texture. (d) DLS exhibits small particles in the range of 1-9 nm for pure GaSe nanodisks in toluene, whereas formation of clusters on the order of hundreds of nanometers in the N-LC. Reproduced with permission from Ref. 105 – Copyright: American Physical Society.

Figure 2.7 (a) Spatially-resolved PL map of QD-LC mixture showing emission in the range of 500-515 nm when N-LC is unaligned. (b) Red-shifting up to 520-530 nm of the same sample when the N-LC is aligned with the director axis along x using a thin coating of rubbed polyimide but no electric field. (c) Further red-shift to 540 nm when an electric field of 0.8 V/μm is applied along the x axis. Reproduced with permission from Ref. 105 – Copyright: American Physical Society.

Figure 2.8 (a) Schematic drawing demonstrating the helical arrangement of the CLC in a Cano-wedge cell. (b) Polarized optical microscopy transmission image of the CLC. Spatially-resolved PL scans of QD-CLC mixture at: (c) 35 °C shows that emission of QDs varies across the sample film following the Grandjean step pattern of the cholesteric phase, (d) when heated to 43 °C systematic wavelength gradient disappears due to random distribution of QDs in isotropic mixture, and (e) when it cools back to 25 °C QDs emission gradient reforms. Adapted with permission from Ref. 107 – Copyright: American Physical Society.

Figure 2.9 Images of nematic (a-c) and cholesteric (d-f) phases doped with QDs. Images (a) and (d) that show LC texture are taken using polarized optical microscope; images (b) and (e) were taken using fluorescence optical microscope thus showing localization of the QDs in the LC host; images (c) and (f) are the overlays of both images shown for comparison with the overall QD distribution marked by lines to demonstrate where the QDs are with respect to the LC texture. Lines are intended to guide the eye. Each set of images represents the same sample area. Reproduced with permission from Ref. 108 – Copyright: SPIE.

Figure 2.11 POM images of the 2wt% mixtures of CdSe480 – CdSe610 (numbers indicating the wavelength of the emission maximum) in the nematic phase of 5-n-heptyl-2-(4-n-octyloxyphenyl)-pyrimidine (Felix-2900-03) at $T_{Iso/N} - T = 9$ ˚C between plain glass slides (a–e) and in planar aligned cells (f–j). Red arrows show rubbing direction of the planar, rubbed polyimide coated ITO cells. The inset in each figure shows the same area with parallel (un-crossed) or slightly un-crossed polarizers. Reproduced with permission from Ref. 127 – Copyright: Royal Society of Chemistry.

Figure 2.12 POM images of the 2wt% mixtures of the CdTe530 – CdTe610 QDs in the nematic phase of Felix-2900-03 at $T_{Iso/N}$ – T = 9 ˚C between plain glass slides (a–d) and planar aligned cells (e–h). Red arrows show rubbing direction of the planar cells. Mixtures at this concentration showed homogenous planar alignment similar to non-doped LC. Reproduced with permission from Ref. 127 – Copyright: Royal Society of Chemistry.

Figure 2.13 Comparison of experimental voltage dependencies of maximum diffraction efficiency for pure and functionalized liquid crystal structures. Green line corresponds to pure LC on un-doped photoconductive polymer; other lines correspond to doped LC and/or photoconductive polymers. Reproduced with permission from Ref. 131 – Copyright: American Institute of Physics.

Figure 2.14 DSC thermograms of pure LC (H4TP) and composites with CdSe (2.3 nm) at various concentrations. Adapted from Ref. 134 – Copyright: Royal Society of Chemistry.

Figure 2.15 Dielectric permittivity at different DC biases of CdTe-QDs doped FLCS: (a) LAHS19, (b) LAHS18, and (c) FLC 6304 in 4 μm-cells; (d) KCFLC 7S in 10 μm-cell. Reproduced with permission from Ref. 135 – Copyright: American Institute of Physics.

Figure 2.16 Phase transition of CS1026 FLC and optical micrographs showing the transformation from homeotropic to homogeneous (planar) configuration of CS1026 material doped with (a), (b) 1wt% (c) and (d) 3wt% of CdTe QDs by application of dc bias field at room temperature. Reproduced with permission from Ref. 137 – Copyright: American Institute of Physics.

Figure 2.17 Dielectric anisotropy (a) 1 and (b) 3wt% CdTe QDs doped CS1026 material with temperature at different (10 and 100 kHz) frequencies. Reproduced with permission from Ref. 137 – Copyright: American Institute of Physics.

Figure 2.18 (a) Comparison of excitation (inset) and emission spectra (recorded at $\lambda_{exc.}$= 293 nm) of the FLC material KCFLC 7S doped with different (1, 3, and 5 µl) concentrations of ZnS QDs and (b) emission spectra of FLC material KCFLC 7S doped with different (1, 3, and 5 µl) concentrations of ZnS QDs by exciting with 336 nm. Reproduced with permission from Ref. 138 – Copyright: American Institute of Physics.

List of Abbreviations and Symbols

3D	Three Dimensional
5CB	4-Cyano-4'-pentylbiphenyl
8CB	4-Cyano-4′-n-octylbiphenyl
AC	Alternating Current
Ag NP(s)	Silver Nanoparticle(s)
Au NP(s)	Gold Nanoparticle(s)
Au NP@SiO_2	Silica coated gold nanoparticle
BP(s)	Blue Phase(s)
BTBP	N,N'-bis(2,5-di-tert-butylphenyl)-3,4,9,10-perylenedicarboximide
C	Capacitance
$C_{\parallel}$	Parallel Capacitance
$C_{\perp}$	Perpendicular Capacitance
C_0	Capacitance of the capacitor with vacuum inside
C60	Buckminsterfullerene
$CDCL_3$	Deuterated chloroform
C-dot(s)	Carbon Dot(s)
CdSe	Cadmium Selenide
C_{empty}	Capacitance of Empty Cell
CLC	Cholesteric LC

C_m	Measured Capacitance of Empty Cell
-CN	Cyano group
CNT(s)	Carbon Nanotube(s)
COC	Cholesteryl Oleyl Carbonate
C_p	Parasitic Capacitance
Cr	Crystalline
C-V	Capacitance versus Driving Voltage
DC	Direct Current
DDAB	Didodecyldimethylammonium bromide
DLS	Dynamic Light Scattering
DMAP	4-(N,N-Dimethylamino)pyridine
DSC	Differential Scanning Calorimetry
E	Electric Field
EDS	Energy Dispersive X-ray Spectroscopy
EELS	Electron-Energy Loss Spectroscopy
$E_{g,\,b}$	Bandgap Energy of the bulk solid
$E_{g,\,QD}$	Bandgap Energy of the quantum dots
EO	Electro-Optical
eV	Electron Volt
f	Total Elastic Free Energy Density
f	Frequency
f_0	Minimum Elastic Free Energy Density

FCPM	Fluorescence Confocal Polarized Microscopy
f_E	Electric field energy density
FLC	Ferroelectric LC
FWHM	Full Width at Half Maximum
$\hbar$	Planck's constant
$HAuCl_4$	Hydrogen tetrachloroaurate(III)
HR-TEM	High Resolution TEM
I_0	Initial Light Intensity
I_{det}	Detected Light Intensity
IPS	In-Plane Switching
Iso	Isotropic
ITO	Indium Tin Oxide
K_{11}	Splay Elastic Constant
K_{22}	Twist Elastic Constant
K_{33}	Bend Elastic Constant
K_{eff}	Effective Elastic Constant
kHz	Kilohertz
LC(s)	Liquid Crystal(s)
LCAS	Liquid Crystal Analyzer System
LCD(s)	Liquid Crystal Display(s)
LLC	Lyotropic LC
m_e	Effective mass of the electron

m_h	Effective mass of the hole
MPA	3-Mercaptopropionic acid
MPS	(3-Mercaptopropyl)trimethoxysilane
MSN(s)	Magic-Sized Nanocrystal(s)
MSNC(s)	Magic-Sized Nanocrystal(s)
MVA	Multi-Domain Vertical Alignment
N	Nematic
n	LC director
N^*	Chiral Nematic
$NaBH_4$	Sodium borohydride
n_e	Extraordinary Refractive Index
N-LC(s)	Nematic Liquid Crystal(s)
nm	nanometer
NMR	Nuclear Magnetic Resonance
n_o	Ordinary Refractive Index
NP(s)	Nanoparticle(s)
P3HT	Poly(3-hexylthiophene-2,5-diyl)
PDLC	Polymer Dispersed Liquid Crystal
pF	picofarad
PI	Polyimide
PL	Photoluminescence
POM	Polarized Optical Microscopy

PVA	Patterned Vertical Alignment
QD(s)	Quantum Dot(s)
R	Resistance
RPM	Rotations Per Minute
RT	Room Temperature
S	Scalar Order Parameter
SiC-dot(s)	Organosilane-Functionalized Carbon Dot(s)
SiO	Silicon Monoxide
SmA	Smectic A
SmA^*	Chiral smectic A
SmC	Smectic C
SmC^*	Chiral smectic C
SPR	Surface Plasmon Resonance
STN	Super Twisted Nematic
TBAB	Tetrabutylammonium borohydride
T_c	Clearing Point
TEM	Transmission Electron Microscope/Microscopy
TEOS	Tetraethyl orthosilicate
TGA	Thermogravimetric Analysis
TGS	tri-glycine sulfate
THF	Tetrahydrofuran
$T_{Iso\text{-}N}$	Isotropic-nematic phase transition temperature

TMODS	Trimethoxy(octadecyl)silane
TN	Twisted Nematic
TOP	Trioctylphosphine
TOPO	Trioctylphosphine oxide
UV-vis	Ultraviolet-visible spectrophotometry
V	Voltage
V_{rms}	Root Mean Square Voltage
V_{th}	Threshold Voltage
W	Anchoring Energy
wt%	Weight Percentage
XPS	X-ray Photoelectron Spectroscopy
XRD	X-ray Diffraction
ZBD	Zenithal Bistability Device
γ	Rotational Viscosity
Δn	Birefringence Parameter
Δn_{eff}	Effective Birefringence
$\Delta\varepsilon$	Dielectric Anisotropy
ε	Dielectric Constant
$\varepsilon_{\parallel}$	Parallel Permittivity
$\varepsilon_{\perp}$	Perpendicular Permittivity
ε_0	Dielectric Constant of vacuum
ε_{iso}	Permittivity of the LC material in the isotropic liquid state

θ	Polar Angle
θ_0	Pretilt Angle
λ	Wavelength of Light
τ_{decay}	Decay Time
τ_{rise}	Rise Time
φ	Azimuthal Angle
ϕ	Phase Retardation

Authors' Contributions

The idea of nematic nanocomposites was conceptualized by *Prof. Torsten Hegmann* (*TH*). The presented work in this thesis was mainly performed by the author, *Javad Mirzaei* (*JM*) under the supervision of *Prof. Hegmann*. The contributions of the various co-authors are detailed below. For all the chapters (except Appendix D of Chapter 5), *JM* wrote the first draft.

Chapter 2

JM wrote the first draft with all the figures and sections. *Dr. Mitya Reznikov* contributed to the writing and editing of the manuscript by adding further examples in the section "Alignment of QDs in LCs". *TH* was responsible for the final revisions of the manuscript, prior to its publication.

Chapter 3

JM performed all the experimental procedure for the preparation of the nematic nanocomposites and additional characterization of QD samples. *JM* also carried out all the optical and electro-optical characterization including POM and FCPM studies and capacitance measurements. *Dr. Kui Yu* provided the magic-sized QD samples. The complementary transmittance measurements were provided through collaboration with the *Prof. Heinz Kitzerow's* (*HK*) group at the University of Paderborn, Germany. *Dr. Martin Urbanski* (MU) from this group, performed these measurements and provided comments

in the manuscript preparations. *HK* and *TH* were responsible for the final revisions of the manuscript before its publication.

Chapters 4 and 5

JM was responsible for the choice of gold nanoparticle synthetic strategy and surface functionalization. All experiments related to the syntheses of organosilane ligands and silanized gold nanoparticles and their characterization were designed and carried out by *JM*. The procedures for the preparation of nematic nanocomposites in plain glass slides and electro-optic test cells were modified and performed by *JM*. Initial POM studies and the electro-optical characterization of nematic samples was conducted by *JM*. The first drafts of chapters 4 and 5 with the figures and tables were prepared by *JM*. *MU* completed the transmittance and dynamic measurements in Chapters 4 and 5 and performed the numerical simulations presented in Appendix D (chapter 5). *MU* contributed to manuscript preparation and editing of the main text of chapter 4 and 5 and wrote the draft of Appendix D. *TH* and *HK* edited the manuscripts and made the final revisions before publication.

List of Appendices

Chapter 1

Introduction and Background

1.1 Introduction

The liquid crystalline state which was discovered in 1888, represents a state of matter which shares properties of both its neighbouring isotropic liquid and crystalline solid phases. Liquid crystals (LCs) are also considered anisotropic fluids with some degree of ordering. Since their discovery, various industrial applications have been identified for them in fields as different as biology, rheology, photonics, as well as in optical elements such as controllable lenses and lasing.[1, 2] However the predominant application of liquid crystals remains in the field of electro-optic displays.[3]

The anisotropic nature of the physical properties of LCs, due to their shape anisotropy, combined with the ability of magnetic and electric fields to influence the bulk spatial orientation of these molecules renders them of such importance to electro-optic display devices.[3] In most of the liquid crystal display (LCD) cells, there is a layer of LC material over a pre-treated surface (alignment layer) for obtaining a particular type of alignment, and switching between the 'on' and 'off' states is achieved by changing the molecular orientations from a surface-aligned to a field-aligned arrangement. The first commercially patented LCD technology in 1970 by Helfrich and Schadt[4] was based on the electric field-induced reorientation of nematic liquid crystals (N-LCs) between crossed polarizers as a switchable light shutter. Since then, major scientific and engineering developments such as the design and application of new LC phases and switching modes, as well as the invention of new electronics, have led to the current state-of-the-art LCD technologies used in home theaters, computer and television monitors, tablets, mobile phones, etc.

Despite the variety of liquid crystalline materials and phases, LCs showing the nematic phase, are still the most frequently used materials in LCD technology. N-LCs are mainly used in the form of mixtures composed of different pure LCs, to achieve optimum switching behaviour, dielectric, elastic and viscous properties.[5] Physical properties of liquid crystalline materials play a significant role in display performance characteristics such as switching speed, viewing angle and contrast.[5] Desired properties are fast response times, high contrast, and low switching voltages of fields for energy efficiency.

A relatively established method for tuning and achieving certain properties in LCs is using particle additives also known as "nanoparticle doping". Historically, the first theoretical research into the doping of LCs with particles in order to lower the required field intensities for LC switching, was performed by Brochard and de Gennes in 1970's.[6] They provided an unprecedented description of ferronematics or ferrocholesterics made by adding low concentrations of small or elongated magnetic grains into nematic or cholesteric materials.[6] Similar to Brochard and de Gennes' experiments, many other initial studies were also focused on the modulation of magnetic and ferroelectric properties of LCs, by using small magnetic or ferroelectric particles, needles, or platelets along with the formation of defects induced by the immersed particles in the host LC.[7, 8]

With the emergence of nanotechnology and advances in the synthesis of nanoparticles (NPs) with different core materials and shapes in recent years, LC nanocomposites have drawn significant attention. Research on LC nanocomposite systems focuses on the combination of the unique properties of LCs and NPs, offering mutual benefits for both components. In general, the use of nano-sized building blocks is motivated by new properties emerging from the quantum size effect of the NP inclusions.[9] This effect occurs

when the dimensions of the material are reduced to a scale of 100 nm or less and the surface percent of its constituent atoms is greatly increased. Thus, the nanomaterial gains specific optical, electrical or chemical properties that are not necessarily present in its bulk form. These new properties are mainly dominated by the surface atoms and can be tuned by the size, shape or capping ligand of the nanomaterial.

One important aspect of the studies on LC-NP composites, is the creation of stable dispersions of NPs in LC phases in order to improve optical and electro-optical responses of the LC. For example: Multiple studies performed by Dr. Hegmann's research group have shown that spherical NPs with diameters smaller than 5 nm made of gold or semiconductor CdSe or CdTe cores, can significantly change the optical texture and electro-optical properties of the host nematic LCs.[10, 11] Another equally important aspect of LC nanoscience is the application of various LCs phases as an organizing medium to induce the self-assembly of NPs.[12] The self-organization of nanomaterials in two- and three dimensional space offered by the LC medium seems to be an ideal method to explore and control the organization of matter on the nanometre to the micrometre scale, with the potential for obtaining metamaterials.[12, 13] In addition, the capacity of the LC medium to respond to external stimuli such as applied electric fields, can offer adjustable control over the orientation of NPs and nanocomposite properties which may be utilised in various applications such as tunable lasers, sensors, etc.

Despite the growing interest in the LC-NP composites and their potential technological applications, fundamental research and development in the field is often hampered by chemical instability of NPs and/or limited miscibility of the NPs within the LC medium. It has been shown that organic ligand shells required to passivate the NPs and protect them

from irreversible agglomeration, also plays a key role in the interaction of the dopant particles and the nematic host molecules.[13, 14] If surface ligands of NPs are not chemically compatible/miscible enough with the rod-like N-LC host molecules, ordered LC molecules are likely to expel spherical dopant NPs to minimize the distortion in elastic energy caused by the NPs.[15] Depending on the extent of segregation between NPs and LC molecules, the NPs may eventually completely agglomerate.[15] This problem can be exacerbated in the absence of robust capping agents on the NP surface or at higher temperatures when ligands are prone to dissipation.

Despite the importance of the properties and chemical functionalization of surface ligands in producing stable colloidal LC dispersions, the precise mechanisms of interplay between the NP surface ligands and the nematic host molecules are not yet fully understood. There is a need for well-defined and stable LC-NP systems to systematically study the interrelations of host LC molecules and NP parameters from composition, size and shape to those related to NP surface ligands including structure, size and density. Therefore, this thesis is mainly focusing on addressing low stability and compatibility of the NPs in N-LCs and study the optical and electro-optical behaviour of such composites. Silanization (silane conjugation) has been utilized to deliver chemically and thermally stable gold nanoparticles (Au NPs) for dispersions in nematic hosts for the first time. This method has also enabled us to functionalize Au NPs with ligands structurally similar to nematic LC molecules and to those of LC hosts. The influence of the NPs on the alignment of the nematic LC are studied using polarized optical microscopy, and fluorescence confocal polarized microscopy in the case of luminescent quantum dots (QDs). Electro-optical parameters such as threshold voltage and dielectric anisotropy of nanocomposites

at different concentrations of the NPs depending on the temperature, are measured using two standard and complimentary methods: capacitance and transmittance measurements. The detailed and combined measurements performed in this work provide reliable results beyond the limitation of either method alone. A numerical simulation is also performed to study the distinction between surface and bulk effects of NPs in an N-LC medium. Results of this simulation and a comparison with previous experimental data have been discussed in the appendix to Chapter 5.

The results obtained in this work are based on the dispersion of CdSe quantum dots, hydrophobic silanized Au NPs and LC-decorated silanized Au NPs in N-LCs. However, many of the findings are not limited to the presently investigated systems and may be expanded to other nanoscale particles of different compositions and sizes. Further advances based on the results of this work can lead to the realization of the envisioned applications for the field of LC-NP composites as further elaborated on in the following chapters.

1.2 Goals

The work presented in this thesis investigates optical and electro-optical properties in composites of nematic LCs doped with small concentrations of metallic gold and semiconductor CdSe NPs. The main goal is to address major challenges and questions faced by LC nanoscience community. It is desired to tackle low compatibility and stability of colloidal LC dispersions and improve the existing knowledge of the interrelations of host LC molecules and NPs within the nanocomposites with respect to the core composition and surface ligands of NPs in certain size regimes. In this thesis, polarized

optical microscopy, different techniques of electro-optic measurements and fluorescence confocal polarized microscopy are extensively applied for studying the impacts of NP dopants on the alignment and electro-optical responses of the N-LC. Using a series of CdSe quantum dots similar in size and type of the surface ligands, but different in surface defects and possibly density of surface ligands, the impact of these QD dopants on the properties of the N-LC are highlighted with respect to small changes of the surface defects and core composition in the QDs.

In this thesis, I also sought to develop a method for the synthesis and functionalization of Au NPs yielding particles with hydrophobic, robust and compatible surface ligands similar to or structurally related to those of the host LC molecules. Silane conjugation has been studied as a method for synthesizing hydrophobic Au NPs. Silanized Au NPs bearing aliphatic chains have been used for the first time as an additive for modulating optical and electro-optical properties, and the obtained results showed significant improvements in the thermal and chemical stability of the nematic nanocomposites. Silane conjugation is also utilized as the method for the synthesis of robust Au NPs functionalized with LC moieties. Studying numerous colloidal nematic nanocomposites and evaluating the results obtained by optical and electro-optic measurements, will help us understand the effects of NPs in the doped nematic samples with respect to type or nature of their size, surface ligands and chemical stability. The proposed model should facilitate rationalization of the altered optical and electro-optic behaviour in doped nematic mixtures, and as a result thereof enhances our understanding of the complex interrelations between NPs and LC molecules. Ultimately this should open up the potential technological applications of LC nanocomposites.

1.3 Organization of the Thesis

This thesis has been compiled according to the "Sandwich Thesis" format. Chapters 2-5 include published results from my graduate research, reformatted from their original form for consistency and clarity.

Chapter 1 provides background information on LCs, especially N-LCs and their physical properties such as dielectric anisotropy and birefringence, and methods for the characterization of these properties. Characterization methods include polarized optical microscopy (POM), fluorescence confocal polarized optical microscopy (FCPM), differential scanning calorimetry (DSC), and electro-optical (EO) measurements. Chapter 1 continues with the description of the main synthetic and surface functionalization techniques for Au NPs, as well as the main experimental techniques used for characterization of the NPs. A summary of the research on LC-NP composites with Au NPs and some other types of nanostructured materials is also provided in Chapter 1, focusing on particular aspects such as defect formations, modulation of LC properties and LC-decorated NPs.

A significant number of the studies in the LC-NP composite field have used QDs due to their unique photoluminescent properties and subsequent application as analytical tracers to measure the particle distribution in LC hosts. In Chapter 2 of this thesis, a detailed review of colloidal dispersions of QDs in different LC phases is presented highlighting applications and challenges in this field. Although Chapter 2 focuses on the various LC nanocomposites doped with semiconductor QDs, most of the presented ideas, challenges

and applications are substantially descriptive of the other nanoparticulate systems as LC dopants.

Chapter 3 presents the results of a study on a series of small and monodispersed CdSe QDs also known as magic-sized CdSe in a nematic LC. The three types of CdSe QDs are similar in size and shape but vary in core composition, as the first two are different in the amount of defects as manifested in their photoluminescent properties, and the third is doped with a small concentration of Zn atoms (CdSe/Zn). Using POM and FCPM studies of the doped samples, the impact of particles on the alignment of LC molecules within plain glass slides and polyimide coated test cells is studied. Further electro-optic characterization of test cells filled with the doped nematic samples, shows different electro-optical behaviour in the samples doped with CdSe/Zn QDs, highlighting the roles of core composition and surface defects. Appendix 1 contains spectral and experimental data, as well as supplemental electro-optical measurements.

In Chapter 4, the synthesis and characterization of hydrophobic Au NP using silane conjugation chemistry is discussed along with their composites in N-LC at different concentrations of the dopant. The surface of the Au NP is coated with long alkyl chains ($C_{18}H_{37}$-) which appears critical for the induction of homeotropic alignment on plain glass as well as facilitating better dispersion in unidirectionally rubbed planar alignment cells. In addition, DSC and POM results are presented, both indicating an expansion of the mesophase range of the N-LC on heating and cooling cycles. The results in Chapter 4 demonstrate the importance of silanization to provide chemical and thermal stability to gold nanoparticle dopants in LC nanocomposites, in order to prevent aggregation and consequently giving access to higher NP loads with more pronounced electro-optical

effects. The appendix of this chapter includes experimental and characterization results for the nanocomposites.

Chapter 5 details the synthesis of LC-functionalized gold nanoparticles using silane conjugation chemistry. Nematic nanocomposites made of the three different Au NPs with surface ligands structurally similar to the host nematic molecule, are discussed with respect to the surface ligands type (structure perhaps) and their chemical stability and compatibility with the nematic LC host. Finally in this chapter a model for the interaction between NPs and LC molecules is proposed. Chapter 5 has two appendices: The first appendix includes experimental and spectral data for the intermediate and final organic compounds as well as for the Au NPs and nematic nanocomposites. In the second appendix of this chapter, results of numerical simulations performed based on the nanoparticles used in this thesis as well as in prior studies, are presented.

Chapter 6 summarizes the important aspects of the work in this thesis. Here, the data collected during previous work in the Hegmann group and this thesis are compared, and potential avenues for future work are highlighted. In view of the importance of providing easy-to-make and benign NPs for the LC-NP field, carbon nanoparticles also known as carbon dots, are briefly introduced and the preliminary results from dispersion of these carbon dots in N-LCs, are shown.

1.4 Liquid Crystals

The first recorded observation of a liquid crystal (LC) was in 1888 by the Austrian botanist Friedrich Reinitzer.[16] When Reinitzer was investigating cholesterol samples extracted from

carrots, he noticed that there were what appeared to be phase changes at two different temperatures: At room temperature the compound was solid, but when the temperature was raised to 145 °C, it appeared to be in a sort of milky state until it turned into a transparent liquid at 179 °C. Unable to explain what he had observed, Rienitzer turned to his friend the German physicist and crystallographer, Otto Lehmann.

In his laboratory, Lehmann started his investigation with one of the world's first polarizing microscopes and for the first time observed the phase changes in what was later to be identified as a mesophase of cholesteryl benzoate. The term "mesophase" (between two phases) indicates a state of matter or a phase existing between solid and liquid phases of the LC compound having this type of phase behaviour. Inheriting some properties of the rigid crystalline state and the disordered isotropic liquid, LCs are also considered as a fourth state of matter featuring a long-range orientational order and a reduced to zero positional order within the LC molecules.[3] LC molecules at the phase transition from a crystalline state lose the long-range order while keeping some order and degree of mobility as they enter into the mesophase. The outcome of such transitions is different types of mesophases depending on the orientational and positional order of the LC molecules (also known as "mesogens") along with their chemical structure and physical properties.

After the discovery of liquid crystals (LCs) and studies of their physical and chemical properties throughout the years, they have become an established part of an interdisciplinary science and are investigated by physicists, chemists, engineers and materials scientists, mainly as anisotropic fluids and underlying materials in most of the today's liquid crystal display (LCD) devices due to the presence of unique optical and electro-optical properties in specific types of LCs.

1.5 Liquid Crystal Phases

LCs are mainly classified as thermotropic and lyotropic. Thermotropic LC phases are observed when temperature changes, while lyotropic LC phases are observed as a function of temperature and as the concentration of a surfactant in a solvent changes. Lyotropic LC molecules are amphiphilic molecules containing both a hydrophobic and a hydrophilic group. Lyotropic LC are abundantly present in human body cells, brain, nerves, muscles, blood, and organs, and they play a critical role in biological functions. Lyotropic LCs have the fluidity required for membrane diffusion and the molecular structure for biologic function.[17] Lyotropic LCs are critical for biologists and biochemists to understand life mechanisms and disease. Recently, certain lyotropic LC materials have been used as templates for the synthesis of nanomaterials including semiconductor QDs. Some examples of such approaches are highlighted in section 2.2.1.

Materials capable of displaying thermotropic mesophase behaviour are commonly but not always non-amphiphilic molecules with strong anisometric shapes. As demonstrated in **Figure 1.1**, thermotropic LCs can be further classified according to their molecular shape. These include calamitic (rod-like), discotic (disk-like), sanidic (board-like) and bent-core (banana-shaped). A common feature in all the above shapes is an anisometric molecule shape, which enables orientational arrangement of molecules in a form of a partially ordered mesophase. The LC materials studied in this thesis are rod-like thermotropic LCs therefore, other classes and shapes of LC materials will not be discussed in any further detail. Calamitic or rod-like LCs are the most well-known and widely-used LCs in display and electro-optic devices.

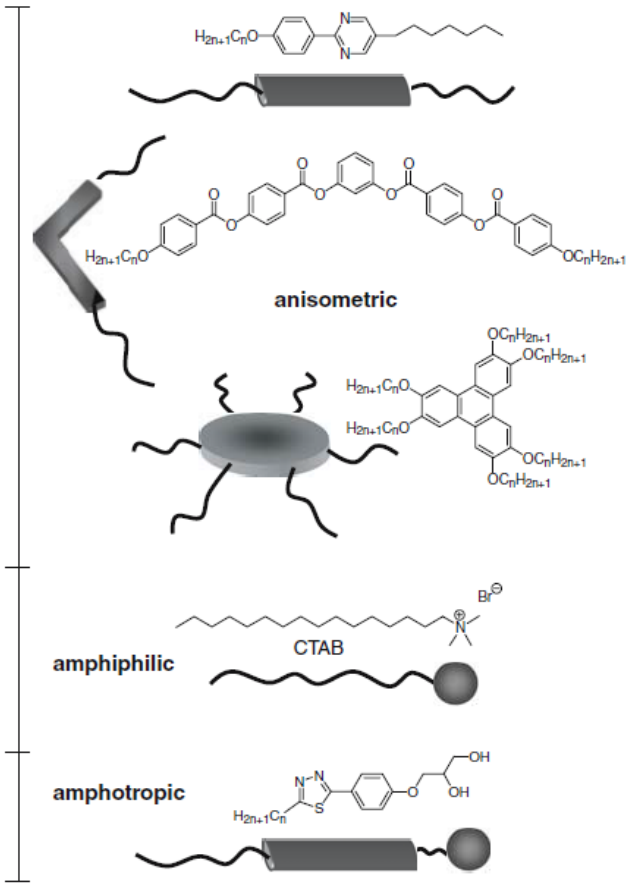

Figure 1.1 Typical examples (and molecular shapes) of the main types of molecules forming LC phases. Reproduced with permission from Ref.[18]- Copyright: Springer Science.

Rod-like LC molecules have one long dimension and two short dimensions and often consist of a rigid core of two or more ring systems, and one or two flexible side chains (see **Figure 1.2**). Formation of the mesophase is a consequence of a delicate interaction between rigid and flexible moieties in these molecules.[19] The rigid core is often made of phenyl- or cyclohexane-rings, and sometimes heterocycles such as pyrimidine. These rigid units shape the molecules into anisometric rod structures and induce orientational arrangement of molecules by providing strong intermolecular interactions. However, as it was mentioned earlier, formation of mesophases requires the presence of both rigid and flexible units in

the LC molecules.[19] Flexible units in the LC molecules are usually alkyl- or alkoxy side chains of various length. **Figure 1.2** shows a schematic liquid crystalline structure and some LC molecules.

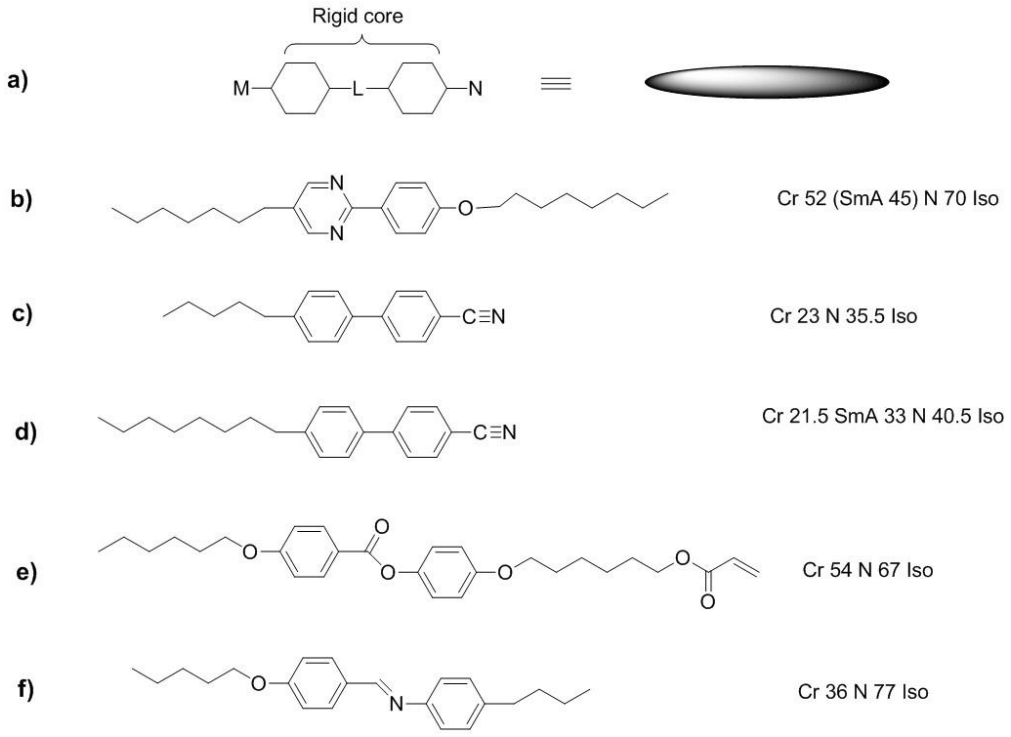

Figure 1.2 a) Schematic drawing of the general molecular structure of a rod-like LC showing rigid core with M and N flexible side chains. (b-f). Examples of some LC molecules and their phase transition temperatures in °C (b-d) (Cr = Crystalline, SmA = Smectic A, N = Nematic, Iso = Isotropic liquid). By convention, a phase transition temperature in parenthesis indicates a monotropic phase; i.e. that particular phase can only be observed on cooling.

In general, the design of an LC molecule involves selection of rigid core units as well as side chains. In addition, other molecular features such as a linking group within the rigid core (shown by L in **Figure 1.2**) or introducing functional groups to the side chains or the core can significantly influence the physical properties and mesophase behaviour of the

resulting LC molecules. For example, in a class of LC molecules including 5CB and 8CB, LC molecules contain a cyano (-CN) group instead of one side chain. This molecular feature increases the polarizability along the long axis of the molecules and thus can result in a high positive dielectric anisotropy in these LCs. Dielectric anisotropy of LCs will be discussed in section 1.7.2.

LC phases are further classified based on their degrees of positional and orientational order. Each thermotropic rod-like LC molecule can form one or more mesophases upon heating from a crystalline state or cooling from an isotropic liquid state. Some common liquid crystalline mesophases for rod-like molecules are shown in **Figure 1.3**. Nematic is the least ordered LC phase, characterized by a long-range orientational ordering and no positional ordering. In the nematic phase of rod-like molecules, LC molecules are oriented along the average direction of the molecular long axes, called director. Smectic phases are higher ordered mesophases than nematic, possessing long-range orientational ordering with additional layer ordering. The two most commonly observed smectic phases are the smectic-A phase (SmA) and the smectic-C phase (SmC). In the SmA phase, long molecular axes of the molecules are perpendicular to the layer planes, and in the SmC phase the molecules are tilted by an angle with respect to the layer normal.[19] The greater positional and orientational order in the smectic LCs obviously results in a greater viscosity as compared with the less-ordered nematic LC. In general, this lower viscosity is the reason that nematics usually respond more sensitively to external applied electric fields than smectics and why the nematic is the LC of choice for displays. The higher viscosity renders the smectics less suitable for use in fast-motion displays, but because smectic displays can retain an image in the absence of an external electric field, they consume less energy and

thus may be used efficiently in static or slower-moving displays, such as advertising panels, light-blocking and imaging windows, and electronic books.[17] It should be noted here that chiral smectic-C (SmC*) ferroelectric LCs switch orders of magnitude faster than nematics as their molecular motion does not require a full 90° flip of the entire molecule, but only a rotation around a tilt cone (in microseconds vs milliseconds for nematics). The higher order however creates problems for the alignment of these ferroelectric LCs. The phase sequence required for FLCs to obtain good alignment is Iso-N*-SmA-SmC*, where the tilt from SmA to SmC* goes along with a layer shrinkage, which is why several LC research groups work on de Vries materials where this is not the case.[17]

The chiral nematic phase (N*) (also called cholesteric) is another type of mesophase where mesogenic molecules contain a chiral center and organize in quasi-layers with no positional ordering within layers. However, the director axis varies between layers and this variation tends to be periodic in nature. This leads to the formation of a structure which can be visualized as a stack of very thin 2-dimensional nematic-like layers with the director in each layer twisted with respect to those above and below, forming a helical pattern (**Figure 1.3**).

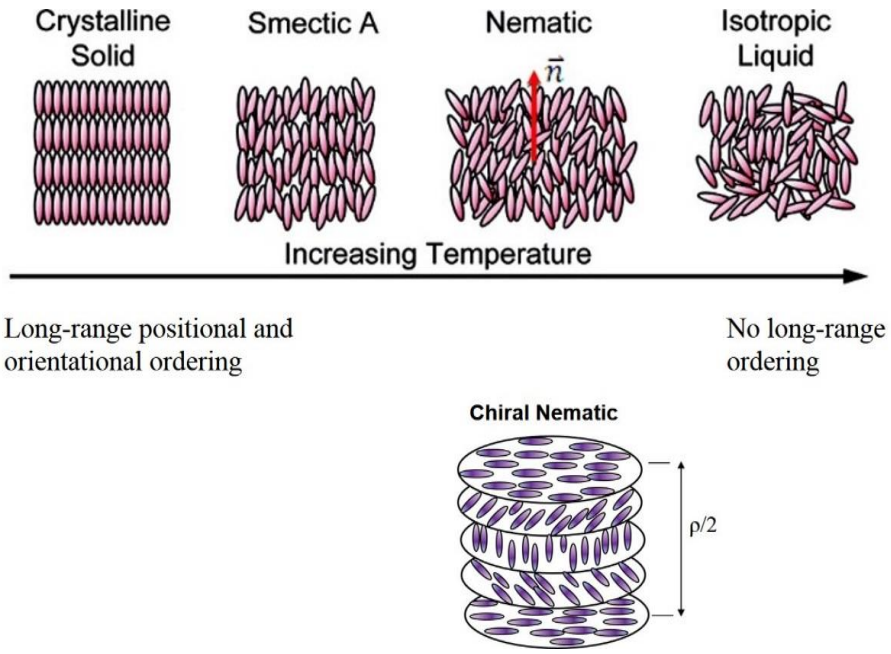

Figure 1.3 (top) Schematic representation of LC phases in thermotropic rod-like liquid crystals as the temperature is increased. Adapted from Ref. [20] (bottom) Schematic of the chiral nematic ordering present in chiral nematic molecules, along with an illustration of the half-helical pitch $\rho/2$.

The temperature and the range of temperature at which a mesophase forms and exists are characteristics of each LC material and its molecular structure.[3] When a mesophase can be observed on both heating and cooling cycles, it is called enantiotropic and if it is only present on cooling monotropic. In this thesis only rod-like N-LCs are studied, therefore in the following sections a summary about the properties and key characterization techniques of this phase will be presented.

1.6 Nematic Liquid Crystals

The nematic phase is the simplest and least ordered mesophase and features a long-range orientational order only. In rod-like nematics, the long molecular axes are preferably

oriented in one direction, defined as the director **n** (**Figure 1.3**). In most uniaxial N-LCs without permanent dipole moment both directions of the vector **n**, +**n** and –**n** are equivalent. The degree of orientational order in the nematic phase can be quantified by

$$S = \frac{1}{2} < 3\cos^2\theta - 1 > \qquad \text{(Eq. 1.1)}$$

where S is the scalar order parameter, θ is an angle between the individual molecular long axis and the director **n**, and the brackets indicate the average value.[3] The order parameter decreases as the temperature increases. The maximum value of S = 1 is for a perfectly oriented system and the minimum value of S = 0 signifies the isotropic liquid state with no orientational order. Typical values for an N-LC are in the range 0.3-0.9.[3]

The nematic phase is the least ordered quite similar to an isotropic liquid state. This means that a nematic mesophase will melt into the isotropic liquid state with relatively low thermal energy required for the transition. The temperature corresponding to this phase transition is called the clearing point (T_c) which is characteristic for every LC material.

1.7 Physical Properties of Nematic Liquid Crystals

With anisometric rod-shaped molecules and the resulting uniaxial symmetry around the director, LC phases like nematics show anisotropy in many of their physical properties. That is, physical properties such as the refractive index, the dielectric permittivity, or the

magnetic susceptibility, have a different value parallel to the director n and perpendicular to it.

The nematic mesophase is without a doubt the most studied mesophase and is still the most frequently used LC phase in the display and other electro-optical applications due to its preferred birefringence and electro-optic response. The following sections introduces the most important properties of this phase including elastic, dielectric and optical properties along with the corresponding characterization techniques.

1.7.1 Birefringence

LCs show birefringence due to the optical anisotropy of the phase which occurs when light polarized along the director **n** propagates at a different velocity than light polarized perpendicular to it. As the polarized light enters a nematic LC sample, the light splits into two components due to the two different principal refractive indices: ordinary refractive index (n_o) and extraordinary refractive index (n_e).

In a uniaxial birefringent medium like an N-LC with optical axis parallel to **n**, the index n_e is measured for the light wave where the electric vector vibrates parallel to the optical axis (extraordinary wave, $n_e = n_{\parallel}$) and the index n_o, is measured for the light wave where the electric vector vibrates perpendicular to the optical axis (ordinary wave, $n_o = n_{\perp}$.).[3] The birefringence then is described by Equation 1.2. In N-LCs usually $n_e > n_o$ and, therefore, Δn is positive and varies in the range from values close from zero to about 0.4.

$$\Delta n = n_e - n_o \qquad \text{(Eq. 1.2)}$$

1.7.2 Dielectric Anisotropy

Dielectric properties of LCs are related to the response of LC molecules to an external electric field. LC materials with often low electrical conductivity values (as low as 10^{-17} S/m) are considered as non-conducting dielectric medium and can be placed between the plates of a capacitor.[22] In the capacitor with vacuum between its plates, the capacitance is equal to C_0 (calculated from Equation 1.3, where ε_0 is the dielectric constant of vacuum, A is the plate area and d is the distance between the two plates). In the capacitor filled with the LC (an LC test cell), the capacitance will be increased by the factor ε and is calculated according to Equation 1.4. The value of ε represents the permittivity of the dielectric LC material.[22]

$$C_0 = \varepsilon_0 \times \frac{A}{d} \qquad \text{(Eq. 1.3)}$$

$$C = \varepsilon \times \varepsilon_0 \times \frac{A}{d} \qquad \text{(Eq. 1.4)}$$

The permittivity is a physical quantity that shows how an external electric field affects and is affected by a dielectric medium and is determined by the ability of a material to become polarized in response to an applied electric field, and thereby to cancel partially the field inside the material. In the LC materials consisting of non-polar molecules, there is only an induced polarization. In the LCs with polar molecules, in addition to the total induced polarization, there is the orientation polarization, due to the tendency of the permanent dipole moments to orient themselves parallel to the applied electric field.

Considering an N-LC, two possible permittivities can be characterized with respect to the director: parallel to the director $\varepsilon_{\parallel}$, and perpendicular to the director $\varepsilon_{\perp}$. The dielectric anisotropy value is therefore the difference between the two permittivities ($\Delta\varepsilon$) and can be obtained by following Equation 1.5:

$$\Delta\varepsilon = \varepsilon_{\parallel} - \varepsilon_{\perp} \qquad \text{(Eq. 1.5)}$$

Depending on the structure of the N-LC, $\Delta\varepsilon$ can take positive and negative values. LCs studied in this thesis are N-LCs with positive $\Delta\varepsilon$. The dielectric anisotropy depends on the temperature as parallel and perpendicular permittivities do. **Figure 1.4** shows the graph of temperature versus dielectric permittivities for a typical LC with positive $\Delta\varepsilon$. As the temperature increases the difference between $\varepsilon_{\parallel}$ and $\varepsilon_{\perp}$ become narrower until there is only one permittivity present for the LC and that belongs to the isotropic liquid state of the LC material (ε_{iso}).

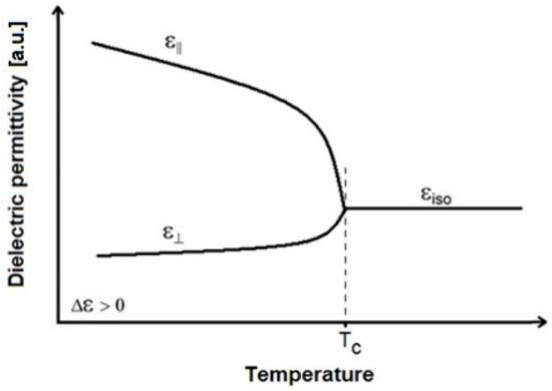

Figure 1.4 Temperature dependence of dielectric permittivity in liquid crystals with $\Delta\varepsilon > 0$; T_c and ε_{iso} are clearing temperature and permittivity of isotropic liquid, respectively. Reproduced from Ref.[21] – Open Access Journal

1.7.3 Elastic Constants

Under certain external forces such as electric or magnetic fields deformation of the director can occur. A deformed N-LC shows a distorted director field, i.e. the director changes its direction from point to point as opposed to an undeformed nematic where the director points in the same direction throughout the LC.

In general, there are three types of deformation in LCs: splay, twist, bend and combinations thereof. When the external force (e.g. applied electric field) exerts and exceeds a certain value, relative position of the LC molecules will change and deformation will occur in which the molecules are forced to splay, twist or bent until equilibrium. This equilibrium will be achieved when the system reached its minimum energy state. **Figure 1.5** shows the three deformations of splay, twist and bend in the director field of a rod-like N-LC. The total elastic free energy density or the Frank energy density (free volume elastic energy) can be written as Equation 1.6 using the elastic constants corresponding to these deformations:

$$f = f_0 + \frac{1}{2}[K_{11} \times (\nabla . n)^2 + K_{22} \times (\nabla . n)^2 + K_{33} \times (\nabla . n)^2] \quad \text{(Eq. 1.6)}$$

where f is the elastic free energy density (free energy density is defined as the free energy in a unit volume of LC), f_0 is the minimum free energy of the N-LC with a uniform director, n is the unit director of the liquid crystal, K_{11} (splay), K_{22} (twist), and K_{33} (bend) are elastic constants.

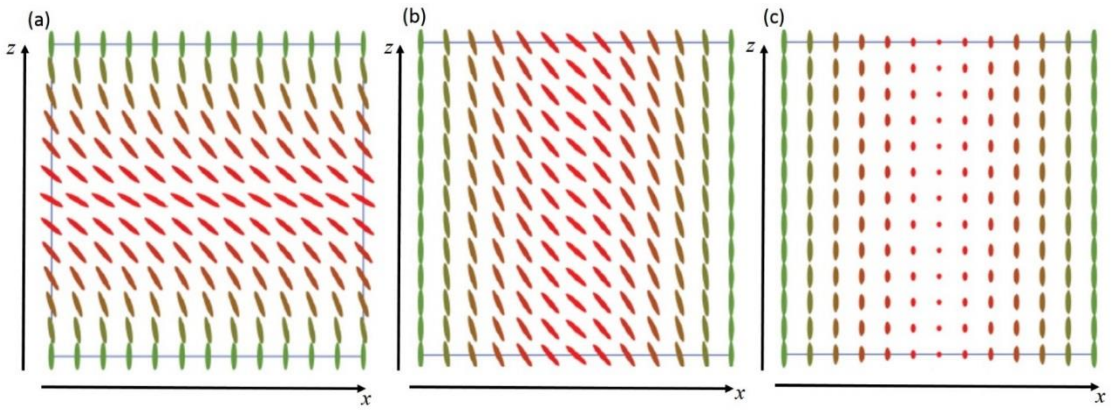

Figure 1.5 Schematic representation of unidirectional deformations; a) bend, b) splay, and c) twist imposed on the system. Images represent the director field in a two dimensional slice of a three dimensional sample. Director **n** is set to be aligned with the *z-axis.* Reproduced with permission from Ref. [23] – Copyright: The Royal Society of Chemistry.

The value of elastic constants for each LC or LC nanocomposite is unique to that LC or nanocomposite at a given temperature. The Unit of elastic constants is Newton. For example, the K_{11} for the nematic 5CB is 6.65×10^{-12} N at 24 °C.[24]

1.7.4 Alignment and Surface Interaction

Interactions between N-LC molecules and surfaces can lead to the orientation of the LC molecules at these surfaces**.** Alignment of the LC molecules near the surface, though limited, will be transferred into the bulk of the LC sample over macroscopic distance of a given volume by elastic forces. The resulting orientation of the director **n** in a specific direction in the bulk corresponds to the tendency of the system to achieve a minimum free energy state. There are three main types of the LC director **n** alignment. These are planar,

tilted and homeotropic orientations (**Figure 1.6**). The planar alignment itself can exist in two forms of homogenous and heterogeneous.

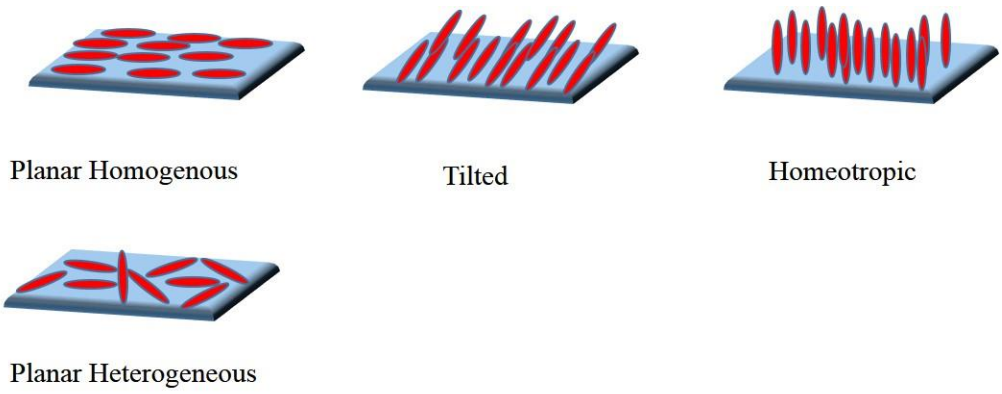

Figure 1.6 Schematic drawing of three types of alignment mode of rod-like LCs on a substrate. Planar alignment can be either homogeneous or heterogeneous (random or free planar) with respect to the direction the director **n**.

The surface or substrate is expected to be flat on the microscopic scale and in all the electro-optical applications of LCs is made of a transparent material such as glass coated with a conductive layer of transparent indium tin oxide (ITO) and an alignment layer. The position of the director near the surface is determined by polar θ and azimuthal φ angles (**Figure 1.7**).

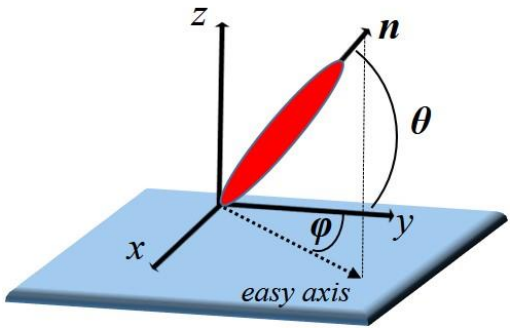

Figure 1.7 Definitions of polar θ and azimuthal φ angles indicating position of director **n** near surface. The preferred direction of the director **n** at the surfaces set by alignment is called "easy axis".

In planar alignment the director lies in the plane of the surface or interface between the mesophase and the surface and the polar angle $\theta = 0°$. As mentioned earlier, there are two possible orientations for the planar alignment: 1) homogeneous planar orientation in which the director is oriented uniformly over the surface and azimuthal angel φ is fixed. 2) Heterogeneous planar orientation, in which the orientation of the director is not uniform over the surface and φ has different fixed values at different points of the surface. In homeotropic (also known as vertical) alignment $\theta = 90°$ and in case of tilted orientation θ is fixed ($0° < \theta < 90°$) and φ is random.

Orientation of N-LC molecules on a substrate depends on several factors including the surface energy and topographical features of the substrate, as well as on the intermolecular interactions, steric factors, and the elasticity of the LC molecules.[3, 22] Mechanical or chemical treatment of the surface, usually glass substrate of the LC test cell prior to loading the LC materials is a common method for achieving a particular type of alignment.

Coating the glass substrates with an amphiphilic surfactant such as lecithin can induce homeotropic alignment. Hydrophilic heads of surfactant molecules point to the glass

substrate and the hydrophobic tails spread into the bulk of the LC sample. Steric interaction of the aliphatic side chains of rod-like LCs and the hydrophobic tails of the surfactant cause the homeotropic alignment.

Coating the surface with polyimide followed by a unidirectional rubbing provide a substrate with high surface energy and strong planar anchoring of molecules, thus is suitable for obtaining the homogenous planar alignment of the LC molecules. Similarly, homogeneous planar orientation of the director can be achieved by simply rubbing the surface with a velvet cloth in some pre-defined direction. This technique is called Chatelain's method.[22] Tilted orientation can be obtained with the oblique evaporation of the SiO_x thin films on the substrate surface.[22]

1.7.5 Fréedericksz Transition

N-LC materials containing polar or non-polar molecules respond to an external applied electric field. In calamitic nematics, if the permanent dipole in the case of polar molecules or induced dipole in the case of non-polar molecules is along the long molecular axis then $\Delta\varepsilon>0$ and molecules tend to orient along the direction of the applied electric field (**Figure 1.8**). If the molecules possess dipole moments that are more or less perpendicular to the long molecular axis then $\Delta\varepsilon<0$ and molecules tend to orient perpendicular to the electric field direction (**Figure 1.8**).

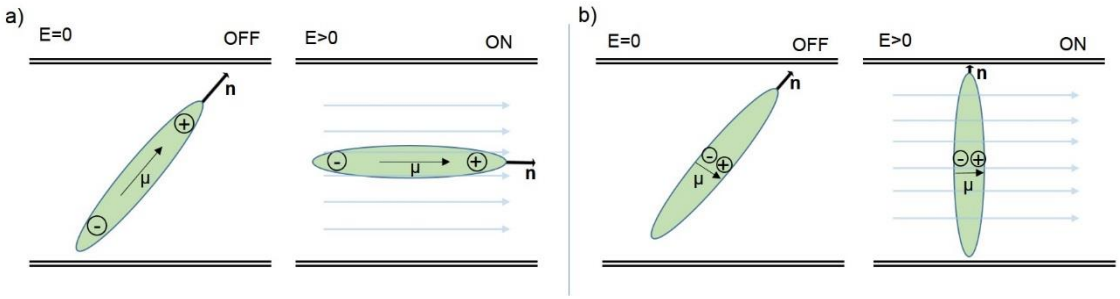

Figure 1.8 Schematic illustration of LC response in electric field: (a) LC with positive dielectric anisotropy ($\Delta\varepsilon > 0$), and (b) LC with negative dielectric anisotropy ($\Delta\varepsilon < 0$).

It should be noted that collective response of the LC molecules to the applied electric field E causes the distortion of the director **n**. Therefore, the electric contribution should be added to the free energy density and is described by

$$F_e = -\frac{1}{2} \times \varepsilon_0 \times \Delta\varepsilon \times (E \times n)^2 \qquad \text{(Eq. 1.7)}$$

where F_e is the electric free energy density, ε_o is the electric permittivity of vacuum. This equation shows the dependency of the electric free energy density on the director field and dielectric anisotropy of the N-LC. For example, in nematic LCs with positive dielectric anisotropy the minimum in free energy density is obtained by parallel orientation of the director to the external electric field. In addition, the larger the dielectric anisotropy the smaller electric field is needed to reorient the LC molecules.

The Fréedericksz transition represents the field-induced reorientation of a uniform director pattern in a nematic LC sample under the influence of an external field, first time reported by Fréedericksz and Zolina.[25] Once the field strength exceeds some threshold or critical value, reorientation begins which causes additional distortions in the director field,

thus increasing the free energy density due to the increase in the elastic energy. The system then achieves a new equilibrium state by a gradual change of the director structure. **Figure 1.9** depicts a type of Fréedericksz transition containing a splay deformation of molecules. The field-induced Fréedericksz transition and the resulting equilibrium director field not only depend on the applied electric field, but also on the elastic properties of the LC and the boundary conditions at the surfaces. Therefore, performing field-induced Fréedericksz transition experiments on a uniformly aligned nematic LC sample can reveal information about boundary conditions of the sample as well as on the dielectric and elastic properties of the nematic material.

Typical electro-optical characterization of the LC nanocomposite samples performed in this thesis involves applying an external electric field to induce director deformation in pre-aligned nematic composite samples with well-defined director field, and detecting changes in the director field using capacitance or transmission measurements. More details about the electro-optical characterization of the LC samples is presented in the following electro-optical characterization section.

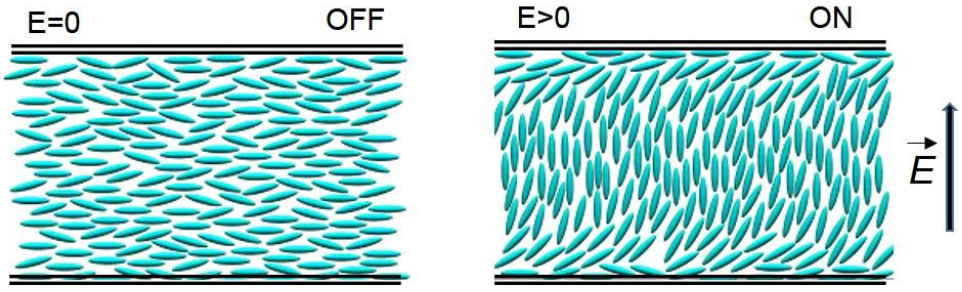

Figure 1.9 Schematic drawing of the splay Fréedericksz transition in a rod-like N-LC with positive $\Delta\varepsilon$. The image on left shows the initial undistorted alignment in the absence of the electric field and the image on the right depicts the distorted state with splay type deformation upon the application of an external electric field.

1.8 Characterization of Liquid Crystals

In this thesis, pure and doped N-LC samples have been fully characterized using multiple techniques including polarized optical microscopy, fluorescence confocal polarized microscopy, differential scanning calorimetry, and electro-optic measurements.

1.8.1 Polarized Optical Microscopy

Polarized optical microscopy (POM) is a key technique to detect the existence of LC phases. It has all the benefits of bright field microscopy and offers a wealth of information about local orientations, formation of characteristic defect textures, alignment and phase transitions, which are not simply available with any other microscopy techniques. In this thesis, all pure and doped nematic samples were fully characterized by the POM to study the influences of the spherical NP dopants on the alignment and optical textures of the nematic composites, as well as test their phase transition temperatures and defects formation.

This technique is based on the polarization of light in an optical microscope. A typical setup of a POM and the equipment for the POM studies at the University of Manitoba are shown in **Figure 1.10**. There are two polarizers in each POM, which are designed to be oriented at an angle to each other, typically oriented at 90° (also termed as crossed polarizers). The light polarized by the first polarizer, will be blocked the second polarizer (also known as analyzer) since this polarizer is oriented perpendicular to the incident wave.

As it was mentioned in section 1.7.1, an anisotropic material like an LC has optical properties that vary with the orientation of incident light with the orientation of the

specimen. In observing LC samples by POM, LC specimen can act as beam splitters and divide light rays into two parts (ordinary and extraordinary rays) due to the birefringent properties. The POM technique exploits the interference of the split rays, as they are reunited along the same optical path. The combined rays can partially pass through the analyzer due to the change in polarization, and therefore usually an optical texture can be observed and photographed by a digital camera. However, when the transmission axis of the first polarizer is parallel to either the ordinary or extraordinary directions, the light is not broken up into components, and no change in the polarization state occurs. In this case, there is not a transmitted component and the region appears dark. In addition, when the sample is not birefringent or the LC is in the isotropic liquid phase, no change to the direction of the polarized light occurs, thus no light can pass through the analyzer and the field of view will be entirely black.

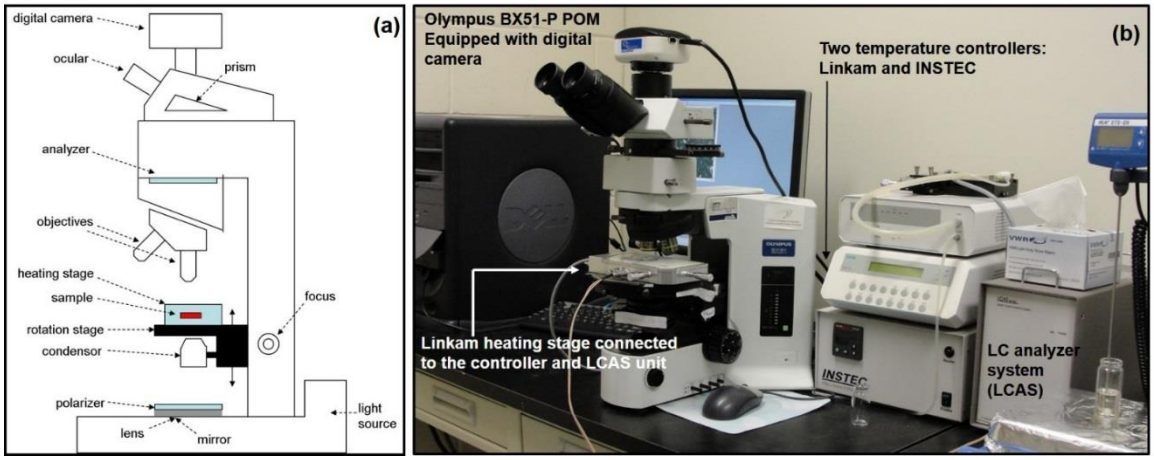

Figure 1.10 a) Schematic setup of a polarized optical microscope, b) POM facility at the LC Nanocomposite Lab, Department of Chemistry, University of Manitoba.

The optical texture observed for each thermotropic LC material at a given temperature has its own characteristic features representing a unique mesophase. In addition, the colors and intensity of each color in the optical texture depends on the local orientation of LC molecule, as well as the thickness of the sample.[26] As it was mentioned earlier, the substrate surface condition and certain treatment of the substrate surfaces determine the orientation of LC molecules and consequently have impacts on the observed POM textures. For example, untreated glass slides promote heterogeneous planar orientation of the N-LC molecules in which the director **n** is parallel to substrates but points in different directions and the texture of the N-LC sandwiched between two glass slides under this condition appears as a *Schlieren* texture. **Figure 1.11**(a) shows a typical *Schlieren* texture of the nematic and **Figure 1.11**(b) shows a typical optical texture of a SmA mesophase.

The *Schlieren* texture shows characteristic sets of dark brushes, mainly four brushes along with two brushes (figure 11a). These dark brushes correspond to the domains with extinction orientation of the N-LC molecules where the director **n** lies parallel to either the polarizer or analyzer axes. The points, where the two or four brushes meet, correspond to the director singularities and are topological defects known as disclination points.[27]

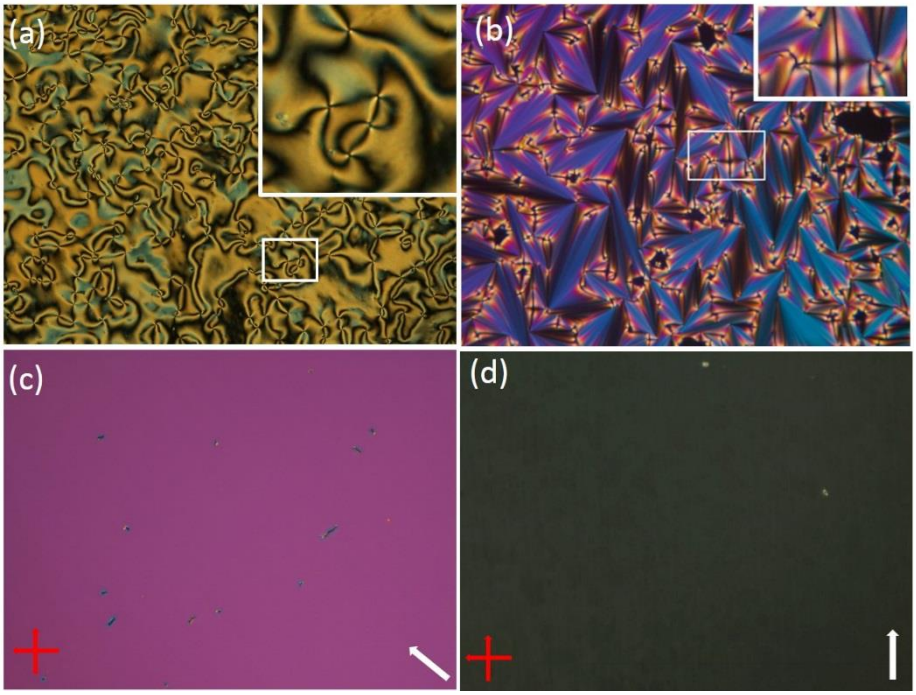

Figure 1.11 POM photomicrographs of LC samples (top, a-b untreated plain glass slides; bottom, c-d polyimide rubbed planer cell). a) *Schlieren* texture of the nematic phase, b) focal conic texture of SmA phase, c) homogenous planar alignment of nematic with the director oriented at 45° with respect to either polarizer and analyzer, and d) homogenous planar alignment of nematic LC with the director parallel to the polarizer. The inset in a and b shows selected areas magnified. The white arrow in the bottom right corner in c and d shows the rubbing direction of the cell, and the crossed arrows indicates crossed polarizer and analyzer. Micron size dark objects which are seen on images c and d are pieces of glass used as spacer in the electro-optic cells.

When the N-LC sample is placed in electro-optic cells featuring rubbed polyimide alignment layers with strong planar anchoring of molecules at the LC interface, homogeneous planar alignment of nematic molecules will be achieved. In this case the POM texture usually appears as a bright uniform color or completely black depending on the orientation of the sample with respect to the direction of polarizer and analyzer. The maximum brightness or birefringence is achieved when the rubbing direction of the test cell surface and therefore the director is at a 45° angle with respect to the crossed polarizer

and analyzer [**Figure 1.11**(c)]. The texture is completely black when the director direction is either parallel or perpendicular to the transmission axis of the polarizer or analyzer [**Figure 1.11**(d)].

1.8.2 Fluorescence Confocal Polarized Microscopy

A more advanced microscopy technique than POM for studying LC materials is fluorescence confocal polarized microscopy (FCPM) which offers 3-dimensional imaging capability by combining the features of fluorescence and confocal microscopies with POM. An FCPM setup offers emission and detection of polarized light, and by adding anisometric fluorescent dye molecules which, on average, align parallel or perpendicular to the molecules of the studied host LC material, orientational order of anisotropic LC samples can be probed.[28] The basic principle of FCPM is illustrated with the help of a schematic drawing shown in **Figure 1.12**. In addition, the confocal feature enables focusing light into a small volume element using a special objective with a high numerical aperture and a pinhole in front of the detector that functions as a spatial filter to reduce the signal emerging from outside the selected volume.[29, 30] As a result, FCPM can resolve the *z*-component of the LC director (along the optical axis of the microscope) in addition to some average of the two orthogonal *x*- and *y*-components.

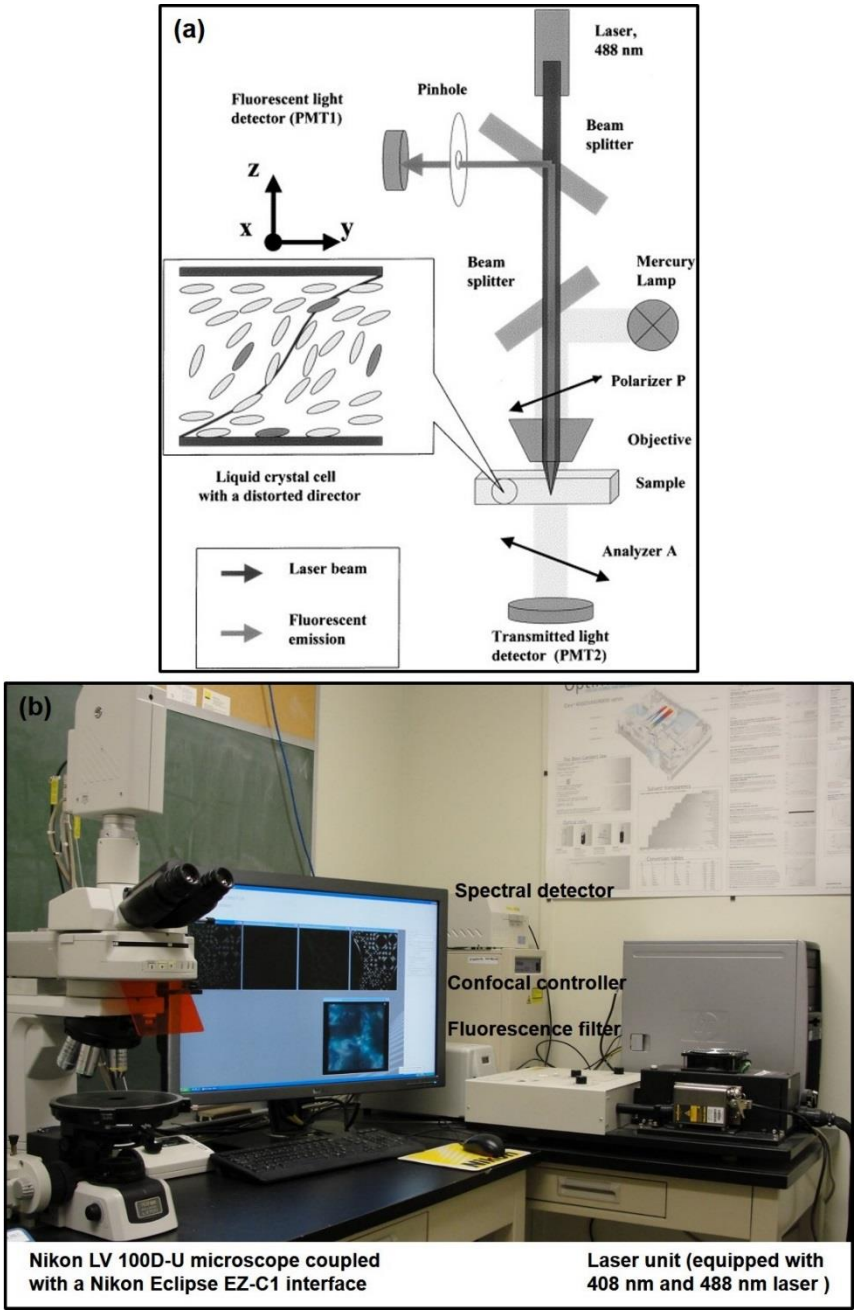

Figure 1.12 a) Schematic drawings representing the principle of FCPM technique. Reproduced with permission from Ref.[28]- Copyright: Elsevier Science. b) FCPM setup at the LC Nanocomposite Lab, Department of Chemistry, University of Manitoba.

The importance of FCPM studies on the dispersion of colloidal semiconductor QDs into different LC phase is twofold. QDs have size-dependent photoluminescence, so they

can be excited separately from the anisometric dye using two different lasers with the appropriate wavelengths. FCPM of the LC-QD nanocomposites can reveal critical information on the spatial distribution of the NPs and their interaction with LC molecules, as well as on the assembly and orientation of QDs within the mesophase. Therefore, LC-QD composites can be used as model systems to study and predict behavior of the nanoscale dopants in liquid crystalline media. Some examples highlighting the role of FCPM investigations on the LC phases doped with different types of QD are discussed in Chapter 2.

The FCPM facility at the LC Nanocomposite Lab is equipped with two lasers (408 nm and 488 nm; **Figure 1.12**) and is suitable for collecting information on the orientation of the nematic director and simultaneously the local distribution and agglomeration of CdSe QDs. The research and experimental aspect of FCPM studies performed in this thesis on the dispersions of a series of CdSe QDs in the nematic phase are presented in Chapter 3.

1.8.3 Differential Scanning Calorimetry

Differential Scanning Calorimetry (DSC) is a versatile tool and a complementary technique to study LC phase transitions. In thermal characterization of the LC phases, POM gives optical texture information along with the appearance or disappearance of the LC phases, while it does not deal with transition temperatures, enthalpy values and order of the transition. In this thesis, phase transition temperatures and mesophase ranges of all nematic nanocomposites have been investigated using both POM and DSC. N-LCs doped with NPs often demonstrate a co-existence of two neighboring phases instead of sharp transitions from one phase to another. POM allows us to collect information about these ranges of

temperature at which phase transitions occur, and to observe selected areas of the nematic nanocomposites with the co-existence of two phases (biphasic regions). On the other hand, phase transition temperatures obtained by DSC, although generally consistent with POM results, represent transitions throughout the bulk of samples rather that local areas observed under the microscope.

The principle of DSC is based on determining the heat supplied or extracted during a phase transition of an LC or any other material.[31] A power compensation DSC like the one in our group at the Department of Chemistry, University of Manitoba typically has two chambers side by side, one for the sample and one as the reference. During the measurement these two chambers are heated equally and the thermal properties of the sample are compared with a standard reference material which has no phase transition in the same temperature range such as an empty alumina holder (or pan). The temperature of each holder is monitored and the heat (power) is supplied to each holder to keep the temperature of the two holders equal. Important information about phase transitions and changes in heat capacity are obtained by plotting the difference in the power supplied against the temperature attained.[31]

Figure 1.13 shows a complete DSC trace (thermograms) obtained for 8CB (8CB: Cr 21.5 SmA 33 N 40.5 Iso). The top thermogram in Figure 13 corresponds to the heating cycle, and the one below that belongs to the cooling cycle. The three peaks in the heating thermograms indicates three phase transition, namely crystalline to SmA, SmA to nematic and finally nematic to isotropic liquid. The cooling cycles proves the enantiotropic nematic and SmA mesophases. It should be noted that in this example significantly lower SmA→Cr

phase transition on cooling compared to the heating cycle, is mainly due to super-cooling of the materials, along with contributions of instrumental hysteresis.

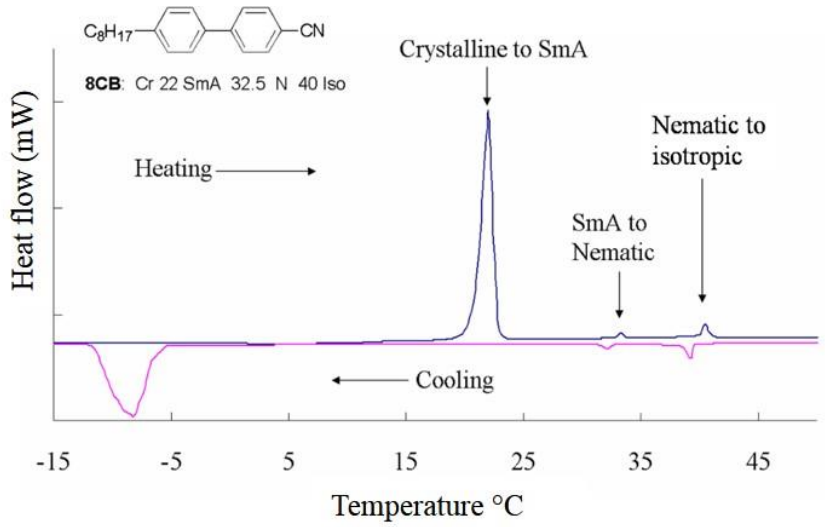

Figure 1.13 DSC plots of 8CB with phase transition temperatures and chemical structure.

1.8.4 Electro-Optical Measurements

One important aspect of this thesis is to investigate colloidal N-LC composites as alternatives for LC-only mixtures for electro-optic and display applications. This can be realized by achieving the desired optical and electro-optical properties in these nanocomposites with the right type and amount of NPs. Therefore, throughout this thesis new doped nematic samples have been made and their electro-optical (EO) parameters have been measured. These parameters mainly include: threshold voltage (V_{th}) for splay-type Fréedericksz transition, parallel and perpendicular permittivity values ($\varepsilon_{\parallel}$, $\varepsilon_{\perp}$),

dielectric anisotropy ($\Delta\varepsilon$), elastic constants (usually K_{11} related to splay deformation), and finally rise and decay times (τ_{rise} , τ_{decay}).

Prerequisite for any electrical measurements of the N-LCs is loading the sample into an EO test cells. There are different types of homemade and commercially available test cells and are typically comprised of transparent substrates such as glass, alignment layer and ITO-coated glass (indium tin oxide, a transparent conductive oxide). **Figure 1.14** depicts a schematic drawing of the EO test cells similar to those used for the EO measurement in this thesis.

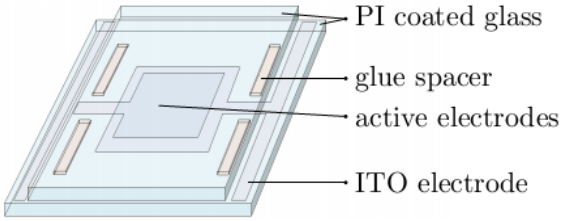

Figure 1.14 Schematic drawing of a commercially available electro-optic test cell.

There is usually one opening on two sides of the cell for filling the LC sample by capillary forces. For this purpose, nematic dispersions are heated to the isotropic phase and a small droplet of the mixture is placed by a glass capillary next to the opening of the test cell, in a way that the liquid enters and is forced into the cell gap. Extensive experiments performed throughout this thesis have shown that filling the test cells in the isotropic phase gives less agglomeration of the NPs due to a relatively higher solubility of NPs in the isotropic phase in comparison to the nematic phase.

Following is a summary of three types of EO measurement performed on the nematic nanocomposites in this work. Further experimental details and information on instrumentation are presented in the experimental sections of Chapters 3, 4, 5.

Capacitance Measurements

Capacitance measurements of the nematic mixtures are based on the "single-cell" method described by Wu *et al*.[32] Pure and doped nematic samples are filled in commercially available EO test cells which promote planar homogeneous alignment of LC molecules and the applied electric field will be perpendicular to the substrate. The EO test cell with the N-LC inside is assumed as a capacitor and the LC analyzer like the one in the Nanocomposite Lab (LCAS by LC-Vision; **Figure 1.10**b) at University of Manitoba are capable of measuring capacitance and resistance of such a capacitor.

The single-cell method relies on obtaining a capacitance versus driving voltage (*C*-*V*) curve by stepping the voltage in non-uniform steps (more steps at lower voltages near the switching threshold of the nematic samples, fewer steps at higher voltages) and nulling the cell at each voltage to measure the test cell capacitance. Following this method, by convention the threshold voltage (V_{th}) above which nematic molecules undergo a splay-type Fréedericksz transition is then measured as a 5% change of capacitance. **Figure 1.15** shows a screen shot of the capacitance versus driving voltage by the LCAS software.

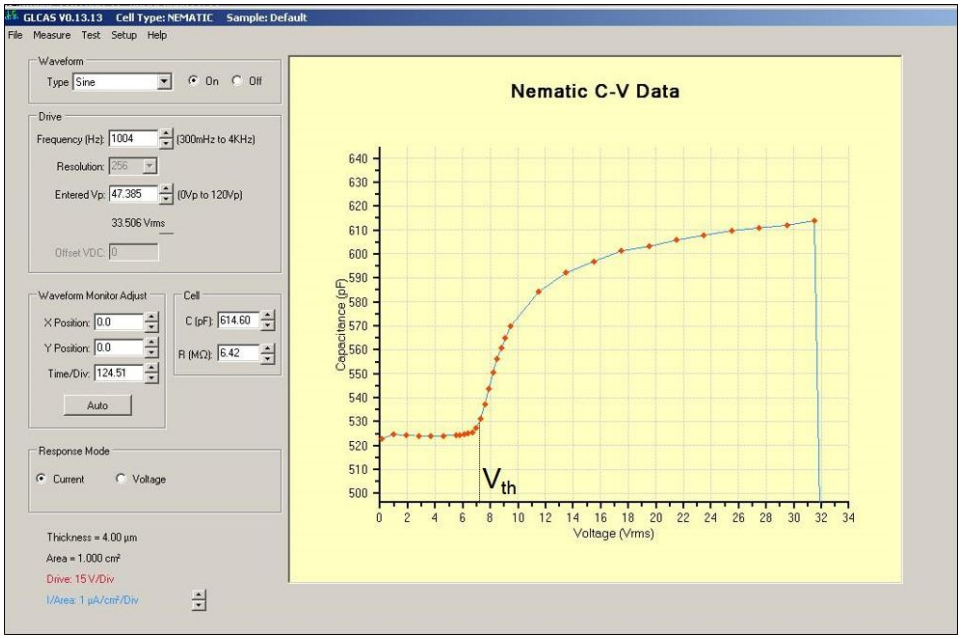

Figure 1.15 A screen shot of the LCAS software and typical *C*-*V* curve for a nematic sample with the position of V_{th} shown on the curve.

Obtaining the curve of capacitance versus RMS voltage normalized to the threshold voltage, and extrapolation of that yields the capacitance for the finite voltage applied to the cell. This capacitance is used for the parallel dielectric permittivity ($\varepsilon_{\parallel}$) calculation[32], which then affords the dielectric anisotropy ($\Delta\varepsilon$) for the N-LC sample. For determining parallel and perpendicular dielectric constants ($\varepsilon_{\parallel}$, $\varepsilon_{\perp}$) and $\Delta\varepsilon$, as well as the test cell thickness (d) and specific resistivity (ρ), Equation 1.5 and the following Equations are used:

$$\varepsilon_{\parallel} = \frac{C_{\parallel}}{C_{\text{empty}}} \qquad \text{(Eq. 1.8)}$$

$$\varepsilon_{\perp} = \frac{C_{\perp}}{C_{\text{empty}}} \qquad \text{(Eq. 1.9)}$$

where $C_{\parallel}$ is the capacitance for the finite voltage (extrapolated) at $V_{th}/V_{rms} = 0$, $C_{\perp}$ is the measured capacitance at $V<<V_{th}$, and C_{empty} is the capacitance of the empty cell which is measured before filling the cell along with the cell thickness according to the Equation 1.10:

$$d = \frac{\varepsilon_0 \times A_c}{C_m - C_p} \quad \text{(Eq. 1.10)}$$

where d is the thickness of the empty cell, ε_0 is the vacuum dielectric constant = 8.85×10^{-12} (F/m), A_C is the area of the liquid crystal, C_m is the measured capacitance of the empty cell and C_p is the measured parasitic capacitance.

By applying the range of voltages specified in the nematic test setup for obtaining the C-V curve, nematic mixtures eventually undergo a splay-type Fréedericksz transition, hence it is critical to compare the splay elastic constant (K_{11}) of the pure N-LC with the doped nanocomposites along with other parameters discussed earlier. K_{11} is determined using Equation 1.11:

$$K_{11} = \left(\frac{V_{th}}{\pi}\right)^2 \times \varepsilon_0 \times |\Delta\varepsilon| \quad \text{(Eq. 1.11)}$$

In this thesis, only splay elastic constants (K_{11}) related to the performed splay-type Fréedericksz transition in the pure and doped N-LC materials have been measured and discussed.

Transmittance and Dynamic Measurements

One aspect of great importance to the research presented in this thesis is that EO parameters of the nematic nanocomposites have been measured using two complementary techniques of capacitance and transmittance measurements. Transmittance measurements are based on probing changes in the birefringence of the LC materials due the field-induced reorientation of the LC molecules. Typically a nematic sample filled in an LC test cell is placed under the microscope with the easy axis at an azimuthal angle of 45° between crossed polarizer. The sample is then illuminated by a monochromatic and stable light source at a specific wavelength using an interference filter (commonly a halogen lamp at 542 nm).

Similar to the capacitance measurements, data acquisition begins by stepping up an applied voltage at a predefined interval to induce reorientation of the director. In the transmittance technique though, changes in the birefringence of LC ample will be detected by a photomultiplier tube (PMT) detector. To ensure a birefringence detection from the LC thermodynamic equilibrium state, a latency period of 250-500 milliseconds is used after each applied voltage before data acquisition. This latency is one magnitude higher than the switching times of the N-LCs 5CB and Felix-2900-03 (used in this thesis), therefore a completion of director reorientation can be expected after this period. No hysteresis between signals on increasing and decreasing voltage is found, which proves that transmittance is measured under equilibrium conditions. A curve like the *C-V* curve is obtained by plotting relative intensity of the detected light versus the applied voltage. **Figure 1.16** depicts a typical example of data obtained in a combined field dependent capacitance/transmittance measurement for the pure N-LC Felix-2900-03 at 58 °C.

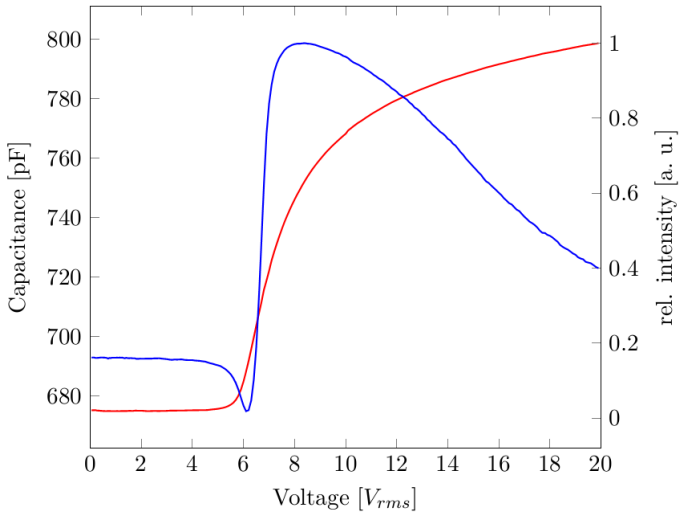

Figure 1.16 C-V (red) and relative intensity versus voltage (blue) curves obtained in a combined capacitance/transmittance measurement, respectively, for pure nematics LC FELIX-2900-03 in a 4-micron test cell at T = 58 °C.

For the calculation of threshold, the transmission data are transformed into phase retardation data, using Equation 1.12:

$$I_{det} = \frac{1}{2} \times I_0 \times sin(2\varphi)^2 \times \sin\left(\frac{\emptyset}{2}\right)^2 \qquad \text{(Eq. 1.12)}$$

where I_{det} and I_0 are the detected and initial light intensity, respectively; φ the polar angle (45°) and ϕ the phase retardation (Equation 1.13).

$$\phi = \frac{2\pi\Delta n_{eff}}{\lambda} \qquad \text{(Eq. 1.13)}$$

where d is the thickness of the sample, Δn_{eff} the effective birefringence, and λ the wavelength of the used light source. The threshold is then defined by a decrease of phase retardation by 5%. **Figure 1.17** shows a plot of an electro-optic transmittance data and its corresponding calculated phase retardation.

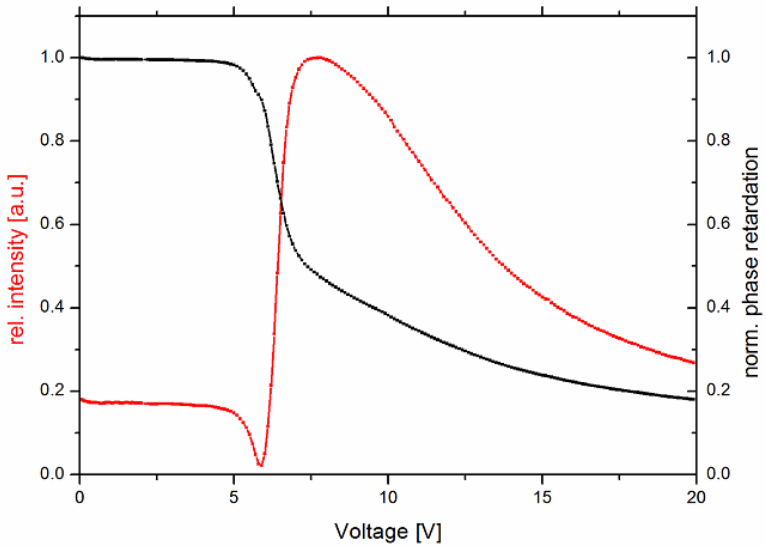

Figure 1.17 Plot of an electro-optic transmittance data (red curve) and its corresponding calculated phase retardation (black curve).

The electro-optic results presented in this thesis are obtained by the two different yet complementary techniques of capacitance and transmittance measurements. Overall, EO results such as threshold voltages obtained from these two techniques agree very well. However, it seems that transmittance measurements are sometimes more stable than capacitance measurements, as the plateau in the latter ones can exhibit high deviations. In addition, transmission measurements can selectively choose small regions from the cell for data acquisition, while the capacitance is always measured over the complete electrode

area. The latter is important in the case of doped nematic samples where it is often observed that some NPs tend to migrate to the interface of LC and substrate. This can impact the boundary condition of the substrate, changing the surface energy, therefore causing some deviations in the threshold voltage values, even within one cell.

Another characteristic of a nematic LC intended for the display application is the switching time which translates into response time of the LC material to the external field. The two switching times studied in this thesis are rise (ON) time and decay (OFF) time and are measured using dynamic analysis. As depicted in **Figure 1.18** two voltages of V_a (well below the V_{th}) and V_b (just below the following maximum in intensity) are chosen.[32] The rise time (τ_{rise}) and decay time (τ_{decay}) obtained by light transmission analysis are then defined as the time between an increase from V_a to V_b and decrease from V_b to V_a accompanying by 90% change in the normalized phase retardation. Using this method, rise and decay times can be observed simultaneously with a high intensity contrast caused by only small changes in the director field. Rise and decay times are given by the Equations 1.14, 1.15 according to the theoretical derivation of rise and decay times of N-LCs.[34]

$$\tau_{decay} = \frac{\gamma \times d^2}{\pi^2 \times K} \qquad \text{(Eq. 1.14)}$$

$$\tau_{rise} = \frac{\gamma \times d^2}{\pi^2 \times K} \left[\left(\frac{V}{V_{th}}\right)^2 - 1\right]^{-1} = \frac{\gamma \times d^2}{\varepsilon_0 \times \Delta\varepsilon \times (V^2 - V_{th}^2)} \qquad \text{(Eq. 1.15)}$$

where γ is the rotational viscosity, d is the cell thickness and K is the effective elastic constant. **Figure 1.18** shows plots related to determination of switching times for the N-

LC Felix-2900-03 in a 4-micron test cell at 58 °C .The decay time at a given cell thickness depends only on the ratio of rotational viscosity (γ_1) and effective elastic constant (K_{eff}). It is therefore independent of applied voltages V_a and V_b that caused the distortion in the director field. In this way, the ratios of γ_1/K_{eff} for different samples can be directly compared by dividing the measured decay times by the square of sample thickness (d^2). The rise time, on the other hand, does depend on the applied field. Therefore, the rise time is characterized by the slope of a plot of measured rise time vs. $[(V/V_{th})^2-1]^{-1}$, as can be seen from Equation 1.15.

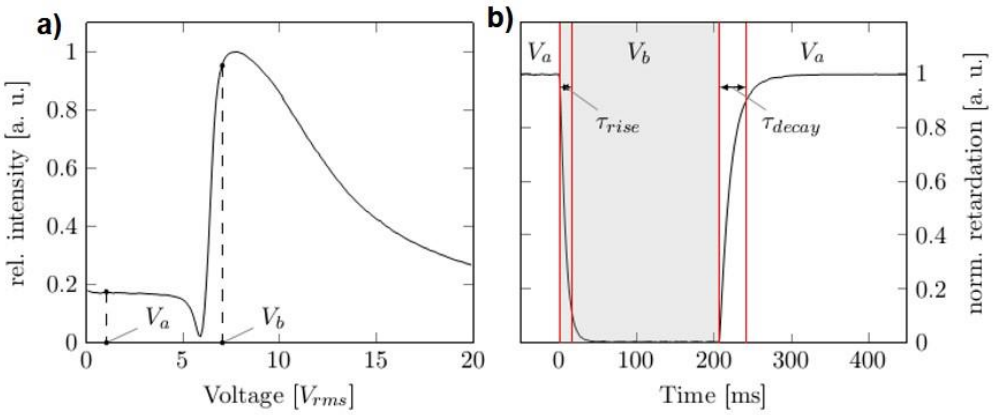

Figure 1.18 a) Determination of V_a and V_b in the transmission characteristic of a 4 µm test cell filled with pure FELIX-2900-03 at 58 °C. b) Example of switching characteristics of pure FELIX-2900-03 at 58 °C.

1.9 Liquid Crystal Displays

In this section, a brief overview of LCD technology is provided. Invention and development of LCDs have been made possible by the invention of transistors and integrated circuits, and developments in electrical and mechanical engineering, as well as in material and LC sciences. As shown in **Figure 1.19** an LCD is comprised of major

optical and electrical components. There are many types of LCDs based on the type of LC materials and particular fabrication and engineering of the alignment and electro-optical layers.

One of the first and most common LCD used for everyday items such as digital watches and calculators is called the twisted nematic (TN) display.[35] A TN cell consists of upper and lower substrate plates separated by a narrow gap (typically 5–10 microns) filled with a layer of nematic LC. The substrate plates are normally transparent glass and carry patterned electrically conducting transparent coatings of indium tin oxide (ITO). A special surface treatment (commonly rubbed polyimide) is given to the glass such that the LC molecules are homogeneous (planar), yet the director at the top of the sample is perpendicular to the director at the bottom. This configuration sets up a 90° degree twist into the bulk of the liquid crystal, hence the name of the display (**Figure 1.20**).

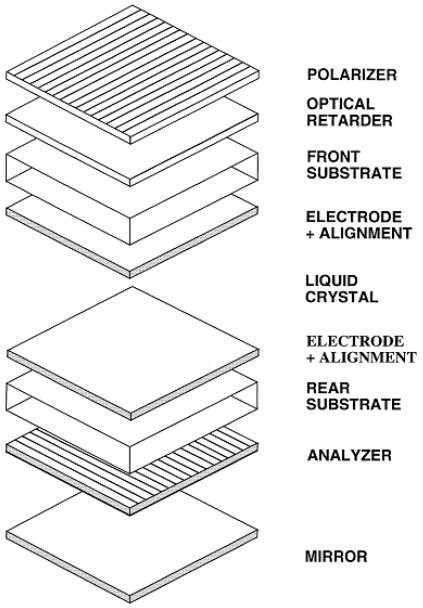

Figure 1.19 Schematic representation of the major optical and electrical components of a liquid crystal display. Reproduced with permission from Ref.[36]- Copyright: Academic Press.

In the absence of an applied voltage, the TN cell in a reflective mode appears to be transparent because the optics of the twisted LC match the crossed arrangement of the polarizers. Application of three to five volts across the LC destroys the twisted state and causes the molecules to orient perpendicular to the substrate plates, giving a dark appearance to the cell. Displaying information and characters is possible by patterning the electrodes in segments or as an array of small squares, producing the so called pixels.[36]

More advanced LCD modes include super twisted nematic mode (STN)[37], in-plane switching (IPS) mode[38, 39], polymer dispersed LC (PDLC) mode[40], multi-domain vertical alignment (MVA) mode[41], patterned vertical alignment (PVA) mode[42], zenithal bistability device (ZBD)[43, 44] and blue phase (BP) mode.[45, 46] **Figure 1.21** represents a flowchart of the development of different modes of the LCD technology from the first invented dynamic scattering mode to the current TN, IPS and VA modes and future ZBD and BP LCD modes.

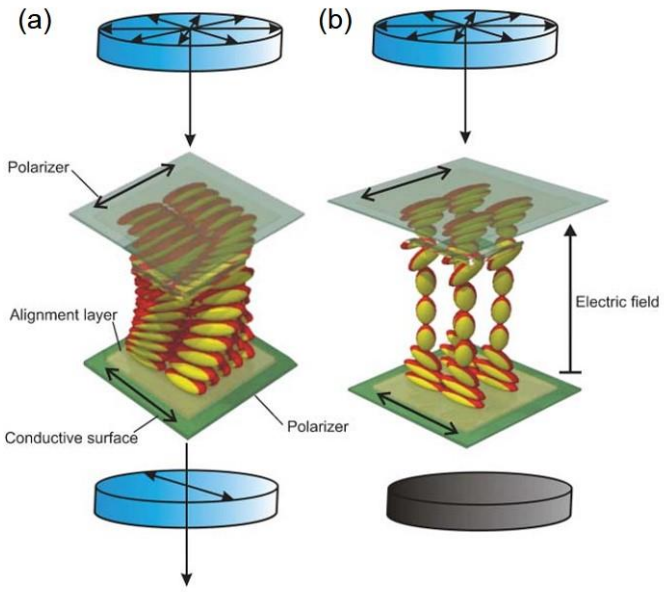

Figure 1.20 Schematic drawing of operating principle of the TN mode; a) OFF-state, b) ON-state. Reproduced with permission from Ref. [165] – Copyright: The Royal Society of Chemistry.

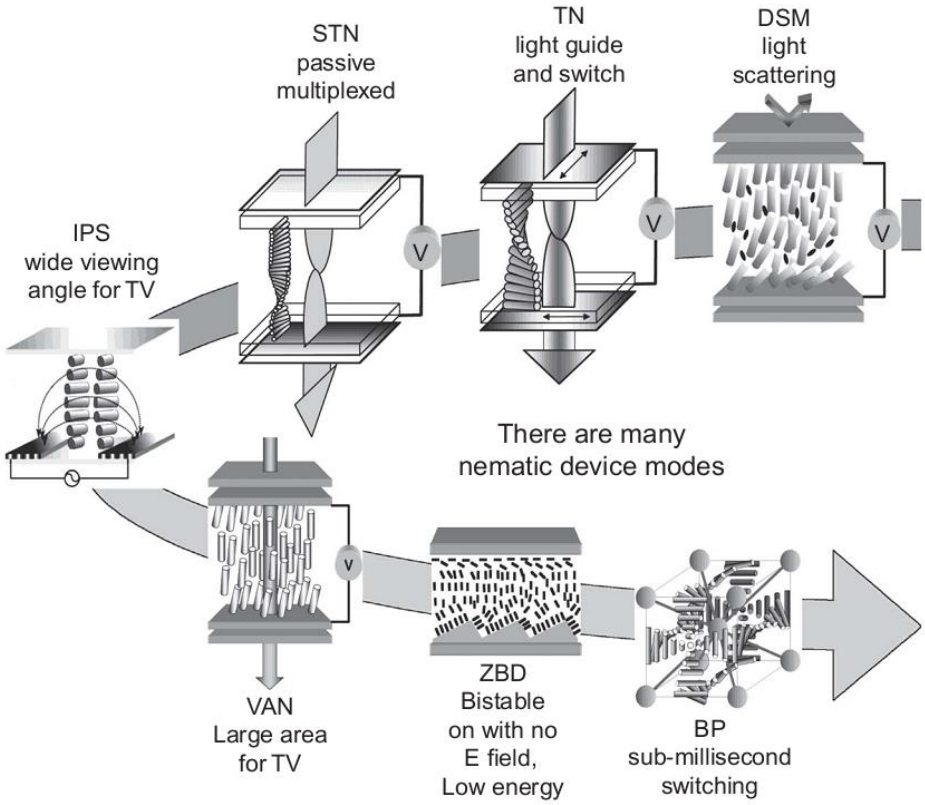

Figure 1.21 Flowchart of the development of LCDs highlighting the advantage of each mode, starting with the dynamic scattering mode to the new Blue Phase concept. Reproduced with permission from Ref. [5b] – Copyright: Taylor & Francis.

1.10 Gold Nanoparticles

1.10.1 Synthesis of Gold Nanoparticles

Colloidal gold nanoparticles (Au NPs) in the size regime between 1-100 nm in diameter have been intensively studied due to their unique size- and shape-dependent physical and chemical properties that have led to applications in catalysis, optoelectronics, imaging, drug delivery as well as chemical and biological sensing.[47-50] Assembly of Au NPs into stable functional materials is another promising area of research of Au NPs and is a hot

topic in nanotechnology.[51, 52] There are several methods for the synthesis of colloidal, quasi-spherical Au NPs, but two of them are more commonly used.[52] The first method to synthesize Au NPs is based on the citrate reduction of $HAuCl_4$ in water as reported by Turkevitch[53] in 1951 (**Figure 1.22**a). This method leads to hydrophilic Au NPs in the range of 10-20 nm in diameter, and the resulting Au NPs are only stable in water and to some extent in alcohols such as methanol and ethanol.

The second method which was first reported by Brust and Schiffrin in 1994, has been regarded as a breakthrough in the research of Au NPs. Both one-phase[54] and two-phase[55] versions of Brust-Schiffrin syntheses are easy to perform and yield very small hydrophobic alkanethiolate-capped Au NPs in the size range of 1-7 nm in diameter (**Figure 1.22**b). The Brust-Schiffrin methods provide relatively easy control of the functionalization and size of NPs by adjusting the thiol/gold precursor ratio (typically n-alkyl thiols with a 6-12 carbon chain length and $HAuCl_4$) and the speed of addition of the reducing reagent.[52]

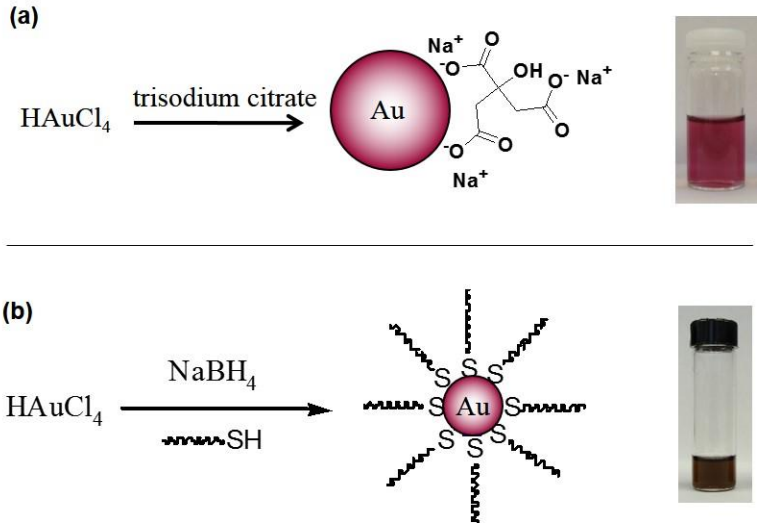

Figure 1.22 Schematic drawing of the Au NP syntheses, a) Turkevitch method and b) Brust-Schiffrin method. Vials contain citrate-stabilized Au NP in water (top) and hexanethiolate-capped Au NP in toluene.

The synthesis of Au NPs and other metallic NPs is the subject of several leading reviews.[48, 56, 57]. In selecting an appropriate method for the synthesis of Au NPs suitable for LC doping, two important considerations are: (1) easy functionalization and (2) stability of the resulting NPs. In the following section and in the introduction of Chapter 4, a review of different surface ligands and functionalization protocols is presented along with the disadvantages of the above mentioned Turkevitch and Brust-Schiffrin methods. Although the focus of the next section and introduction of Chapter 4 is on Au NPs, the concepts and techniques can be generalized to other metal nanoparticulate systems.

1.10.2 Surface Functionalization of Nanoparticles

As in the cases of the Turkevitch and Brust-Schiffrin methods, the synthesis of NPs generally involves ligand molecules or surfactants that initially bind to a metal precursor. Then nucleation of the NPs starts upon addition of a reducing agent or a thermal event and the reaction proceeds with competing process of growth of atom clusters that eventually stops when coordination of the ligands to the surface atoms of the clusters becomes more favorable. At this point, surface ligands not only prevent further growth of the NPs, but also create a layer that protects the NPs against aggregation. The protection is in principle based on repulsive force between nanoparticles, which can be due to electrostatic repulsion (e.g. citrate-stabilized Au NPs), steric exclusion (e.g. alkanethiolate-capped Au NPs), or a hydration layer on the surface. Therefore, choice of ligand and variation of its concentration can have profound impacts on the particle size, geometric shape, and its colloidal stability.[57] For instance, it has been shown that the Brust-Schiffrin methods can be modified to provide Au NPs with the core size ranging from 0.7 to 7 nm by only choosing different

concentrations of the alkyl thiol while using similar amount of gold precursor and reducing agent.[59]

The importance and role of surface coating is not limited to the stability of the NPs and determining the size and shape. Surface ligands are critically relevant for the electronic properties of NP as well. Most importantly, the surface ligand functionalization in NPs seems essential in order to render them compatible or miscible with another material or medium and is a prerequisite for their potential applications in LC nanocomposites. In most cases the surface ligand of NPs can determine their interaction with the medium and these interactions ultimately affect the colloidal behaviour of the NPs and their effects on the host molecules. Likewise, particular properties of certain mediums such as the LC can be transferred to NPs via intermolecular interactions and this may result in self-assembled oriented arrays of NPs.[60]

Today along with advances in synthesis of nanoparticles of different core materials, a number of practical approaches exist that allow alterations of molecular chemistry of the NP surface. All of these methods are based on the insertion of molecules bearing atoms with high affinity toward atoms on the particle surface along with the control of their architecture and surface density. Syntheses of colloidal NP can be divided into two major categories, those performed in hydrophilic and those performed in hydrophobic medium depending on the hydrophilicity or hydrophobicity of the resulting particles. In addition, some types of NPs may have amphiphilic groups on the surface and are expected to be miscible in both environments.

While in some applications, mainly in biological systems and drug delivery,[61] hydrophilic water-soluble NPs are desired, in other applications such as LC composites,

NPs with a hydrophobic surface are essential for miscibility with liquid crystals featuring hydrocarbon segments and non-polar organic solvents.

The common functionalization strategies that stabilize particles in organic or aqueous phases include ligand exchange, ligand modification, and polymer encapsulation. **Figure 1.23** shows a general scheme of different surface functionalizations on hydrophobic NPs coated with greasy surfactants. It should be noted that ligand exchange can result in a phase transfer of the NPs from an organic to an aqueous phase or vice versa. For example, Bruce Lennox's research group at McGill University has developed a facile phase transfer of different types of water-soluble NPs to nonpolar solvents using thiol-terminated polystyrene.[62]

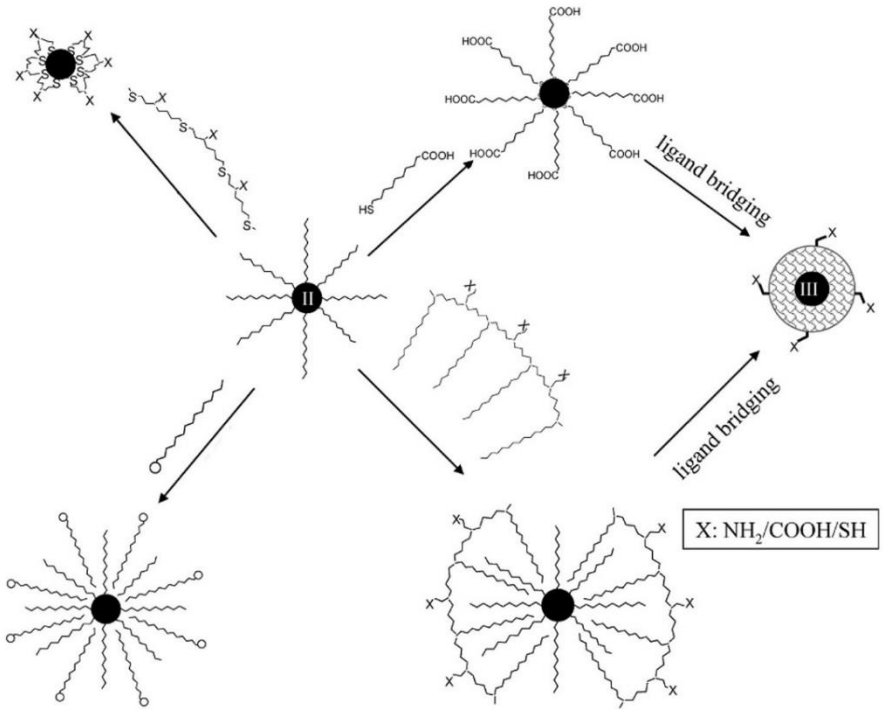

Figure 1.23 Various ligand exchange and modifications of hydrophobic nanoparticles. Reproduced with permission from Ref. [63] – Copyright: The American Chemical Society.

In ligand exchange methods, the new ligand molecules should have relatively high affinity to the inorganic core in order to effectively replace the original surfactant molecules and yet retain the colloidal stability. A well-established ligand exchange method in many metallic NPs employs alkyl thiols, which have a high affinity to noble metal surfaces such as gold.[64, 65] For example, as depicted in **Figure 1.24**, the alkanethiolate ligands of as-synthesized Au NPs using the Brust-Schiffrin methods[66, 67] can be partially replaced by other alkanethiolate molecules carrying mesogens[68-70], dendrimers[71], peptides or modifiable functional groups such as carboxylic acid,[72] terminal double bond for metathesis chemistry,[73] maleimide as dienophile[74] for utilizing in Diels-Alder cycloaddition and pyridine[75] or phosphine[76] groups for further complexation allowing formation of organometallic moieties on the nanoparticles corona.

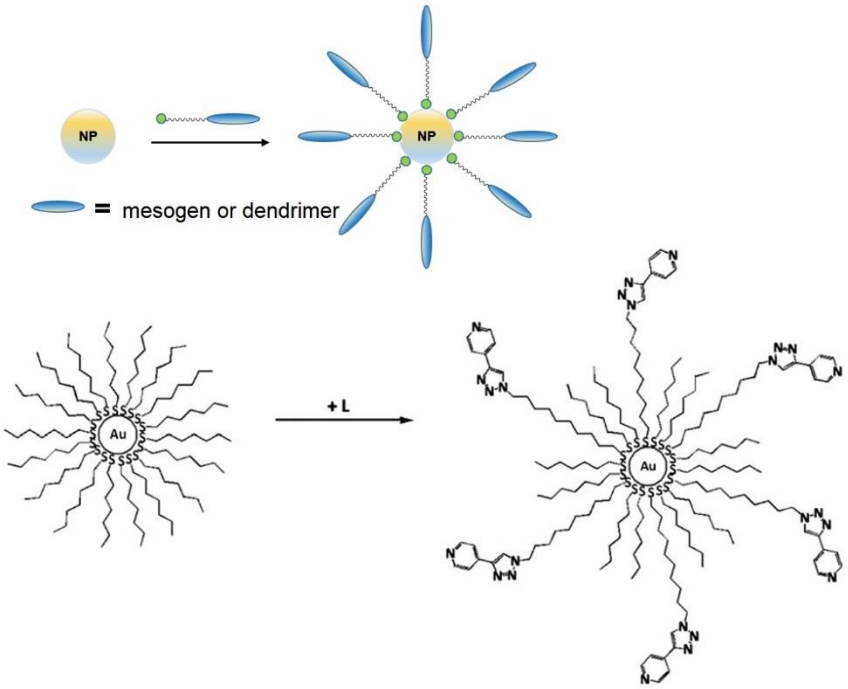

Figure 1.24 Schematic diagram of surface functionalization of a NP with mesogens, dendrimers or pyridine in alkyl thiol-for-alkyl thiol exchange. Adapted from Ref. [75] – Copyright: Elsevier.

Despite the potential of alkyl thiol ligand exchange methods in introducing a variety of surface chemistries for NPs, this method does not always provide a complete displacement of ligands or the formation of robust NPs and requires excess amounts of the new ligands. One possible alternative ligand exchange can be performed on NPs stabilized with amines like 4-(*N*,*N*-dimethylamino)pyridine (DMAP)[77] or phosphines such as triphenylphosphine.[78, 79] The fact that the original amine and phosphine ligands have weaker bonds to the surface of metal NP than thiols brings the advantage of using milder reaction condition and the use of stoichiometric quantities of the incoming thiol. **Figure 1.25** shows how surface of Au NPs can be functionalized by thiol molecules by removing DMAP from the surface.

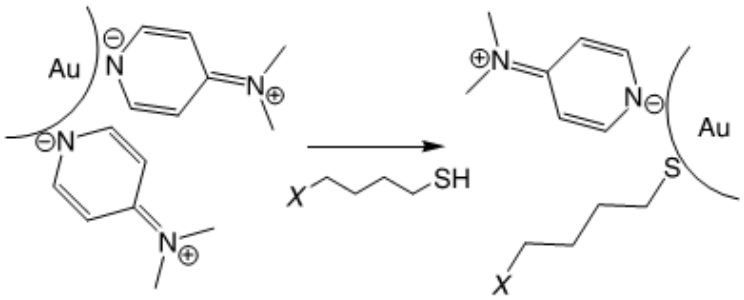

Figure 1.25 Schematic reaction of DMAP to thiol exchange. X moiety may introduce new surface chemistry on the NPs. Reproduced with permission from Ref. [80] – Copyright: Springer-Verlag.

However, it has been shown that the bonds between the inorganic NP surface and thiol, amine or phosphine groups of a ligand molecule experience dynamic binding and unbinding processes.[81, 82] The consequence of such a phenomenon is limited stability of particles against excess washing, surface oxidation, and thermal treatment, which may cause irreversible aggregation (for further details on thermal instability of Au NPs see the

introduction of Chapter 4). Therefore, a surface chemistry which can address this problem is critical, especially in an application such as LC nanocomposites with a demonstrated need for surface modification as well as high chemical and thermal stability of the NPs.

Silica coating of NPs of different core materials and shapes can provide a protective and functionalizable shell through alkoxysilane chemistry around NPs.[83] Most of the protocols are modifications of the classic Stöber method.[84] Typically, for preparing silica coated gold NPs (Au NP@SiO_2) citrate-stabilized Au NP are synthesized. The as-synthesized Au NP in an alcoholic solution undergoes the next step in which a polymeric, cross-linked inorganic silica shell through the controlled hydrolysis of tetraethyl orthosilicate (TEOS) in basic condition (NH_4OH) is deposited on the particles (**Figure 1.26**). The resulting particles are initially water-soluble but provide the opportunity to convert them into hydrophobic NPs by reacting them with organosilanes long alkyl chains such as trichlorooctadecyl silane.[85, 86]

In this thesis, this method was investigated as an approach for the preparation of uniform Au NPs with robust and modifiable surface chemistry. However, a major drawback of the silica coating method using TEOS remains and that is associated with the sensitivity of this method to experimental parameters like the nature of the initial ligand, concentration, and ratios of TEOS, base, and NP, as well as relatively fast hydrolysis of TEOS. In most cases, it is hard to control the silica shell thickness and the resulting NPs are not uniform and have high tendency to aggregate and form multicore particles. Moreover, Au NPs after silica coating are hydrophilic and additional steps are required to render them hydrophobic.

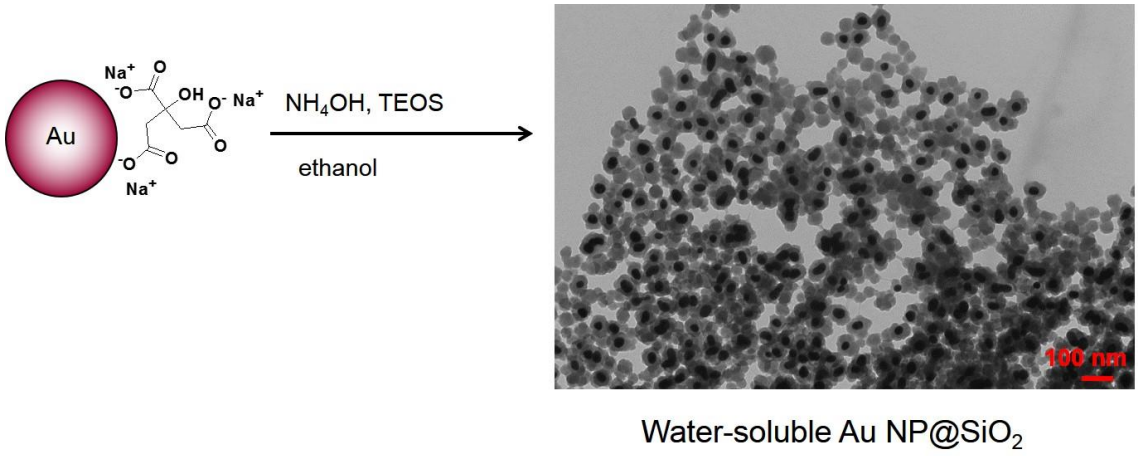

Figure 1.26 Left: Stöber reaction of citrate-stabilized Au NP. Right: Transmission electron microscopy image (scale bar, 100 nm) of resulting silica coated Au NP (non-uniform shells).

Hence, there was a need for an alternative method to the Stöber reaction, and the research in this thesis led to versatile syntheses of silane conjugated Au NPs coated with aliphatic chains or liquid crystalline moieties suitable for the use in nematic LC nanocomposites. The silanized hydrophobic Au NPs synthesized in this thesis are based on the silane conjugation chemistry for coating NPs, first reported by Ying and co-workers.[86] In the modified method (3-mercaptopropyl)trimethoxysilane (MPS) is used to cap the Au NPs. Then, the as-synthesized MPS-coated Au NPs undergo further surface functionalization using a particular trialkoxysilane depending on the desired surface decoration. Controlled hydrolysis and co-condensation of alkoxysilanes form a thin well-defined siloxane shell along with the functional moiety in the outer layer around the NP.

Hydrophobic silanized Au NP with $C_{18}H_{37}$ alkyl chains discussed in Chapter 4 and silanized LC-coated Au NPs discussed in Chapter 5 have been synthesized and functionalized using this method. Results from the nanocomposites of these particles with

nematic LCs show unprecedented thermal and chemical stability of these particles, as well as relatively good dispersibility in the nematic mesophase.

1.10.3 Characterization of Nanoparticles

Multiple techniques have been used for the characterization of Au NPs, QDs, and other synthesized NPs. The main characterization techniques are only discussed in this section including transmission electron microscopy (TEM), UV-vis spectroscopy and to some extent X-ray photoelectron spectroscopy (XPS) and thermogravimetric analysis (TGA). A description of the photoluminescence of QDs and its role in their identification is presented in Chapter 2.

TEM is perhaps the most powerful and the most commonly used technique to determine the size of NPs and other materials with nanoscale dimensions. TEM provides a direct image of size, size distribution and assembly of NPs, as well as quantitative information about their structure. TEM can also provide information about the chemical composition when coupled with energy dispersive X-ray spectroscopy (EDS) and electron energy-loss spectroscopy (EELS).[87]

A schematic setup of a TEM instrument is shown in **Figure 1.27**a. A TEM consists of an illumination system using a thermionic emission source (inside the electron gun) or a field emission source, a specimen stage, an objective lens, a magnification system (with magnification up to 1.5 million times), and a data recording system. The electron-optical column is maintained under high vacuum during TEM analysis. **Figure 1.27**b shows the high-resolution TEM (HR-TEM) facility at the University of Manitoba and **Figure 1.27**c is a TEM image of octadecanethiol-capped Au NP with an average size of 7 nm.

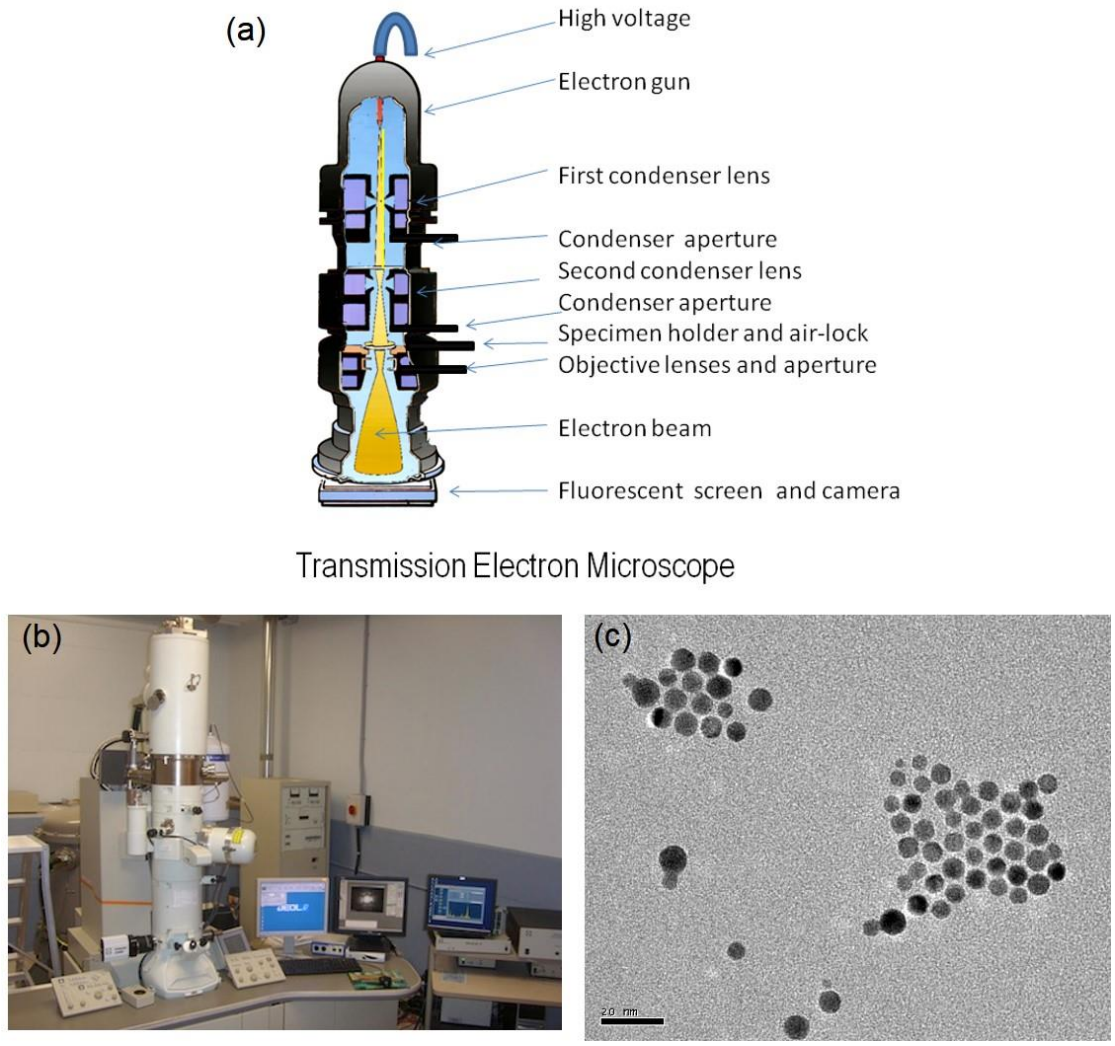

Figure 1.27 (a) Schematic drawing of the TEM electron beam (photo credit: Wikipedia). b) HR-TEM facility (JEOL JEM-2100F) at University of Manitoba (photo credit: Manitoba Institute for Materials). c) TEM image of octadecane thiol protected Au NP (Scale bar: 20 nm).

In this thesis, for calculating the average size of NPs, ImageJ software has been used; a free particle and image analysis tool offered by the US National Institute of Health. With this software, first we need to set the scale in the image by zooming in the scale and measuring the length of the scale bar to the nearest pixel. Then we can use either automatic

or manual particle sizing/counting to obtain the average size, standard deviation or a size histogram using statistical calculations from at least 100 particles.

Depending on the specimen and what is being examined, TEM may encounter some drawbacks. First, the area of view is only a small part of the entire sample and therefore several areas must be studied (imaged) in order to obtain an overall view of the sample. Second, the resolution of the instrument may be problematic especially for very small NPs (<2 nm) when the error range is sometimes larger than the actual size distribution of the particles.[88] Third, it is a two-dimensional image of three-dimensional particles and thus cannot simply provide of a complete image of the shape. However, it should be noted that recent advances in nanostructure imaging and electron tomography have enabled reconstructions of a three-dimensional image of the object from a series of two-dimensional projections obtained by TEM.[89]

Other methods that can be used to measure or calculate the size of NPs include powder X-ray diffraction (XRD), UV-vis absorption spectroscopy and dynamic light scattering (DLS). DLS is a routine technique to obtain the hydrodynamic radius of particles and aggregates such as large carbohydrate molecules, polymers and proteins,[90, 91] but it is not very suitable for finding size and size distribution analysis of small NPs such as the ones studied in this thesis. The primary reason here is that strong optical absorption of small Au NPs along with their weak scattering result in a very low signal-to-noise ratio causing errors in DLS size measurements.[88]

UV-vis spectroscopy is another powerful characterization tool for the Au NPs due to the surface plasmon resonance (SPR) emerging as a broad absorption band in the visible region from ~510 to ~540 nm (for spherical Au NPs larger than 2 nm in diameter).

According to the "electron cloud" model in metals, electrons are not tightly bound to their nuclei and are free to travel within the material.[92] SPR is due to the polarization and subsequent collective oscillations of the free electrons at the nanoparticle's surface in response to the electrical field of light radiation, as shown in **Figure 1.28**a. When the resonance frequency of the free electron cloud hit the frequency of the irradiation light, the electromagnetic wave is not allowed into the material but is instead absorbed or scattered away very efficiently. The origin of purple-red color of colloidal dispersions of Au NPs comes from this specific absorption/scattering phenomenon.[93, 94] According to Mie theory, plasmon resonance frequency and SPR bandwidth depend on the size and shape of the particle as well as dielectric constant of the particle and medium.[94]

In studying UV-vis spectra of batches of Au NP with the same stabilizing ligand and solvent, SPR peaks at different wavelengths can be indicative of the relative different sizes. For larger Au NPs, the peak will be shifted to longer wavelengths while smaller Au NPs absorb at relatively lower wavelength (**Figure 1.28**b). Therefore, the color of Au NPs solutions and UV-vis absorption wavelength maxima can give a quick feedback on the NP size.[88] The strong dependency of the SPR on the local environment has made Au NPs attractive candidates for sensors and biological applications.[95, 96]

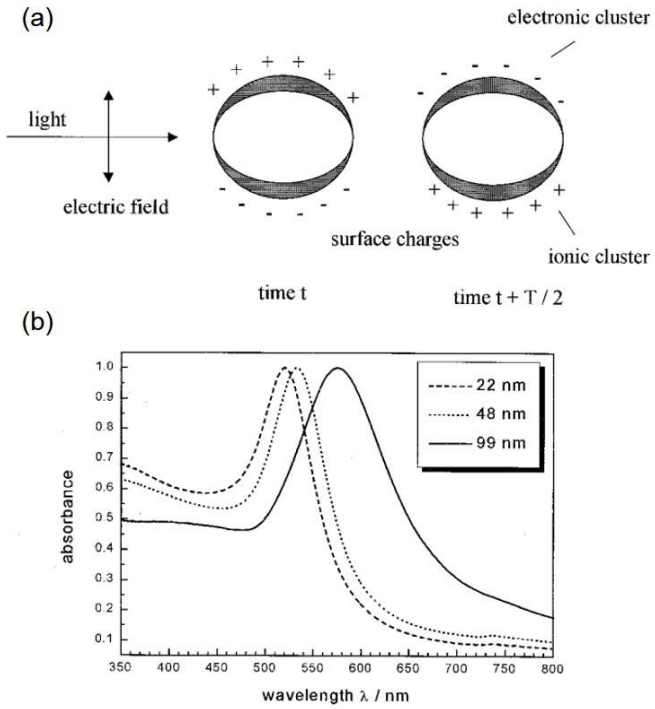

Figure 1.28 (a) Schematic illustration of the origin of the SPR in quasi-spherical Au NPs. (b) Optical absorption spectra of 22, 48 and 99 nm spherical Au NPs. The broad absorption band corresponds to the surface plasmon resonance. Reproduced with permission from Ref. [94] – Copyright: Taylor & Francis.

A spectroscopic technique such as NMR is commonly used to determine the purity of Au NPs (i.e., removal of free, non-bound ligands and the phase transfer agent). However, ^{1}H-NMR spectra of Au NPs usually suffer from broad and weak signals relative to those of free alkanethiols. Factors attributing to this phenomenon include broadening of the spin-spin relaxation time, a distribution in chemical shifts due to differences in Au NP-SR binding sites, and a gradient in monolayer packing density from nearcore to chain terminus with associated dipolar broadening.[97] Previous studies in the solid-state and solution NMR of colloidal thiol-capped Au NPs confirm an overall broadening of the NMR resonances along with disappearance of signals related to the carbons and the protons attached to the

first two carbons closest to the sulfur head group in ^{13}C- and ^{1}H-NMR spectra, respectively.[97, 98]

X-ray photoelectron spectroscopy (XPS) is a useful technique to obtain information about the composition and the chemical state of surface constituents in NPs and other solid materials. XPS is based on the measurements of the kinetic energy of generated photoelectrons when the sample is illuminated with soft (1.5 kV) X-ray radiation in ultrahigh vacuum.[99] The difference between the photon energy and the electron kinetic energy is called the binding energy and is characteristic of the orbital of a specific element from which the electron is ejected. The photoelectrons emitted from the sample are detected by an electron energy analyzer, and their energy is determined as a function of their velocity entering the detector. By counting the number of photoelectrons as a function of their energy, a spectrum is obtained. The energy corresponding to each peak is characteristic of an element present in the sample. The area under a peak in the spectrum is a measure of the relative amount of the element represented by that peak. The peak shape and precise position indicates the chemical state for the element. It should be noted that XPS is a surface sensitive technique because only those electrons generated near the surface escape and are detected.[100]

Thermogravimetric analysis (TGA) is a technique in which the mass of a substance is monitored as a function of temperature or time as the sample specimen is subjected to a controlled temperature program in a controlled atmosphere. In characterizing NPs by TGA samples are heated to very high temperatures (up to 1000 °C) while monitoring the mass of the sample, which yields the decomposition curve. Analysis of the decomposition curve yields the residual mass of the sample which should be mainly due to the inorganic metallic

core of the NPs. By knowing the initial amount of the sample, one can calculate the amount of surface coverage. Further experimental details about TGA studies performed in this thesis are presented in the experimental section of Chapter 5. A drawback on the use of TGA is that a single run can consume several milligrams of a NP with costly and time-consuming synthesis, therefore, limiting additional analysis to gain meaningful statistics.

Recently, new methods known as microthermogravimetric analysis (μ-TGA) for the determination of NP surface coatings and NP purity have been developed that have similar thermal decomposition principle as TGA, but the use of sample is in the order of 1μg. These new techniques can detect mass changes less than a nanogram, thus greatly improving the detection limits of conventional TGA for the nanomaterials where scarcity and high cost are often concerns.[101, 102]

1.11 Doping Liquid Crystals with Nanoparticles

Incorporating different types of nanoparticles, e.g. metal, metal oxides, semiconductor, carbon nanotubes, within different types of lyotropic and thermotropic liquid crystals has been a hot topic over the last decade.[103-105] Doping LCs with NPs can improve the physical properties of LCs and can give rise to various technologies such as improved LC materials for display devices, LC-based sensors and alignment of LCs using NP printing.[106-108] In addition, impacts of the anisotropic and ordered nature of LC phases on the properties and assembly of NPs have been explored in the LC-NP hybrids as a promising bottom-up approach for fabricating novel functional materials.[109-112]

A review of the literature on the topic is given in Chapter 2 presenting LC composites with QDs. Although research discussed in Chapter 2 covers QDs, most of the principles, challenges and applications can be generalized to other nanostructured dopants. In the following sections, a brief overview about LC-NP composites provides basic information about defect formations, modulating LC properties, LC-decorated NPs with a focus on Au NPs, and the dispersion of carbon nanotubes (CNTs) in LCs.

1.11.1 Formation of Defects in Liquid Crystal

The majority of pioneering studies in the field of doping LCs with particles dealt with the nematic phase and microparticles with respect to defect formation induced by the particles.[113] As mentioned in the section 1.6, N-LCs possess orientational ordering along a certain direction, called the director. In a pure nematic and without any perturbation, the local director field in a given domain is uniformly aligned in one direction. Adding particles into the bulk of nematics LC will change the director around the particles, and depending on the boundary conditions around the particles, LC molecules are forced to assume a homeotropic or planar orientation. However, this change is limited to an area around the particle and will disappear at a distance away from the particle, where LC molecules are still uniformly aligned. These dissimilarities in local orientation cause topological defects due to the induced elastic distortions.[114-117]

Theoretical calculations and experimental observations have shown that particles with homeotropic boundary condition can induce hyperbolic hedgehog or Saturn ring defect, and particles with planar anchoring conditions induce a pair of point defects called

boojums.[116, 118] **Figure 1.29**a-c shows schematic drawings of these three possible particle-induced defects.

Depending on the director configuration around the particle, a hedgehog defect behaves like a dipole, whereas a Saturn ring and boojum defects have quadrupolar symmetry. It has been shown that that colloidal particles in this micron size regime can arrange into one-, two- or three-dimensional arrays by sharing topological defects.[116, 119] Topological defects represent a highly distorted director field and self-assembly of particles will minimize the elastic part of free energy density. A schematic drawing and optical image of a chain of droplets formed by the interaction between defects are shown in **Figure 1.29**d and **Figure 1.29**e, respectively.

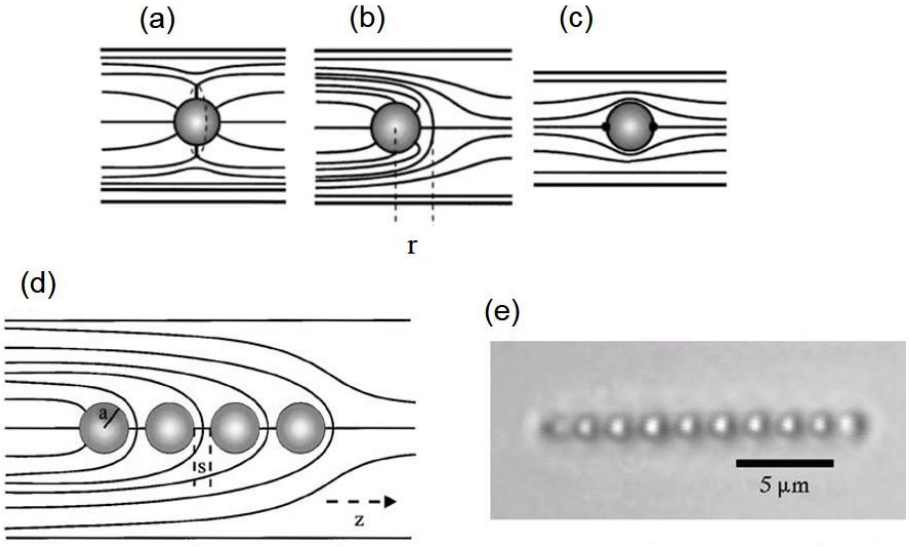

Figure 1.29 Typical defects created by spherical particles in N-LCs. (a) hyperbolic hedgehog, (b) Saturn ring and (c) boojums defect with two surface defects forming around particles with planar boundary conditions. (d) A chain of droplets formed by interaction between the topological dipoles with hedgehog-type defects. (e) Optical microscope picture of several water droplets forming a long chain with hedgehog type of defects. Reproduced with permission from Ref. [117] – Copyright: The American Physical Society.

Examples of microparticles showing these types of defects and arrangements include: water microdroplets,[116, 117, 120] silicon oil,[115, 121] gold-coated glass spheres,[122] magnetic particles,[123, 124] and silica particles.[125]

It has been shown that particle radius (r) is important to the energy of the induced defects. For example, by decreasing r the energy of a Saturn ring defect will be decreased logarithmically while the hyperbolic hedgehog is not affected.[126] In general, formation of defects in colloidal LC composites strongly depends on the size regime of particles as studies show that with decreasing particle size the influence of surface energy decreases.[118] An estimated critical particle radius of ~300 nm has been reported for the particle size that below which the strong anchoring condition of particles is low and therefore formation of topological defects is unlikely.[118] Other theoretical calculations have shown that even particle in the size regime of 10-20 nm can cause distortions and increase in the elastic free energy density of the N-LCs.[127, 128]

Overall, it is assumed that very small spherical NPs in a size regime smaller than 10 nm like those studied in this thesis, show none of the above mentioned topological defects and are expected to be randomly dispersed in the liquid crystalline host. However, this is not entirely the case in this thesis as discussions in Chapters 4 and 5 explain the role of other factors such as stability of and chemical structure of the NP surface ligands.

1.11.2 Modulating Liquid Crystal Properties Using Nanoparticles

Addition of NPs into N-LCs also referred to as doping covers different types of NPs and a wide range of NP concentrations. In this thesis, composites of nematic samples with Au NPs and QDs at concentrations between 0.25 wt% (weight percentage) and 7.5 wt% are

investigated. In general, Au NPs and semiconductor QDs with different sizes and surface ligands are the most frequently used NP-based LC dopants among other types of NPs due to their unique optical and electronic properties (see sections 1.10 and 2.2).

By doping N-LCs with Au NP, Müller *et al*. have shown an electrically controlled light scattering phenomenon[129] and Kossyrev *et al*. have demonstrated a dynamic, continuous and reversible voltage-controlled colour tuning promoted by Au NP arrays formed on a glass substrate of a sandwiched nematic test cell.[130] Further, research by Kobayashi and co-workers successfully demonstrated lower operating voltages, shorter response times, and reduced viscosities in different LCs (nematic and chiral nematic mesophases) via NP doping.[131] Several investigations on nematic LCs doped with alkanethiolate-capped Au NPs (e.g. SC_6H_{13} and $SC_{12}H_{25}$) performed by Hegmann's research group indicated improvement in EO properties such as lower V_{th} values for the planar to homeotropic Fréedericksz transition and higher dielectric anisotropy along with homeotropic alignment of LC molecules and formation of pattern stripes within untreated glass slides.[10, 132, 133] Further studies and FCPM measurements have shown that homeotropic alignment is due to the NPs residing at the LC/substrate interface causing homeotropic anchoring of the nematic director, while birefringent stripes correspond to twist disclination of nematic molecules.[133, 134]

Another interesting concept demonstrated by Hegmann's group is that chirality can be transferred from Au NPs capped with chiral ligands to the non-chiral nematic phase, inducing physical and optical properties of the nematic phase (N^*). It has been shown that low concentration (less than 0.1 wt%) of Au NPs capped with a monolayer of (*S*)-naproxen end-functionalised alkyl thiols act as a chiral dopant in a nematic phase.[135] **Figure 1.30**a-c

show POM images of a pure nematic LC1 (**Figure 1.30**a) and the same N-LC doped with 5wt% of (*S*)-naproxen-functionalized thiol Au NP (**Figure 1.30**b) and 5 wt% of dodecanethiolate-capped Au NP (**Figure 1.30**c).

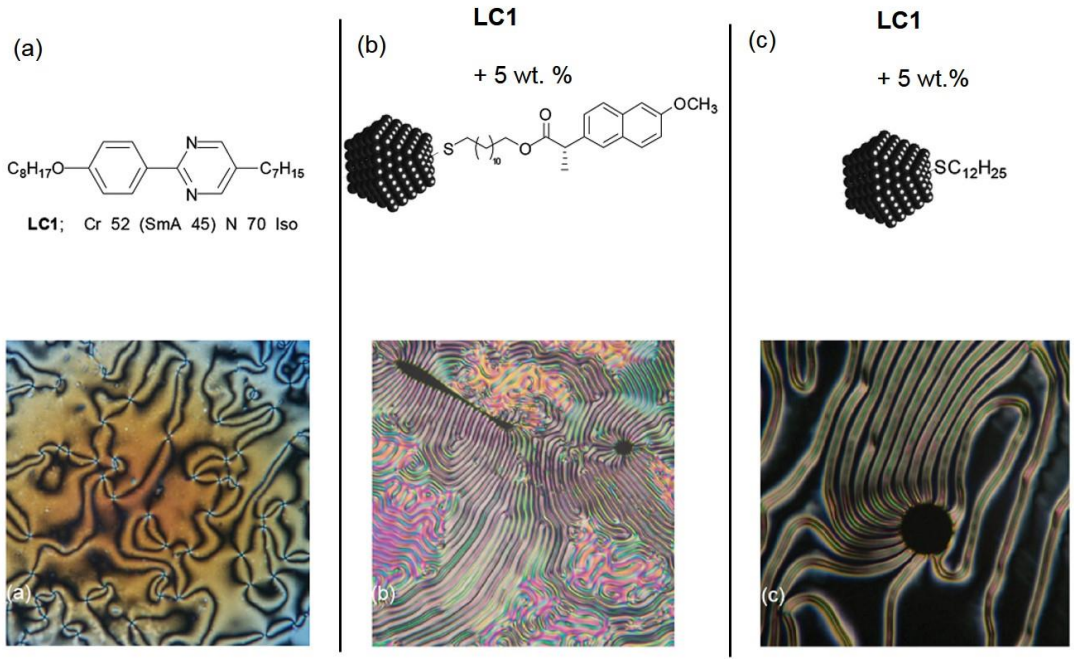

Figure 1.30 a) Structure and phase transition temperatures (°C) of nematic LC1 (top) and its POM photomicrographs taken on cooling just below the Iso–N phase transition (crossed polarisers) showing Schlieren texture of the N phase (bottom). b) Structure of truncated cuboctahedral shape of the Au NP capped with (S)-naproxen-end thiol (top) and fingerprint POM texture of the N^* phase of LC1 doped with 5wt% (S)-naproxen-capped Au NP at 44 °C (bottom). c) Structure of truncated cuboctahedral shape of the Au NP capped with dodecanethiolate (top), and stripe texture of the N phase with coexisting areas of homeotropic alignment of 5wt% dodecyl thiol-capped Au NP in LC1 at 64 °C (bottom). Reproduced with permission from Ref. [10] – Copyright: The Royal Society of Chemistry.

As highlighted, NPs not only influence the optical and EO properties of LCs, but also induce alignment modes of LCs,[136, 137] a critical prerequisite for the application of these materials in many devices. Recently, Torsten Hegmann's group at Kent State University have used this phenomenon to create pre-defined alignment patterns in nematic LC thin films using ink-jet printing of alkylthiol-capped Au NPs.[107] As shown in **Figure 1.31**a

nematic LC molecules show homeotropic alignment on the NP-printed areas of the substrate, and planar alignment on other areas with planer alignment layer. The patterns printed by this technique (e.g. see **Figure 1.31**b) have shown stability over several months and no deterioration with respect to the alignment quality or any migration of the NPs into the bulk of the aligned LC film. This approach has the potential to provide low-cost electro-optical LC devices featuring a wide range of NPs and substrate materials including flexible[138] and uneven substrate for applications in areas such as adaptive LC Fresnel lenses, vertical alignment mode LCDs and flexible LCDs, to name a few.[107]

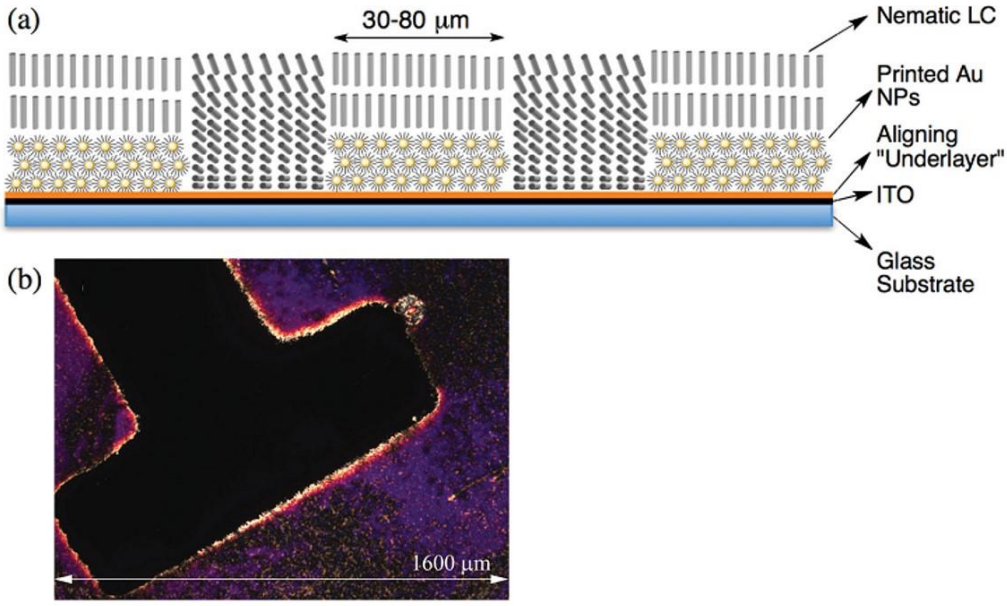

Figure 1.31 a) Schematic image of the substrate design of an LC cell with ITO electrodes and alignment layers comprised of continuous layer of 30° SiO_x and patterned printed layer of gold NPs. b) POM image of the LC texture and alignment pattern in cells (bare ITO and cell gap: 5 μm) created by printed NPs in the nematic mixture MLC-6610 (Reproduced with permission from Ref. [107] – Copyright: WILEY-VCH.

LC composites with other types of NPs such as silica NPs have shown promising results.[139-141] For example, silica NP-doped nematic samples in EO test cells have shown

the so-called memory effect, where the LC orientational state is retained after the applied electric field is removed.[139, 142] This memory effect can be applied for the improvements in bistable display modes.[142] Kobayashi *et al.* described an EO frequency modulation with millisecond or sub-millisecond response time in twisted nematic LCDs as well as lower operating voltages in different LCD switching modes using particles such as Pd, Ag, Ag-Pd, Au, MgO, or SiO_2.[143-145]

In addition, results from colloidal LC dispersions with ferroelectric NPs (e.g. $Sn_2P_2S_6$, $BaTiO_3$) suggest increase in the order parameter and clearing temperature of N-LCs along with enhancement of the dielectric anisotropy.[146-149]

Carbon nanotubes are also found to impact the properties of the liquid crystalline host in various ways including: improvements in dielectric anisotropy,[150, 151] faster response time,[152] and lower or higher driving voltages.[150, 151, 153-155] There are also reports using carbon nanotube films to control the alignment of N-LCs for flexible display applications.[156]

These studies and experimental results confirm that NPs can modulate optical and electro-optical properties of the N-LCs and other mesophases. However, carefully designed nanoparticles and experiments are needed to fully exploit these NP-LC systems particularly with respect to size and chemical/thermal stability of NPs.

1.11.3 Liquid Crystal-Functionalized Nanoparticles

Apart from doping of LCs with NPs, there has been great interest in the formation of liquid crystalline NPs by directly attaching LC building blocks to NPs. Of course, this is not an easy task considering broad size distribution and/or polyhedral structures in synthetic NPs

causing inhomogeneous ligand distribution at the surface.[103] Moreover, other difficulties such as the tuning of thickness, density and fluxionality of surface ligands make this task even more challenging.[103] A common approach toward LC-decorated Au NPs is ligand exchange between alkanethiols and mesogenic molecules. Mehl and Cseh have used this approach for synthesizing Au NPs (1.6-2 nm) decorated with mesogenic molecules and observed the formation of typical nematic marble and *Schlieren* textures[157, 158] (**Figure 1.32**) and later investigated 3–dimensional self-assembly of the Au NP facilitated by ordering of the mesogenic surface ligands.[69]

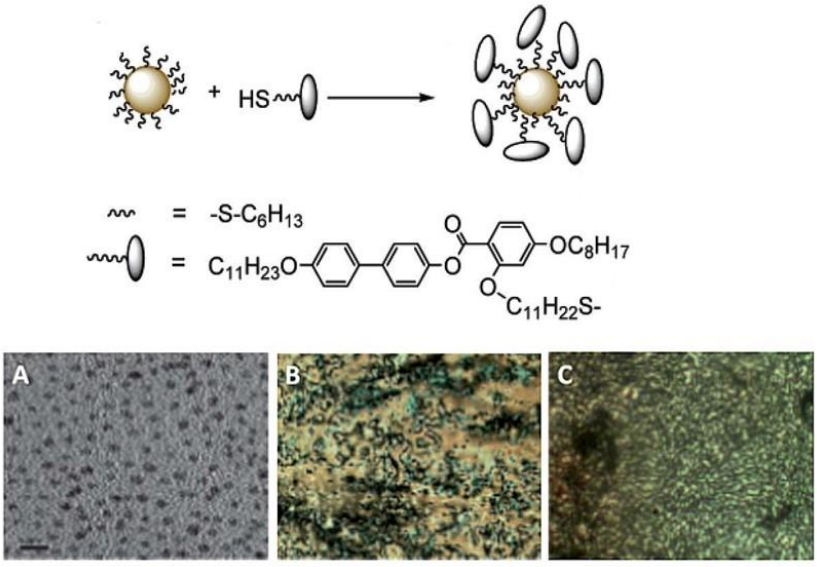

Figure 1.32 Schematic representation of synthesis of LC-functionalized Au NP using LC thiols exchange reaction (top). (a) TEM micrograph (scale bar: 5 nm) of the Au NP (b) POM texture of the LC ligand (c) POM texture of the LC-functionalized Au NP showing the typical nematic *Schlieren* texture. Reproduced with permission from Ref. [157] – Copyright: The American Chemical Society.

Other groups have also used the ligand exchange method for synthesizing liquid crystalline Au NPs.[159-161] For example, Kim *et al.* obtained a 1-dimensional arrangement

of the Au NPs capped with cyanobiphenyl-functionalized thiolates upon heating the Au NPs in the mesophase temperature range.[161]

LC-functionalization of other inorganic nanostructures has also been investigated. Kanie and co-workers reported on the formation of a thermotropic nematic phase by coating TiO_2 and Fe_2O_3 nanoparticles with LC units.[162, 163] Goodby *et al.* showed that C60-fullerene decorated with twelve LC units symmetrically positioned around the C60 core, can form a chiral nematic phase.[164] In all the above mentioned examples of LC-decorated NPs and in NP-LC hybrids a promising avenue is to control the macroscopic organization of NPs by utilizing the capability of LCs phases to respond to external stimuli such as electric or magnetic fields.[165] Similar to NP doping in LCs, this avenue of LC nanocomposites needs further research on a variety of stable, compatible and well-dispersed nanocomposites to reach its full technological potential. More details about LC nanocomposites is provided in Chapter 2.

1.12 References

1. Bahadur, B., *Liquid Crystals: Applications and Uses*. World Scientific: 1992.
2. Demus, D.; Goodby, J. W.; Gray, G. W.; Spiess, H. W.; Vill, V., *Handbook of Liquid Crystals*, Fundamentals, Vol. 1, Wiley: 2008, pp. 17-23.
3. (a) Bruce, D. W.; Goodby, J. W.; Sambles, J. R.; Coles, H. J. *Phil. Trans. R. Soc. A* **2006,** 364, (1847), 2567-2571. (b) Dierking, I., *Textures of Liquid Crystals*. Wiley: 2006, pp. 1-29.
4. Helfrich, W.; Schadt, M. *Lichtsteuerzelle,* Swiss Patent CH532261A. 1970.

5. (a) Kelly, S. M.; O'Neill, M., Liquid crystals for electro-optic applications. In *Handbook of Advanced Electronic and Photonic Materials and Devices*, Nalwa, H. S., Ed. Academic Press: Burlington, 2001; Vol. 7, Ch. 1, pp 10-11. (b) Goodby, J. W. *Liq. Cryst.* **2011,** 38, (11-12), 1363-1387.
6. Brochard, F.; de Gennes, P. *J. Phys. (Paris)* **1970,** 31, 691-708.
7. Rault, J.; Cladis, P.; Burger, J. *Phys. Lett. A* **1970,** 32, (3), 199-200.
8. Hayes, C. *Mol. Cryst. .Liq. Cryst.* **1976,** 36, (3-4), 245-253.
9. Burda, C.; Chen, X.; Narayanan, R.; El-Sayed, M. A. *Chem. Rev.* **2005,** 105, (4), 1025-1102.
10. Qi, H.; Hegmann, T. *J. Mater. Chem.* **2006,** 16, (43), 4197-4205.
11. Kinkead, B.; Hegmann, T. *J. Mater. Chem.* **2010,** 20, (3), 448-458.
12. Stannarius, R. *Nat. Mater.* **2009,** 8, (8), 617-618.
13. Draper, M.; Saez, I. M.; Cowling, S. J.; Gai, P.; Heinrich, B.; Donnio, B.; Guillon, D.; Goodby, J. W. *Adv. Funct. Mater.* **2011,** 21, (7), 1260-1278.
14. Prodanov, M. F.; Pogorelova, N. V.; Kryshtal, A. P.; Klymchenko, A. S.; Mely, Y.; Semynozhenko, V. P.; Krivoshey, A. I.; Reznikov, Y. A.; Yarmolenko, S. N.; Goodby, J. W.; Vashchenko, V. V. *Langmuir* **2013,** 29, (30), 9301-9309.
15. Kim, E. B.; Guzman, O.; Grollau, S.; Abbott, N. L.; de Pablo, J. J. *J. Chem. Phys.* **2004,** 121, (4), 1949-1961.
16. Reinitzer, F. *Monatsh. Chem.* **1888,** 9, 421-441.
17. Chen, R. H., *Liquid Crystal Displays: Fundamental Physics and Technology*. Wiley: 2011, pp: 78-92
18. Hegmann, T.; Qi, H.; Marx, V. M. *J. Inorg. Organomet. P.* **2007,** 17, (3), 483-508.

19. Reddy, R. A.; Tschierske, C. *J. Mater. Chem.* **2006,** 16, (10), 907-961.

20. Bai, Y.; Abbott, N. L. *Langmuir* **2011,** 27, (10), 5719-5738.

21. Marcos, C.; Pena, J. M. S.; Torres, J. C.; Santos, J. I. *Sensors* **2012,** 12, (3), 3204-3214.

22. Blinov, L. M.; Chigrinov, V. G., *Electrooptic Effects in Liquid Crystal Materials*. Springer New York: 1996.

23. Joshi, A. A.; Whitmer, J. K.; Guzman, O.; Abbott, N. L.; de Pablo, J. J. *Soft Matter* **2014,** 10, (6), 882-93.

24. Demus, D.; Goodby, J. W.; Gray, G. W.; Spiess, H. W.; Vill, V., *Handbook of Liquid Crystals, Low Molecular Weight Liquid Crystals I: Calamitic Liquid Crystals*. Wiley: 2011, pp: 90-109.

25. Freedericksz, V.; Zolina, V. *T. Faraday Soc.* **1933,** 29, (140), 919-930.

26. Dierking, I., *Textures of Liquid Crystals*. Wiley: 2006, pp. 33-39

27. Dierking, I., *Textures of Liquid Crystals*. Wiley: 2006, pp. 52-74

28. Smalyukh, I. I.; Shiyanovskii, S. V.; Lavrentovich, O. D. *Chem. Phys. Lett.* **2001,** 336, 88-96.

29. Lavrentovich, O. *Pramana,* **2003,** 61, (2), 373-384.

30. Webb, R. H. *Rep. Prog. Phys.* **1996,** 59, (3), 427.

31. Demus, D.; Goodby, J. W.; Gray, G. W.; Spiess, H. W.; Vill, V., *Handbook of Liquid Crystals*, Wiley: 2008, pp. 310-334

32. Wu, S. T.; Coates, D.; Bartmann, E. *Liq. Cryst.* **1991,** 10, (5), 635-646.

33. Wu, S.-T.; Wu, C.-S. *Phys. Rev. A* **1990,** 42, (4), 2219.

34. Yeh, P.; Gu, C., *Optics of Liquid Crystal Displays*. Wiley: 2010.

35. Schadt, M.; Helfrich, W. *Appl. Phys. Lett.* **1971,** 18, (4), 127-128.

36. Kelly, S. M.; O'Neill, M. Liquid crystals for electro-optic applications. In *Handbook of Advanced Electronic and Photonic Materials and Devices*, Nalwa, H. S., Ed. Academic Press: Burlington, 2001; Vol. 7, Ch. 1, pp 1-66.
37. Scheffer, T. J.; Nehring, J. *J. Appl. Phys.* **1985,** 58, (8), 3022-3031.
38. Kiefer, R.; Weber, B.; Windscheid, F.; Baur, G. In *In-plane switching of nematic liquid crystals*, Japan Display, 1992; pp 547-550.
39. Baur, G.; Kiefer, R.; Klausmann, H.; Windscheid, F. *Liq. Cryst. Today* **1995,** 5, (3), 12-13.
40. Fergason, J. *SID Int. Symp. Dig. Technol.* **1985,** 16, 68-70.
41. Takeda, A.; Kataoka, S.; Sasaki, T.; Chida, H.; Tsuda, H.; Ohmuro, K.; Sasabayashi, T.; Koike, Y.; Okamoto, K. In *41.1: A Super-High Image Quality Multi-Domain Vertical Alignment LCD by New Rubbing-Less Technology*, SID Symposium Digest of Technical Papers, 1998; Wiley Online Library: pp 1077-1080.
42. Kim, K. H. *SID Digest* **2003,** 40, 1208-1215.
43. Davidson, A. J.; Mottram, N. J. *Phys. Rev. E* **2002,** 65, (5), 051710.
44. Jones, J. C.; Bryan-Brown, G. P.; Wood, E. L.; Graham, A.; Brett, P.; Hughes, J. R. In *Novel bistable liquid crystal displays based on grating alignment*, 2000; pp 84-93.
45. Ge, Z.; Gauza, S.; Jiao, M.; Xianyu, H.; Wu, S.-T. *Appl. Phys. Lett.* **2009,** 94, (10), 101104.
46. Kikuchi, H.; Yokota, M.; Hisakado, Y.; Yang, H.; Kajiyama, T. *Nat. Mater.* **2002,** 1, (1), 64-68.
47. Shah, M.; Badwaik, V. D.; Dakshinamurthy, R. *J. Nanosci. Nanotechno.* **2014,** 14, (1), 344-362.

48. Majdalawieh, A.; Kanan, M. C.; El-Kadri, O.; Kanan, S. M. *J. Nanosci. Nanotechno.* **2014,** 14, (7), 4757-4780.

49. Yeh, Y.-C.; Creran, B.; Rotello, V. M. *Nanoscale* **2012,** 4, (6), 1871-1880.

50. Saha, K.; Agasti, S. S.; Kim, C.; Li, X.; Rotello, V. M. *Chem. Rev.* **2012,** 112, (5), 2739-2779.

51. Westerlund, F.; Bjornholm, T. *Curr. Opin. Colloid In.* **2009,** 14, (2), 126-134.

52. Daniel, M. C.; Astruc, D. *Chem. Rev.* **2004,** 104, (1), 293-346.

53. Turkevich, J.; Stevenson, P. C.; Hillier, J. *Discuss. Faraday Soc.* **1951,** 11, 55-75.

54. Brust, M.; Fink, J.; Bethell, D.; Schiffrin, D. J.; Kiely, C. *J. Chem. Soc., Chem, Comm.* **1995**, (16), 1655-1656.

55. Brust, M.; Walker, M.; Bethell, D.; Schiffrin, D. J.; Whyman, R. *J. Chem. Soc. Chem. Comm.* **1994**, (7), 801-802.

56. Yong, K.-T.; Swihart, M. T.; Ding, H.; Prasad, P. N. *Plasmonics* **2009,** 4, (2), 79-93.

57. Yan, Y.; Li, J.; Yang, Y. *Prog. Chem.* **2009,** 21, (5), 971-981.

58. Sperling, R. A.; Parak, W. J. *Phil. Trans. R. Soc. A* **2010,** 368, (1915), 1333-1383.

59. Hostetler, M. J.; Wingate, J. E.; Zhong, C. J.; Harris, J. E.; Vachet, R. W.; Clark, M. R.; Londono, J. D.; Green, S. J.; Stokes, J. J.; Wignall, G. D.; Glish, G. L.; Porter, M. D.; Evans, N. D.; Murray, R. W. *Langmuir* **1998,** 14, (1), 17-30.

60. Stamatoiu, O.; Mirzaei, J.; Feng, X.; Hegmann, T. *Top. Curr. Chem.* **2012**, 318, 331-393.

61. Reddy, L. H.; Arias, J. L.; Nicolas, J.; Couvreur, P. *Chem. Rev.* **2012,** 112, (11), 5818-5878.

62. Goulet, P. J. G.; Bourret, G. R.; Lennox, R. B. *Langmuir* **2012,** 28, (5), 2909-2913.

63. Basiruddin, S. K.; Saha, A.; Pradhan, N.; Jana, N. R. *J. Phys. Chem. C* **2010,** 114, (25), 11009-11017.

64. Kassam, A.; Bremner, G.; Clark, B.; Ulibarri, G.; Lennox, R. B. *J. Am. Chem. Soc.* **2006,** 128, (11), 3476-3477.

65. Templeton, A. C.; Wuelfing, M. P.; Murray, R. W. *Acc. Chem. Res.* **2000,** 33, (1), 27-36.

66. Brust, M.; Schiffrin, D. J.; Bethell, D.; Kiely, C. J. *Adv. Mater.* **1995,** 7, (9), 795-797.

67. Goulet, P. J.; Lennox, R. B. *J. Am. Chem. Soc.* **2010,** 132, (28), 9582-9584.

68. Qi, H.; Kinkead, B.; Marx, V. M.; Zhang, H. R.; Hegmann, T. *ChemPhysChem* **2009,** 10, (8), 1211-1218.

69. Zeng, X. B.; Liu, F.; Fowler, A. G.; Ungar, G.; Cseh, L.; Mehl, G. H.; Macdonald, J. E. *Adv. Mater.* **2009,** 21, (17), 1746-1750.

70. Li, F.; Li, Q.; Chen, Y. *J. Lumin.* **2012,** 132, (8), 2114-2121.

71. Bronstein, L. M.; Shifrina, Z. B. *Chem. Rev.* **2011,** 111, (9), 5301-5344.

72. Hinterwirth, H.; Lindner, W.; Laemmerhofer, M. *Anal. Chim. Acta* **2012,** 733, 90-97.

73. Love, C. S.; Ashworth, I.; Brennan, C.; Chechik, V.; Smith, D. K. *Langmuir* **2007,** 23, (10), 5787-5794.

74. Liu, X.; Zhu, M.; Chen, S.; Yuan, M.; Guo, Y.; Song, Y.; Liu, H.; Li, Y. *Langmuir* **2008,** 24, (20), 11967-11974.

75. Gonzalez de Rivera, F.; Angurell, I.; Rossell, O.; Seco, M.; Llorca, J. *J. Organomet. Chem.* **2012,** 715, 13-18.

76. Friederici, M.; Angurell, I.; Seco, M.; Rossell, O.; Llorca, J. *Dalton T.* **2011,** 40, (31), 7934-7940.

77. Rucareanu, S.; Gandubert, V. J.; Lennox, R. B. *Chem. Mater.* **2006,** 18, (19), 4674-4680.

78. Woehrle, G. H.; Brown, L. O.; Hutchison, J. E. *J. Am. Chem. Soc.* **2005,** 127, (7), 2172-2183.

79. Petroski, J.; Chou, M. H.; Creutz, C. *Inorg. Chem.* **2004,** 43, (5), 1597-1599.

80. Neouze, M.-A.; Schubert, U. *Monatsh. Chem.* **2008,** 139, (3), 183-195.

81. Love, J. C.; Estroff, L. A.; Kriebel, J. K.; Nuzzo, R. G.; Whitesides, G. M. *Chem. Rev.* **2005,** 105, (4), 1103-1169.

82. Ji, X.; Copenhaver, D.; Sichmeller, C.; Peng, X. *J. Am. Chem. Soc.* **2008,** 130, (17), 5726-5735.

83. Guerrero-Martinez, A.; Perez-Juste, J.; Liz-Marzan, L. M. *Adv. Mater.* **2010,** 22, (11), 1182-1195.

84. Stöber, W.; Fink, A.; Bohn, E. *J. Colloid Interf. Sci.* **1968,** 26, (1), 62-69.

85. Graf, C.; Vossen, D. L. J.; Imhof, A.; van Blaaderen, A. *Langmuir* **2003,** 19, (17), 6693-6700.

86. Jana, N. R.; Earhart, C.; Ying, J. Y. *Chem. Mater.* **2007,** 19, 5074-5082.

87. Wang, Z. L.; Liu, Y.; Zhang, Z., *Handbook of Nanophase and Nanostructured Materials*. Kluwer Academic/Plenum: 2003; Vol. 2, pp.372-441.

88. Wilcoxon, J.; Abrams, B. *Chem. Soc. Rev.* **2006,** 35, (11), 1162-1194.

89. Weyland, M.; Midgley, P. A. *Mater. Today* **2004,** 7, (12), 32-40.

90. Xie, H.; Gill-Sharp, K. L.; O'Neal, D. P. *Nanomedicine* **2007,** 3, (1), 89-94.

91. Chakraborty, S.; Sahoo, B.; Teraoka, I.; Gross, R. A. *Carbohydr. Polym.* **2005,** 60, (4), 475-481.

92. Ashcroft, N. W.; Mermin, N. D., *Solid State Physics*. Saunders College: 1976.

93. Link, S.; El-Sayed, M. A. *J. Phys. Chem. B* **1999,** 103, (40), 8410-8426.

94. Link, S.; El-Sayed, M. A. *Int. Rev. Phys. Chem.* **2000,** 19, (3), 409-453.

95. De, M.; Ghosh, P. S.; Rotello, V. M. *Adv. Mater.* **2008,** 20, (22), 4225-4241.

96. Rosi, N. L.; Mirkin, C. A. *Chem. Rev.* **2005,** 105, (4), 1547-1562.

97. Badia, A.; Gao, W.; Singh, S.; Demers, L.; Cuccia, L.; Reven, L. *Langmuir* **1996,** 12, (5), 1262-1269.

98. Badia, A.; Cuccia, L.; Demers, L.; Morin, F.; Lennox, R. B. *J. Am. Chem. Soc.* **1997,** 119, (11), 2682-2692.

99. Zhang, J. Z., *Optical Properties and Spectroscopy of Nanomaterials*. World Scientific: **2009**, pp: 47-72.

100. Vickerman, J. C.; Gilmore, I., *Surface Analysis: The Principal Techniques*. Wiley: **2011**.

101. Mansfield, E.; Kar, A.; Quinn, T. P.; Hooker, S. A. *Anal. Chem.* **2010,** 82, (24), 9977-9982.

102. Mansfield, E.; Tyner, K. M.; Poling, C. M.; Blacklock, J. L. *Anal. Chem.* **2014,** 86, (3), 1478-1484.

103. Saliba, S.; Mingotaud, C.; Kahn, M. L.; Marty, J. D. *Nanoscale* **2013**, 5, (15), 6641-6661.

104. Stamatoiu, O.; Mirzaei, J.; Feng, X.; Hegmann, T. *Top. Curr. Chem.* **2012,** 318, 331-393.

105. Shivakumar, U.; Mirzaei, J.; Feng, X.; Sharma, A.; Moreira, P.; Hegmann, T. *Liq. Cryst.* **2011,** 38, (11-12), 1495-1514.

106. Guzmán, O.; Abbott, N. L.; de Pablo, J. J. *J. Chem. Phys.* **2005,** 122, (18), 184711.

107. Reznikov, M.; Sharma, A.; Hegmann, T. *Part. Part. Syst. Char.* **2014**, 31, (2), 257-265.

108. Lagerwall, J. P. F.; Scalia, G. *Curr. Appl. Phys.* **2012,** 12, (6), 1387-1412.

109. Dintinger, J.; Tang, B.-J.; Zeng, X.; Liu, F.; Kienzler, T.; Mehl, G. H.; Ungar, G.; Rockstuhl, C.; Scharf, T. *Adv. Mater.* **2013,** 25, (14), 1999-2004.

110. Pratibha, R.; Park, K.; Smalyukh, I. I.; Park, W. *Opt. Express* **2009,** 17, (22), 19459-19469.

111. Chen, X.; Chen, L.; Chen, Y. *RSC Adv.* **2014,** 4, (7), 3627-3632.

112. Coursault, D.; Grand, J.; Zappone, B.; Ayeb, H.; Levi, G.; Felidj, N.; Lacaze, E. *Adv. Mater.* **2012,** 24, (11), 1461-1465.

113. Stark, H. *Phys. Rep.* **2001,** 351, (6), 387-474.

114. Loudet, J.; Hanusse, P.; Poulin, P. *Science* **2004,** 306, (5701), 1525.

115. Loudet, J.; Barois, P.; Auroy, P.; Keller, P.; Richard, H.; Poulin, P. *Langmuir* **2004,** 20, (26), 11336-11347.

116. Poulin, P.; Stark, H.; Lubensky, T.; Weitz, D. *Science* **1997,** 275, (5307), 1770-1773.

117. Poulin, P.; Weitz, D. A. *Phys. Rev. E* **1998,** 57, (1), 626-637.

118. Lubensky, T. C.; Pettey, D.; Currier, N.; Stark, H. *Phys. Rev. E* **1998,** 57, (1), 610-625.

119. Ravnik, M.; Škarabot, M.; Žumer, S.; Tkalec, U.; Poberaj, I.; Babič, D.; Osterman, N.; Muševič, I. *Phys. Rev. Lett.* **2007,** 99, (24), 247801.

120. Mondain-Monval, O.; Dedieu, J.; Gulik-Krzywicki, T.; Poulin, P. *Eur. Phys. J. B* **1999,** 12, (2), 167-170.

121. Loudet, J.-C.; Barois, P.; Poulin, P. *Nature* **2000,** 407, (6804), 611-613.

122. Gu, Y.; Abbott, N. L. *Phys. Rev. Lett.* **2000,** 85, (22), 4719-4722.

123. Poulin, P.; Cabuil, V.; Weitz, D. A. *Phys. Rev. Lett.* **1997,** 79, (24), 4862-4865.

124. Da Cruz, C.; Sandre, O.; Cabuil, V. *J. Phys. Chem. B* **2005,** 109, (30), 14292-14299.

125. Kreuzer, M.; Tschudi, T.; de Jeu, W. H.; Eidenschink, R. *Appl. Phys. Lett.* **1993,** 62, (15), 1712-1714.

126. Fukuda, J.-i.; Yoneya, M.; Yokoyama, H. *Eur. Phys. J. E* **2004,** 13, (1), 87-98.

127. Voloschenko, D.; Pishnyak, O. P.; Shiyanovskii, S. V.; Lavrentovich, O. D. *Phys. Rev. E Stat. Nonlin. Soft Matter Phys.* **2002,** 65, (6), 060701.

128. West, J. L.; Glushchenko, A.; Liao, G.; Reznikov, Y.; Andrienko, D.; Allen, M. P. *Phys. Rev. E* **2002,** 66, (1), 012702.

129. Müller, J.; Sönnichsen, C.; von Poschinger, H.; von Plessen, G.; Klar, T. A.; Feldmann, J. *Appl. Phys. Lett.* **2002,** 81, (1), 171-173.

130. Kossyrev, P. A.; Yin, A.; Cloutier, S. G.; Cardimona, D. A.; Huang, D.; Alsing, P. M.; Xu, J. M. *Nano Lett.* **2005,** 5, (10), 1978-1981.

131. Sono, S.; Miyama, K.; Takatoh, K.; Kobayashi, S. *Proc. SPIE-Int. Soc. Opt. Eng.* **2006,** 6135, 1.

132. Qi, H.; Kinkead, B.; Hegmann, T. *Adv. Funct. Mater.* **2008,** 18, (2), 212-221.

133. Qi, H.; Hegmann, T. *ACS Appl. Mater. In.* **2009,** 1, (8), 1731-1738.

134. Urbanski, M.; Kinkead, B.; Hegmann, T.; Kitzerow, H.-S. *Liq. Cryst.* **2010,** 37, (9), 1151-1156.

135. Qi, H.; O'Neil, J.; Hegmann, T. *J. Mater. Chem.* **2008,** 18, (4), 374-380.

136. Jeng, S.-C.; Kuo, C.-W.; Wang, H.-L.; Liao, C.-C. *Appl. Phys. Lett.* **2007,** 91, (6), 061112.

137. Kuo, C.-W.; Jeng, S.-C.; Wang, H.-L.; Liao, C.-C. *Appl. Phys. Lett.* **2007,** 91, (14), 141103.

138. Jensen, G. C.; Krause, C. E.; Sotzing, G. A.; Rusling, J. F. *Phys. Chem. Chem. Phys.* **2011,** 13, (11), 4888-4894.

139. Huang, C.-Y.; Lai, C.-C.; Tseng, Y.-H.; Yang, Y.-T.; Tien, C.-J.; Lo, K.-Y. *Appl. Phys. Lett.* **2008,** 92, (22), 221908.

140. Dolgov, L.; Yaroshchuk, O. *Mol. Cryst. Liq. Cryst.* **2004,** 409, (1), 77-89.

141. Yaroshchuk, O. V.; Dolgov, L. O.; Kiselev, A. D. *Physical Review E* **2005,** 72, (5), 051715.

142. Sikharulidze, D. *Appl. Phys. Lett.* **2005,** 86, (3), 033507.

143. Miyama, T.; Thisayukta, J.; Shiraki, H.; Sakai, Y.; Shiraishi, Y.; Toshima, N.; Kobayashi, S. *Jpn. J. Appl. Phys.* **2004,** 43, (5A), 2580-2584.

144. Sakai, Y.; Nishida, N.; Shiraki, H.; Shiraishi, Y.; Miyama, T.; Toshima, N.; Kobayashi, S. *Mol. Cryst. Liq. Cryst.* **2005,** 441, 143-152.

145. Kobayashi, S.; Miyama, T.; Nishida, N.; Sakai, Y.; Shiraki, H.; Shiraishi, Y.; Toshima, N. *J. Display Techn.* **2006,** 2, (2), 121-129.

146. Reznikov, Y.; Buchnev, O.; Tereshchenko, O.; Reshetnyak, V.; Glushchenko, A.; West, J. *Appl. Phys. Lett.* **2003,** 82, (12), 1917-1919.

147. Ouskova, E.; Buchnev, O.; Reshetnyak, V.; Reznikov, Y.; Kresse, H. *Liq. Cryst.* **2003,** 30, (10), 1235-1239.

148. Li, F.; Buchnev, O.; Cheon, C. I.; Glushchenko, A.; Reshetnyak, V.; Reznikov, Y.; Sluckin, T. J.; West, J. L. *Phys. Rev. Lett.* **2006,** 97, (14), 147801.

149. Reshetnyak, V. Y.; Shelestiuk, S. M.; Sluckin, T. J. *Mol. Cryst. Liq. Cryst.* **2006,** 454, (1), 201-206

150. Huang, C.-Y.; Hu, C.-Y.; Pan, H.-C.; Lo, K.-Y. *Jpn. J. Appl. Phys.* **2005,** 44, (11R), 8077-8081.

151. Huang, C.-Y.; Pan, H.-C.; Hsieh, C.-T. *Jpn. J. Appl. Phys.* **2006,** 45, (8R), 6392-6394.

152. Chen, H.-Y.; Lee, W.; Clark, N. A. *Appl. Phys. Lett.* **2007,** 90, (3), 033510.

153. Lee, W.; Wang, C.-Y.; Shih, Y.-C. *Appl. Phys. Lett.* **2004,** 85, (4), 513-515.

154. Lagerwall, J. P. F.; Scalia, G. *J. Mater. Chem.* **2008,** 18, 2890-2898.

155. Scalia, G.; Lagerwall, J. P. F.; Schymura, S.; Haluska, M.; Giesselmann, F.; Roth, S. *Phys. Status Solidi B* **2007,** 244, 4212-4217.

156. Schindler, A.; Brill, J.; Fruehauf, N.; Novak, J. P.; Yaniv, Z. *Physica E: Low-Dimensional Systems and Nanostructures* **2007,** 37, (1), 119-123.

157. Cseh, L.; Mehl, G. H. *J. Am. Chem. Soc.* **2006,** 128, (41), 13376-13377.

158. Cseh, L.; Mehl, G. H. *J. Mater. Chem.* **2007,** 17, (4), 311-315.

159. Kanayama, N.; Tsutsumi, O.; Kanazawa, A.; Ikeda, T. *Chem. Commun.* **2001**, (24), 2640-2641.

160. Wojcik, M.; Lewandowski, W.; Matraszek, J.; Mieczkowski, J.; Borysiuk, J.; Pociecha, D.; Gorecka, E. *Angew. Chem. Int. Ed.* **2009,** 48, (28), 5167-5169.

161. In, I.; Jun, Y.-W.; Kim, Y. J.; Kim, S. Y. *Chem. Commun.* **2005**, (6), 800-801.

162. Kanie, K.; Muramatsu, A. *J. Am. Chem. Soc.* **2005,** 127, (33), 11578-11579.

163. Kanie, K.; Sugimoto, T. *J. Am. Chem. Soc.* **2003,** 125, (35), 10518-10519.

164. Campidelli, S.; Eng, C.; Saez, I. M.; Goodby, J. W.; Deschenaux, R. *Chem. Commun.* **2003**, (13), 1520-1521.

165. Hoogboom, J.; Rasing, T.; Rowan, A. E.; Nolte, R. J. *J. Mater. Chem.* **2006,** 16, (14), 1305-1314.

Chapter 2

Quantum Dots as Liquid Crystal Dopants

Quantum Dots as Liquid Crystal Dopants

Javad Mirzaei[a], Mitya Reznikov[b], and Torsten Hegmann[a-d]*

[a] Department of Chemistry, University of Manitoba, Winnipeg, MB, R3T 2N2 Canada

[b] Chemical Physics Interdisciplinary Program & Liquid Crystal Institute, Kent State University, Kent, OH 44242 USA

[c] Department of Pharmacology and Therapeutics, University of Manitoba, Winnipeg, MB, R3T 2N2 Canada

[d] Department of Chemistry & Biochemistry, Kent State University, Kent, OH 44242 USA

Reproduced with permission from *Journal of Materials Chemistry*, **2012**, 22, (42), 22350-22365.

Abstract

Liquid crystal nanoscience, a field exploring the mutually beneficial combination of the unique properties of nanoscale materials and fluid, yet ordered liquid crystalline phases, is increasingly focusing on semiconductor quantum dots. In one major research thrust, the anisotropic properties of the liquid crystal host are sought to facilitate the assembly of quantum dot into arrays, in another, both size- and shape-dependent optical and electronic properties of quantum dots are used to manipulate optical, electro-optical and alignment properties of liquid crystalline materials. This chapter highlights recent accomplishment and new insights in this fascinating area of soft matter nanocomposites including work from our laboratory on a series of CdSe and CdTe quantum dots as additives in nematic liquid crystal hosts.

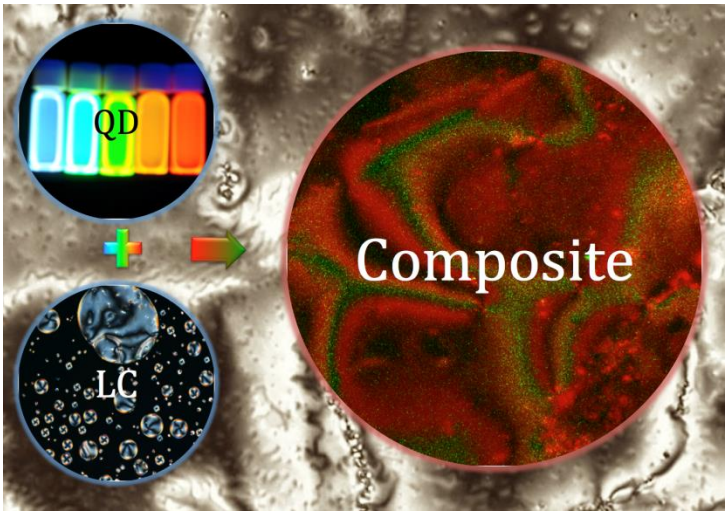

Graphical abstract

2.1 Introduction

Over the last two decades the development of nanomaterials and nanostructures experienced tremendous innovative impacts on science and technology. Nanoscale materials with physical dimensions of 1 to 100 nanometers (nm), featuring unique properties different from individual atoms or molecules as well as the bulk, have revolutionized many fields in R&D including catalysis, computing, photonics, energy, and medicine. Along with the 'nanomaterial revolution', the field of liquid crystals (LCs) is a particular vibrant area benefitting from both use and advancement of nanomaterials that vary in size, shape, core material, and surface functionality.

Liquid crystal nanoscience as a subject can be approached from two major perspectives. One perspective focuses on using reconfigurable liquid crystals either for template-assisted syntheses of nanomaterials or using these self-organizing anisotropic fluids to assemble and manipulate nanoscale materials. The second one encompasses approaches where nanomaterials such as nanoparticles (NPs) impact liquid crystals based on very fundamental interactions between liquid crystal host molecules and nanomaterials as dopants. Here, the modulation of optical and electro-optical effects in liquid crystal-nanomaterial composites for potential application in devices such as liquid crystal displays (LCDs) appears to be the main focus. Many important aspects of liquid crystal nanoscience, including studies elucidating the roles of nanomaterial shapes and sizes, were summarized in various review papers.[1-6] This chapter will primarily focus on recent developments in the use of semiconductor nanoparticles, also known as quantum dots (QDs), as dopants in

LC phases. In addition, recent advances in the assembly and organization of QDs in anisotropic LC media will be highlighted.

2.2 Quantum Dots

Inorganic metal and semiconductor NPs are zero-dimensional (quasi-spherical) nanomaterials. Among the various colloidal NPs with diverse core compositions, semiconductor QDs are being extensively developed and studied for their promising applications in medicine (bio-labelling/imaging,[7-13] cancer therapy[12, 14-16]), photonics (light-emitting diodes,[17-20] lasers[21, 22]), alternative energy sources (QDs-sensitized solar cells[23-28]), and possible future QD-based devices (e.g., superconductor nanodevices).[29-31]

QD semiconductors in the range of 2 to 10 nm in diameter are made of hundreds to thousands of atoms of group IIB and VIA elements (e.g., CdSe, CdTe, and ZnO), group IIIA and VA elements (e.g., InP and InAs), and group IVA-VIA elements (e.g., PbS). Their unique size- and shape-dependent optical and electronic properties differing from the bulk and from the atomic/molecular level are attributed to the 3-dimensional quantum confinement effect, i.e. the strong confinement of electrons and holes in the case where the radius of a particle is below the exciton Bohr radius of the material.[32-34] In a semiconductor, an electron will be promoted from the valence to the conduction band, leaving a ‘hole’ or ‘absence of an electron’ in the valence band upon irradiation by photons with greater energy than the bandgap. Therefore, this ‘hole’ is assumed to behave as a ‘particle’ with a certain effective mass and positive charge. The bound state of the electron–hole pair is called an ‘exciton’.[35] The relation between the size and the bandgap energy of

semiconductor nanocrystals was developed by Luis Brus by applying the particle in sphere model approximation to the bulk Wannier Hamiltonian.[35, 36] According to the approximation, the lowest Eigenvalue in a quantum confined system is given by Equation 2.1[35]:

$$E_{g,QD} = E_{g,b} + \left(\frac{\hbar^2}{8R^2}\right)\left(\frac{1}{m_e} + \frac{1}{m_h}\right) - \left(\frac{1.8e^2}{4\pi\varepsilon_0\varepsilon R}\right) \quad \text{(Eq. 2.1)}$$

here the first two energy terms (E) are the bandgap energies of the quantum dots and bulk solid, respectively. R is the quantum dot radius, m_e is the effective mass of the electron in the solid, 'e' is elementary charge of the electron, '$\hbar$' is Planck's constant, the m_h is the effective mass of the hole in the solid, and 'ε' is the dielectric constant of the solid. The middle term and the last term represent the exciton of a 'particle-in-a-box-like' and Coulomb attraction of the electron-hole pair, respectively. As we can see, E_g of QDs is correlated with the size. As the dimension (R) decreases, the bandgap energy increases. In other words, the smallest QD will emit light with the shortest wavelength (highest energy) as governed by the bandgap.[37] Hence, the photoluminescence (PL) colors of QDs can be tuned by controlling the particle radius.[38, 39] This also means that fluorescence spectroscopy can be utilized to determine the relative size and size distribution of QDs using the emission wavelength, where the relative size distribution is determined by the full-width-at-half-maximum (FWHM) of the emission peak.[40] **Figure 2.1** shows the size-dependent photoluminescence of semiconductor nanocrystals throughout the visible region of the electromagnetic spectrum.

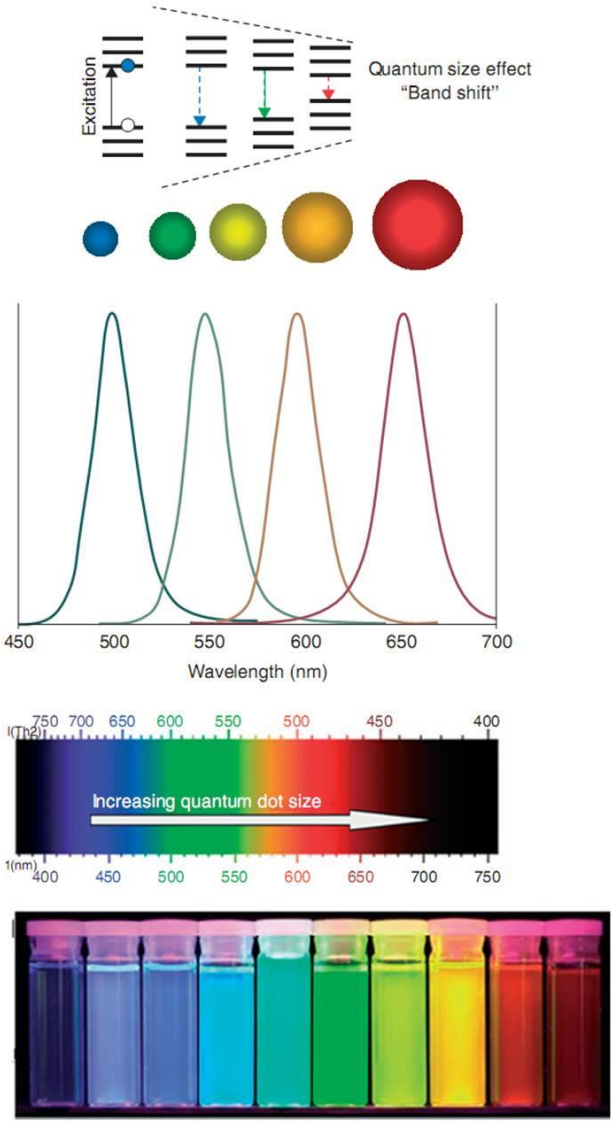

Figure 2.1 Size-dependent PL colors of semiconductor QDs. Electronic structure of QDs correlated with the QD radius and resulting 'blue shift' due to quantum confinement. Reproduced with permission from Ref. [41] – Copyright: Wiley VCH.

Despite the fact that size control of QDs in a given synthesis procedure should allow for different peak emission wavelengths as expected from the bandgap approximation, problems associated with the surface of QDs known as "surface traps" often cause emission at wavelengths higher than expected. In QDs with very high surface-to-volume ratio, these

surface traps are due to imperfections (surface defects) and dangling bonds. Such surface trap sites have their electronic energy states, which are usually localized within the QD's bandgap.[41] This concept was first suggested by Efros and Rosen.[42] Defects on the surface of the QD act as temporary surface traps for an electron or hole (i.e. a charge carrier), leading to non-radiative relaxation, therefore preventing radiative recombination that greatly reduces the quantum yield (**Figure 2.2**).[41] The resulting low fluorescence quantum yield, broad fluorescence range and blinking due to the charge recombination pathway are among major problems in utilizing QDs for optical applications. A review by Carrillo-Carrión and co-workers elaborated on QD luminescence and the important aspects affecting the photoactivation of QDs.[43] One approach to minimize the negative effects of surface traps and increasing quantum yields in QDs is composition of two or more semiconductors or doping one semiconductor with a small quantity of another metallic or semiconductor element. Combination of two or more semiconductors forming heterojunctions in so-called 'core-shell' semiconductor QDs can diminish the instability caused by the abundance of surface states.[44-48] In these core-shell systems, a semiconductor QD core is surrounded by another semiconducting material with wider bandgap as a shell to passivate the surface states of the nanocrystal (**Figure 2.2**). However, the surface trap phenomenon is not always a disadvantage for QDs. One can selectively use controlled trap states to tune the emission of QDs. A bifunctional linker molecule, such as 3-mercaptopropionic acid (MPA), assists in joining the two semiconductors close together with a uniform coverage.[25, 49, 50] By varying the alkyl chain length of the linker molecule, it was shown that electron injection yields increase with decreasing inter-particle separation[51] (**Figure 2.3**). Thiols, such as MPA, or other ligands noticeably alter the

chemical and physical states of the quantum surface and affect photophysical properties of semiconductor QDs by interacting with surface atoms.[52-54]

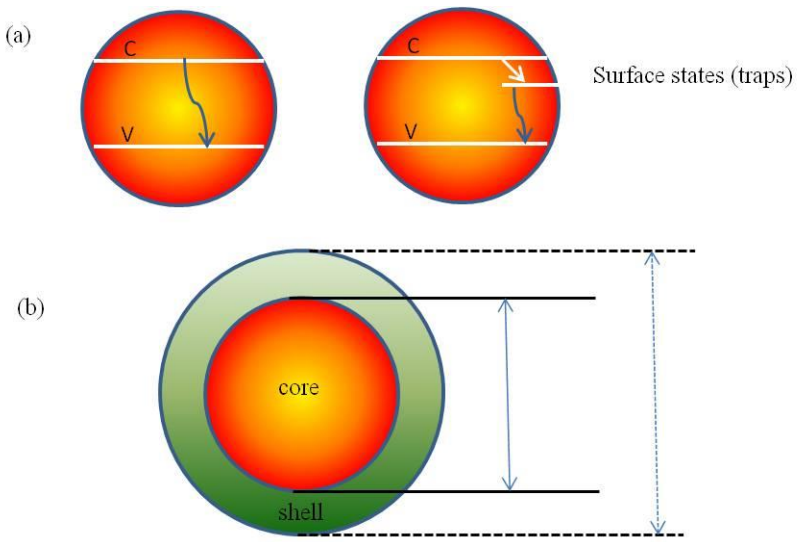

Figure 2.2 (a) Schematic representation of surface trap sites and their effect on quenching PL. Adapted from Ref. [50] – Copyright: American Chemical Society. (b) Electronic structure of a core-shell quantum dot made of two semiconductors forming a heterojunction (core surrounded by the shell of a wider bandgap). Adapted from Ref. [41] – Wiley VCH.

In addition, doping of semiconductors nanocrystals with transition-metal ions or other semiconducting elements is another alternative approach to modulate the electronic and optical properties of QDs. Such approach, in addition, can introduce exotic magnetic and magneto-optical properties in QDs.[55] For instance, doping of non-magnetic CdSe QDs by Mn^{2+} leads to formation of diluted magnetic semiconductors (DMSs).[56] These doped nanocrystals are showing interesting phenomena such as the giant Zeeman splitting of electronic states and carrier-induced ferromagnetism arising from the *sp-d* exchange

interaction between the transition-metal ions and the electronic states of the host semiconductor.[55, 57, 58]

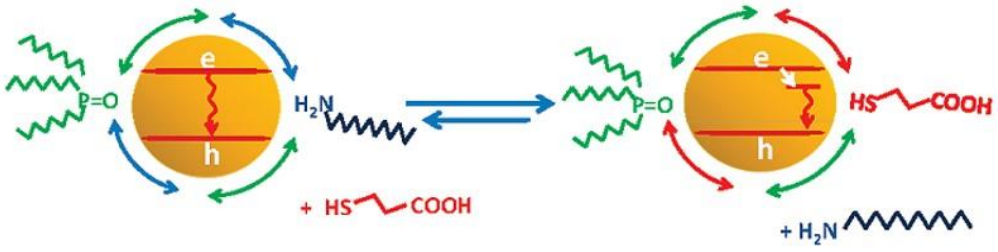

Figure 2.3 Exchange of dodecylamine with 3-mercaptopropionic acid and its effect on charge recombination dynamics of TOPO-capped CdSe QDs. Reproduced with permission from Ref. [50] - Copyright: American Chemical Society.

2.2.1 Synthesis of colloidal quantum dots

Synthesis efforts to obtain QDs focus on the preparation of QDs with highly desired monodispersity and uniformity of shape (i.e. with narrow FWHM). In the early 1980s, syntheses of QDs in aqueous solutions resulted in broad size distributions of the particles, often characterized by poor luminescence efficiencies.[59-61] In 1993, Murray and co-workers for the first time[62] synthesized high-quality, monodisperse chalcogenide QDs at high temperature. However, in their method a toxic, unstable and expensive precursor like dimethyl cadmium was used. Since then, many attempts have been made to develop methods without such drawbacks. Aqueous phase synthesis (mainly at high temperatures), vapor phase deposition, microwave-assisted syntheses, Langmuir-Blodgett films, polyol methods, and sol-gel process are the most common synthetic methods for QDs which have been discussed along with following surface modifications for different applications in some recent reviews.[12, 16, 26, 59, 63, 64]

Ligand selection is one of important aspects having a considerable effect on QD quality. Many approaches have been reported where the nature and concentration of the ligand, ratios of precursors, controlled nucleation and growth time, and tuning the temperature led to stable QDs with high photoluminescence efficiencies. Yu and co-workers have reported several syntheses of a series of single-sized CdSe nanocrystals by choosing distinct precursors in various ratios as well as careful ligand choice and adjusted reaction media.[65, 66] These so-called magic-sized nanocrystals (MSNs) have sharp absorption and strong bandgap PL.[67] A wide variety of molecules such as trioctylphospine, trioctylphosphine oxide and trioctylphosphine selenide,[32, 62, 68-70] thioglycolic acid, tiopronin, glutathione,[71] l-cysteine ethyl ester hydrochloride,[72] oleylamine,[73] and polyethylenimines of various molecular weights[74] served as successful ligands for the synthesis of QDs with high PL quantum yields.

Template-based syntheses of QDs, mainly using lytropic LC (LLC) phases is a fascinating topic relevant to the scope of this article to point out some of the most prominent approaches on the synthesis of QDs in liquid crystal media. Liquid crystalline materials naturally exhibit space partitioning and organization making them a suitable medium for the synthesis of many nanostructures. Utilizing LCs as templates for the synthesis can offer remarkable advantages including the ability to control the size and shape of nanomaterials simultaneously by choosing different mesophases and LC compositions. This can be a very versatile pathway for synthesizing semiconductor nanocrystals, and a precise tool to tune their optical and electronic properties as well as their overall functionality for potential applications.[75] Among the different LC materials and phases, LLC phases namely, lamellar, columnar and cubic, have been frequently reported in the literature due to broad

variety of LLC phases which can be organized by various amphiphilc molecules in a well-chosen solvent. The leading synthesis of QDs in LLC phases was reported by Braun and co-workers in 1996.[76] They demonstrated that CdSe and CdS superlattices can be formed in LLC phases formed by a nonionic organic amphiphiles in water using a semiconductor precursor. Their results showed that the nanostructures followed the symmetry of the hexagonal LC medium.[76] Inspired by this work, several groups utilized this approach to fabricate metal[77-79] and semiconductor NPs such as CdSe,[80, 81] CdS,[82] ZnSe,[83, 84] ZnO,[85, 86] and ZnS[87] in LLCs. Among these, the work carried out by Mountziaris et al. for the formation of ZnSe nanostructures seems the most intriguing.[83] They have shown that by using cubic, hexagonal and lamellar phases of LLCs in self-assembled ternary systems consisting of a block copolymer as the surfactant, hexane and formamide as non-polar and polar phases, respectively, ZnSe nanostructures of different morphologies could be obtained. More precisely, QDs, nanowires and nanodisks of ZnSe were successfully synthesized using cubic, hexagonal and lamellar LLCs as templates.

Another interesting topic related to the synthesis of QDs is the post-synthesis surface modification of QDs for designated applications. Different surfaces or ligands on QDs can induce different physical and chemical behavior, and it is often necessary for the surface to be pre-modified for a particular application.[88] Silica encapsulation is one of the most interesting and facile approaches to obtain QDs with characteristic properties such as water solubility, buffer stability, photo-stability, and the prevention of aggregation frequently occurring in colloidal nanoparticle solutions due to ligand dissipation.[89, 90] The latter advantage can be very critical for making robust QDs for the use in LC nanocomposites.

There are many reports on the silica coating of QDs via reverse microemulsion[91-97] and Stöber methods.[96, 98-101]

2.3 Alignment of QDs in liquid crystals

As mentioned earlier, LC-QD composites can have mutually beneficial effects on both optical and electro-optical properties of LC materials as well as on the collective spectroscopic, dynamic and electronic properties of particulate semiconductor QDs. In this section we will focus on the latter topic. Unique properties of as-synthesized colloidal semiconductor nanoparticles that originate from the quantum confinement effect can be harnessed for various applications if one can organize QDs in well-defined morphologies with both control over the orientation and inter-nanoparticles interactions and distances.[102] Only then can QDs exhibit well-defined collective properties due to coupling of discrete energy states. For instance, coherent coupling of discrete electronic and excitonic states is the main topic in quantum computational research,[102, 103] while incoherent long-range energy-transfer mechanism in close-packed assemblies can be useful in photovoltaic devices.[19, 104]

However, realizing organized arrays of QDs and manipulating the formed assemblies seem challenging in practice because of insufficiencies arising from improper solvents and suitable conditions for assembly, causing formation of unwanted aggregations of nanoparticles. Other detrimental factors are the low monodispersity and the inadequate solubility of QDs. It has been shown that the LC materials can be a very promising medium for assembly and alignment of a variety of nanostructures with fascinating results (see

earlier reviews highlighted in the introduction). The LC materials are self-organized fluids in which the constituent molecules with diverse molecular structures and shapes possess long-range orientational order in one, two or three dimensions, producing a variety of mesophases depending on the temperature (in thermotropic LCs) or their concentration in solution (in lyotropic LCs).

Among the various liquid crystalline phases, the most widely used and well-studied are thermotropic nematic (N-LC) and smectic (Sm) phases (**Figure 2.4**). Also, mostly these phases have been used as hosts for QD dopants, as described in this article. In N-LCs as depicted in **Figure 2.4 a**, all molecules tend to align along one selected direction called the director. The chiral nematic or cholesteric phase (N* or CLC), produced either by chiral nematogens or by addition of a chiral additive, is characterized by a continuous chiral (helical) distortion of the director along the long molecular axis. Smectic phases consist of layers of molecules. In the smectic A phase, molecules are aligned perpendicular to the boundaries between layers; in the smectic C phase molecules are tilted with respect to the layer normal (**Figure 2.4 b-c**). If the molecules in a smectic C liquid crystal are chiral, or if a chiral dopant is added, it can display ferroelectric (if molecules in every next layer are rotated slightly with respect to the previous layer) or anti-ferroelectric (when the tilt is reversed from layer to layer) properties.

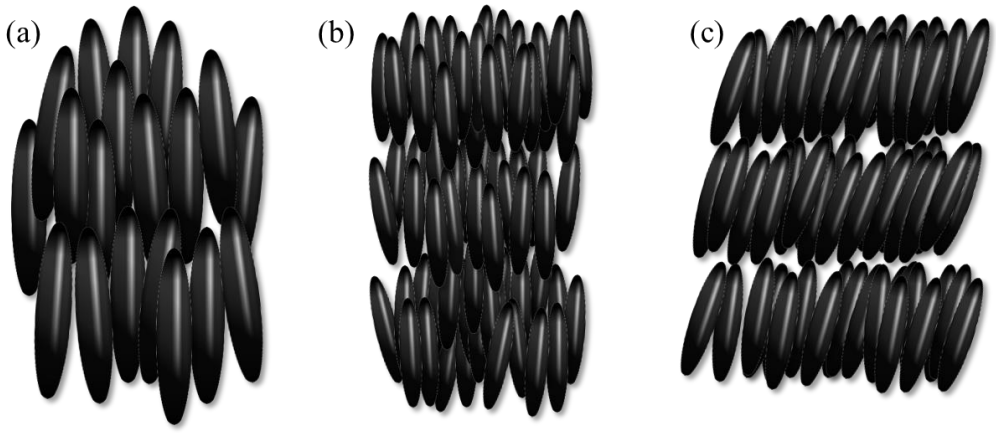

Figure 2.4 Liquid crystalline phases: (a) nematic; (b) smectic A; (c) smectic C

LC materials are also optically anisotropic and therefore are usually birefringent. Their anisotropy allows for the creation and manipulation of macroscopic domains with a defined optical axis, for example, by inducing anisotropy on ordered/pre-treated substrates confining the liquid crystalline sample. Moreover, the molecular orientation in most LC phases can be further controlled reversibly by an external force like electric or magnetic fields. In particular, an applied electric field induces a reorientation of the molecules in certain LC phases (e.g., N, N*, SmC*, and others), leading to the collective switching of the LC sample by the *E*-field. In turn, anisotropic ordering of LCs can translate order to nano-sized guest particles, and an external force can selectively reconfigure the assembled array. Some of the recent papers on assembly of semiconductor QDs and nanorods as well as on tuning their electro-optical properties by LCs are summarized in **Table 2.1**.

Table 2.1 Examples of QDs arrays in LC media.

Semiconductor	Shape / Size(s)	LC(s) / Phase(s)	Effect(s)	Ref(s).
GaSe	Disk-shaped / 2.5-12 nm in diameter; thickness: 0.8 nm	5CB / nematic	Increasing inter-particle coupling in assembled aggregates of GaSe, *E*-field in-plane reorientation of arrays	105, 106
CdSe/ZnS (core-shell)	Spherical / ~1.2 nm and ~5 nm – core and shell diameters, respectively	Cholesteryl oleyl carbonate (COC) (60 wt%) and 5CB (40 wt%) / cholesteric	Modulation of spectral emission of QDs embedded in CLC	106, 107
CdSe	Spherical / 3-6 nm	5CB / nematic 5CB + COC / cholesteric 8CB + chiral ferroelectric material AIS179	Dispersions of QDs with respect to particle surface and concentrations, Pattern formations in different phases and potential assembly of QDs	108
CdS	Spherical / 2.3 nm	5CB / nematic	Formation of one-dimensional chain-like arrays, larger dielectric constant for doped sample	109
GaSe/InAs	Spherical / size not specified (QDs are embedded in fabricated microdisks)	5CB / nematic	Thermal and *E*-field induced tuning of photonic modes of microdisk device containing QDs	110
GaSe	Spherical / 8 nm	8CB / smectic A	Alignment of aggregates of QDs in LC	111
CdSe	Spherical / 2.4, 2.6 and 3.2 nm	Polymerizable poly[4-(n-acryloyloxyalkoxy)]	Formation of aligned layers of CdSe nanocomposites via surface modification	112, 113

		benzoic acid (BA-*n*PA) / smectic C_A	of QDs by hydrogen-bonded LC polymer (LC-decorated ligand)	
CdSe/ZnS (core-shell)	Spherical / 4 nm	E7 + chiral dopant + LC diacrylate monomer + gelator / cholesteric	Modulation of photoluminescence of QDs using *E*-field	114
CdSe/ZnS	Spherical / 6.2 nm	Commercial nematic LC + chiral dopant + azobenzene / cholesteric	Light-induced switching of QDs photoluminescence	115, 116
CdSe	Spherical / 4.1 nm	E7 mixture / nematic	Modulation of coupling between excitonic state of QDs and surface plasmon band of gold nanoparticles	117
CdSeTe	Spherical / from Qdot® 800 ITK™	Left-handed oligomeric cyclosiloxane / cholestric	Tuning QDs emission in CLC phase	118
InGaAsP	Not mentioned	5CB / nematic	Optical and thermal tuning of photonic crystal nanocavities	119
CdSe	Spherical and rod-shape	E7 mixture / nematic	Self-alignment of QDs and nanorods	120
CdSe	Spherical / 5 nm rod-shape/ 7 nm × 25 nm (diameter and length, respectively)	E7 mixture / nematic	Orientation of QDs and semiconductor nanorods along the LC molecules orientation and impact on emission under *E*-field	121
CdS	Rod-shape / 5 nm × 40 nm	E7 mixture / nematic	Alignment of nanorods using *E*-field	122
CdSe	Nanotube / 200 nm × ~ 60 μm	E7 mixture / nematic	Alignment of nanotubes and increasing emission anisotropy	123
CdSe/ZnS	Rod-shape / two types: 3 × 25 nm 7 × 50 nm	5CB / nematic	Alignment and effects on photoluminescence of nanorods	124

ZnS, PbS	Rod-shape/ ZnS, 1.2 nm × 5 nm PbS, 1.7 nm × ~13 nm	Commercial LC mixture (ZLI-4792) / nematic	Alignment of nanorods along the direction of the *E*-field and effects of nanorods on switching behaviors of nematic LC	125

In most of these articles, the authors demonstrated effective self-assembly of quasi-spherical QDs or nanorods induced by the LC medium. An exceptional example is the work of Basu and Iannacchione,[109] who demonstrated the assembly of CdS QDs into nanoscale macroscopic chain-like configurations (**Figure 2.5**).

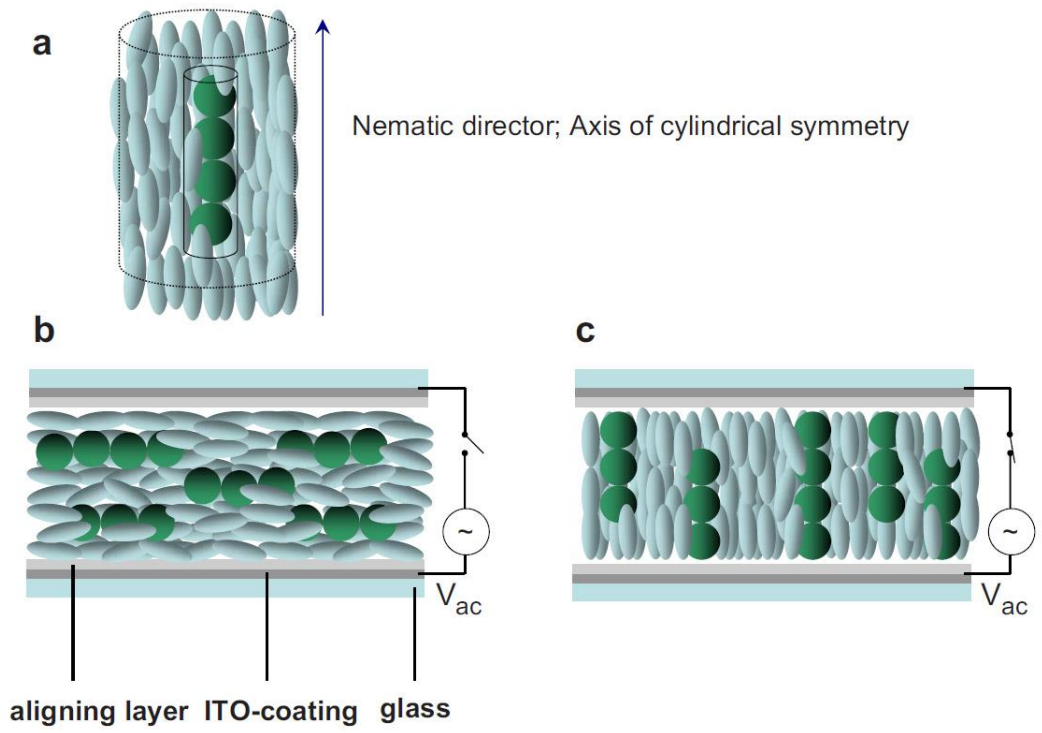

Figure 2.5 Self-assembly of CdS QDs in the 5CB nematic host as a function of applied electric field: (a) symmetry of the QDs chain aggregates in the nematic phase; (b) QD aggregates in the nematic host below the Fréedericksz transition; (c) switching of the QDs aggregates by the electric field above the Fréedericksz transition. Reproduced with permission from Ref. [109] – Copyright: American Physical Society.

The authors used indirect techniques to demonstrate the presence of anisotropic assemblies by measuring dielectric properties and the relaxation times of the LC-QDs colloidal mixture. It was shown that doping nematic 5CB with CdS QDs led to longer relaxation times, which could not be explained by simple increase of the material's viscosity due to very low concentrations of the dopant. Therefore, slower relaxation is explained by presence of long anisotropic "pearl-necklace" strands made of QDs. Also, measurements of the dielectric anisotropies of the colloid below and above the Fréedericksz threshold in comparison with pure 5CB demonstrated considerable changes in the dielectric response due to the presence of the QDs. This result points to the existence of highly anisotropic structures aligned along the director of the LC. Measuring the dielectric response of the same materials at elevated temperatures above the clearing point of the LC showed that the QDs in the absence of the ordered nematic matrix are probably homogeneously distributed and do not form self-assembled arrays. Another example of the assembly of QDs in nematic 5CB has been discussed by Ghosh and co-workers.[105-107] They have shown that nanodisks of GaSe at concentrations up to 10% assemble into ordered aggregates each composed of 15-60 GaSe nanodisks in the nematic phase of 5CB.[105, 106] Emission spectra, optical textures and size distribution of GaSe clusters in the N-LC mixture are shown in **Figure 2.6**.

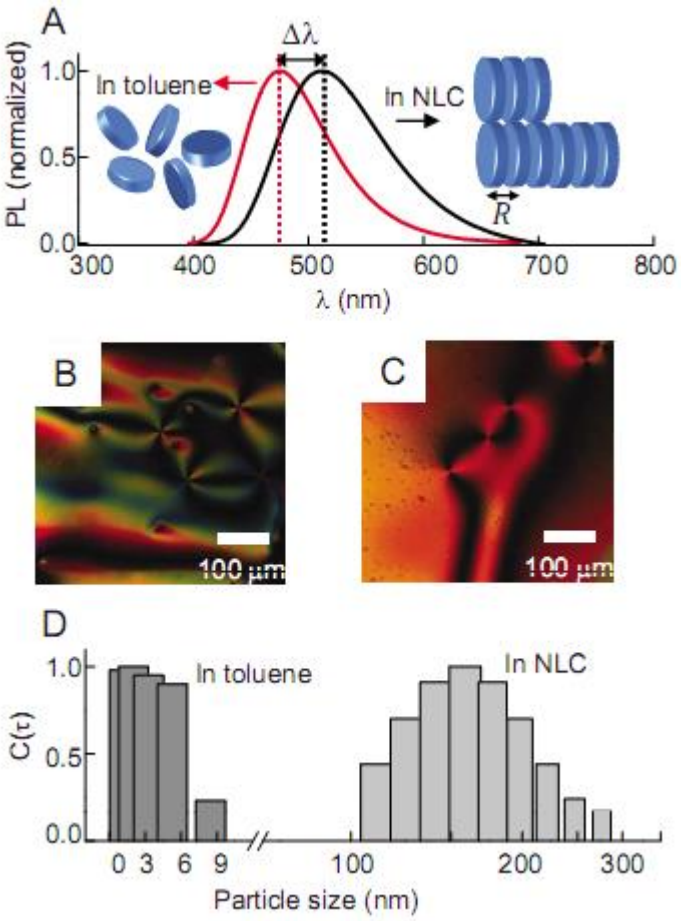

Figure 2.6 (a) Comparison of normalized photoluminescence spectra of QDs in toluene and in N-LC matrix. The emission of the latter is red-shifted by $\Delta\lambda$ = 37 nm. Optical texture of the nematic phase imaged with polarized optical microscopy for (b) unaligned pure N-LC, (c) unaligned mixture of N-LC with QDs 30:1 by volume confirming the nematic phase in the mixture by showing typical Schlieren texture. (d) DLS exhibits small particles in the range of 1-9 nm for pure GaSe nanodisks in toluene, whereas formation of clusters on the order of hundreds of nanometers in the N-LC. Reproduced with permission from Ref. [105] – Copyright: American Physical Society.

Their investigation using spatially and polarization-resolved PL spectroscopy coupled with confocal microscopy not only revealed the spatial distribution and orientation of nano-sized aggregates but also showed the effect of a well-defined director configuration of the N-LC in the mixture sandwiched between rubbed polyimide coated films as well as an

applied in-plane electric field on the inter-dot-dependent intensity of the emitted light by QDs aggregates in the N-LC mixture (**Figure 2.7**). The wavelength and polarization analysis of the emission maps indicated strong anisotropic absorptions and emissions emerging from the assembled stacks of QDs in the N-LC while the QD-toluene samples remained isotropic.

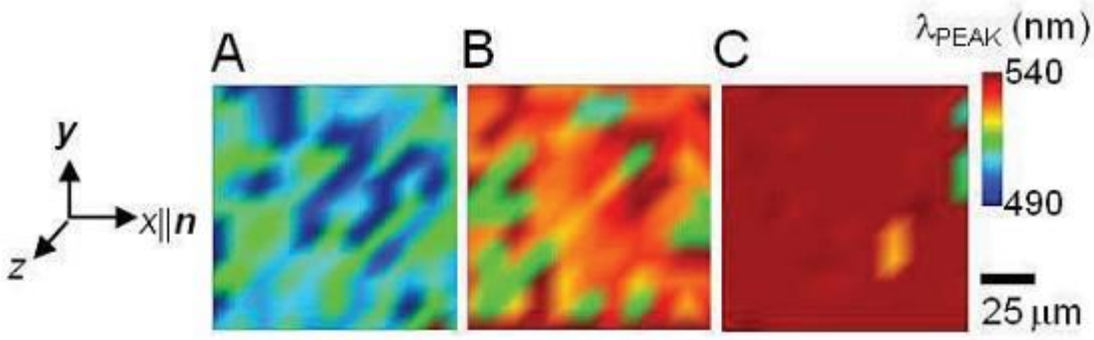

Figure 2.7 (a) Spatially-resolved PL map of QD-LC mixture showing emission in the range of 500-515 nm when N-LC is unaligned. (b) Red-shifting up to 520-530 nm of the same sample when the N-LC is aligned with the director axis along x using a thin coating of rubbed polyimide but no electric field. (c) Further red-shift to 540 nm when an electric field of 0.8 V/μm is applied along the x axis. Reproduced with permission from Ref. [105] – Copyright: American Physical Society.

Following their research on QD-based optical materials, Ghosh and co-workers have also studied composites of core-shell CdSe/ZnS QDs emitting at 609 nm with an LC host material showing a cholesteric phase.[107] This cholesteric mixture was composed of 60% cholesteryl oleyl carbonate and 40% of nematic 5CB and exhibited a cholesteric pitch of about 600 nm at 25 °C. They selected this type of QDs in such way that the emission has a significant overlap with the reflection stop band of the CLC. In these experiments Cano-

wedge cells were used in which CLCs show textures known as Grandjean steps under polarized light due to formations of different pitch lengths (**Figure 2.8 a and b**). Their results are indicating that CLC phases can be utilized as one-dimensional photonic band-gap material which enable tuning of the emission of assemblies of QDs by spatially changing the pitch of a CLC host using these wedge cell (**Figure 2.8 c and e**).

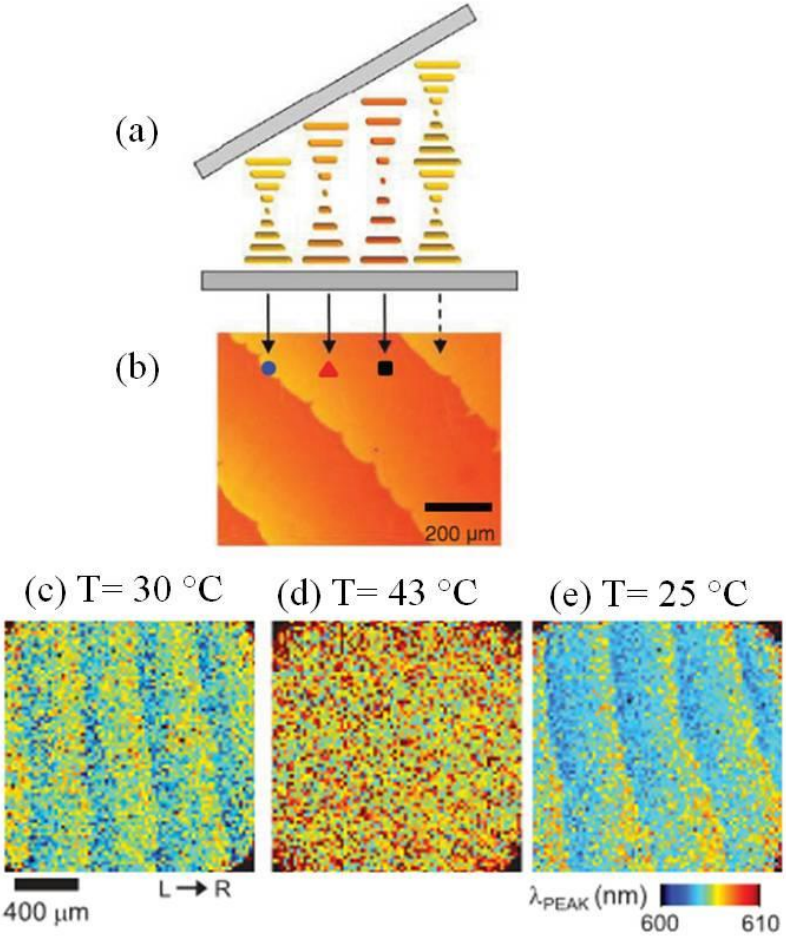

Figure 2.8 (a) Schematic drawing demonstrating the helical arrangement of the CLC in a Cano-wedge cell. (b) Polarized optical microscopy transmission image of the CLC. Spatially-resolved PL scans of QD-CLC mixture at: (c) 35 °C shows that emission of QDs varies across the sample film following the Grandjean step pattern of the cholesteric phase, (d) when heated to 43 °C systematic wavelength gradient disappears due to random distribution of QDs in isotropic mixture, and (e) when it cools back to 25 °C QDs emission gradient reforms. Adapted with permission from Ref. [107] – Copyright: American Physical Society.

As it was mentioned in section 1.5, chiral nematic or cholesteric LCs can be seen as a stack of layers of molecules with an orientational order, rotating each layer with a constant angle with respect to its neighbouring layer. The periodicity of this arrangement results in an alternating modulation of the refractive index, creating a one-dimensional photonic band-gap material.

In another study, both the mechanism of QDs alignment using an anisotropic LC medium and the possibility for the fabrication of multifunctional switchable devices have been explored.[108] In general, QD self-assembly in LCs depends on particle surface properties and concentration in the LC medium. The authors observed interesting structures and a phase behavior in nematic, cholesteric and smectic LCs by varying these parameters using polarized optical microscopy and fluorescence microscopy.

While higher concentrations of QDs led to the appearance of large fractal-shaped aggregates, lower concentrations did not tend to aggregate, but still affected the LC host. In particular, in the cholesteric phase, adding QDs led to a change in a helical pitch. In order to study QD pattern formation, the authors compared images of the same LC-QDs sample taken by polarized and fluorescence optical microscopy (**Figure 2.9**). The formed QDs pattern did not coincide with the defect walls in either the nematic or the cholesteric phases. This suggests that the observed QD patterns (marked by lines in **Figure 2.9 c and f**) resulted from the phase transition of the LC host from the isotropic phase to the nematic/cholesteric phase, i.e. the QDs remained in the isotropic islands, where they are better soluble, for as long as possible during the phase transition until the isotropic islands disappeared. Then, QDs form a network of QD-rich areas in the sample, leaving an 'image' of the growth pattern of the LC phase from the isotropic.

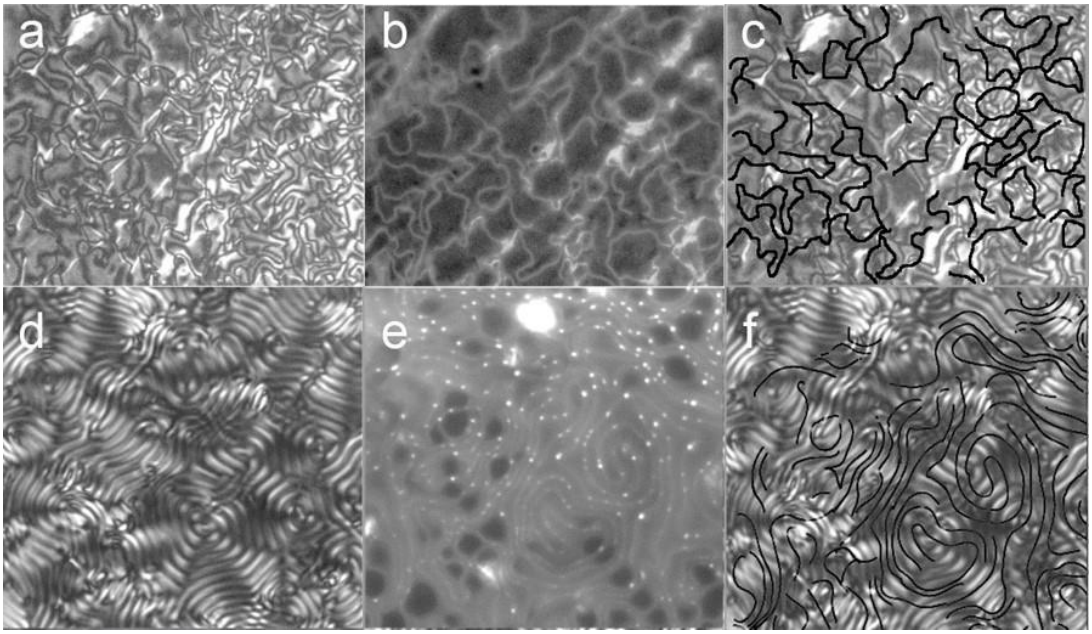

Figure 2.9 Images of nematic (a-c) and cholesteric (d-f) phases doped with QDs. Images (a) and (d) that show LC texture are taken using polarized optical microscope; images (b) and (e) were taken using fluorescence optical microscope thus showing localization of the QDs in the LC host; images (c) and (f) are the overlays of both images shown for comparison with the overall QD distribution marked by lines to demonstrate where the QDs are with respect to the LC texture. Lines are intended to guide the eye. Each set of images represents the same sample area. Reproduced with permission from Ref. [108] – Copyright: SPIE.

2.4 Modulating liquid crystals via QD doping

Over the last decade, along with continuing efforts focusing on the creation of novel metamaterials and devices based on assembled arrays of semiconducting nanoparticles in LC nanocomposites, there has been a steady increase in the number of articles describing the use of nanomaterials as additives in LC phases. Zero- and one-dimensional nanomaterials with metallic, semiconducting, ferromagnetic, or ferroelectric

characteristics have been investigated in mixtures with LCs for optimizing optical and electro-optical properties of the host LC and in some cases applications in device and display industries are emerging. Dispersions of different types of nanomaterials, particularly metallic NPs, in LCs were discussed earlier. For more in-depth information, a reader should refer to the following review articles.[1-3]

In the following section we will only review mixtures of LCs with semiconductor nanoparticles. Semiconductor QDs and nanorods can impact optical and electro-optical properties of LCs and, depending on their elemental composition, can potentially induce several new effects, unlike those seen in the well-studied metallic nanoparticle LC colloids. Aside from the fact that QDs are a new promising platform for research on modulating LC properties, they also facilitate LC-NP research by providing two advantageous tools in understanding the intriguing interactions between molecules of an LC host and nanoparticles. First, the size-dependent photoluminescence of QDs allow, in principle, the use of size-separated batches containing predominantly monodisperse QDs. This can be very important in systematic investigations of LC-NPs interactions, since a comprehensive understanding of many puzzling effects requires the change of only one NP parameter at a time (similar to all other structure-property relationships in LCs), such as NP size (average size and size distribution), while the other parameters like NP composition and surface functionality are kept unchanged. It is worth pointing out that despite the fact that there have been significant advancements in syntheses of metallic and semiconducting NPs, obtaining series of these particles varying in one parameter only, such as size or surface is still practically challenging in cases when pure and stable NPs are required for maximal LC property optimizations. Overall, QDs seem the better candidates compared to other

types of NPs in terms of synthesis versatility and size homogeneity. Another rational for the advantage of QDs over metallic NPs is the wide variety of available QD compositions as highlighted in the synthesis section above.

The second advantageous point in doping LCs with QD is also related to their size-dependent emission when photoluminescence measurements coupled with confocal polarized microscopy techniques are used as an analytical tool to trace the distribution and orientation of QDs in the LC host (i.e. fluorescence confocal polarizing microscopy, FCPM). These techniques allow for a much more detailed picture of the spatial distribution and optical defects of QDs in LC.

Despite such promising features, examples of modulating LC properties using QDs are still rather rare in comparison to their metal-based NP counterparts. The increasing number of examples using QDs as additives in LCs shows the great promise and capacity of this field. **Table 2.2** summarizes recent articles on the topic. The discussion here will be limited to those QDs capped mainly with aliphatic amines and phosphine, thiols and fatty acid. Because of their hydrophobic nature and better solubility in organic solvents, these QDs are likely of more interest due to their predicted better dispersibility in LC phases composed of rod- or disc-like molecules featuring flexible alkyl chains.

Table 2.2 Examples of QDs as additives in LC media.

Semiconductor	Size(s) / Surface ligand	LC(s) / Phase(s)	Effect(s)	Ref(s)
CdTe	3.5 nm / mixed thioglycolic acid and hexane thiolate 4.1 nm / mixed thioglycolic acid dodecane thiolate	Felix-2900-03 / nematic 8CB / nematic	Effects of concentration of QDs on optical properties, dielectric anisotropy ($\Delta\varepsilon$) and threshold voltage (V_{th}) of N-LC	126
CdSe	2.5, 3, 3.5 4.2 and 5 nm / hexadecylamine	Felix-2900-03 / nematic	Mainly homeotropic alignment with birefringent stripes in plain-glass slides and planar in EO cells, concentration and size-dependent effects on V_{th}	127
CdTe	3.2, 3.4, 3.7 and 4 nm / thioglycolic acid	Felix-2900-03 / nematic	Planar alignment in plain-glass slides and in EO cells, concentration and size-dependent effects on V_{th}	127
CdSe	5 nm / hexadecylamine	Felix-2900-03 / nematic	FCPM studies of optical texture of LC-QDs film in plain-glass slides	128
CdSe CdSe@Zn	2 nm / myristic acid (two types with different defects) 2 nm / myristic acid (doped with Zn)	Felix-2900-03 / nematic	Effects of different core composition and surface defects in QDs on EO properties of nematic LC at different concentrations and temperatures	129, 130
CdSe	4 nm / TOP and TOPO	1658 LC mixture / nematic	Enhancing diffraction efficiency in nematic LC cells	131

CdSe/ZnS	4.5-6 nm / fatty acid	Cyanobiphenyl-based mixture / nematic	Lower switching voltage for planar to homeotropic transition in the cell	132
CdSe/ZnS	~3.5 nm / TOPO	Cyanobiphenyl-based mixture / nematic	Lower phase delay and dielectric permittivity values for doped samples	133
CdSe	2.4 and 3.5 nm / TOPO and octadecyl amine	Hexabutyloxytriphenylene (H4TP) discotic LC / hexagonal columnar	Investigation on phase behavior of mixtures of columnar LC with QDs	134
CdTe	2-7 nm / poly(3-hexylthiophene) (P3HT)	Various ferroelectric LC (FLC) materials / SmA* and SmC*	Charge storage, electro-optical modulation and reversing of alignment in QDs doped FLC	135-137
ZnS	~2-7 nm / 3-mercaptopropenoic acid	KCFLC 7S, LC (FLC) / SmA* and SmC*	Effects of QDs on photoluminescence of FLC	138
ZnO	7 nm / not specified	KCFLC 7S, LC (FLC) / SmA* and SmC*	Lowering of switching voltage and improving optical behavior in doped FLC	139

Since 2004 Dr. Hegmann's research group at the Department of Chemistry, University of Manitoba has been actively engaged in systematic studies of optical and electro-optical effects of different NPs namely Au, Ag, CdSe and CdTe QDs of various sizes and with multiple surface functionalities in nematic, smectic and columnar LC materials. In 2008, they reported that mixtures of two types of CdTe QDs of two different sizes (3.5 and 4.1 nm) capped with a mixed monolayer consisting of thioglycolic acid and hexane or dodecane thiolate, respectively, in nematic 5-n-heptyl-2-(4-n-octyloxyphenyl)-pyrimidine (Felix-2900-03; **Figure 2.10**) and 4-octyl-4'-cyanobiphenyl (8CB) showed lower threshold

voltages, V_{th}, and altered dielectric permittivities ($\varepsilon_{\parallel}$ and $\varepsilon_{\perp}$).[126] The results obtained from electro-optic measurements using these two CdTe QDs as additives indicated that the QDs with shorter alkyl chain length in the capping layer induced more pronounced effects regarding the electro-optic parameters of the N-LC used in comparison to other QDs and even gold NPs at the same size-regime.[126]

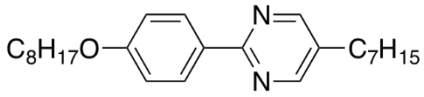

Felix-2900-03; Cr 52 (SmA 45) N 70 Iso

Figure 2.10 Chemical structure and phase transition temperatures of 5-n-Heptyl-2-[4-(n-octyloxy)-phenyl]-pyrimidine a nematic LC (Felix-2900-03) (Cr = crystalline solid, SmA = smectic-A phase, N = nematic phase, Iso = isotropic liquid).

In another study focusing on nematic LC-QD composites, data collected from optical as well as electro-optic measurements indicated that different LC-QD mixtures depending on the size, capping agent and concentration of added CdSe and CdTe QDs can have different alignment and electro-optic characteristics.[127] The five investigated CdSe QDs varied in size from 2.5 to 5.2 nm, and the four CdTe QDs sizes ranged from 3.2 to 4.0 nm. The miscibility of these QDs in Felix-2900-03 showed clear size-dependencies. Polarized optical microscopy (POM) studies of different concentrations of these QDs in Felix-2900-03, established that the mixture doped with 2wt% CdSe QDs in Felix-2900-03 favored homeotropic (vertical) alignment of the N-LC molecules with the commonly observed birefringent stripe patterns between plain glass slides and planar alignment in planar electro-optic cells (**Figure 2.11**). Samples doped with 1 wt% of CdSe showed homeotropic not only within plain glass slides but also in the planar cells, indicating that above 1wt%

these QDs began to aggregate also in the bulk, in addition to the segregation of the QDs to the substrates responsible for the induced homeotropic alignment (see below). In all LC-QD composites, decreases in the threshold voltage (V_{th}) and the splay elastic constant (K_{11}) were observed. The most significant reduction over the entire temperature range, however, was seen for the smallest QD, CdSe480 (2.5 nm in core diameter), which clearly showed the least tendency of all investigated QDs to aggregate in this nematic host (see **Figure 2.11**; aggregation is clearly visible for CdSe590 in the inset image of **Figure 2.11**d taken with parallel polarizers).[127]

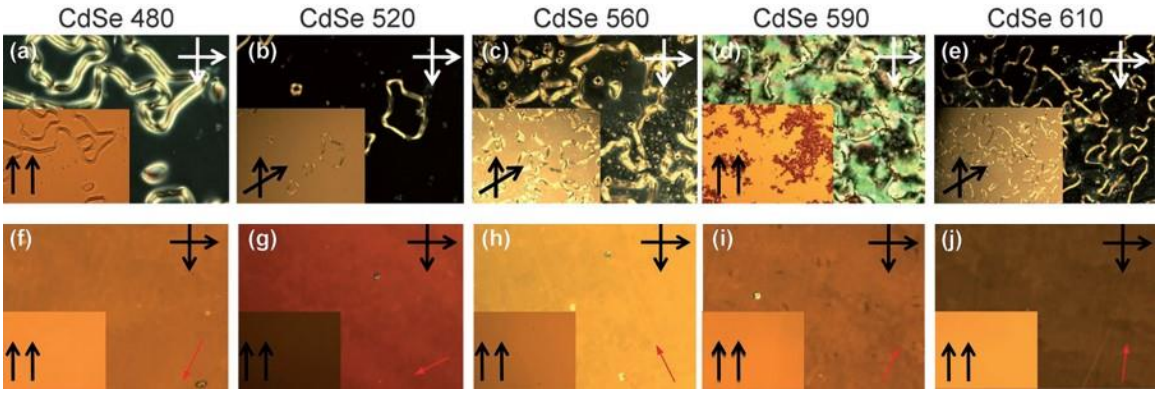

Figure 2.11 POM images of the 2wt% mixtures of CdSe480 – CdSe610 (numbers indicating the wavelength of the emission maximum) in the nematic phase of 5-*n*-heptyl-2-(4-*n*-octyloxyphenyl)-pyrimidine (Felix-2900-03) at $T_{Iso/N} - T = 9$ ˚C between plain glass slides (a–e) and in planar aligned cells (f–j). Red arrows show rubbing direction of the planar, rubbed polyimide coated ITO cells. The inset in each figure shows the same area with parallel (un-crossed) or slightly un-crossed polarizers. Reproduced with permission from Ref. [127] – Copyright: Royal Society of Chemistry.

The CdTe QDs in this series were capped with thioglycolic acid rendering the QD surface hydrophilic, i.e. soluble in water or alcohol/water mixtures. However, we were able to demonstrate that such hydrophilic-capped QDs can be dispersed in quasi non-polar N-LCs like Felix-2900-03 with two terminal hydrocarbon chains.[127] This would be indicative

of the fact that both the solubility and dispersibilty in an N-LC with flexible alkyl chains do not necessarily require a hydrophobic capping agent. POM studies of the CdTe doped samples containing lower concentrations of the QDs (up to 2 wt%), showed similar optical and alignment behavior in the nematic phase as pure Felix-2900-03 (planar alignment between plain glass slides and in rubbed polyimide EO cells, see **Figure 2.12**). Higher concentration (>2wt%) of CdTe caused small changes in V_{th} (lower values) and K_{11} for the mixture.[127] The results of POM studies of this type of CdTe QD were particularly surprising. It appeared that planar anchoring of the N-LC molecules to the QD surface induced by the hydrophilic capping favored planar alignment in thin films. This was in contrast to previously observed homeotropic alignment, independent of the thermal and electric field history, in mixtures with the same nematic host doped with CdTe QDs (4.1 nm, emission at λ = 620 nm) capped with a mixed monolayer of thioglycolic acid and dodecane thiolate,[126] similar to our frequently-used mixed monolayer-capped gold NP.[2, 140] These mixed monolayer CdTe QDs also decreased V_{th} values more significantly than the thioglycolic acid-capped CdTe QDs investigated later.[126]

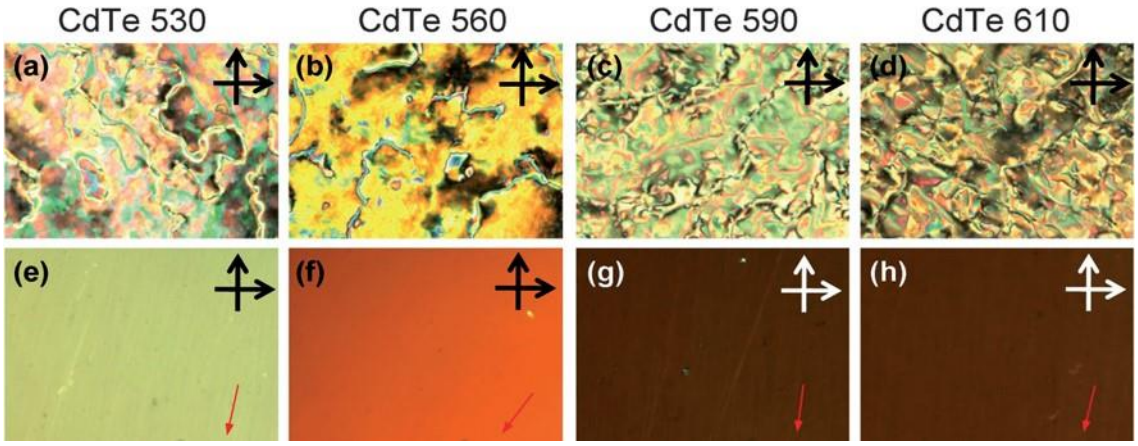

Figure 2.12 POM images of the 2wt% mixtures of the CdTe530 – CdTe610 QDs in the nematic phase of Felix-2900-03 at $T_{Iso/N}$ – T = 9 ˚C between plain glass slides (a–d) and planar aligned cells (e–h). Red arrows show rubbing direction of the planar cells. Mixtures at this concentration showed homogenous planar alignment similar to non-doped LC. Reproduced with permission from Ref. [127] – Copyright: Royal Society of Chemistry.

In the next chapter another series of QD-LC composites will be discussed. These new composites are based on the dispersions of three types of monodisperse CdSe QDs in nematic Felix 2900-03.

Two other examples of doping LCs with CdSe QDs, I wish to highlight are reports by Anczykowska *et al*. as well as Kumar and co-workers. The first group demonstrated how incorporating 4 nm CdSe QDs into a photoconductive polymer layer of a fabricated 5 µm cell as well as to the bulk of the LC can enhance diffraction efficiency of the nematic LC mixture.[131] It was shown that doping LCs with semiconductor QDs as well with metallic NPs could help to develop and optimize faster and more efficient holographic materials (**Figure 2.13**).

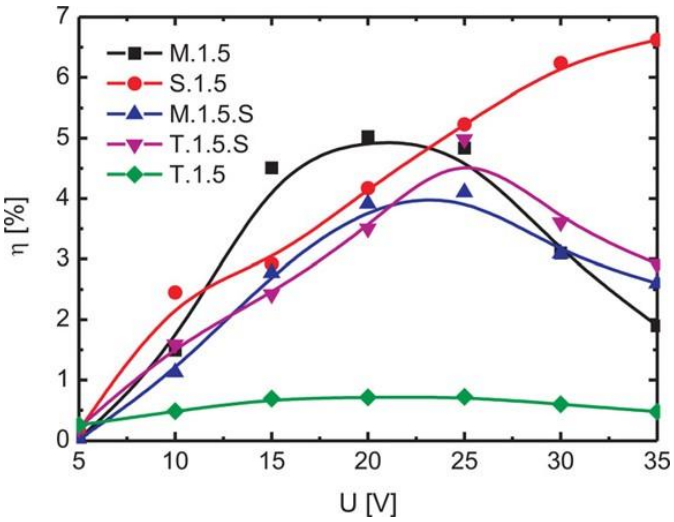

Figure 2.13 Comparison of experimental voltage dependencies of maximum diffraction efficiency for pure and functionalized liquid crystal structures. Green line corresponds to pure LC on un-doped photoconductive polymer; other lines correspond to doped LC and/or photoconductive polymers. Reproduced with permission from Ref. [131] – Copyright: American Institute of Physics.

Kumar and co-workers studied the effects of different concentrations of CdSe QDs (2.3 and 3.5 nm) capped with mixed-monolayer of TOPO and octadecylamine on the LC phase behavior of a discotic columnar phase formed by a triphenylene derivative (H4TP).[134] Their results including data obtained with SAXS measurements indicated that in all composites that form Col_h phase, mesophases remain largely undisturbed with the exception of a minor shift in transition temperatures. This is also supported by differential scanning calorimeter (DSC) thermograms as shown in **Figure 2.14**. Most notably, these composites exhibited an enhancement in the DC conductivity when compared with pure H4TP.

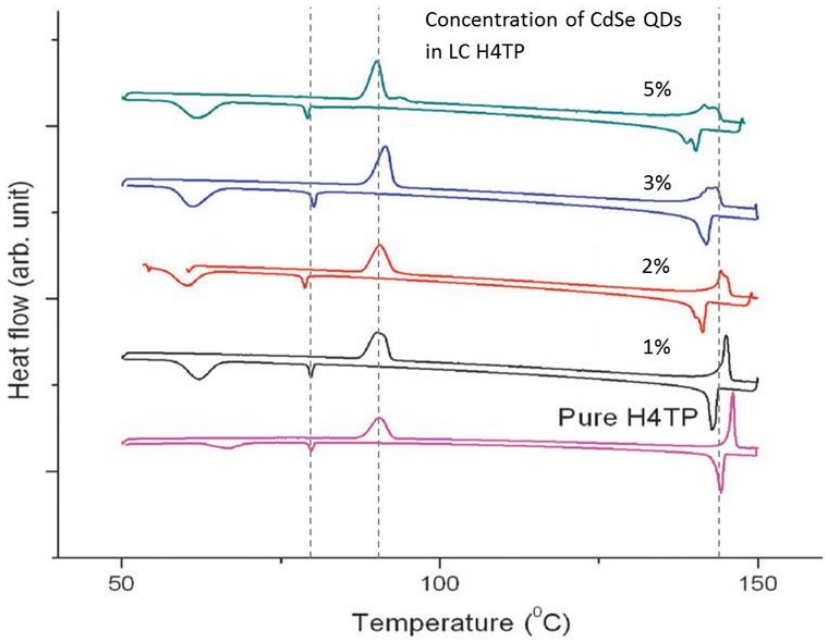

Figure 2.14 DSC thermograms of pure LC (H4TP) and composites with CdSe (2.3 nm) at various concentrations. Adapted from Ref. [134] – Copyright: Royal Society of Chemistry.

Other combinations of CdSe QDs in the form of core-shell semiconductor nanocrystals have been applied to LC composites as well. Two groups have used CdSe/ZnS QDs as dopants to modulate the electro-optical properties of the nematic phase of cyanophenyl-based mixtures. Here, a decrease in the ON and OFF switching times (rise and fall times)[132] with larger CdSe/ZnS (4.5 – 6 nm) as well as reduced V_{th} values, phase delay and dielectric permittivity[133] with smaller particles (3.5 nm) have been demonstrated separately.

Another emphasis of recent research dealing with LC-QDs colloids focuses on tuning ferroelectrics LC (FLC) materials by doping with QDs such as CdTe, ZnS and ZnO. Kumar and co-workers presented results on FLC-QDs composites publishing several papers in the field.[135-139] They presented and discussed concentration-dependent effects on dielectric and

electro-optical parameters of an FLC material after doping with CdTe QDs.[135, 136] The results indicated pronounced memory effects, enhanced values of physical parameters like spontaneous polarization and rotational viscosity at lower concentrations of CdTe QDs (1–3wt%) and changed alignment (at higher concentration of CdTe QDs, greater than 5wt%) in the doped-FLC material, similar to our alignment scenarios in nematic LCs.

These results may eventually have an impact on the practical application of FLC-based devices. Their fascinating properties such as bistability and ultrafast switching rates promised a great future, but due to numerous technological complications such as formation of chevron defects they were only able to occupy a niche area of micro-display LCOS devices. One of those complications is the necessity for very small cell gaps (<2 μm) to ensure a surface-stabilized mode that suppresses the intrinsic helix of the chiral SmC* ferroelectric phase. A possible advantage of QD-doped FLC materials is the possibility of using thicker cell gaps, as both memory effect and bistability are the result of interactions of the FLC molecules with the CdTe-QDs capped with poly-3-hexylthiophene (P3HT) in contrast to common surface stabilization. Both memory effect and electrical bistability depend on the QD capping agent that is in this case the conductive polymer P3HT. The application of a DC bias across the QD doped FLC layer induces charge transfer from FLC molecules to CdTe-QDs. The P3HT provides a low resistive path to the charges in reaching the QDs. The charge is stored in CdTe-QDs and can remain there for minutes after removal of the DC bias. This charge makes the nearby FLC molecules stay in the switched state, which leads to the memory effect. The FLC molecules form a helix in the SmC* phase and show a higher value of dielectric permittivity (ε') due to the contribution of so-called Goldstone mode that corresponds to the rotation of the molecules

around the director cone. Application of DC bias leads to unwinding of a helix and suppressing the Goldstone mode. The material exhibits memory upon removal of the bias, the helix remains in the unwound state with the lower value of ε'. **Figure 2.15** from [135] demonstrates results of the memory effect in CdTe QD-doped FLC for various FLCs and cell gaps.

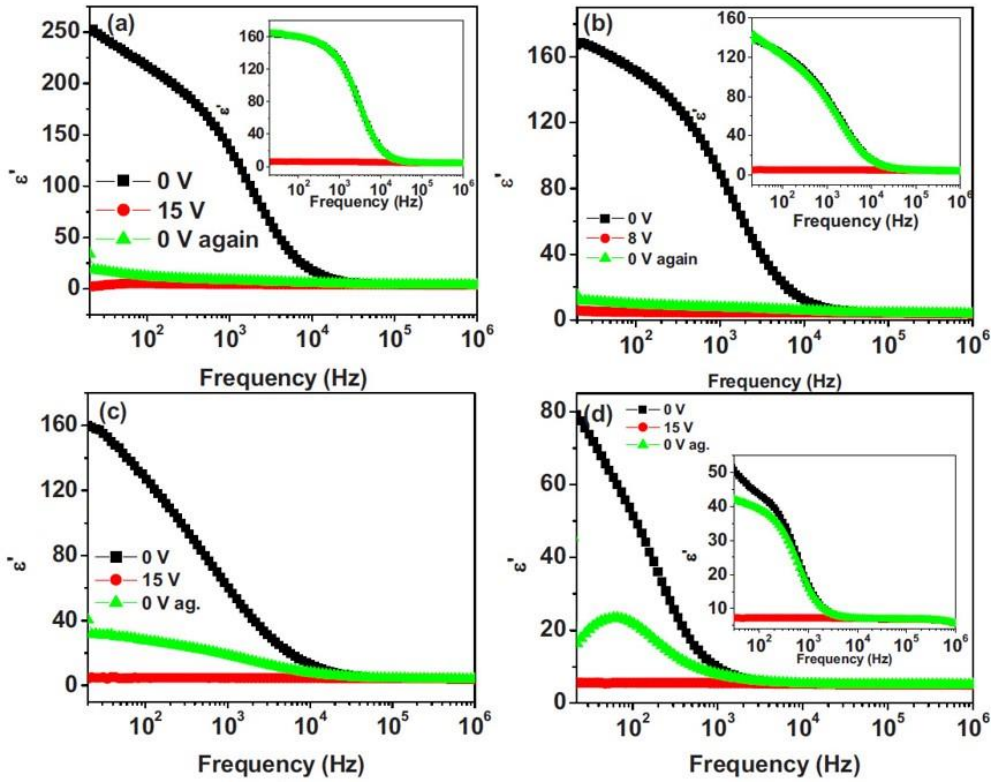

Figure 2.15 Dielectric permittivity at different DC biases of CdTe-QDs doped FLCS: (a) LAHS19, (b) LAHS18, and (c) FLC 6304 in 4 µm-cells; (d) KCFLC 7S in 10 µm-cell. Reproduced with permission from Ref. [135] – Copyright: American Institute of Physics.

The authors also reported that a small percentage (~3 wt%) of CdTe QDs in various FLC mixtures induced a uniform homeotropic alignment (dark state). With one of the FLC mixtures (CS1026) with positive $\Delta\varepsilon$, it was possible to switch the cell to a homogenous

configuration (bright state) by applying a high DC voltage (**Figure 2.16**).[137] A change of the sign of $\Delta\varepsilon$ at some temperatures was shown to cause this effect (**Figure 2.17**).

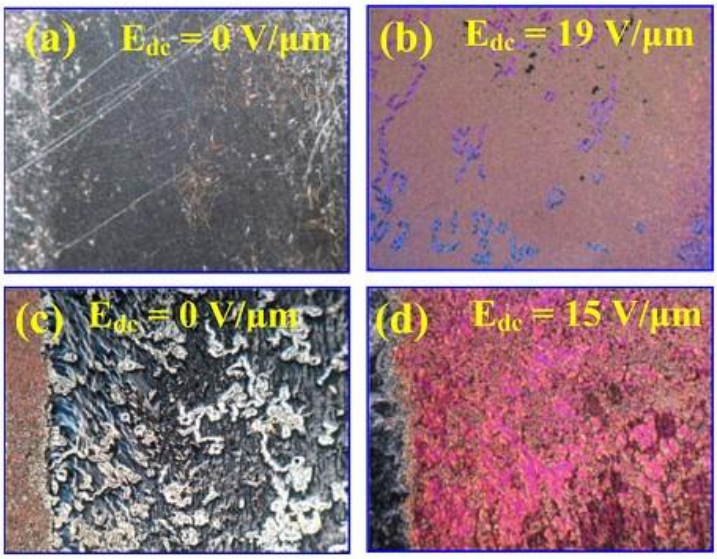

Figure 2.16 Phase transition of CS1026 FLC and optical micrographs showing the transformation from homeotropic to homogeneous (planar) configuration of CS1026 material doped with (a), (b) 1wt% (c), (d) 3wt% of CdTe QDs by application of dc bias field at room temperature. Reproduced with permission from Ref. [137] – Copyright: American Institute of Physics.

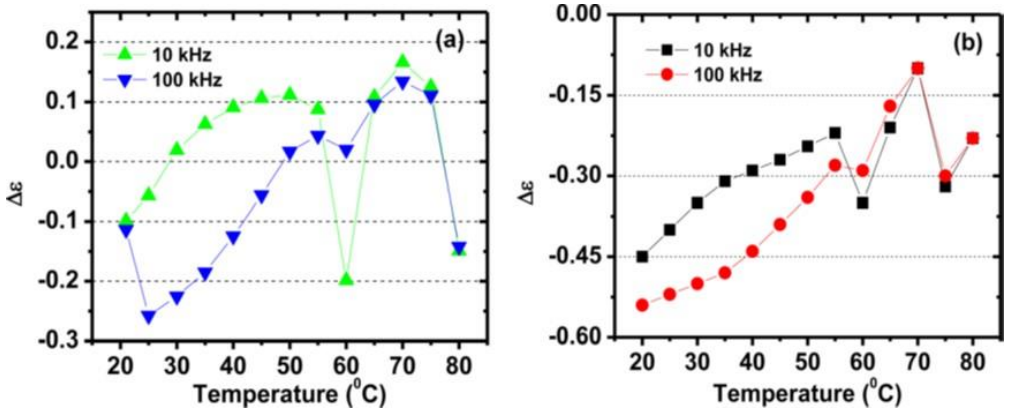

Figure 2.17 Dielectric anisotropy (a) 1 and (b) 3wt% CdTe QDs doped CS1026 material with temperature at different (10 and 100 kHz) frequencies. Reproduced with permission from Ref. [137] – Copyright: American Institute of Physics.

Other types of QDs in FLC mixtures and their electro-optical effects were investigated as well. Biradar et al. showed that ZnO NP-doped FLC mixtures display lower switching voltage and higher optical tilt angles compared to the un-doped FLCs.[139] The effects were explained by larger dipole moment of ZnO-NPs enhancing the anchoring of FLC molecules around ZnO semiconductor NPs.

Also, ZnS in FLC mixtures can have concentration-dependent impact on increasing the intensity and wavelength of photoluminescence in doped FLC mixtures (**Figure 2.18**).[138] An enhancement in PL intensity and a red shift in the maxima of the PL emission wavelength were observed for the FLC host doped with ZnS QDs. The PL emission from the ZnS QDs was thought to combine constructively with that of the FLC yielding enhanced PL intensity. On the other hand, the FLC itself provided strong light scattering and improved the PL intensity of the composite. The red shift was caused by the change in effective refractive index of FLC due to different concentrations of the ZnS QDs.

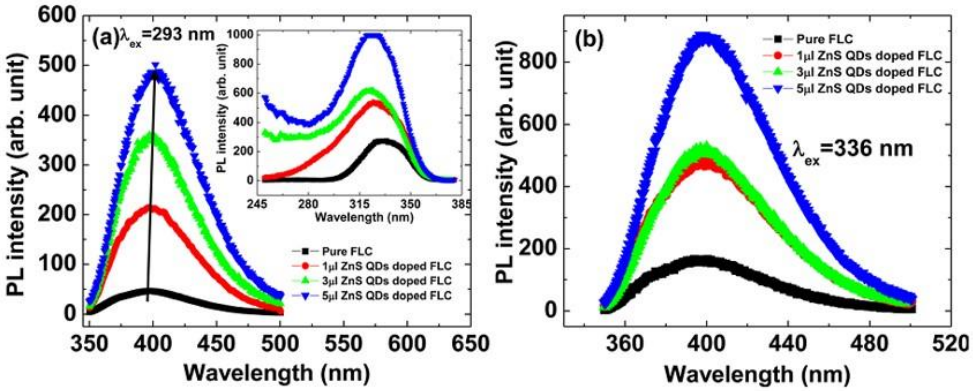

Figure 2.18 (a) Comparison of excitation (inset) and emission spectra (recorded at $\lambda_{exc.}$= 293 nm) of the FLC material KCFLC 7S doped with different (1, 3, and 5 µl) concentrations of ZnS QDs and (b) emission spectra of FLC material KCFLC 7S doped with different (1, 3, and 5 µl) concentrations of ZnS QDs by exciting with 336 nm. . Reproduced with permission from Ref. [138] – Copyright: American Institute of Physics.

2.5 Conclusion

Explorations of new aspects of soft matter nanoscience along with advancements in the synthesis of semiconductor QDs and nanorods coupled with an enhanced experimental and theoretical understanding of their optical and electronic properties at ensemble and single-particle levels are opening new doors for creation of novel photonic devices from tuneable assembled arrays of QDs in LC mixtures. Simultaneously, applications of nanoparticles as dopant for improving LC properties is gaining more attraction with the hope for innovation of new LC mixtures with higher quality and less energy consumption for the next generation of display technology. Here QDs emitting white light would be extremely useful candidates.[141] However, this demands more interdisciplinary investigations to address many questions regarding role of intrinsic electronic properties at the atomic level to the size, shape, surface coating, aggregation and other interferences in particles at the nanoscale.

Besides, further research on practical aspect of this field in terms of improving characterization techniques and increasing quality of LC-QD composites by maximizing homogenous dispersion is indispensable. In this regard, exploration of liquid crystal motif-capped QDs will prove to be a valuable strategy. Finally, aside from the use of QDs as analytical emissive tracers (using FCPM) furthering the understanding of processes in nanomaterial-doped LC mixtures, the manipulation of QD properties using LCs, for example for photonic bandgap structures, appears to be the most promising avenue for future research in this field.

Acknowledgements

The authors would like to thanks the Natural Science and Engineering Research Council (NSERC) of Canada, the Canada Foundation for Innovation (CFI), the Manitoba Research and Innovation Fund (MRIF), and the University of Manitoba's Technology Transfer Office (NSERC/CIHR Intellectual Property Mobilization Grants) for financial support of part of the work by the authors summarized in this review. TH also acknowledges financial support from Kent State University and the Government of Ohio's Third Frontier Program for Ohio Research Scholars.

2.6 References

1. Stamatoiu, O.; Mirzaei, J.; Feng, X.; Hegmann, T. *Top. Curr. Chem.* **2012,** 318, 331-93.
2. Shivakumar, U.; Mirzaei, J.; Feng, X.; Sharma, A.; Moreira, P.; Hegmann, T. *Liq. Cryst.* **2011,** 38, (11-12), 1495-1514.
3. Hegmann, T.; Qi, H.; Marx, V. M. *J. Inorg. Organomet. P.* **2007,** 17, (3), 483-508.
4. Qi, H.; Hegmann, T. *J. Mater. Chem.* **2008,** 18, (28), 3288-3294.
5. Lagerwall, J. P. F.; Scalia, G. *Curr. Appl. Phys.* **2012**, 12, (6), 1387-1412.
6. Bisoyi, H. K.; Kumar, S. *Chem. Soc. Rev.* **2011,** 40, (1), 306-319.
7. Bruchez Jr, M.; Moronne, M.; Gin, P.; Weiss, S.; Alivisatos, A. *Science* **1998,** 281, (5385), 2013-2016.
8. Chan, W. C. W.; Nie, S. M. *Science* **1998,** 281, (5385), 2016-2018.
9. Shuhendler, A. J.; Prasad, P.; Chan, H. K. C.; Gordijo, C. R.; Soroushian, B.; Kolios, M.; Yu, K.; O'Brien, P. J.; Rauth, A. M.; Wu, X. Y. *ACS Nano* **2011,** 5, (3), 1958-1966.
10. Barreto, J. A.; O'Malley, W.; Kubeil, M.; Graham, B.; Stephan, H.; Spiccia, L. *Adv. Mater.* **2011,** 23, (12), 18-40.
11. Hutter, E.; Maysinger, D. *Microsc. Res. Techniq.* **2011,** 74, (7), 592-604.
12. Zrazhevskiy, P.; Sena, M.; Gao, X. *Chem. Soc. Rev.* **2010,** 39, (11), 4326-4354.
13. Gill, R.; Zayats, M.; Willner, I. *Angew. Chem. In.t Edit.* **2008,** 47, (40), 7602-7625.
14. Shi, L. X.; Hernandez, B.; Selke, M. *J. Am. Chem. Soc.* **2006,** 128, (19), 6278-6279.
15. Shao, L.; Gao, Y.; Yan, F. *Sensors* **2011,** 11, (12), 11736-11751.

16. Obonyo, O.; Fisher, E.; Edwards, M.; Douroumis, D. *Crit. Rev. Biotechnol.* **2010,** 30, (4), 283-301.

17. Coe, S.; Woo, W. K.; Bawendi, M.; Bulovic, V. *Nature* **2002,** 420, (6917), 800-803.

18. Bowers, M. J.; McBride, J. R.; Rosenthal, S. J. *J. Am. Chem. Soc.* **2005,** 127, (44), 15378-15379.

19. Caruge, J. M.; Halpert, J. E.; Wood, V.; Bulovic, V.; Bawendi, M. G. *Nat. Photonics* **2008,** 2, (4), 247-250.

20. Tan, Z. N.; Zhang, Y.; Xie, C.; Su, H. P.; Liu, J.; Zhang, C. F.; Dellas, N.; Mohney, S. E.; Wang, Y. Q.; Wang, J. K.; Xu, J. *Adv. Mater.* **2011,** 23, (31), 3553-3558.

21. Klimov, V. I.; Mikhailovsky, A. A.; Xu, S.; Malko, A.; Hollingsworth, J. A.; Leatherdale, C. A.; Eisler, H. J.; Bawendi, M. G. *Science* **2000,** 290, (5490), 314-317.

22. Klimov, V. I.; Ivanov, S. A.; Nanda, J.; Achermann, M.; Bezel, I.; McGuire, J. A.; Piryatinski, A. *Nature* **2007,** 447, (7143), 441-446.

23. Gur, I.; Fromer, N. A.; Geier, M. L.; Alivisatos, A. P. *Science* **2005,** 310, (5747), 462-465.

24. Zhong, H. Z.; Zhou, Y.; Yang, Y.; Yang, C. H.; Li, Y. F. *J. Phys. Chem. C* **2007,** 111, (17), 6538-6543.

25. Mora-Sero, I.; Gimenez, S.; Fabregat-Santiago, F.; Gomez, R.; Shen, Q.; Toyoda, T.; Bisquert, J. *Acc. Chem. Res.* **2009,** 42, (11), 1848-1857.

26. Nozik, A. J.; Beard, M. C.; Luther, J. M.; Law, M.; Ellingson, R. J.; Johnson, J. C. *Chem. Rev.* **2010,** 110, (11), 6873-6890.

27. Ruhle, S.; Shalom, M.; Zaban, A. *ChemPhysChem* **2010,** 11, (11), 2290-2304.

28. Kongkanand, A.; Tvrdy, K.; Takechi, K.; Kuno, M.; Kamat, P. V. *J. Am. Chem. Soc.* **2008,** 130, (12), 4007-4015.

29. Burgess, D. S. *Photon. Spectra* **2005,** 39, (10), 117-117.

30. Bayer, M. *Nat. Phys.* **2011,** 7, (2), 103-104.

31. Guo, F. M.; You, H.; Gu, W. Q.; Han, D. D.; Zhu, Z. Q. *Proc. SPIE* **2011,** 8194.

32. Talapin, D. V.; Rogach, A. L.; Kornowski, A.; Haase, M.; Weller, H. *Nano Lett.* **2001,** 1, (4), 207-211.

33. Franzl, T.; Muller, J.; Klar, T. A.; Rogach, A. L.; Feldmann, J.; Talapin, D. V.; Weller, H. *J. Phys. Chem. C* **2007,** 111, (7), 2974-2979.

34. Mandal, A.; Nakayama, J.; Tamai, N.; Biju, V.; Isikawa, M. *J. Phys. Chem. B* **2007,** 111, (44), 12765-12771.

35. Brus, L. E. *J. Chem. Phys.* **1984,** 80, (9), 4403-4409.

36. Brus, L. *J. Phys. Chem.* **1986,** 90, (12), 2555-2560.

37. Borchert, H.; Talapin, D. V.; McGinley, C.; Adam, S.; Lobo, A.; de Castro, A. R. B.; Moller, T.; Weller, H. *J. Chem. Phys.* **2003,** 119, (3), 1800-1807.

38. Michalet, X.; Pinaud, F.; Lacoste, T. D.; Dahan, M.; Bruchez, M. P.; Alivisatos, A. P.; Weiss, S. *Single Mol.* **2001,** 2, (4), 261-276.

39. Medintz, I. L.; Uyeda, H. T.; Goldman, E. R.; Mattoussi, H. *Nat. Mater.* **2005,** 4, (6), 435-446.

40. Mandal, A.; Nakayama, J.; Tamai, N.; Biju, V.; Isikawa, M. *J. Phys. Chem. B* **2007,** 111, (44), 12765-12771.

41. Mansur, H. S. *WIREs Nanomed. Nanobiotechnol.* **2010,** 2, (2), 113-129.

42. Efros, A. L.; Rosen, M. *Phys. Rev. Lett.* **1997,** 78, (6), 1110-1113.

43. Carrillo-Carrion, C.; Cardenas, S.; Simonet, B. M.; Valcarcel, M. *Chem. Commun.* **2009**, (35), 5214-5226.

44. Ghosh Chaudhuri, R.; Paria, S. *Chem. Rev.* **2011,** 112, (4), 2373-2433.

45. Abel, K. A.; FitzGerald, P. A.; Wang, T.-Y.; Regier, T. Z.; Raudsepp, M.; Ringer, S. P.; Warr, G. G.; van Veggel, F. C. J. M. *J. Phys. Chem. C* **2012,** 116, (6), 3968-3978.

46. Maikov, G. I.; Vaxenburg, R.; Sashchiuk, A.; Lifshitz, E. *ACS Nano* **2010,** 4, (11), 6547-6556.

47. Pal, B. N.; Ghosh, Y.; Brovelli, S.; Laocharoensuk, R.; Klimov, V. I.; Hollingsworth, J. A.; Htoon, H. *Nano Letters* **2011,** 12, (1), 331-336.

48. Rawalekar, S.; Kaniyankandy, S.; Verma, S.; Ghosh, H. N. *J. Phys. Chem. C* **2011,** 115, (25), 12335-12342.

49. Guijarro, N.; Lana-Villarreal, T.; Mora-Sero, I.; Bisquert, J.; Gomez, R. *J. Phys. Chem. C* **2009,** 113, (10), 4208-4214.

50. Baker, D. R.; Kamat, P. V. *Langmuir* **2010,** 26, (13), 11272-11276.

51. Dibbell, R. S.; Watson, D. F. *J. Phys. Chem. C* **2009,** 113, (8), 3139-3149.

52. Kalyuzhny, G.; Murray, R. W. *J. Phys. Chem. B* **2005,** 109, (15), 7012-7021.

53. Ekimov, A. I.; Onushchenko, A. A. *Sov. Phys. Semicond+* **1982,** 16, (7), 775-778.

54. Efros, A. L.; Efros, A. L. *Sov. Phys. Semicond+* **1982,** 16, (7), 772-775.

55. Bryan, J. D.; Gamelin, D. R. *Prog. Inorg. Chem.* **2005,** 54, 47-126.

56. Cheng, S.-J. *Phys. Rev. B* **2009,** 79, (24), 245301.

57. Yu, J. H.; Liu, X. Y.; Kweon, K. E.; Joo, J.; Park, J.; Ko, K. T.; Lee, D.; Shen, S. P.; Tivakornsasithorn, K.; Son, J. S.; Park, J. H.; Kim, Y. W.; Hwang, G. S.; Dobrowolska, M.; Furdyna, J. K.; Hyeon, T. *Nat. Mater.* **2010,** 9, (1), 47-53.

58. Zutic, I.; Fabian, J.; Das Sarma, S. *Rev. Mod. Phys.* **2004,** 76, (2), 323-410.

59. Brichkin, S. B.; Chernykh, E. V. *High Energ. Chem.* **2011,** 45, 1-12.

60. Kurth, D. G.; Lehmann, P.; Lesser, C. *Chem. Commun.* **2000**, (11), 949-950.

61. Gao, M. Y.; Sun, J. Q.; Dulkeith, E.; Gaponik, N.; Lemmer, U.; Feldmann, J. *Langmuir* **2002,** 18, (10), 4098-4102.

62. Murray, C. B.; Norris, D. J.; Bawendi, M. G. *J. Am. Chem. Soc.* **1993,** 115, (19), 8706-8715.

63. Selvan, S. T. *Biointerphases* **2010,** 5, (3), 110-115.

64. Biju, V.; Itoh, T.; Anas, A.; Sujith, A.; Ishikawa, M. *Anal. Bioanal. Chem.* **2008,** 391, 2469-2495.

65. Ouyang, J.; Zaman, M. B.; Yan, F. J.; Johnston, D.; Li, G.; Wu, X.; Leek, D.; Ratcliffe, C. I.; Ripmeester, J. A.; Yu, K. *J. Phys. Chem. C* **2008,** 112, (36), 13805-13811.

66. Yu, K.; Ouyang, J.; Zaman, M. B.; Johnston, D.; Yan, F. J.; Li, G.; Ratcliffe, C. I.; Leek, D. M.; Wu, X. H.; Stupak, J.; Jakubek, Z.; Whitfiel, D. *J. Phys. Chem. C* **2009,** 113, (9), 3390-3401.

67. Yu, K. *Adv. Mater.* **2012,** 24, 1123-1132.

68. Katari, J. E. B.; Colvin, V. L.; Alivisatos, A. P. *J. Phys. Chem.* **1994,** 98, (15), 4109-4117.

69. Qu, L. H.; Peng, Z. A.; Peng, X. G. *Nano Lett.* **2001,** 1, (6), 333-337.

70. Trindade, T.; OBrien, P. *Adv. Mater.* **1996,** 8, (2), 161-163.

71. Liu, Y. F.; Yu, J. S. *J. Colloid Interf. Sci.* **2009,** 333, (2), 690-698.

72. Oluwafemi, S. O.; Revaprasadu, N.; Ramirez, A. J. *J. Cryst. Growth* **2008,** 310, (13), 3230-3234.

73. Kim, D. J.; Lee, J. H.; Yu, J. W.; Kim, E. J.; Koo, K. K. *Colloids and Surfaces. A: Physicochem. Eng. Aspects* **2008,** 313, 211-215.

74. Mao, H.; Yao, J. N.; Wang, L. N.; Liu, W. S. *J. Colloid Interf. Sci.* **2008,** 319, (1), 353-356.

75. Xiong, Y.; Xie, Y.; Yang, J.; Zhang, R.; Wu, C.; Du, G. *J. Mater. Chem.* **2002,** 12, (12), 3712-3716.

76. Braun, P. V.; Osenar, P.; Stupp, S. I. *Nature* **1996,** 380, (6572), 325-328.

77. Huang, L. M.; Wang, H. T.; Wang, Z. B.; Mitra, A.; Bozhilov, K. N.; Yan, Y. S. *Adv. Mater.* **2002,** 14, (1), 61-64.

78. Sun, Z. W.; Chen, X.; Wang, L. Y.; Zhang, G. D.; Jing, B. *Colloids and Surfaces. A: Physicochem. Eng. Aspects* **2008,** 326, (1-2), 23-28.

79. Wang, L. Y.; Chen, X.; Zhan, J.; Chai, Y. C.; Yang, C. J.; Xu, L. M.; Zhuang, W. C.; Jing, B. *J. Phys. Chem. B* **2005,** 109, (8), 3189-3194.

80. Karanikolos, G. N.; Alexandridis, P.; Mountziaris, T. J. *Mat. Sci. Eng. B-SOLID* **2008,** 152, (1-3), 66-71.

81. Karanikolos, G. N.; Alexandridis, P.; Mountziaris, T. J. *Macromol. Symp.* **2010,** 289, 43-51.

82. Nassar, I.; Osipova, V. V.; Safiullin, G.; Lobkov, V.; Galyametdinov, Y. *Int. J. Green Nanotechnol.* **2011,** 3, 22-36.

83. Karanikolos, G. N.; Alexandridis, P.; Mallory, R.; Petrou, A.; Mountziaris, T. J. *Nanotechnology* **2005,** 16, (10), 2372-2380.

84. Karanikolos, G. N.; Law, N. L.; Mallory, R.; Petrou, A.; Alexandridis, P.; Mountziaris, T. J. *Nanotechnology* **2006,** 17, (13), 3121-3128.

85. Amornpitoksuk, P.; Suwanboon, S.; Sangkanu, S.; Sukhoom, A.; Wudtipan, J.; Srijan, K.; Kaewtaro, S. *Powder Technol.* **2011,** 212, (3), 432-438.

86. Saliba, S.; Davidson, P.; Imperor-Clerc, M.; Mingotaud, C.; Kahn, M. L.; Marty, J. D. *J. Mater. Chem.* **2011,** 21, (45), 18191-18194.

87. Jiang, X.; Xie, Y.; Lu, J.; Zhu, L. Y.; He, W.; Qian, Y. T. *Chem. Mater.* **2001,** 13, (4), 1213-1218.

88. Basiruddin, S. K.; Saha, A.; Pradhan, N.; Jana, N. R. *J. Phys. Chem. C* **2010,** 114, (25), 11009-11017.

89. Selvan, S. T.; Tan, T. T. Y.; Yi, D. K.; Jana, N. R. *Langmuir* **2009,** 26, (14), 11631-11641.

90. Selvan, S. T.; Tan, T. T. Y.; Yi, D. K.; Jana, N. R. *Langmuir* **2010,** 26, (14), 11631-11641.

91. Bagwe, R. P.; Yang, C. Y.; Hilliard, L. R.; Tan, W. H. *Langmuir* **2004,** 20, (19), 8336-8342.

92. Darbandi, M.; Thomann, R.; Nann, T. *Chem. Mater.* **2005,** 17, (23), 5720-5725.

93. Han, Y.; Jiang, J.; Lee, S. S.; Ying, J. Y. *Langmuir* **2007,** 24, (11), 5842-5848.

94. Koole, R.; van Schooneveld, M. M.; Hilhorst, J.; de Mello Donegá, C.; Hart, D. C.; van Blaaderen, A.; Vanmaekelbergh, D.; Meijerink, A. *Chem. Mater.* **2008,** 20, (7), 2503-2512.

95. Wang, G. N.; Wang, C.; Dou, W. C.; Ma, Q.; Yuan, P. F.; Su, X. G. *J. Fluoresc.* **2009,** 19, (6), 939-946.

96. Wang, S.; Li, C.; Yang, P.; Ando, M.; Murase, N. *Colloids and Surfaces. A: Physicochem. Eng. Aspects* **2012,** 395, 24-31.

97. Yang, Y.; Jing, L.; Yu, X.; Yan, D.; Gao. *Chem. Mater.* **2007,** 19, (17), 4123-4128.

98. Insin, N.; Tracy, J. B.; Lee, H.; Zimmer, J. P.; Westervelt, R. M.; Bawendi, M. G. *ACS Nano* **2008,** 2, (2), 197-202.

99. Li, H.; Li, Y.; Cheng, J. *Chem. Mater.* **2010,** 22, (8), 2451-2457.

100. Sathe, T. R.; Agrawal, A.; Nie, S. *Anal Chem* **2006,** 78, (16), 5627-5632.

101. Shan, F.; Lu, X.; Zhang, Q.; Su, B.; Lu, Q. *Langmuir* **2011,** 28, (1), 812-817.

102. (a) Mowbray, D. J.; Skolnick, M. S. *J. Phys. D, Appl. Phys.* **2005,** 38, (13), 2059-2076. (b) Imamoglu, A.; Awschalom, D. D.; Burkard, G.; DiVincenzo, D. P.; Loss, D.; Sherwin, M.; Small, A. *Phys. Rev. Lett.* **1999,** 83, (20), 4204-4207.

103. Kako, S.; Santori, C.; Hoshino, K.; Gotzinger, S.; Yamamoto, Y.; Arakawa, Y. *Nat. Mater.* **2006,** 5, (11), 887-892.

104. Kikuchi, E.; Kitada, S.; Ohno, A.; Aramaki, S.; Maenosono, S. *Appl. Phys. Lett.* **2008,** 92, (17), 173307.

105. Verma, Y. K.; Inman, R. H.; Ferri, C. G. L.; Mirafzal, H.; Ghosh, S. N.; Kelley, D. F.; Hirst, L. S.; Ghosh, S.; Chin, W. C. *Phys. Rev. B.* **2010,** 82, 165428.

106. Rodarte, A. L.; Ferri, C. G. L.; Gray, C.; Hirst, L. S.; Ghosh, S. *Proc. SPIE* **2012,** 8279, 82790H.

107. Rodarte, A. L.; Gray, C.; Hirst, L. S.; Ghosh, S. *Phys. Rev. B* **2012,** 85, (3), 035430.

108. Hirst, L. S.; Kirchhoff, J.; Inman, R.; Ghosh, S.; Chien, L.-C. *Proc. SPIE* **2010,** 7618, 76180F/1-76180F/7.

109. Basu, R.; Iannacchione, G. S. *Phys. Rev. E* **2009,** 80, (1), 010701.

110. Piegdon, K. A.; Declair, S.; Foerstner, J.; Meier, T.; Matthias, H.; Urbanski, M.; Kitzerow, H.-S.; Reuter, D.; Wieck, A. D.; Lorke, A.; Meier, C. *Opt. Express* **2010,** 18, (8), 7946-7954.

111. Shoute, L. C. T.; Kelley, D. F. *J. Phys. Chem. C* **2007,** 111, (28), 10233-10239.

112. Talroze, R.; Shandryuk, G.; Matukhina, E.; Merekalov, A.; Vasiliev, R.; Gaskov, A. *Polym. Prepr.* **2007,** 48, 775-776.

113. Shandryuk, G. A.; Matukhina, E. V.; Vasil'ev, R. B.; Rebrov, A.; Bondarenko, G. N.; Merekalov, A. S.; Gas'kov, A. M.; Talroze, R. V. *Macromolecules* **2008,** 41, (6), 2178-2185.

114. Tong, X.; Zhao, Y. *J. Am. Chem. Soc.* **2007,** 129, (20), 6372-6373.

115. Cheng, M.-C.; Su, Y.-C.; Hsiao, V. K. S. *Proc. SPIE* **2011,** 8114, 811419.

116. Cheng, M.-C.; Chu, C.-C.; Su, Y.-C.; Chang, W.-T.; Hsiao, V. K. S.; Yong, K.-T.; Law, W.-C.; Prasad, P. N. *IEEE Photonics* **2012,** 4, (1), 19-25.

117. Chen, C. T.; Liu, C. C.; Wang, C. H.; Chen, C. W.; Chen, Y. F. *Appl. Phys. Lett.* **2011,** 98, (26), 261918.

118. Lukishova, S. G.; Bissell, L. J.; Winkler, J.; Stroud, C. R. *Opt. Lett.* **2012,** 37, (7), 1259-61.

119. Dundar, M. A.; Wang, B.; Notzel, R.; Karouta, F.; van der Heijden, R. W. *J. Opt. Soc. Am. B* **2011,** 28, (6), 1514-1517.

120. Gardner, D. F.; Evans, J. S.; Smalyukh, I. I. *Mol. Cryst. Liq. Cryst.* **2011,** 545, 1227-1245.

121. Chen, H.-S.; Chen, C.-W.; Wang, C.-H.; Chu, F.-C.; Chao, C.-Y.; Kang, C.-C.; Chou, P.-T.; Chen, Y.-F. *J. Phys. Chem. C* **2010,** 114, (17), 7995-7998.

122. Wu, K. J.; Chu, K. C.; Chao, C. Y.; Chen, Y. F.; Lai, C. W.; Kang, C. C.; Chen, C. Y.; Chou, P. T. *Nano Lett.* **2007,** 7, (7), 1908-1913.

123. Lin, T.-J.; Chen, C.-C.; Cheng, S.; Chen, Y.-F. *Opt. Express* **2008,** 16, (2), 671-678.

124. Danilov, V. V.; Artem'ev, M. V.; Baranov, A. V.; Ermolaeva, G. M.; Utkina, N. A.; Khrebtov, A. I. *Opt. Spectrosc.* **2008,** 105, 306-309.

125. Kundu, S.; Hill, J. P.; Richards, G. J.; Ariga, K.; Khan, A. H.; Thupakula, U.; Acharya, S. *J. Nanosci. Nanotechnol.* **2011,** 11, (9), 7729-7734.

126. Qi, H.; Kinkead, B.; Hegmann, T. *Proc. SPIE* **2008,** 6911, 691106/1-691106/11.

127. Kinkead, B.; Hegmann, T. *J. Mater. Chem.* **2010,** 20, (3), 448-458.

128. Urbanski, M.; Kinkead, B.; Hegmann, T.; Kitzerow, H.-S. *Liq. Cryst.* **2010,** 37, (9), 1151-1156.

129. Mirzaei, J.; Urbanski, M.; Yu, K.; Kitzerow, H.-S.; Hegmann, T. *J. Mater. Chem.* **2011,** 21, (34), 12710-12716.

130. Mirzaei, J.; Sawatzky, R.; Sharma, A.; Urbanski, M.; Yu, K.; Kitzerow, H.-S.; Hegmann, T., *Proc. SPIE* **2012,** 8279, 827913-827913-9.

131. Anczykowska, A.; Bartkiewicz, S.; Nyk, M.; Mysliwiec, J. *Appl. Phys. Lett.* **2011,** 99, (19), 191109.

132. Shurpo, N. A.; Vakshtein, M. S.; Kamanina, N. V. *Tech. Phys. Lett.* **2010,** 36, 319-321.

133. Konshina, E. A.; Gavrish, E. O.; Orlova, A. O.; Artem'ev, M. V. *Tech. Phys. Lett.* **2011,** 37, (11), 1011-1014.

134. Kumar, S.; Sagar, L. K. *Chem. Commun.* **2011,** 47, 12182-12184.

135. Kumar, A.; Prakash, J.; Khan, M. T.; Dhawan, S. K.; Biradar, A. M. *Appl. Phys. Lett.* **2010,** 97, (16), 163113.

136. Kumar, A.; Biradar, A. M. *Phys. Rev. E* **2011,** 83, (4), 041708.

137. Kumar, A.; Silotia, P.; Biradar, A. M. *Appl. Phys. Lett.* **2011,** 99, (7)., 072902.

138. Kumar, A.; Prakash, J.; Deshmukh, A. D.; Haranath, D.; Silotia, P.; Biradar, A. M. *Appl. Phys. Lett.* **2012,** 100, (13), 134101.

139. Joshi, T.; Kumar, A.; Prakash, J.; Biradar, A. M. *Appl. Phys. Lett* **2010,** 96, (25).

140. Qi, H.; Hegmann, T. *Liq. Cryst. Today* **2011,** 20, (4), 102 - 114.

141. Belaissaoui, A.; Saez, I. M.; Cowling, S. J.; Zeng, X.; Goodby, J. W. *Chem-Eur J.* **2012,** 18, (8), 2366-2373.

Connecting Text for Chapter 3

Chapters 1 and 2 provided background information and introduced concepts in nematic LCs and doped LC nanocomposites, along with the main characterization techniques utilized in this thesis to study optical and electro-optical properties of the nematic samples. Chapter 1 also provided a summary of the approaches for the synthesis and functionalization of gold NPs applied and developed in this thesis. Chapter 2 presented opportunities and challenges in colloidal LC dispersions in further detail by exploring semiconductor QD as LC dopants. Chapter 3 describes nematic nanocomposites with a series of small and monodispersed CdSe QDs. The three types of CdSe QDs are similar in size and shape and all passivated with a monolayer of myristic acid but vary in their core compositions. The first two vary in the amount of defects as demonstrated by different photoluminescent properties compared to the third one doped with a small concentration of Zn atoms (CdSe/Zn). While the first two CdSe QDs showed no significant influence on the nematic LC, the nematic samples doped with different concentrations of the third CdSe QD surprisingly proved to have different optical and electro-optical behaviour from the undoped LC. Based on these observations, it was proposed that the small changes in synthesis protocols can change the core composition of QDs and introduce surface defects which may ultimately alter the ligand coverage of QDs and their impacts on the nematic LC host. Overall, this chapter investigates the mechanism of LC-NP interactions by looking at the role of small changes in the core composition and surface defects of NP dopants.

Chapter 3

Nanocomposites of a Nematic Liquid Crystal Doped with Magic-Sized CdSe Quantum Dots

Nanocomposites of a Nematic Liquid Crystal Doped with Magic-Sized CdSe Quantum Dots

Javad Mirzaei[a], Marin Urbanski[b], Kui Yu[c], Heinz-S. Kitzerow[b] and Torsten Hegmann[a,d,e]

[a] Department of Chemistry, University of Manitoba, Winnipeg, MB, R3T 2N2 Canada

[b] Department of Chemistry, University of Paderborn 33098 Paderborn, Germany

[c] Steacie Institute for Molecular Sciences, National Research Council of Canada, Ottawa, ON, K1A 0R6, Canada

[d] Chemical Physics Interdisciplinary Program & Liquid Crystal Institute, Kent State University, Kent, OH 44242 USA

[e] Department of Pharmacology and Therapeutics, University of Manitoba, Winnipeg, MB, R3T 2N2 Canada

Reproduced with permission from *Journal of Materials Chemistry*, **2011,** 21, (34), 12710-12716.

Abstract

This chapter demonstrates the optical, alignment and electro-optic properties of a nematic liquid crystal affected by the presence of semiconductor CdSe magic-sized nanocrystals (MSNCs). Three single-sized CdSe samples were tested, exhibiting bright bandgap photoluminescence (PL) with λ_{max} ~ 463 nm and ~ 10 nm full width at half maximum (FWHM). The three quantum dot (QD) samples were passivated with a monolayer of myristic acid. Two of them (**QD1** and **QD2**) only vary in the amount of defects as indicated by different bandgap and deep trap PL. The third MSNC sample (**QD3**) is compositionally different, doped with Zn. These MSNCs with almost identical sizes were doped at different concentrations (1-5 wt%) into the nematic phase of 5-*n*-heptyl-2-(4-*n*-octyloxyphenyl)-pyrimidine (**LC1**). Only **QD3** showed the formation of birefringent stripes surrounded by areas of homeotropic alignment between plain glass slides at all concentrations as observed for many other nanoparticle-doped nematic liquid crystals reported earlier by our group. In polyimide-coated glass slides favouring planar orientation of the nematic director, planar alignment was observed. Surprisingly, only the Zn-doped magic-sized QD3 quantum dots (CdSe@Zn) significantly lower the dielectric anisotropy as well as the splay elastic constant of the nematic host, despite identical size and surface functionality, which highlights the tremendous effect of the nanocrystal core composition on the electro-optic properties of the nematic host. In addition, fluorescence confocal (polarizing) microscopy studies show the director field within and around the birefringent stripes and confirm locally elevated concentrations or aggregates of the MSNC that are otherwise randomly distributed in the nematic host.

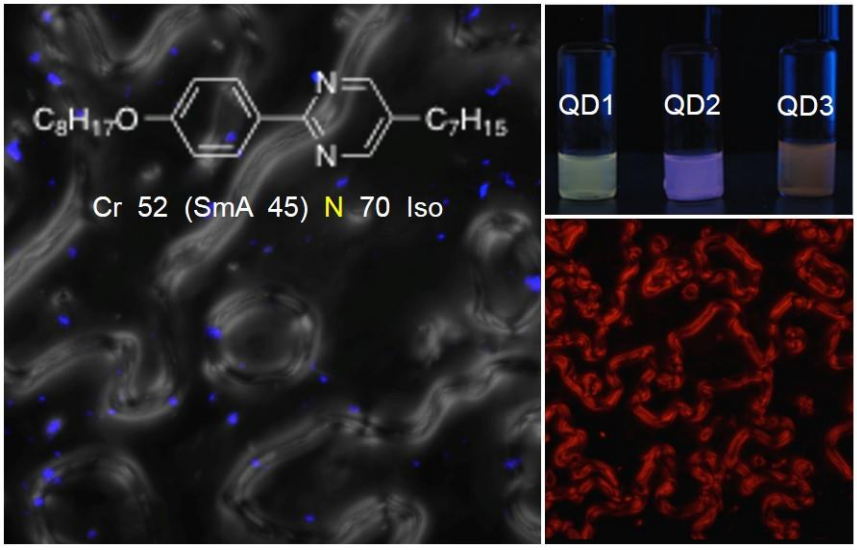

Graphical abstract

3.1 Introduction

Doping, i.e. the intentional incorporation of small quantities of an additive into a nematic liquid crystal (N-LC), is one of the most prominent processes to tune both the optical and electro-optical properties of anisotropic nematic fluids.

The response of a nematic liquid crystal such as LC1 (**Figure 3.1**) to an applied electric field is an important property in the application of N-LCs in many optical devices such as liquid crystal displays (LCDs). The ability of the director (parallel to the long molecular axis for a rod-like N-LC) to align along an external field results from permanent or induced electric dipoles within the molecules. Pure LCs or custom LC mixtures for LCD applications are generally desirable with low threshold voltage (V_{th}) and maximal dielectric anisotropy $\Delta\varepsilon$ ($\Delta\varepsilon = \varepsilon_{\parallel} - \varepsilon_{\perp}$ where $\varepsilon_{\parallel}$ is the electrical permittivity along the long molecular axis and $\varepsilon_{\perp}$ the electrical permittivity perpendicular to $\varepsilon_{\parallel}$), either positive or negative, along with low viscosity and short switching times (rise and fall times).

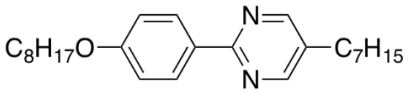

Felix-2900-03; Cr 52 (SmA 45) N 70 Iso

Figure 3.1 Chemical structure and phase transition temperatures of LC1 (Cr = crystalline solid, SmA = smectic-A phase, N = nematic phase, Iso = isotropic liquid).

For an N-LC such as **LC1** in a planar, rubbed polyimide-coated cell, the splay elastic constant (K_{11}) is also of significance. Splay is the deformation that arises when an electric field is applied to such cell.[1] Above V_{th}, the director gradually reorients from a planar

orientation near the alignment layers to a vertical (or homeotropic) orientation in the bulk of the LC film in the so-called Freedericksz transition. K_{11}, as shown in Equation 3.1 below, is directly proportional to V_{th}^2 and $\Delta\varepsilon$ where ε_0 is the permittivity of free space.[1]

$$K_{11} = \left(\frac{V_{th}}{\pi}\right)^2 \times \varepsilon_0 \times |\Delta\varepsilon| \quad \text{(Eq. 3.1)}$$

Doping LCs with colloidal particles such as aerosils,[2-5] or more recently with nanoscale materials such as carbon nanotubes[6-12] or quasi-spherical nanoparticles (NPs) is an active interdisciplinary research topic attracting interest from both academia and industry since such suspensions exhibit striking properties not observed for pure LCs or LC mixtures. For example, changing the optical behaviour by imposing discrete alignment modes different from the corresponding non-doped LC, generating rheological changes due to topological defects, improving response times, and lowering of V_{th} values have all been reported for N-LCs doped with metal-based, ferroelectric, dielectric or semiconductor NPs, among others.[13-24] However, irreversible aggregation or phase separation or segregation of NPs in the LC host as well as defect formation induced by the presence of NPs were often either neglected, difficult to ascertain, or did simply not result in a visualizable or measurable event or effect. Earlier work from our group on the other hand has frequently described multiple alignment modes and defect textures due to NP segregation along with lower V_{th} (as a result thereof), altered elastic constants, and dielectric properties in N-LCs doped with alkylthiol-capped gold NPs as well as CdSe and CdTe quantum dots (QDs).[17, 25-27]

QDs were particularly attractive for addressing the problem of larger size distributions known to arise from the synthesis of gold NPs and particularly for investigating trends in the effects of NP size and surface functionality (non-polar aliphatic vs. polar) in N-LCs. An important piece of the puzzle still missing to gain a more complete understanding of NP-LC interactions is the use of truly monodisperse NPs, which, in a series, would ideally differ in one or more parameter such as core composition or coating.

Building on our earlier data on NP doped N-LCs including the formation of electrohydrodynamic instabilities (i.e. convection rolls or Kapustin-Williams domains).[26, 28, 29] In this chapter new detailed data from optical (textures and defects), electro-optic as well as alignment studies using magic-sized QDs with very low polydispersity index as dopants in the N-LC host **LC1** (frequently used in earlier studies) will be presented. To demonstrate effects of small changes in QD surface disorder or the QD surface composition on the optical, electro-optic and alignment properties of **LC1**, we selected three CdSe QDs with **QD1**[30] and **QD2**[31] only differing in the degree of surface defect states (indicated by differences in deep trap PL emission) due to an altered preparation procedure, and **QD3**[32] differing from the other two by Zn doping, CdSe@Zn. All three QDs are quasi identical in core size and are consistently capped, in principle, with the same fatty acid (i.e. myristic acid).

The strong, narrow bandgap PL emission of these QDs (**Figure 3.2**) was also used in fluorescence confocal polarizing microscopy (FCPM) experiments to determine the distribution of the QDs in the N-LC as well as their aggregation and segregation behaviour. Several of these imaging studies were performed in conjunction with a dichroic dye (*vide infra*) to clarify LC alignment as well as director fields within or around defects in the

absence or presence of an applied electric field, using plain glass or rubbed polyimide ITO-coated glass cells.

3.2 Experimental

LC1 was used as received from Synthon Chemicals GmbH. The three QDs (**QD1 – QD3**) were prepared using a non-injection, one-pot synthesis as reported earlier,[30-32] using $Cd(OAc)_2 \cdot 2H_2O$, Se, and Zn (for **QD3** only) in 1-octadecene in the presence of myristic acid ($CH_3(CH_2)_{12}CO_2H$) and trioctylphosphine (TOP) in a small quantity (to activate Se) as surface ligands (see

Table 3.1).

Photoluminescence spectra were collected using a Varian Cary Eclipse (λ_{exc} = 400 nm). UV-vis spectra were collected using a Varian Cary 5000 UV-vis-NIR spectrophotometer (for absorption spectra of the three QDs see supplementary information presented in Appendix A). The mixtures of the CdSe quantum dots in **LC1** were prepared by weighing accurate amounts of the solid LC using a micro-balance and dissolving it in a known amount of toluene for **QD1** and **QD2** or hexane for **QD3**. The toluene solutions of the **QD1** and **QD2** QDs and the hexane solution of CdSe@Zn QDs (**QD3**) were combined in a V-vial® with the LC solution to produce the exact concentration of the QDs in **LC1** (1, 2.5 & 5wt% mixtures).

The solvent was then allowed to evaporate under a steady stream of dry N_2 at ~ 70 °C for about 24 - 48 h followed by sonication. The importance of direct, pulsed sonication

using a sonotrode (output power: 750 W, *f* = 20 kHz, 5 s ON then 5 s OFF at an output power amplitude of 21%) is demonstrated in the supplementary information.

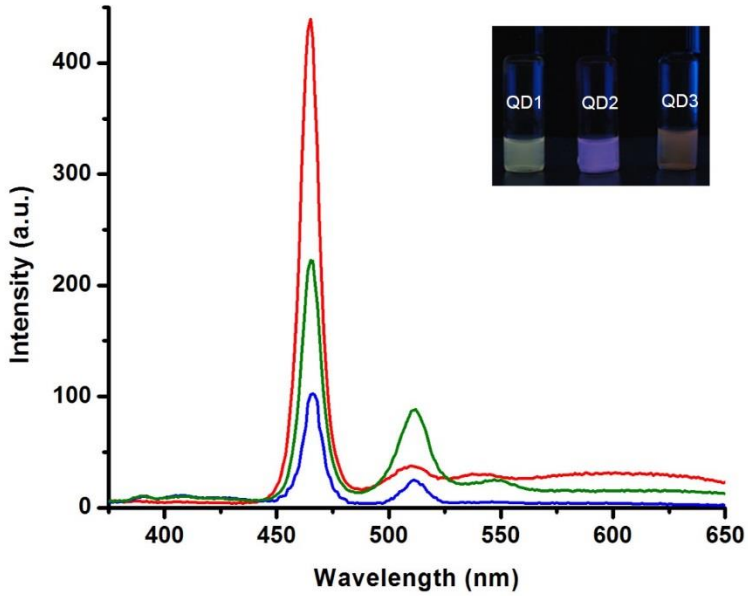

Figure 3.2 PL emission spectra (λ_{exc} = 400 nm) of magic-sized quantum dots QD1 (green), QD2 (blue), and QD3 (red) in toluene. The spectra were normalized with the same optical density at the excitation wavelength. Note that compared to QD2, QD1 exhibits relatively enhanced deep trap emission, while QD3 much decreased deep trap emission at ~ 512 nm (with respect to the bandgap emission at ~ 463 nm) as a result of the Zn doping.

Table 3.1 Size-distribution of magic-sized QDs **QD1-QD3**[#]

QD*x*	Size ± SD (diameter / nm)	Capping agent
QD1 (CdSe)[30]	2.0 ± 0.1[‡] (quasi-spherical)	$CH_3(CH_2)_{12}COOH$
QD2 (CdSe)[31]	2.0 ± 0.1[‡] (quasi-spherical)	$CH_3(CH_2)_{12}COOH$[§]
QD3 (CdSe@Zn)[32]	2.0 ± 0.1[‡] (quasi-spherical)	$CH_3(CH_2)_{12}COOH$[§]

[#] Calculated from the 1st excitonic absorption peak position. [‡] On TEM grids, some aggregation after solvent evaporation leads to larger QD assemblies, which can be broken up by re-dispersing them in toluene or hexane. Size distributions as small as 0.1 nm (as calculated from spectroscopic data including XRD and Diffusion Ordered NMR

Spectroscopy (DOSY)) are difficult to estimate by TEM image analysis. [§] The surface of these QDs is simultaneously capped with a small percentage TOP (trioctylphosphine) used to 'activate' Se. For more details, see references [30-32]. For XPS data, see supplementary information.

Polarized optical microscopy (POM) images were taken using an Olympus BX51-P polarized optical microscope in conjunction with a Linkam LS350 heating/cooling stage. Electro-optic (EO) analysis was performed using an LCAS 1 automated liquid crystal analyzer (LC Vision). EO data were obtained using the single-cell method built into the LCAS 1 software as originally described by Wu et al.[33] The LC test cells used were planar 4.0 µm cells with antiparallel polyimide alignment layers and 1° to 3° pre-tilt (LC Vision). For all POM imaging and EO measurements, the LC mixtures were heated above the isotropic/nematic phase transition temperature ($T_{\text{Iso-N}}$) and cooled at a rate of 1 °C min^{-1} until the desired temperature below $T_{\text{Iso-N}}$ was reached. The average of all values and standard deviations of each electro-optic parameter were calculated from at least five or up to ten measurements at any given temperature for the each mixture (also using different cells). FCPM images were obtained using a Nikon LV 100D-U upright microscope coupled with a Nikon Eclipse C1 Plus scanner/controller using two excitation lasers; λ_{excI} = 408 nm to excite the QDs and λ_{excII} = 488 nm to excite the dichroic dye *N*,*N'*-bis(2,5-di-*tert*-butylphenyl)-3,4,9,10-perylenedicarboximide (obtained from Aldrich) used at 0.001 wt%. The dye shows a bright fluorescence at λ = 540 nm that was easily separated from the PL emission of the QDs using a beam splitter cube or interference beam splitter as well as by-pass filters. Moreover, for some experiments, the microscope was equipped with a polarizer, a quarter wave plate, and an analyzer for polarization control.

3.3 Results and Discussion

3.3.1 Polarized light optical microscopy (POM)

POM investigations, as in all the studies on NP-doped N-LCs, are always the starting point for further optical and electro-optic measurements. POM provides first clues on the aggregation and segregation behaviour of the NPs dispersed in the N-LC host. The formation of characteristic birefringent stripe defects as well as the temperature-dependent induction of homeotropic alignment for several N-LC hosts despite the presence of surfaces known to promote planar alignment were frequently observed in our lab for NP-doped mixtures showing the most drastic changes of the EO properties. Most likely, altered EO properties were observed as a consequence of these aggregation and segregation phenomena.

Hence, all mixtures were first studied by POM between plain, untreated microscopy glass slides and then in rubbed polyimide-coated, ITO-glass cells promoting planar alignment. **Figure 3.3**, **Figure 3.4** and **Figure 3.5** show optical photomicrographs of textures observed between plain glass slides (a-c) and the alignment as well as defects in planar EO cells (d-f) of **LC1** doped with **QD1** – **QD3** at 1, 2.5, and 5wt%. A close inspection of these images reveals the first major differences in the behaviour of the three QDs in **LC1**.

Both **QD1** and **QD2** in **LC1** mainly show *schlieren* textures between plain glass slides (with the exception of the 2.5wt% **QD1** in **LC1** mixture showing the typical birefringent stripe texture). **QD3**, however, only shows homeotropic alignment with an

increasing area density of birefringent stripe defects usually observed by our group for NP-doped N-LCs.

This observation provides the first important hint that **QD1** and **QD2** are significantly better miscible with the N-LC host, and that **QD3** segregates to the LC-glass interfaces (top and/or bottom) inducing homeotropic alignment of the director on plain glass. The same trend is also observed in rubbed polyimide-coated ITO-glass cells (thickness: 4 μm). Mixtures of **LC1** doped with **QD1** and **QD2** show relatively defect-free planar alignment with some point-like defects (not exclusively caused by spacers), which in some cases follow the rubbing direction of the cell (see both images of 5wt% **QD1** or **QD2** in **LC1** in **Figure 3.3 f** and **Figure 3.4 f**). These circular, point-like defects are most likely caused by minor aggregation of the QDs in the N-LC film (very pronounced for 2.5wt% of **QD2** in **LC1** in **Figure 3.4 e**). Results of FCPM imaging discussed in the Appendix A shine more light onto the origin of these defects. **QD3**, however, notably distorts the homogeneous planar alignment of **LC1** in planar cells **Figure 3.5 d-f**). Here, just 1wt% of **QD3** in **LC1** produces quasi chain-like networks of point defects (similar to the highest concentrations of **QD1** and **QD2** in **LC1**). Increasing the amount of **QD3** in **LC1** initially produces defect domains with reduced birefringence (**Figure 3.5 e** at 2.5 wt%) and at 5wt% a network of defects with homeotropic alignment (**Figure 3.5 f**). These homeotropic areas are probably caused by a combination of some QD aggregation and most certainly by QD segregation to the alignment layer-LC interface.

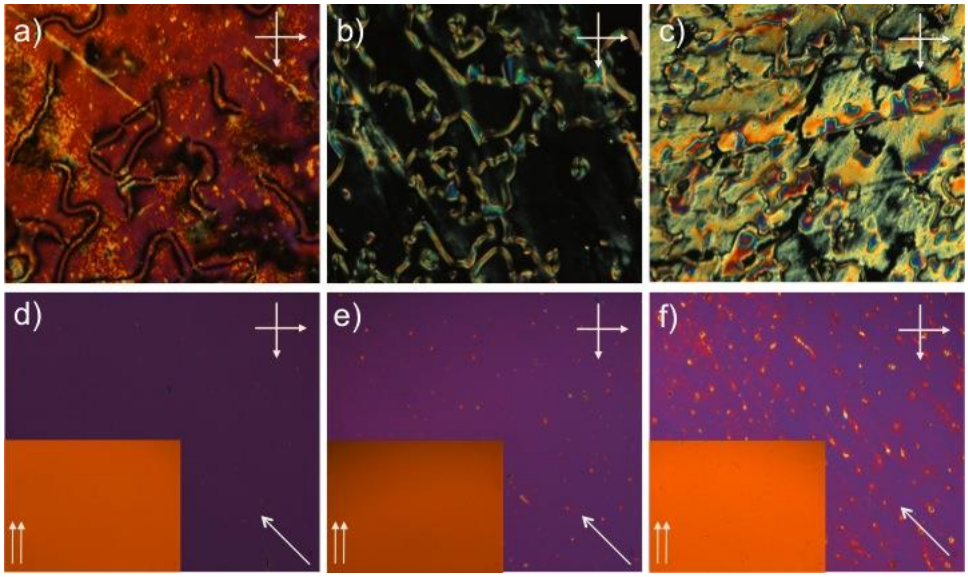

Figure 3.3 POM photomicrographs (crossed polarizers) of **LC1** doped with **QD1** at $T_{Iso\text{-}N}$ – T = 9 °C (top, a-c: plain glass; bottom, d-f: 4.0 mm anti-parallel planar cell): (a, d) 1wt%, (b, e) 2.5wt%, (c, f) 5wt%. The white arrow in the bottom right corner in d-f shows the rubbing direction of the cell, and the inset in d-f shows the same area with parallel polarizers.

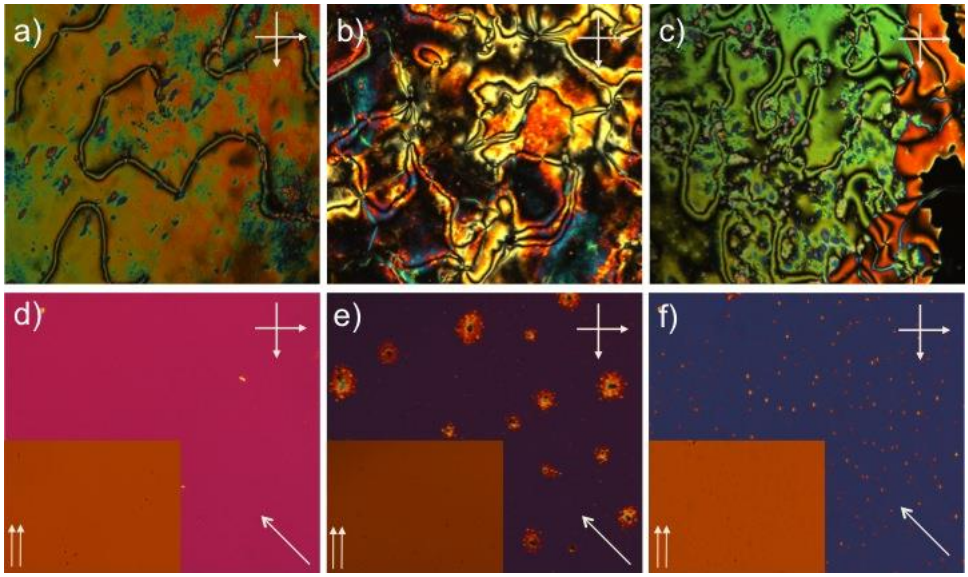

Figure 3.4 POM photomicrographs (crossed polarizers) of **LC1** doped with **QD2** at $T_{Iso\text{-}N}$ – T = 9 °C (for details, see caption **Figure 3.3**).

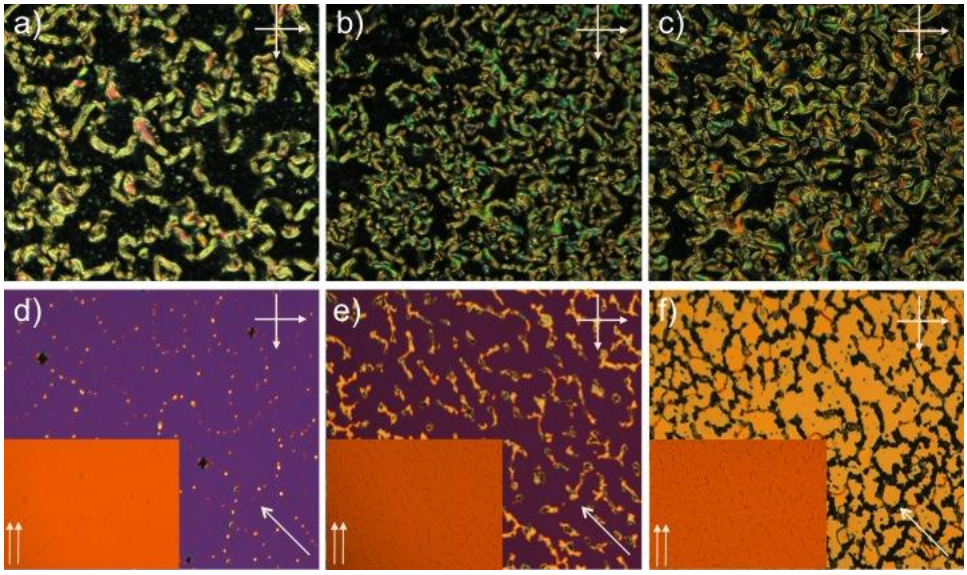

Figure 3.5 POM photomicrographs (crossed polarizers) of LC1 doped with QD3 at TIso-N – T = 9 °C (for details, see caption **Figure 3.3**).

However, major aggregation of the QDs in all mixtures with **LC1** is not observed as can be seen in the images with parallel, un-crossed polarizers. With respect to their optical behaviour in thin films, both **QD1** and **QD2** in **LC1** behave similar to hydrophilic CdTe QDs capped with thioglycolic acid ranging in size from 3.2 to 4.0 nm,[25] and **QD3** similar to alkylthiol-capped gold NPs of similar size[17] and hydrophobic CdSe QDs capped with hexadecylamine ranging in size from 2.5 to 5.2 nm reported earlier (the latter only at lower concentrations, i.e. 1wt%).[25]

The difference in alignment, texture and defect behaviour is all the more significant considering that Zn doping for **QD3** is the only difference to **QD1** and **QD2** with all other parameters such as size and monolayer capping kept largely constant.

3.3.2 Electro-optic (EO) characterization

To see if this difference in defect formation between **QD1**/**QD2** and **QD3** in **LC1** affects the response of this N-LC host to an applied electric field, we next performed detailed electro-optic tests (i.e. measuring the capacity vs. applied voltage) using the single-cell method described in the experimental section.

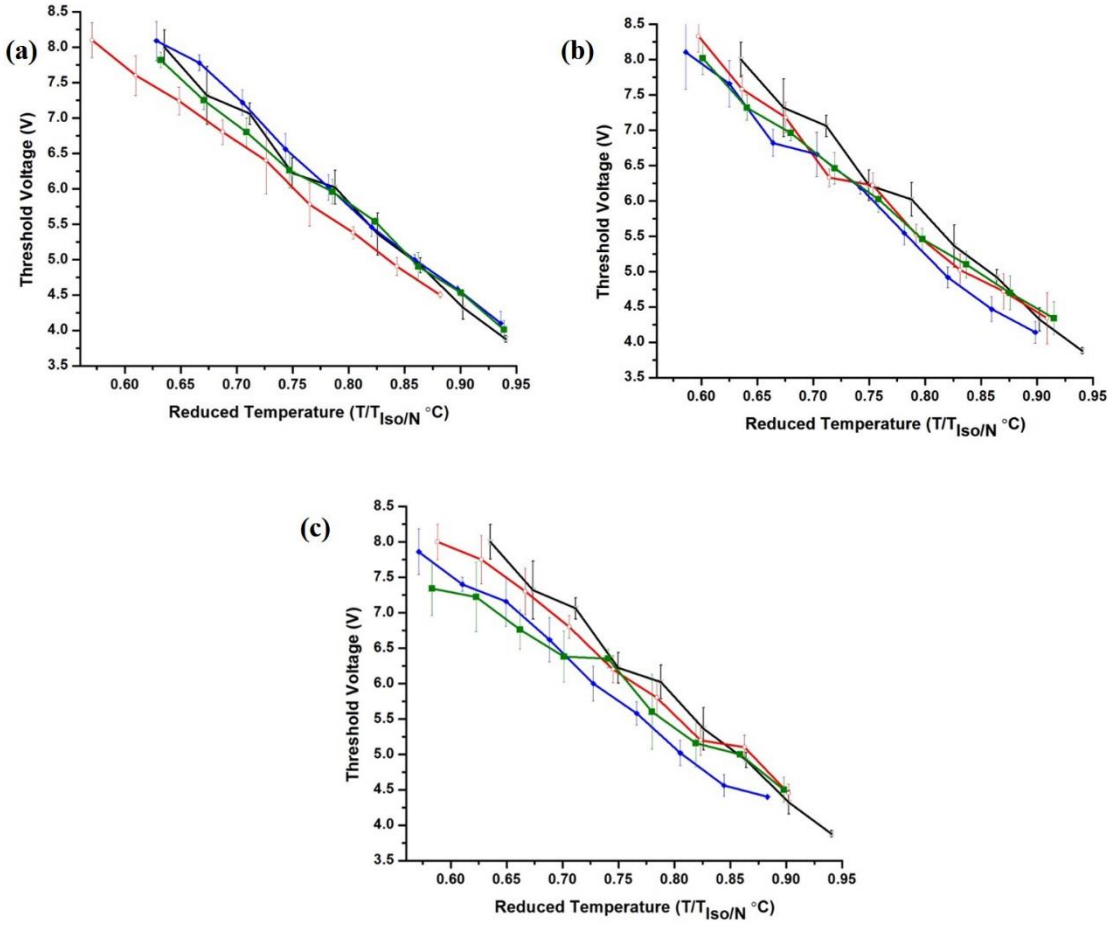

Figure 3.6 Plots of the threshold voltage, V_{th} vs. the reduced temperature $T/T_{Iso\text{-}N}$ (V_{th} was plotted against $T/T_{Iso\text{-}N}$ to account for changes in the Iso-N phase transition temperature due to an increasing amount of dispersed QDs) of pure **LC1** (black data set) as well as **QD1** (green), **QD2** (blue) or **QD3** (red) in **LC1** at: (a) 1wt%, (b) 2.5wt%, and (c) 5wt%.

Rather surprisingly, considering most of our earlier work on Au NPs and QDs in **LC1**,[25-27] data collected in **Figure 3.6** show that none of the QDs exerts any significant effect on V_{th} of **LC1** over the investigated concentration range up to 5wt%. Only at 5wt%, and at temperatures well below the Iso-N phase transition, the slope of V_{th} vs. $T/T_{Iso\text{-}N}$ begins to show a trend to lower values of V_{th}. Transmission *vs*. applied voltage measurements confirm a steady decrease of V_{th} with increasing QD concentration for **QD3** in **LC1**, and show the lowest value of V_{th} for the 2.5wt% mixture of **QD1** in **LC1** (the mixture with a QD concentration showing a birefringent stripe texture in **Figure 3.3**. (see supplementary information provided in Appendix A).[34]

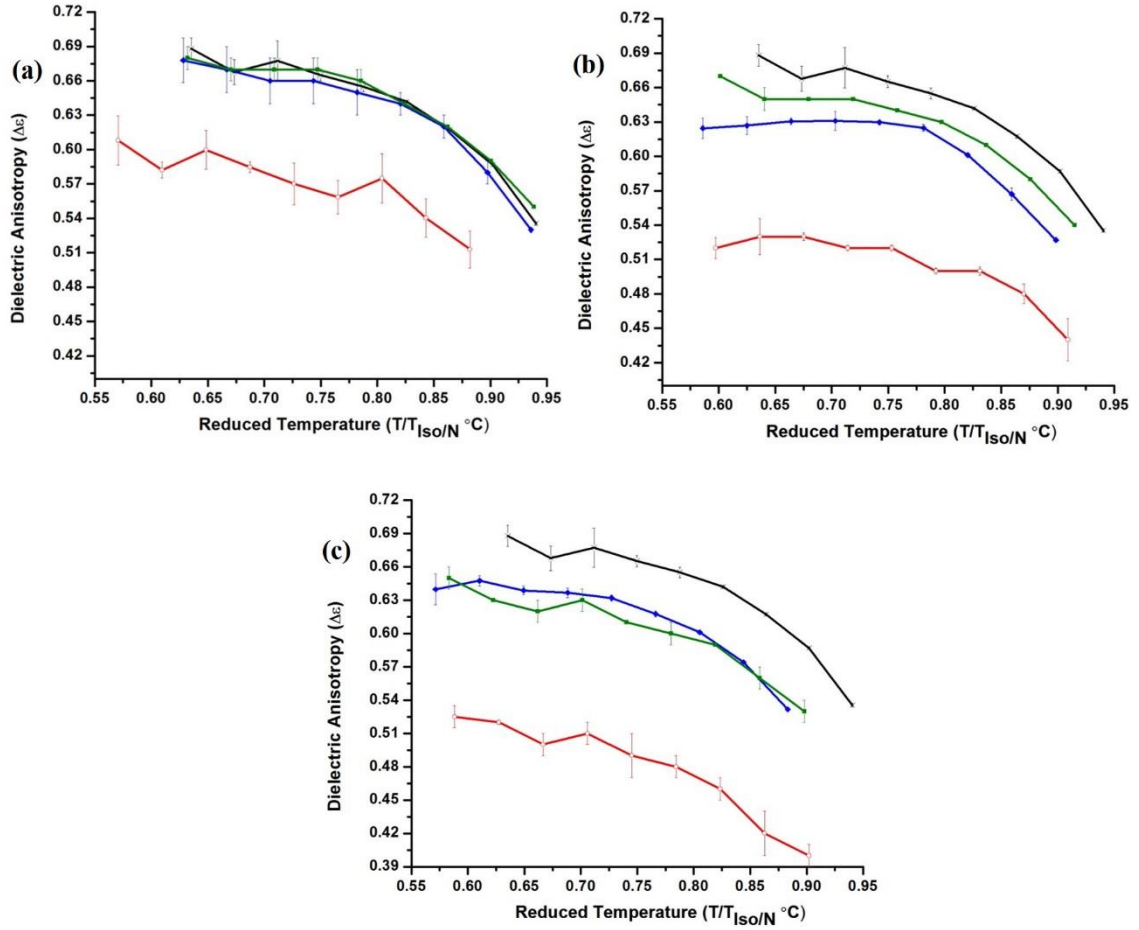

Figure 3.7 Plots of the dielectric anisotropy, $\Delta\varepsilon$ vs. the reduced temperature $T/T_{\text{Iso-N}}$ of pure **LC1** (black data set) as well as **QD1** (green), **QD2** (blue) or **QD3** (red) in **LC1** at: (a) 1wt%, (b) 2.5wt%, and (c) 5wt%. $\Delta\varepsilon$ values especially for the 5wt% sample are affected (i.e. slightly higher) because not the entire electric field-addressed area participates in the reorientation.

Since nearly all metal NPs and semiconductor QDs capped with hydrophobic hydrocarbon monolayers reduced V_{th} in the past, the question we asked is: Do these magic-sized QDs, at that particular size, impart any effect on the electro-optic properties of **LC1**? Plots of the dielectric anisotropy ($\Delta\varepsilon$) vs. $T/T_{\text{Iso-N}}$ (see **Figure 3.7**) demonstrate that this is indeed the case.

Two unique trends can be seen in these plots. First, increasing the concentration of all three QDs gradually lowers $\Delta\varepsilon$ (little at 1wt%, but more and more significantly at 2.5 and 5wt%); with a largely identical slope of $\Delta\varepsilon$ vs. $T/T_{\text{Iso-N}}$. Second, and particularly striking, the Zn-doped **QD3**, which are compositionally different from **QD1** and **QD2**, induce significantly lower values of $\Delta\varepsilon$ than **QD1** and **QD2**, highlighting that changes in surface composition of these QDs intrinsically or concurrently via induced local changes of the alignment in planar EO cells (see alignment defect network in **Figure 3.5 f**) can have a considerable effect on the dielectric properties of a given N-LC host.

Considering Equation 3.1, and unaltered values for V_{th} discussed earlier, one would expect that the splay elastic constant, K_{11}, of **LC1** in this cell geometry would also be reduced with an increasing concentration of all three QDs. In addition, the most drastic decrease would be expected for **QD3**. Data collected in **Figure 3.8** confirm this, showing that the two effects, a reduction in $\Delta\varepsilon$ and in K_{11} cancel each other out. Consequently, the measured V_{th} values are similar to those obtained for pure **LC1**.

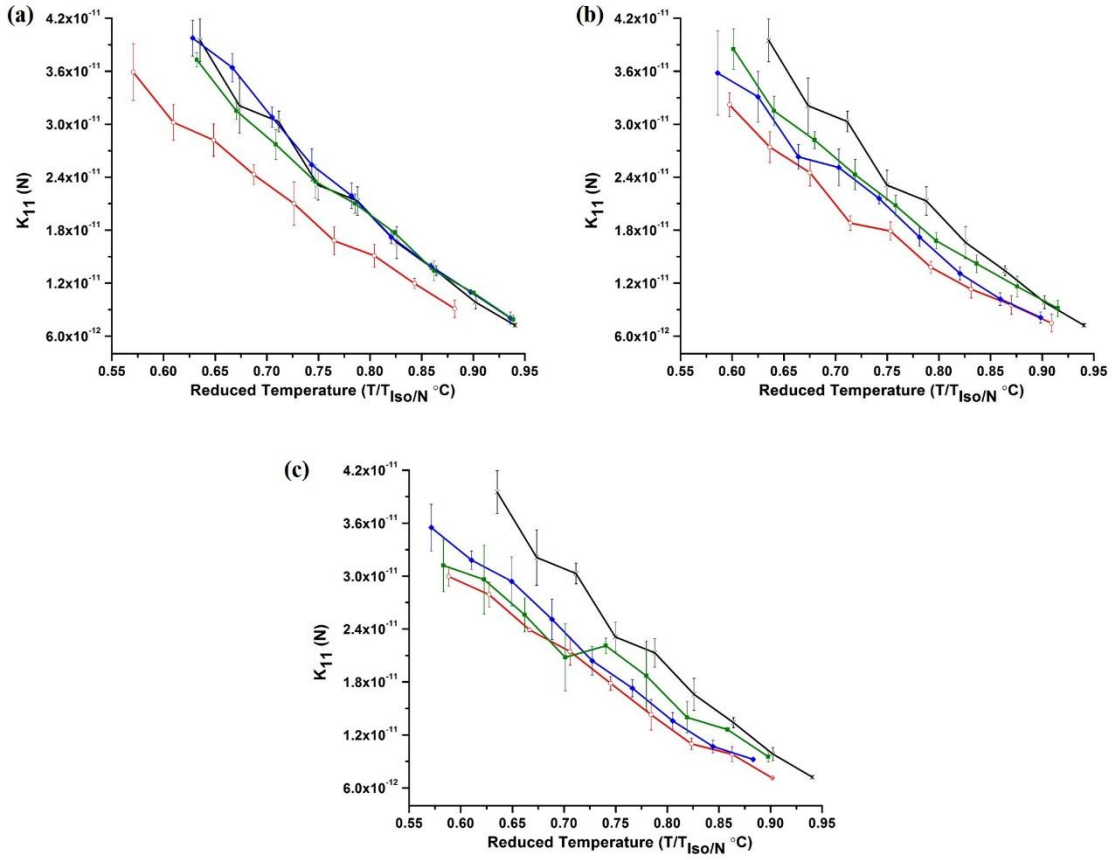

Figure 3.8 Plots of the splay elastic constant, K_{11} vs. the reduced temperature $T/T_{Iso\text{-}N}$ of pure **LC1** (black data set) as well as **QD1** (green), **QD2** (blue) or **QD3** (red) in **LC1** at: (a) 1wt%, (b) 2.5wt%, and (c) 5wt%.

Additional electro-optic data such as $\varepsilon_{\parallel}$ and $\varepsilon_{\perp}$ vs. $T/T_{Iso\text{-}N}$ as well as transmission *vs.* applied voltage measurements at various frequencies can be found in the supplementary information in Appendix A. It is important to note that the decrease in $\Delta\varepsilon$ is caused by a decrease in $\varepsilon_{\parallel}$, with $\varepsilon_{\perp}$ showing values similar to pure **LC1**. Considering all electro-optic measurements, one can conclude that the new magic-sized QDs featuring a much narrower size distribution in comparison to previously examined QDs and Au NPs induce noticeably less significant changes in the electro-optic properties of **LC1**, and most notably no

changes in V_{th}. We also noticed, however, that the magic-sized QDs used in the current study appear to be better dispersible (even in the form of aggregates) in **LC1** judging from the texture characteristics between plain glass (with the exception of the Zn-doped **QD3**) and more importantly in planar EO test cells. Only **QD3** significantly reduces both $\Delta\varepsilon$ and K_{11}. **QD3** is the only QD of the three in this series that shows the formation of birefringent stripes between plain glass slides and, at higher concentration, the induction of domains with homeotropic alignment in planar test cells. In this respect, **QD3** behaves similar to previously studied Au NPs[25] featuring almost identical core size and *n*-alkylthiol capping agents with similar alkyl chain length as myristic acid used here ($C_{12}H_{25}SH$ vs. $C_{13}H_{27}COOH$).

3.3.3 Fluorescence confocal polarizing microscopy (FCPM)

To obtain more detailed information on the distribution of these magic-sized QDs in films of **LC1** between plain glass slides, we performed FCPM studies. Of specific interest are here mixtures of **QD1** at 2.5wt% and **QD3** (2.5wt% are here representative for the entire concentration range) in **LC1**, since only those two QDs showed textures between plain glass slides featuring birefringent stripes and homeotropic alignment in all domains surrounding the stripes.

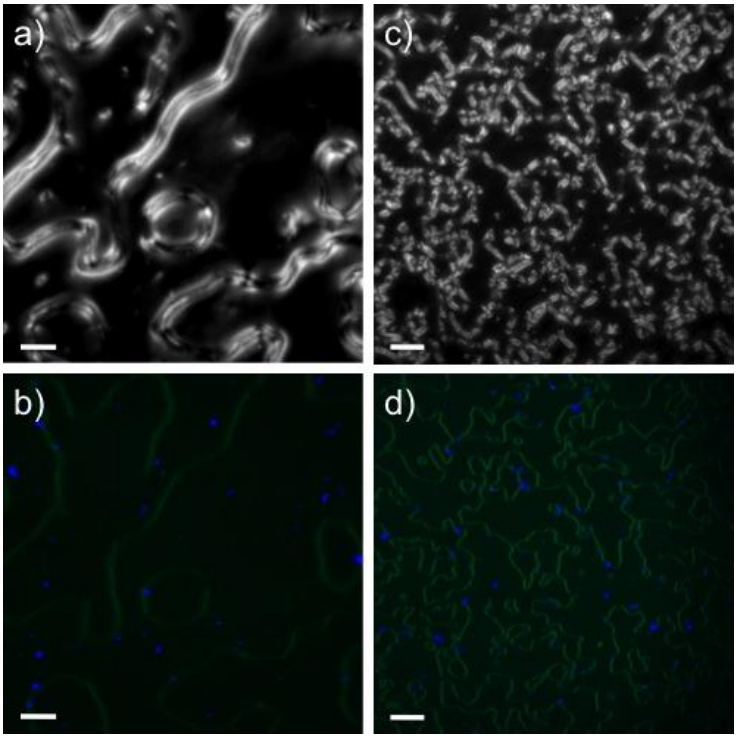

Figure 3.9 POM and two-channel FCPM images of 2.5wt% **QD1** (a, b) and 2.5wt% **QD3** in **LC1** (c, d). (a, c) Transmission channel (POM); (b, d) (*x*-*y*) scan of blue (QD) and green (dye) channel. Scale bars: (a, b) 20 mm; (c, d) 60 mm.

The emission of the dichroic dye mimicking the director orientation of the nematic LC in these domains[35] and the emission from the QDs are easily separated. The final combined images showing both channels confirm homeotropic alignment of **LC1**, planar alignment of the molecules within the birefringent stripes, as well as the (*x*-*y*) distribution of the QDs. Earlier experiments using larger Au NPs have already shown that these birefringent stripes correspond to twist disclinations located at the substrate interface,[36] and established that larger CdSe QDs (4.0 to 4.3 nm in diameter) segregate to the bottom and top interfaces using (*x*-*z*) scans.[37]

Figure 3.9 evidently demonstrates the existence of homeotropic alignment in the areas surrounding the birefringent stripes (no dye emission, see **Figure 3.9**b and d). The

orientation of the LC director within the birefringent stripes was also confirmed as in our previous work[36] by comparison of linearly polarized scans with a circularly polarized (*x*-*y*) scan (see supplementary information). Limited spatial resolution in the *z*-direction while imaging both channels (i.e. dye and QDs), however, prevented us so far from determining the *z*-distribution of these QDs in contrast to earlier FCPM experiments using larger CdSe QDs.[36]

It is important to highlight that all three QDs are generally reasonably well dispersed in **LC1**. Locally elevated PL intensities imaged by confocal microscopy (intense blue signals in **Figure 3.9**b and d) only show that the QDs aggregate in some areas more than in others. The dispersion of the QDs can be demonstrated by adjusting the gain on the PL detector and by using the most suitable aperture of the objective lens. The image in **Figure 3.10** for 2.5wt% **QD3** in **LC1** clearly shows that the QD are dispersed throughout the entire nematic film.

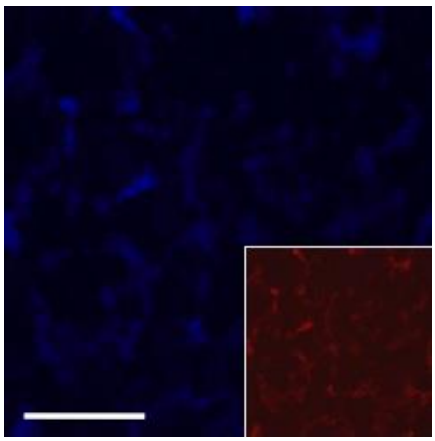

Figure 3.10 FCPM image of 2.5wt% **QD3** in **LC1** (blue channel, i.e. **QD3** only). Inset shows a false colour image of the same area with much better contrast. Scale bar: 20 mm.

3.4 Conclusions

We have, for the first time, tested if truly monodisperse, so-called magic-sized semiconductor quantum dots can be used as dopants in a nematic LC host to unravel fundamental structure-property relationships governing interactions in LC/NP dispersions. Three different magic-sized quantum dots were investigated; two differing in surface defect states (due to differences in the preparation protocol and very small amounts of TOP on the QD surface in addition to the general monolayer capping of myristic acid, and a third one differing from the other two in the core composition (Zn doping). These quantum dots are smaller in comparison to quantum dots studied previously in the same nematic host,[25] but similar in size to gold nanoparticles with a comparable chain length of the aliphatic capping agent.[26]

Surprisingly, the magic-sized quantum dots investigated here only marginally alter the electro-optic properties, yet some very distinct trends are clearly observable. Only the Zn-doped **QD3** quantum dots, which are core-compositionally different from the other two (**QD1** and **QD2**), affect both the electric permittivity along the long molecular axis of the nematic host (**LC1**), $\varepsilon_{\parallel}$ and the splay elastic constant K_{11}, but the effects largely cancel each other out with respect to the threshold voltage, V_{th}. Hence, only slightly lower values for V_{th} were observed, both in capacitance and transmission vs. applied voltage measurements for **QD3** in **LC1**. **QD3** is also the only of the three quantum dots (and **QD1** at 2.5wt% - the mixture with the lowest value for V_{th} in transmission vs. applied voltage measurements) inducing significant textural changes in **LC1** between plain glass slides as well as in rubbed polyimide-coated ITO/glass cells favouring planar alignment over the entire concentration

range (from 1 to 5wt%). In this respect, only **QD3** behaves similar to alkylthiol-capped gold NPs, which induce homeotropic alignment and the formation of birefringent stripes between plain glass and in planar test cells.[27] In fact, since only **QD3** induces significant alignment changes in some smaller localized domains, as observed by POM, one could conclude that primarily segregation phenomena producing altered alignment scenarios are responsible for significant changes in the electro-optic behaviour of this particular N-LC host. Recent experiments by Goodby *et al.*,[38] however, revealed that both types of NPs, NPs that segregate as in most of our NP-doped mixtures as well as well-miscible, LC-decorated NPs, are capable of inducing sizeable electro-optic effects. Considering the series presented here, differences in the density of the monolayer capping (or quality of the monolayer) due to variations in surface defect states might well account for the differences in QD miscibility. Future work will now address the role of electroconvection (or perhaps surface polarization effects[39]) as described in previous work from our groups using Au NPs in the same N-LC host.[29, 37] Finally, images obtained from FCPM studies (*x*-*y* scans) confirm the director field in the birefringent stripes,[36] prove homeotropic alignment in the surrounding domains, show that these magic-sized QDs are reasonably well dispersed in the nematic host, and finally that some domains show more significant QD aggregation than others.

Acknowledgement

This work was financially supported by the Natural Science and Engineering Research Council (NSERC) of Canada, the Canada Foundation for Innovation (CFI), the Manitoba Research and Innovation Fund (MRIF), The University of Manitoba's Technology Transfer Office (NSERC/CIHR Intellectual Property Mobilization), the Deutsche Forschungsgemeinschaft (DFG, KI 411), the European Science Foundation (ESF-EUROCORES, SONS II program, LCNANOP project), and by the National Research Council (NRC) of Canada. The authors would like to thank A. Billy and Md. Badruz Zaman (at the Steacie Institute for Molecular Science) for the synthesis of the quantum dots, and Dr. X. Wu for the TEM analysis of **QD3**. Finally, we are grateful for the help of Dr. K. McEleney (Chemistry, University of Manitoba) for XPS measurements on the quantum dots, and Dr. M. S. Freund for access to the XPS instrument.

3.5 References

1. Gennes, P. G. d.; Prost, J., *The Physics of Liquid Crystals*. Clarendon Press: 1995.
2. Leys, J.; Glorieux, C.; Thoen, J. *Phys. Rev. E* **2008,** 77, (6), 061707.
3. Cordoyiannis, G.; Kralj, S.; Nounesis, G.; Kutnjak, Z.; Žumer, S. *Phys. Rev. E* **2007,** 75, (2), 021702.
4. Różański, S. A.; Thoen, J. *Liq. Crys.* **2005,** 32, (3), 331 - 340.
5. Zakharov, A. V.; Thoen, J. *Eur. Phys. J. E* **2005,** 17, (4), 447-453.
6. Scalia, G. *ChemPhysChem* **2010,** 11, 333-340.
7. Dolgov, L.; Yaroshchuk, O.; Lebovka, M. *Mol. Cryst. Liq. Cryst.* **2008,** 496, 212-229.
8. Jo, E. M.; Srivastava, A. K.; Bae, J. J.; Kim, M.; Lee, M. H.; Lee, H. K.; Lee, S. E.; Lee, S. H.; Lee, Y. H. *Mol. Cryst. Liq. Cryst.* **2009,** 498, 74-82.
9. Basu, R.; Iannacchione, G. S. *Appl. Phys. Lett.* **2008,** 93, (18), 183105-3.
10. Dierking, I.; Casson, K.; Hampson, R. *Jpn. J. Appl. Phys.* **2008,** 47, 6390-6393.
11. Huang, C.; Lin, Y.; Huang, Y. *Jpn. J. Appl. Phys.* **2008,** 47, (8), 6407-6409.
12. Kim, J. Y.; Kim, D. K.; Kim, S. H. *Eur. Polym. J.* **2009,** 45, 316-324.
13. Miyama, T.; Thisayukta, J.; Shiraki, H.; Sakai, Y.; Shiraishi, Y.; Toshima, N.; Kobayashi, S. *Jpn. J. Appl. Phys.* **2004,** 43, (5A), 2580-2584.
14. Nishida, N.; Shiraishi, Y.; Kobayashi, S.; Toshima, N. *J. Phys. Chem. C* **2008,** 112, (51), 20284-20290.
15. Rivoire, O.; Barre, J. *Phys. Rev. Lett.* **2006,** 97, (14), 148701.
16. Haraguchi, F.; Inoue, K.-i.; Toshima, N.; Kobayashi, S.; Takatoh, K. *Jpn. J. Appl. Phys.* **2007,** 46, (33-35), L796-L797.

17. Qi, H.; Hegmann, T. *J. Mater. Chem.* **2006,** 16, (43), 4197-4205.

18. Li, F. H.; Buchnev, O.; Il Cheon, C.; Glushchenko, A.; Reshetnyak, V.; Reznikov, Y.; Sluckin, T. J.; West, J. L. *Phys. Rev. Lett.* **2006,** 97, (14), 147801.

19. Hegmann, T.; Qi, H.; Marx, V. M. *J. Inorg. Organomet. P.* **2007,** 17, (3), 483-508.

20. Qi, H.; Hegmann, T. *J. Mater. Chem.* **2008,** 18, (28), 3288-3294.

21. Stamatoiu, O.; Mirzaei, J.; Feng, X.; Hegmann, T. *Top. Curr. Chem.* **2012,** 318, 331-93.

22. Kobayashi, S.; Miyama, T.; Nishida, N.; Sakai, Y.; Shiraki, H.; Shiraishi, Y.; Toshima, N. *J. Display Techn.* **2006,** 2, (2), 121-129.

23. Dierking, I.; Scalia, G.; Morales, P.; LeClere, D. *Adv. Mater.* **2004,** 16, 865-869.

24. Schymura, S.; Kuehnast, M.; Lutz, V.; Jagiella, S.; Dettlaff-Weglikowska, U.; Roth, S.; Giesselmann, F.; Tschierske, C.; Scalia, G.; Lagerwall, J. *Adv. Funct. Mater.* **2010,** 20, 3350-3357.

25. Kinkead, B.; Hegmann, T. *J. Mater. Chem.* **2010,** 20, (3), 448-458.

26. Qi, H.; Kinkead, B.; Hegmann, T. *Adv. Funct. Mater.* **2008,** 18, (2), 212-221.

27. Qi, H.; Hegmann, T. *ACS Appl. Mater. Inter.* **2009,** 1, (8), 1731-1738.

28. Qi, H.; Kinkead, B.; Hegmann, T. *Proc. of SPIE-Int. Soc. Opt. Eng.* **2008,** 6911, 691106.

29. Urbanski, M.; Kinkead, B.; Qi, H.; Hegmann, T.; Kitzerow, H. S. *Nanoscale* **2010,** 2, (7), 1118-1121.

30. Ouyang, J.; Zaman, M. B.; Yan, F. J.; Johnston, D.; Li, G.; Wu, X.; Leek, D.; Ratcliffe, C. I.; Ripmeester, J. A.; Yu, K. *J. Phys. Chem. C* **2008,** 112, (36), 13805-13811.

31. Yu, K.; Hu, M. Z.; Waing, R. B.; Le Piolet, M.; Frotey, M.; Zaman, M. B.; Wu, X. H.; Leek, D. M.; Tao, Y.; Wilkinson, D.; Li, C. S. *J. Phys. Chem. C* **2010,** 114, (8), 3329-3339.

32. Wang, L.; Sun, X. D.; Liu, W. J.; Yu, X. *Colloids and Surfaces. A: Physicochem. Eng. Aspects* **2010,** 353, (2-3), 232-237.

33. Wu, S. T.; Coates, D.; Bartmann, E. *Liq. Cryst.* **1991,** 10, (5), 635-646.

34. Mixtures of **QD1** and **QD3** in **LC1** at 1wt% show similar steep slope changes as pure **LC1** in transmission vs. applied voltage scans allowing for an easy determination of V_{th}. Mixtures at higher QD concentrations (2.5 to 5wt%) feature a more gradual increase in the slope of intensity vs. applied voltage (see supplemantary information) and lower values for V_{th} can be derived. For **QD1**, however, the lowest V_{th} is observed for the 2.5wt% mixture in **LC1**. For **QD3**, V_{th} decreases gradually with increasing QD concentration in **LC1**.

35. Smalyukh, I. I.; Shiyanovskii, S. V.; Lavrentovich, O. D. *Chem. Phys. Lett.* **2001,** 336, 88-96.

36. Urbanski, M.; Kinkead, B.; Hegmann, T.; Kitzerow, H.-S. *Liq. Cryst.* **2010,** 37, (9), 1151-1156.

37. Kinkead, B.; Urbanski, M.; Qi, H.; Kitzerow, H.-S.; Hegmann, T. *Proc. SPIE-Int. Soc. Opt. Eng.* **2010,** 7775, 77750C/1-77750C/11.

38. Draper, M.; Saez, I. M.; Cowling, S. J.; Gai, P.; Heinrich, B.; Donnio, B.; Guillon, D.; Goodby, J. W. *Adv. Funct. Mater.* **2011,** 21, (7), 1260-1278.

39. Nazarenko, V. G.; Klouda, R.; Lavrentovich, O. D. *Phys. Rev. E* **1998,** 57, (1), R36-R38.

Appendix A

Appendix A: Supplementary Information for Chapter 3

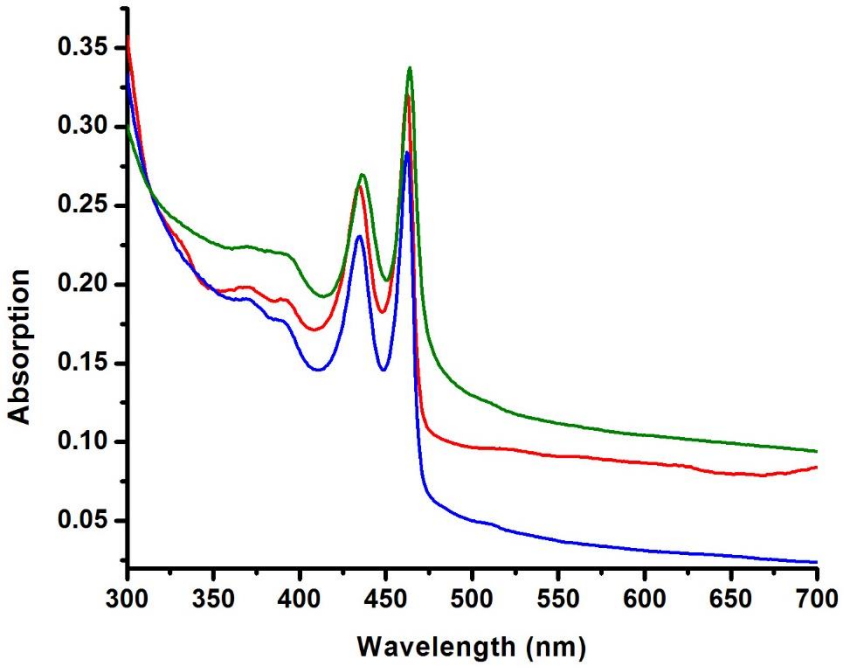

Figure A3.1 Absorption spectra of magic-sized quantum dots **QD1** (green), **QD2** (blue), and **QD3** (red) in toluene. Note the exact identical absorption maxima and FWHM.

Additional FCPM images

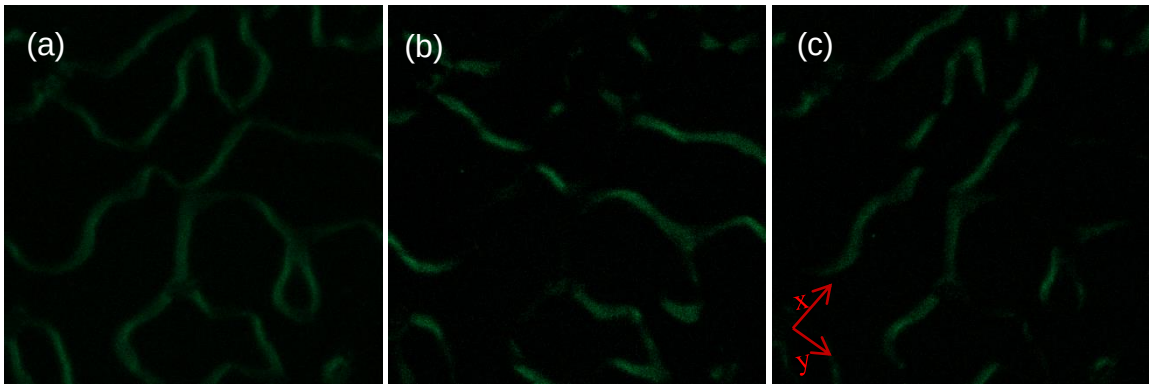

Figure A3.2 Fluorescence confocal polarising microscopy image of a sample obtained by adding 0.007% (by weight) of the dichroic fluorescent dye BTBP to the 2.5wt% QD3 in LC1. Illumination (only green channel; emission of dye) with (a) circularly polarised light, (b) linearly polarised light (E along y), and (c) linearly polarised light (E along x), respectively.

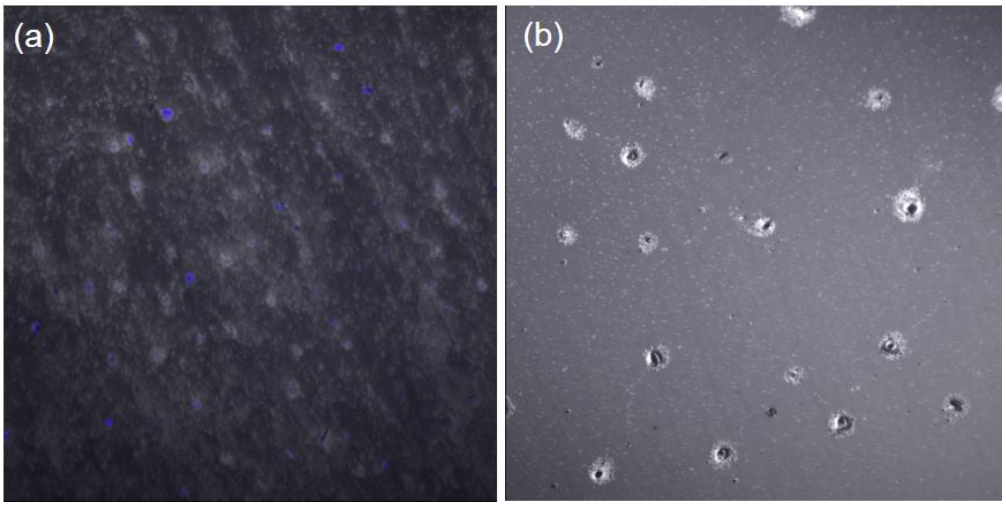

Figure A3.3 Fluorescence confocal microscopy images of LC1 in polyimide-coated ITO test cells (4 micron spacers): (a) 5wt% QD1 (compare to image in Figure 2f in the main text), and (b) 2.5wt% QD2 (compare to image in Figure 3e in the main text). Only the blue (QDs) and the transmission channel are observed in both images. These images highlight that the QDs are only to some extent responsible for the point-like defects observed by POM in planar cells.

Permittivities measured on cooling

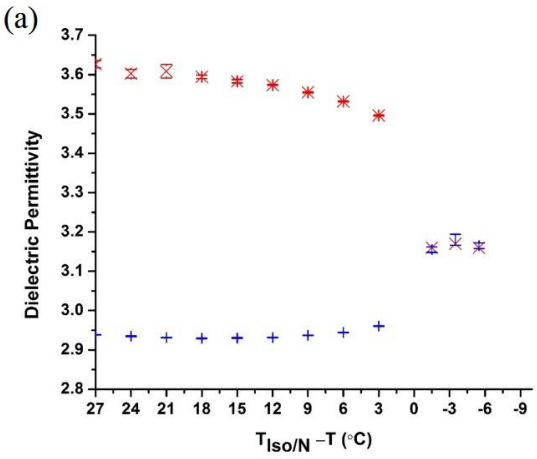

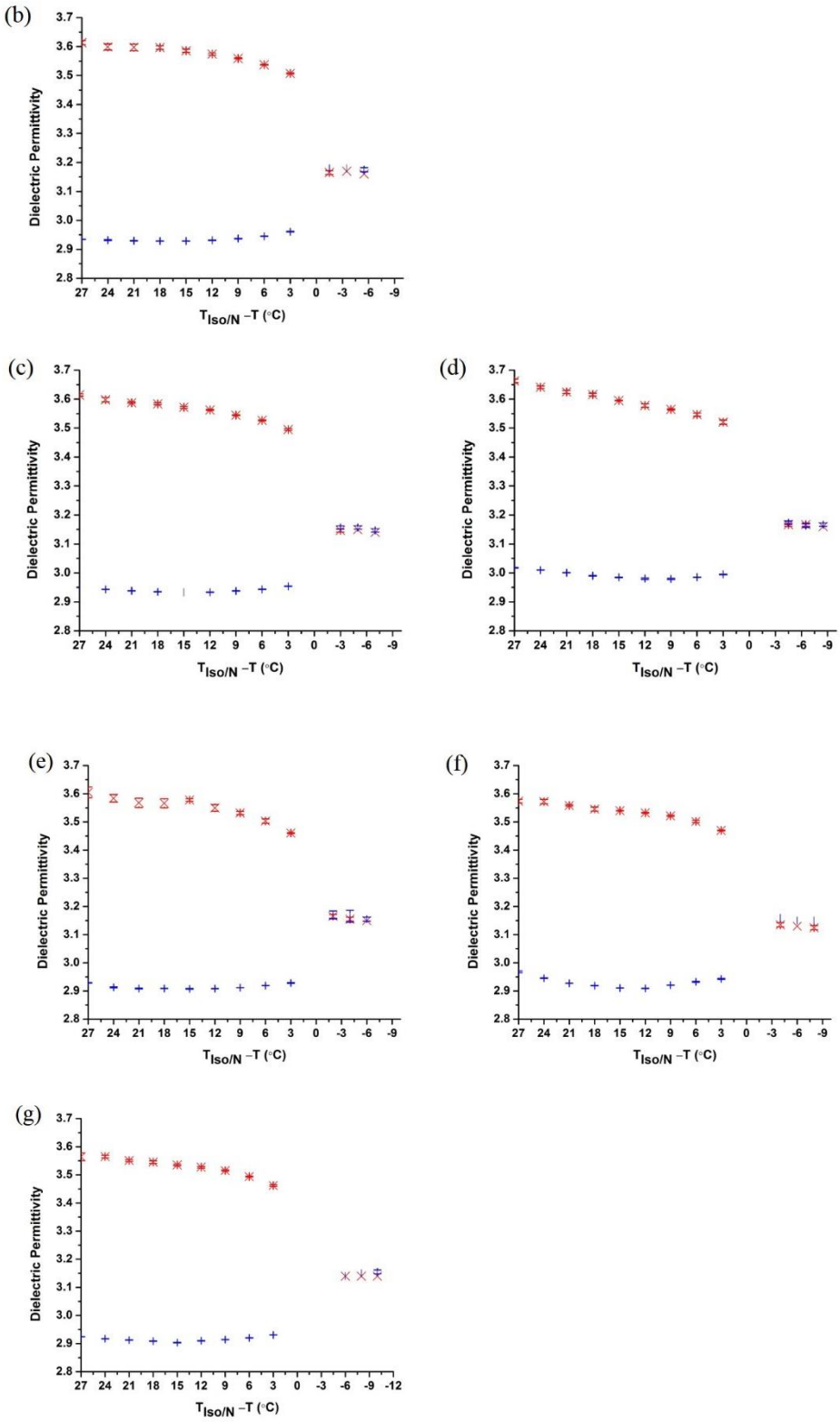
(b)
(c)
(d)
(e)
(f)
(g)
Dielectric Permittivity
$T_{Iso/N} - T$ (°C)

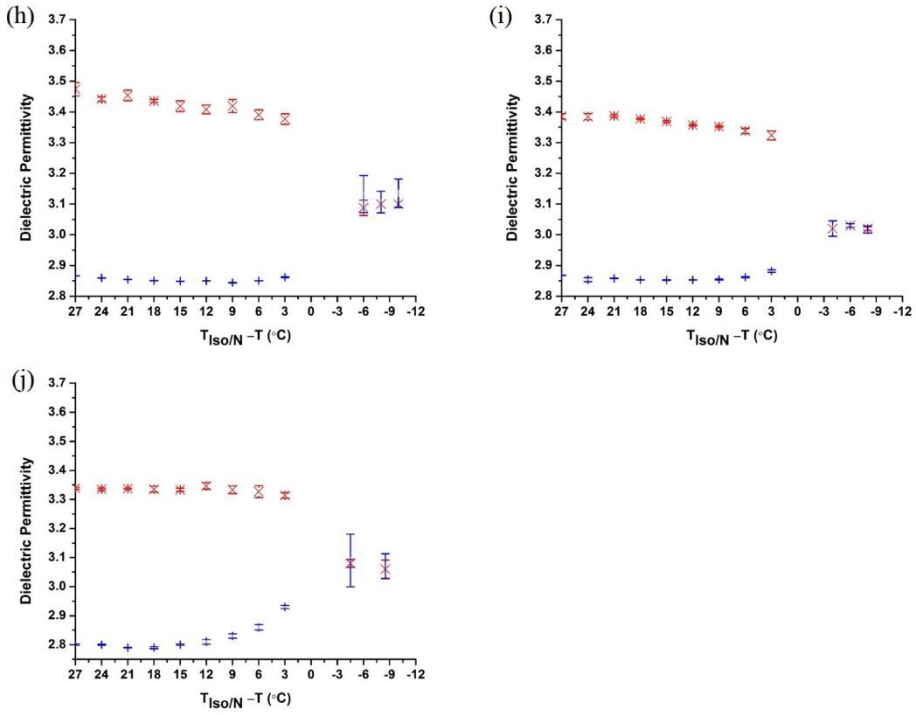

Figure A3.4 Plots of the parallel (red cross) and the perpendicular (blue line) permittivity vs. the reduced temperature measured on cooling for pure LC1 (a), and mixtures of LC1 with 1, 2.5 and 5 wt% of QD1 (b-d), QD2 (e-g) and QD3 (h-j)

Resistivity

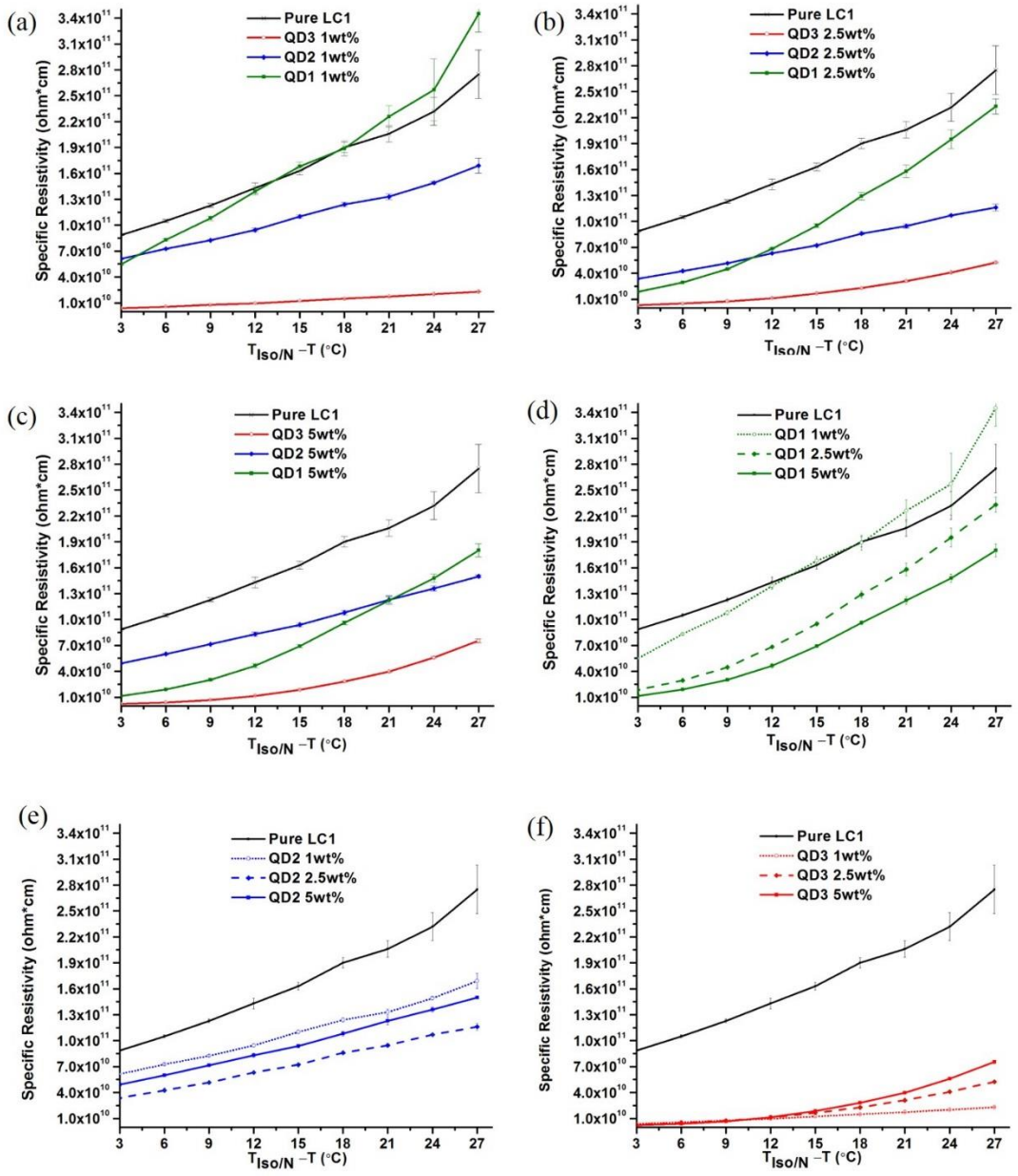

Figure A3.5 Plots of the specific resistivity vs. reduced temperature for pure LC1 and mixtures of LC1 with 1, 2.5 and 5 wt% of QD1-3 (a-f)

Frequency dependence

Experimental setup:

The electro-optical measurements were performed on a Leica Ortholux II POL-BK microscope with a white light source and a green interference filter (541 nm). All samples were positioned in the beam path under an angle of 45° between crossed polarizers. To apply voltages, an Analogic 2030 waveform synthesizer and a Krohn-Hite model 7500 amplifier were used. The light intensity was detected using an Oriel photomultiplier tube and a Keithley 197 DMM. Both signals (voltage and intensity) were averaged (8 to 256 circles) and stored on a Gould 4064 oscilloscope.

Results:

The electro-optical response was measured at different frequencies (0.1 Hz, 1 Hz, 5 Hz, 10 Hz, 50 Hz, 100 Hz, 500 Hz and 1000 Hz). To point out differences or unusual effects due to nanoparticle doping, we first measured the electro-optic response of the pure LC. The results for pure **LC1** are plotted below, followed by the QD-doped samples:

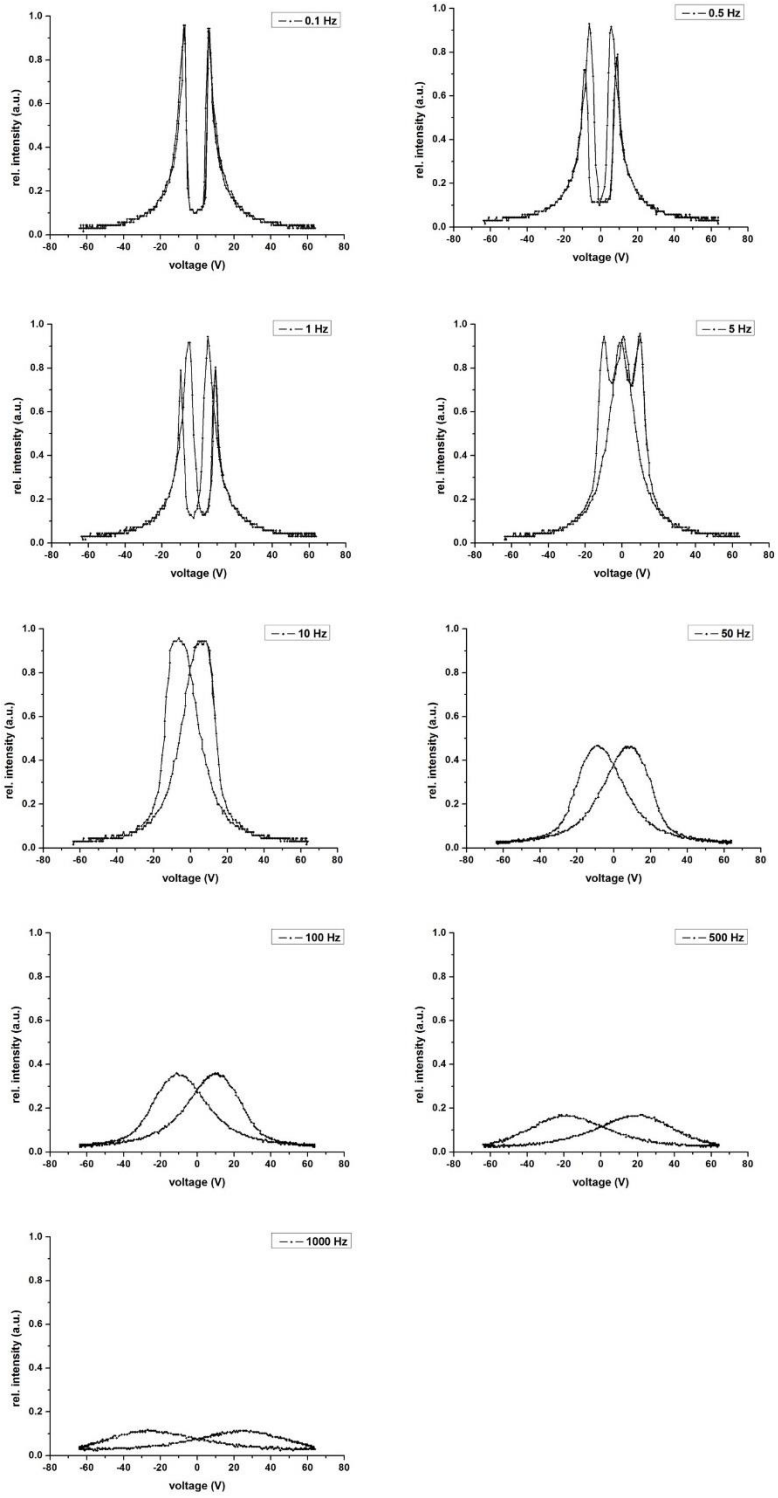

Figure A3.6 Plots of the intensity vs. voltage measured at different frequencies for electro-optic response of pure LC1

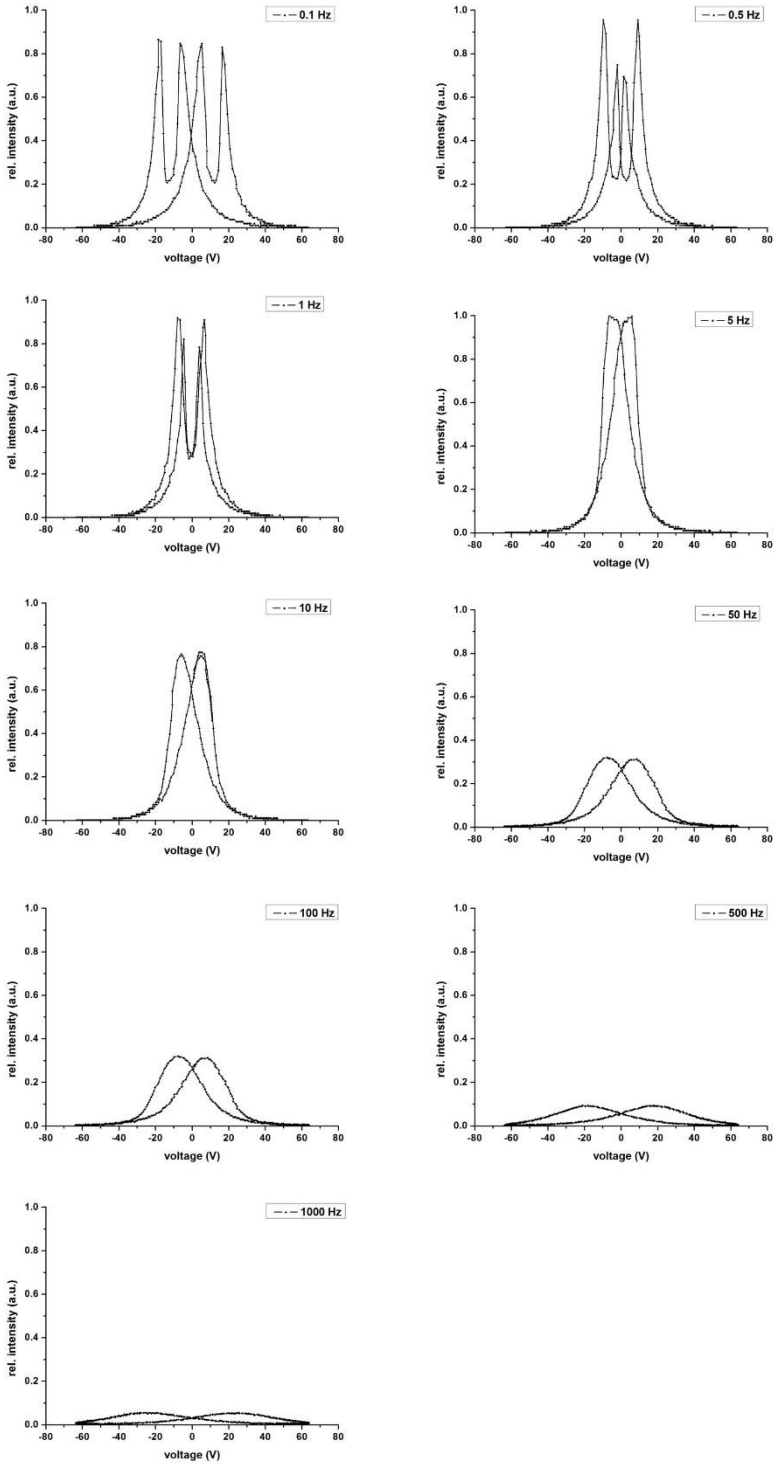

Figure A3.7 Plots of the intensity vs. voltage measured at different frequencies for electro-optic response of LC1 samples doped with QD1 at 1 wt%

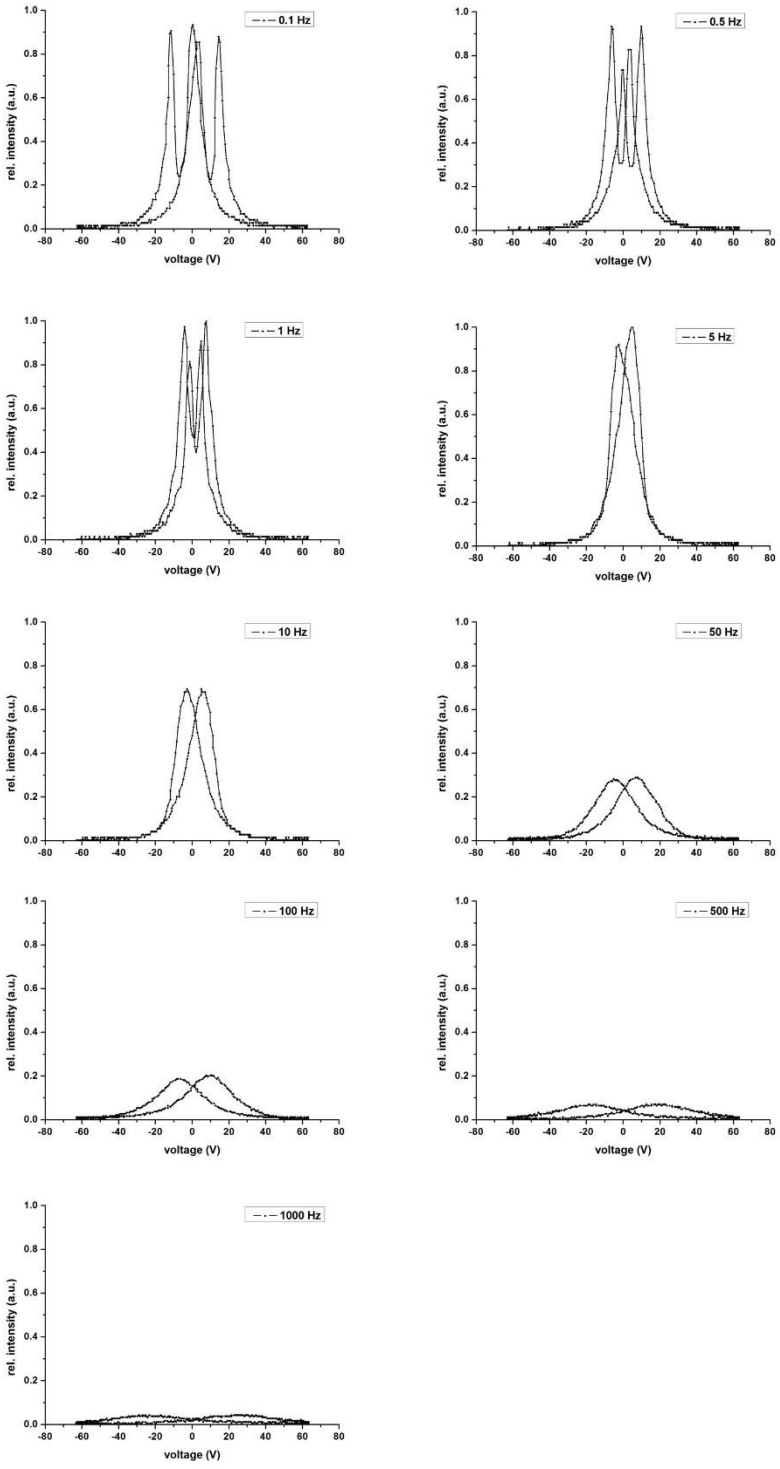

Figure A3.8 Plots of the intensity vs. voltage measured at different frequencies for electro-optic response of LC1 samples doped with QD1 at 2.5 wt%

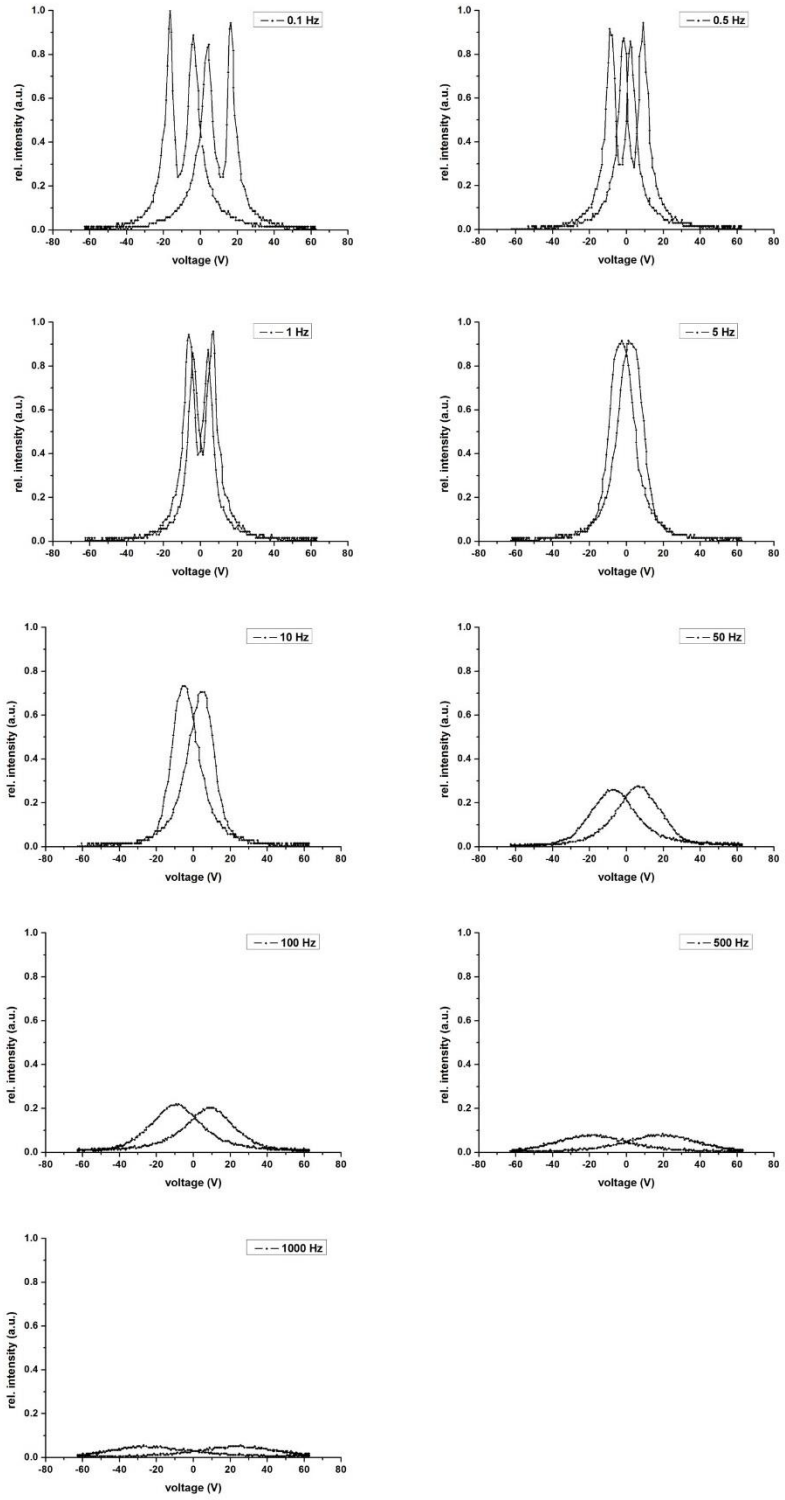

Figure A3.9 Plots of the intensity vs. voltage measured at different frequencies for electro-optic response of LC1 samples doped with QD1 at 5 wt%

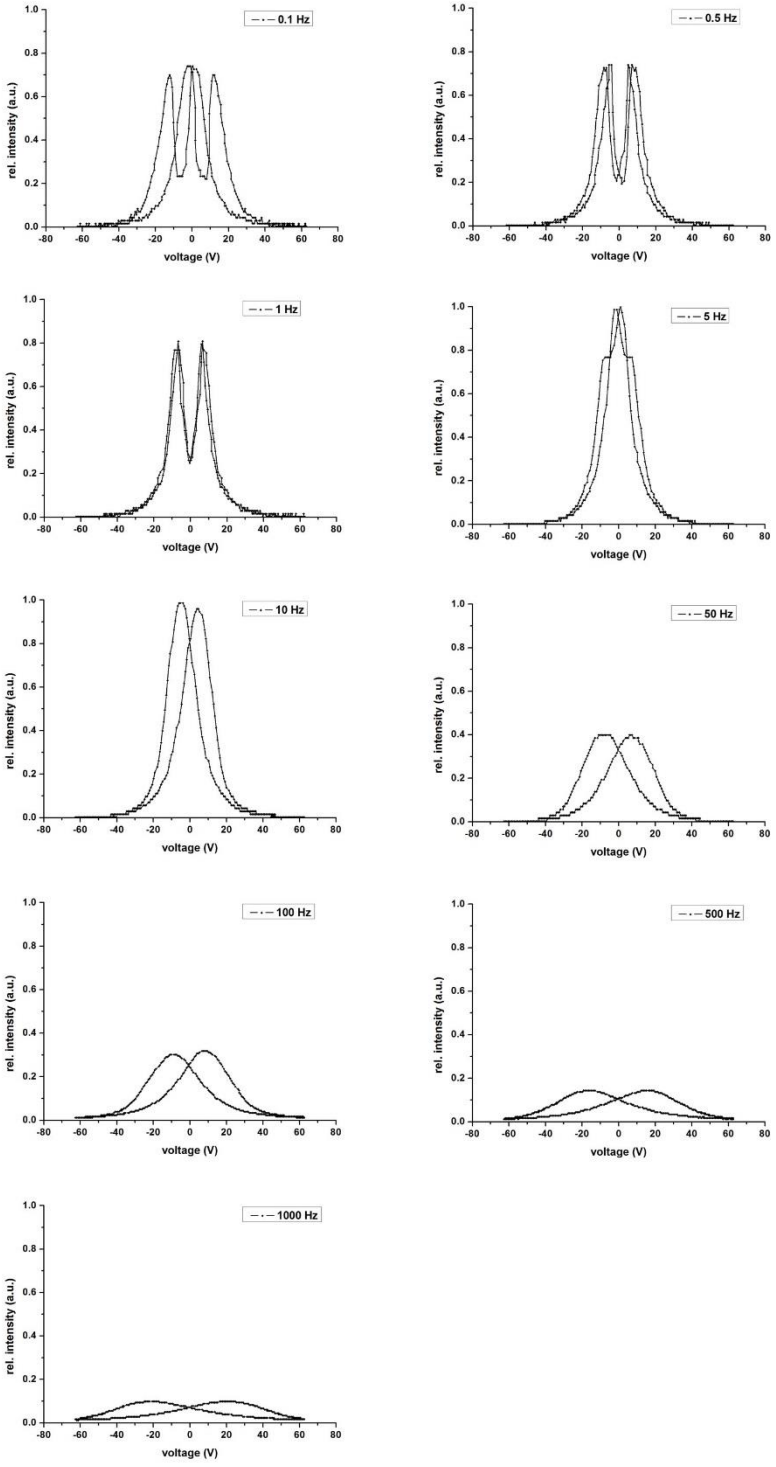

Figure A3.10 Plots of the intensity vs. voltage measured at different frequencies for electro-optic response of LC1 samples doped with QD3 at 1 wt%

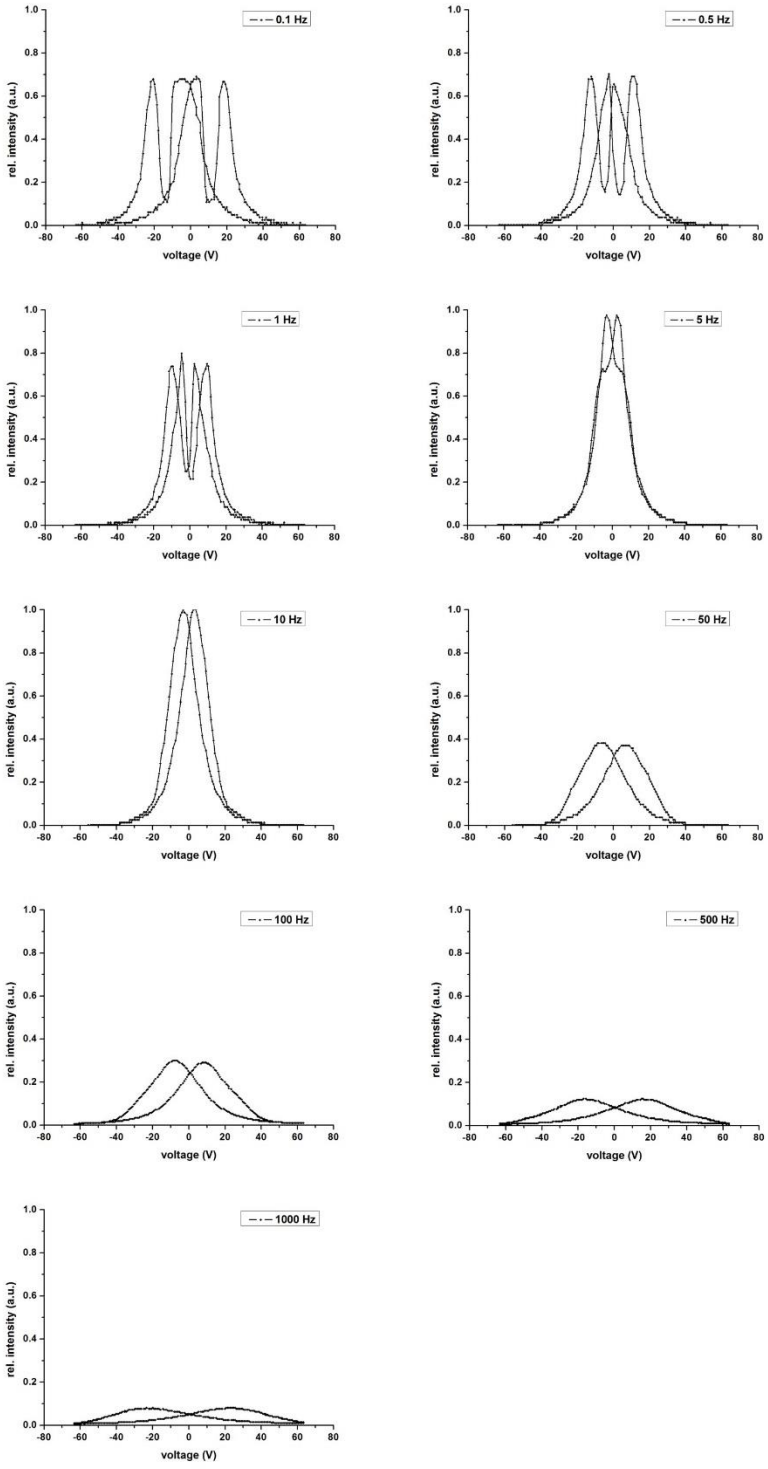

Figure A3.11 Plots of the intensity vs. voltage measured at different frequencies for electro-optic response of LC1 samples doped with QD3 at 2.5 wt%

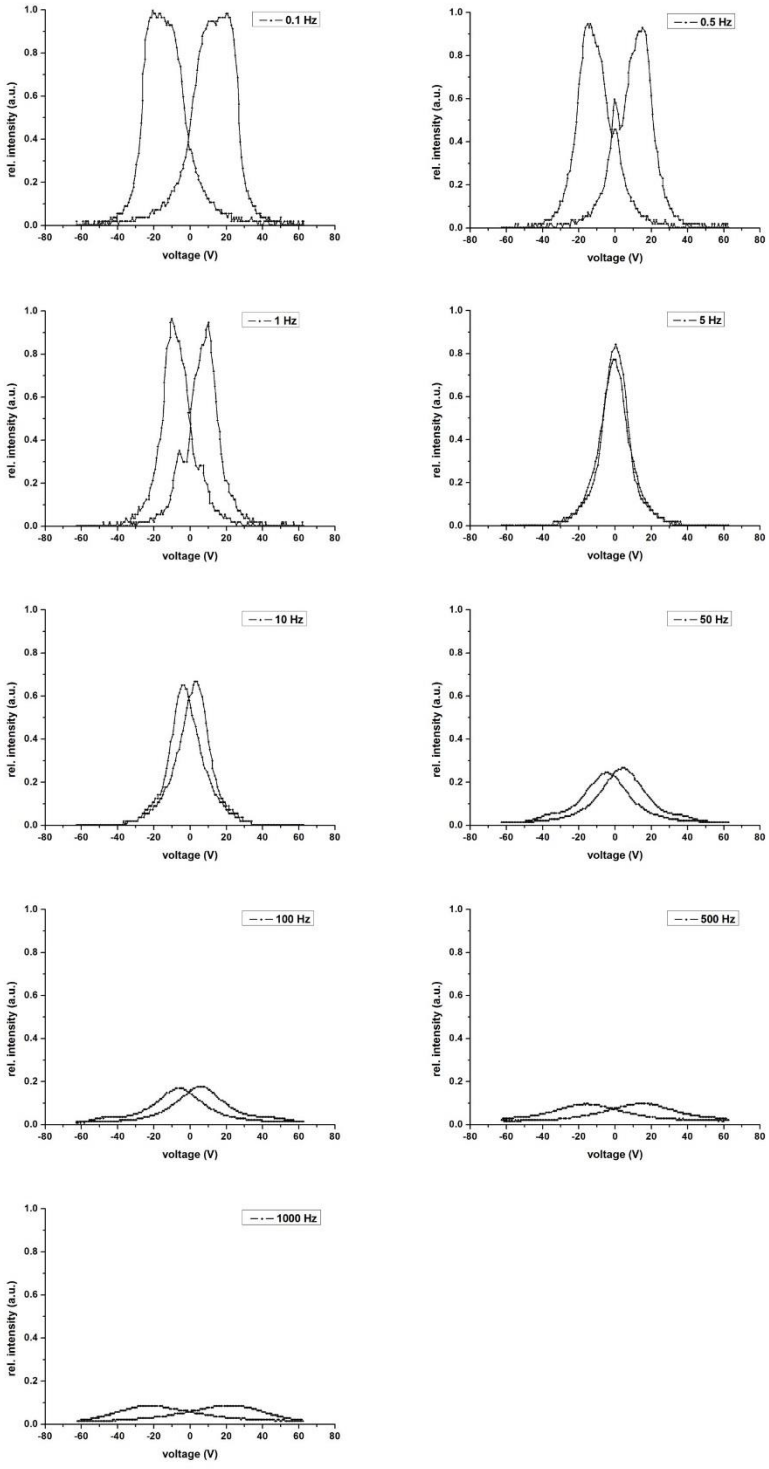

Figure A3.12 Plots of the intensity vs. voltage measured at different frequencies for electro-optic response of LC1 samples doped with QD3 at 5 wt%

Transmission vs. applied voltage

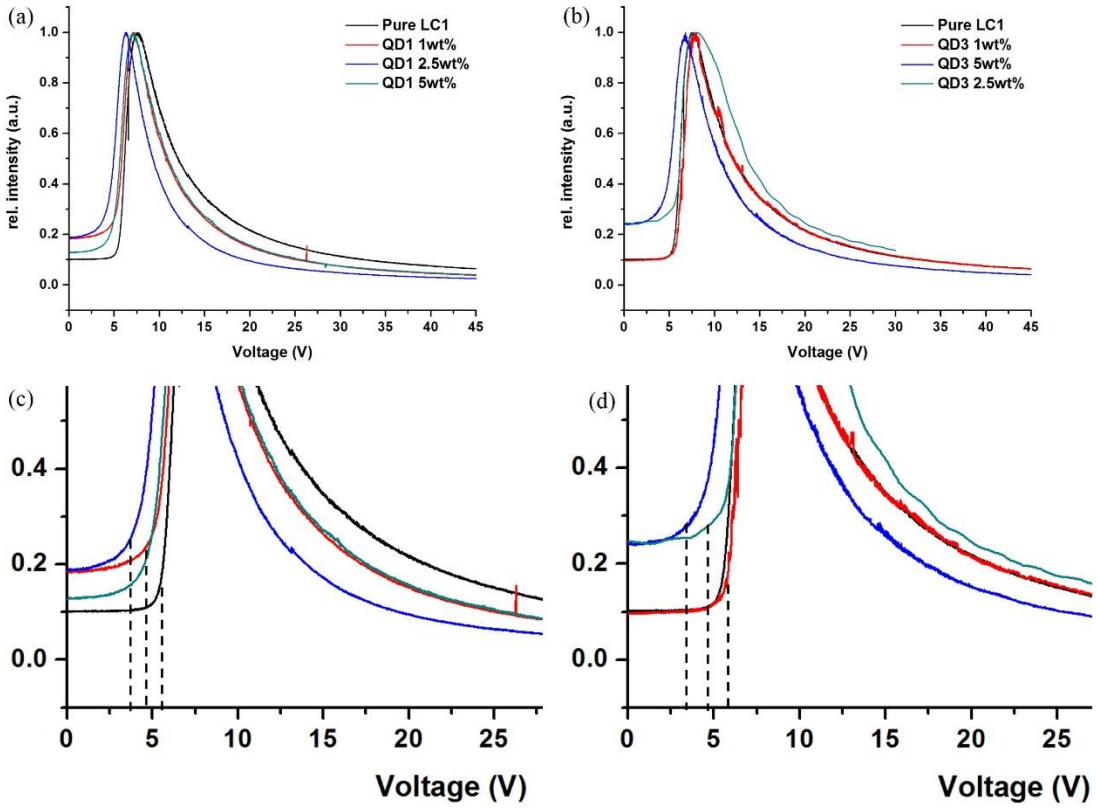

Figure A3.13 Plots of the intensity vs. voltage based on electro-optic response obtained from transmission measurements for pure LC1 and doped LC1 at different concentrations of QD1 (a, c) or QD3 (b, d). In such plots, 10% increase in intensity is accounted for threshold voltage. Lower threshold voltage values are observed for doped LC1 samples. Plots c and d are enlarged section of plots a and d, respectively.

Comparison of ultrasonication using sonotrode (internal sonication) vs. sonication bath (external sonication)

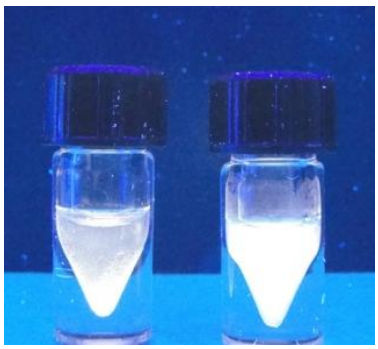

Figure A3.14 Photograph of vials under UV light irradiation (λ_{exc} = 366 nm) showing the effect of sonication conditions for **LC1** doped with **QD1** (as a representative example) at 5wt% 10 minutes after sonication: (left vial) using 5 minutes regular sonication bath, and (right vial) using 5 minutes ultrasonication (Sonics VCX 750 Watts, Frequency 20 kHz) in pulse mode (5 seconds *On* followed by 5 seconds *Off* at an amplitude of 21%). Note the improved homogeneity of the mixture on the right.

XPS

XPS analysis of the QD samples was performed using a Kratos AXIS ULTRA spectrometer with a 300 W monochromated Al Kα source and a delay line detector. The survey and high-resolution scans were recorded with pass energies of 160 and 40 eV, respectively. All spectra were collected at 90° take-off angle and referenced to the C 1s peak set at 285 eV. The background pressure in the analyzer chamber was ~10^{-9} Torr. For quantitative analysis sensitivity factors supplied by the instrument manufacturer were used.

QD1 (CdSe)

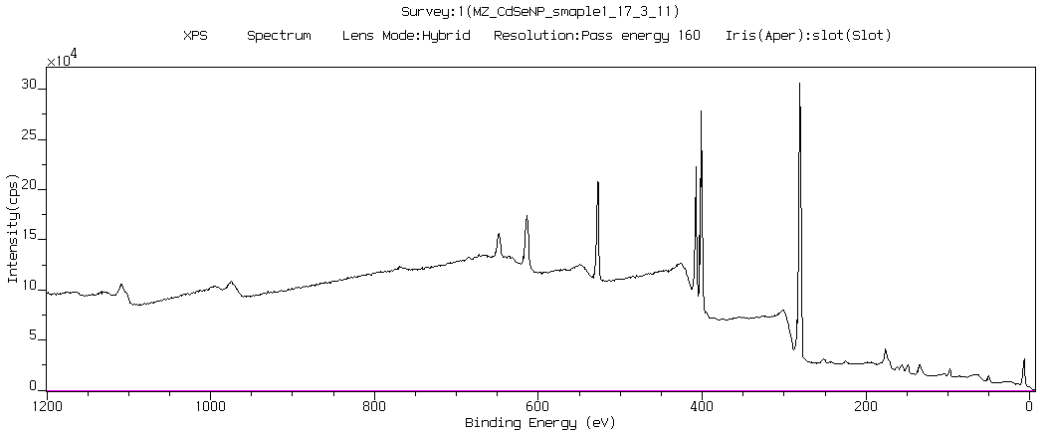

Peak	Type	Position BE (eV)	FWHM (eV)	Raw Area (cps eV)	RSF	Atomic Mass	Atomic Conc %	Mass Conc %
C 1s	Reg	285.023	1.154	103130.8	0.278	12.011	85.35	62.07
O 1s	Reg	531.823	1.763	39531.6	0.780	15.999	10.33	10.01
Cd 3d	Reg	405.323	1.163	109032.4	6.623	112.422	3.58	24.37
Se 3d	Reg	54.023	1.593	2507.3	0.853	78.982	0.74	3.55

Peak	Type	Position BE (eV)	FWHM (eV)	Raw Area (cps eV)	RSF	Atomic Mass	Atomic Conc %	Mass Conc %
Cd 3d	Reg	405.323	1.163	109032.4	6.623	112.422	82.83	87.29
Se 3d	Reg	54.023	1.593	2507.3	0.853	78.982	17.17	12.71

QD2 (CdSe)

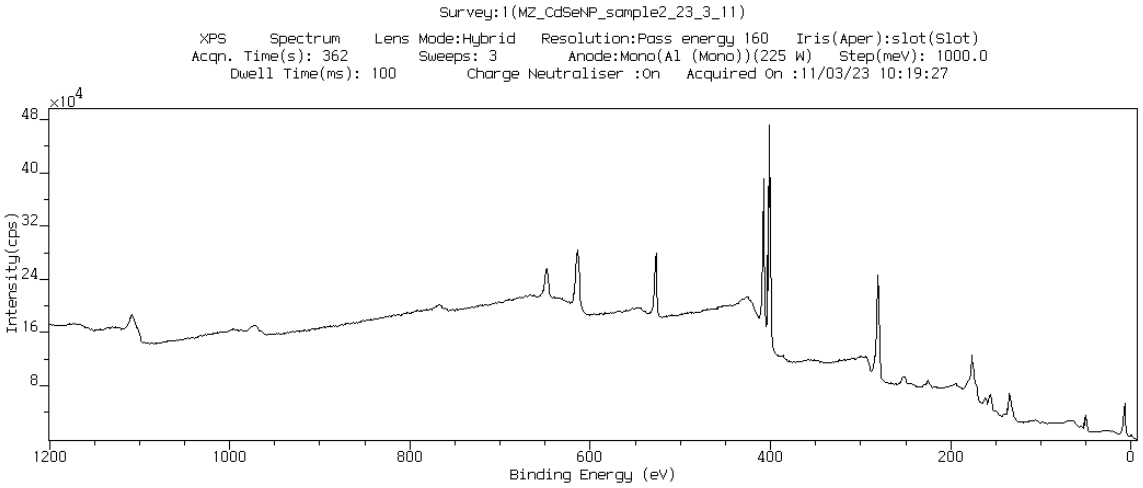

Peak	Type	Position BE (eV)	FWHM (eV)	Raw Area (cps eV)	RSF	Atomic Mass	Atomic Conc %	Mass Conc %
C 1s	Reg	285.024	1.127	51670.3	0.278	12.011	71.78	35.28
O 1s	Reg	531.724	1.608	34385.4	0.780	15.999	15.09	9.88
Cd 3d	Reg	405.524	1.045	164580.4	6.623	112.422	9.07	41.72
Se 3d	Reg	54.424	1.659	8179.0	0.853	78.982	4.06	13.13

Peak	Type	Position BE (eV)	FWHM (eV)	Raw Area (cps eV)	RSF	Atomic Mass	Atomic Conc %	Mass Conc %
Cd 3d	Reg	405.524	1.045	164580.4	6.623	112.422	69.06	76.06
Se 3d	Reg	54.424	1.659	8179.0	0.853	78.982	30.94	23.94

QD3 (CdSe@Zn) → Zn-rich surface (surface doping)

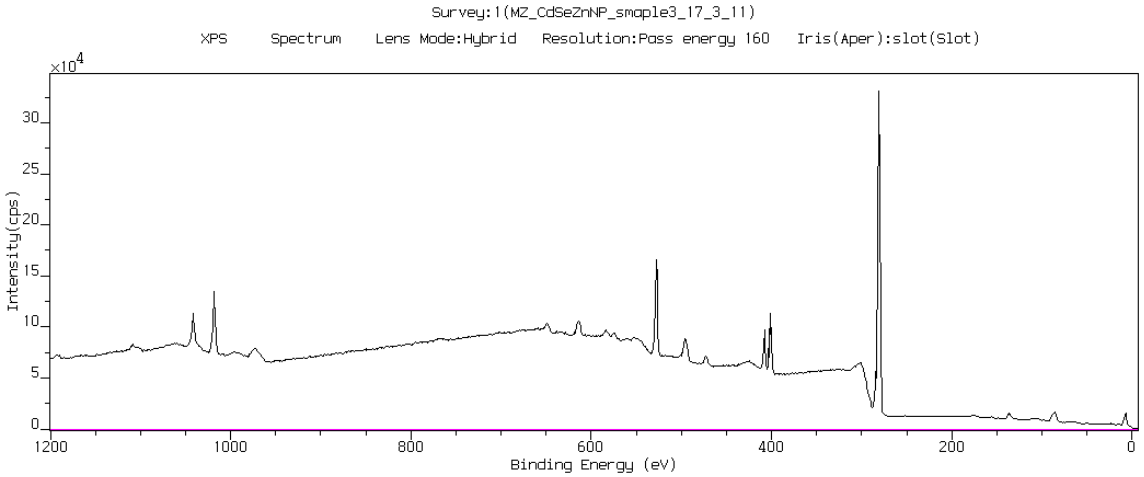

Peak	Type	Position BE (eV)	FWHM (eV)	Raw Area (cps eV)	RSF	Atomic Mass	Atomic Conc %	Mass Conc %
C 1s	Reg	285.002	1.234	109850.9	0.278	12.011	88.99	74.48
O 1s	Reg	532.002	1.639	31933.9	0.780	15.999	8.17	9.11
Cd 3d	Reg	405.502	1.330	31809.6	6.623	112.422	1.02	8.01
Se 3d	Reg	54.602	1.547	431.7	0.853	78.982	0.13	0.69
Zn 2p	Reg	1022.502	2.003	61732.0	5.589	65.387	1.69	7.72

Peak	Type	Position BE (eV)	FWHM (eV)	Raw Area (cps eV)	RSF	Atomic Mass	Atomic Conc %	Mass Conc %
Cd 3d	Reg	405.502	1.330	31809.6	6.623	112.422	35.98	48.79
Se 3d	Reg	54.602	1.547	431.7	0.853	78.982	4.40	4.19
Zn 2p	Reg	1022.502	2.003	61732.0	5.589	65.387	59.62	47.02

Peak	Type	Position BE (eV)	FWHM (eV)	Raw Area (cps eV)	RSF	Atomic Mass	Atomic Conc %	Mass Conc %
Cd 3d	Reg	405.502	1.330	31809.6	6.623	112.422	89.10	92.09
Se 3d	Reg	54.602	1.547	431.7	0.853	78.982	10.90	7.91

TEM

A discussion on the synthesis and characterization including detailed TEM analyses of QD1 and QD2 can be found in earlier publications by Yu *et al.* (see references [30] and [31] of chapter 3). A high-resolution TEM image for **QD3** is shown below (TEM was performed on a JEOL JEM-2100F electron microscope operating at 200 kV and equipped with a Gatan UltraScan 1000 CCD camera. A TEM sample was prepared by depositing a dilute dispersion of a purified sample in toluene onto a 300 mesh carbon-coated TEM copper grid and dried in air.) On TEM grids, some aggregation after solvent evaporation leads to larger QD assemblies, which can be broken up by re-dispersing them in toluene or hexane.

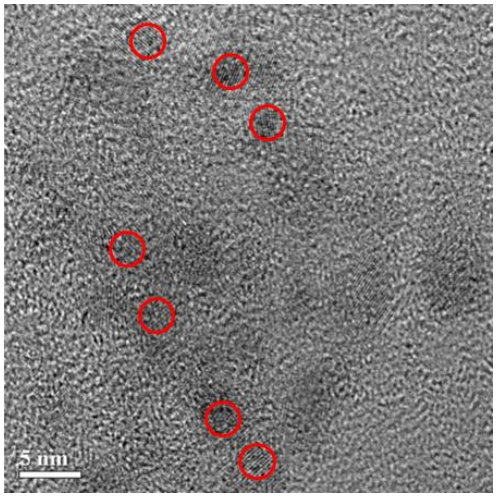

Figure A3.15 HR-TEM of QD3

Connecting Text for Chapter 4

Chapters 2 and 3 described many aspects of colloidal dispersions in nematic LCs. The stability of NP dopants in the LC medium is an important issue that needs to be resolved in order to fully exploit applications of LC-NP composites. In Chapter 4, we presents the synthesis and functionalization of Au NPs using silane conjugation chemistry. The silanized Au NPs are shown to have improved thermal and chemical stability in the colloidal form and in LC media. Our observations and measurements confirmed higher stability and miscibility of silanized Au NPs functionalized with aliphatic chains in nematic LC hosts. Electro-optic data collected for the silanized Au NPs, allowed a comparison with previous data from studies using non-silanized alkanethiolate-capped Au NPs, and a better understanding of the role and importance of robust ligands for NPs used as LC dopants.

Chapter 4

Hydrophobic Gold Nanoparticles via Silane Conjugation – Chemically and Thermally Robust Nanoparticles as Dopants for Nematic Liquid Crystals

Hydrophobic Gold Nanoparticles via Silane Conjugation – Chemically and Thermally Robust Nanoparticles as Dopants for Nematic Liquid Crystals

Javad Mirzaei[a], Marin Urbanski[b], Heinz-S. Kitzerow[b] and Torsten Hegmann[a,c,d]

[a] Department of Chemistry, University of Manitoba, Winnipeg, MB, R3T 2N2 Canada

[b] Department of Chemistry, University of Paderborn 33098 Paderborn, Germany

[c] *C*hemical Physics Interdisciplinary Program & Liquid Crystal Institute, Kent State University, Kent, OH 44242 USA

[d] Department of Pharmacology and Therapeutics, University of Manitoba, Winnipeg, MB, R3T 2N2 Canada

Reproduced with permission from *Philosophical Transactions of the Royal Society A,* **2013,** 371, 20120256.

Abstract

We examine for the first time how chemically and thermally stable gold nanoparticles, prepared by a silane conjugation approach, affect both the thermal and the electro-optical properties of a nematic liquid crystal when doped at concentrations ranging from 0.25 to 7.5wt%. We find that the octadecyl-silane conjugated gold nanoparticles stabilize both the enantiotropic nematic and the monotropic smectic-A phase of the liquid crystal host with a maximum stabilization of 2 °C for the nematic and 3.5 °C for the smectic-A phase for the mixture containing 1wt% of the silanized particles. The same mixture shows the lowest values for the Fréedericksz transition threshold voltage and the highest value for the dielectric anisotropy. Generally, all nanoparticle-containing mixtures, except mixtures with nanoparticle concentrations exceeding 5wt%, reduce the threshold voltage, increase the dielectric anisotropy and reduce both rise and decay time; the latter particularly at temperatures at least 10 °C below the isotropic-nematic phase transition on cooling.

4.1 Introduction

Liquid crystal-particle composites have been extensively studied owing to their importance and potential use in modulating optical and electro-optical properties of anisotropic ordered fluids. Traditionally, dyes[1, 2] and chiral additives[3-7] were most commonly pursued to induce properties such as photoswitching, lasing,[8-10] helical twisting, or spontaneous polarization.

Many of these induced properties were tuned and optimized for applications in liquid crystal displays (LCDs) using chiral smectic-C and nematic (or chiral nematic) phases. The response of a nematic liquid crystal (LC) to an applied electric field is of great importance for such display applications. While the key display modes, namely twisted nematic (TN), vertical alignment (VA) and in-plane switching (IPS) use different nematic LC materials and alignment approaches, the ON and OFF state of each pixel always relies on an electric field being applied through the LC material to induce a bulk change of the LC orientation.[11, 12] In general, it is desirable that the LC material or mixture of interest for an LC display has a minimal threshold voltage (V_{th}), maximal dielectric anisotropy $\Delta\varepsilon$ (positive or negative), low viscosity (γ), high birefringence (Δn), and short switching times (i.e. rise and fall times, τ).

Minimizing the V_{th} is generally important for maximizing energy efficiency of an LC display.[13] V_{th} is typically measured as the voltage at which a 5 or 10% change in capacitance (or 10% in transmittance) occurs. The dielectric anisotropy and the elastic constants of the nematic LC are governed by the slope of the *C*-*V* plot. The splay elastic constant (K_{11}) is particularly important for the cell geometry used to study these systems (Fréedericksz transition in a planar cell), because the splay deformation (re-orientation from a planar to

a vertical configuration and *vice versa*) is the deformation that occurs when an electric field is applied to a rubbed polyimide-coated planar cell. The splay elastic constant (K_{11}) is derived from Equation 4.1:

$$K_{11} = \left(\frac{V_{th}}{\pi}\right)^2 \times \varepsilon_0 \times |\Delta\varepsilon| \qquad \text{(Eq. 4.1)}$$

where V_{th} is the threshold voltage, $\Delta\varepsilon$ the dielectric anisotropy ($\Delta\varepsilon = \varepsilon_{\parallel} - \varepsilon_{\perp}$) , and ε_o is the permittivity of free space.

Over the past decade, doping LCs with nanoparticles (NPs) has provided an intriguing and viable way of manipulating the properties of LCs.[14-17] If stable dispersions can eventually be achieved, this pathway may well provide the means to be of significant importance for LC-based device and display applications. Tremendous global research efforts demonstrated that doping LCs with NPs can introduce original effects related to NP pattern formation, NP-guided LC alignment, and alteration of optical or electro-optic characteristics in both nematic and smectic LC phases.[18] For example, several reports demonstrated lower values for V_{th}, induced homeotropic alignment or faster switching in nematics, and higher values for the spontaneous polarization in ferroelectric SmC* materials.[18]

Using larger, micron-sized particulate systems as dopants to alter the properties of nematic LCs is an area of research that has been ongoing for quite some time. Early studies focused on defect formation induced by aerosils particles.[19-34] Commonly, these particles produced a large number of defects resulting in intense light scattering of the mixture in

the field-OFF state, and becoming transparent when driven with an electric field.[35-37] As more nanomaterials varying in shape, size, and composition, became available, research focused on incorporating nanomaterials.

Previous work in our laboratory has shown that alkylthiolate-capped gold (Au NPs) and silver NPs (Ag NPs) can modulate the optical and electro-optic properties in dispersion with nematic LC hosts in a unique fashion.[16, 38-40] For example, we have demonstrated that alkylthiol-capped Au NPs induce multiple alignment modes in nematic LCs (e.g., a thermal history-dependent dual alignment and electro-optic switching mode) in addition to minimized threshold voltages and altered elastic constants (particularly the splay elastic constant K_{11}) and dielectric properties ($\varepsilon_{\parallel}$, $\varepsilon_{\perp}$, and $\Delta\varepsilon$).[38, 40]

Au NPs, as the likely most frequent choice to dope LCs, display unusual and unique size-dependent chemical and physical properties;[41] their surface can be passivated in situ or via place exchange reactions with molecules ranging from simple alkanethiols, phosphines, and amines to more complex molecular structures including dendrimers, polymers, and LC moieties. Drawbacks of these Au NP dopants have always been the fairly large size distribution and the difficulty to obtain series of these particles just differing in size using the one-[42, 43] or two-phase Brust-Schiffrin methods.[44] While the ease as well as speed in preparing and modifying these Au NPs has to be considered an advantage, their stability under various conditions is not. Factors to consider arise from the chemical and thermal (in)stability of metal NPs as well as from the mobility of surface bound capping agents (usually thiols). The chemical stability or instability of thiol-capped metal NPs towards oxidation (i.e. oxidation of surface-bound thiols to disulfides in air or in the presence of other oxidants)[45], towards halides[46], and towards alkaline metal ions has been

studied by a number of groups[47] highlighting the importance of determining NP purity. The thermal stability of Au NPs is particularly considering the use in composites with LCs, where sample preparation protocols often call for annealing and slow cooling from isotropic liquid phases. Both thermogravimetric analysis (TGA) data[48] and temperature-dependent XPS studies frequently reveal that thiols with an alkyl chain length longer than C6 start to or completely desorb (forming dithiols) from the Au NP surface at temperatures above 160 °C; thiols with shorter chain length desorb at even lower temperatures (between 90 °C and 140 °C for C3–C5).[49] Sintering of Au NPs is often observed for particle sizes below 4 nm as shown by Brust and co-workers, rapidly (i.e. 10 min) at elevated temperatures (e.g., 250 °C), but also appreciably at room temperature, an effect known as coarsening.[48] For example, alkylthiol-capped Au NPs with an average core diameter of 2 nm are easily converted into Au NPs with a core diameter larger than 5 nm simply by refluxing them in toluene.[40] Related to this coarsening process, migration of thiols on the NP surface is relevant. Using electron paramagnetic resonance (EPR) spectroscopy on Au NPs passivated with spin labels such as TEMPO, Chechik and others demonstrated that thiol ligands on Au NPs surfaces undergo slow lateral diffusion (even at room temperature) that may take several hours at temperatures around 90 °C.[50-52] While slow, such migration might lead to segregation of thiols on the surface of mixed monolayer-capped Au NPs (different ligands simultaneously cap the surface of the NP).[53, 54]

4.2 Experimental

Hydrogen tetrachloroaurate(III) trihydrate was purchased from Alfa Aesar, didodecyldimethylammonium bromide (DDAB), and tetrabutylammonium Borohydride (TBAB), 3-mercaptopropyltrimethoxysilane (MPS), and trimethoxy(octadecyl)silane (TMODS) were purchased from Sigma-Aldrich. All chemicals were used without further purification. Pure **LC1** (Felix 2900-03) was purchased from Synthon Chemicals. All solvents used for the synthesis and purification were Aldrich purification grade purified via a PureSolv solvent system (Innovative Technology). Millipore water (18 MΩ) was used to rinse glassware and vials used for sample preparation. In addition, all vials used to store, handle and mix NPs with the LC host were cleaned with aqua regia.

UV-vis spectra were recorded using a Varian Cary 5000 UV-vis-NIR spectrophotometer. TEM imaging for **Au NP$_{Sil}$** was performed using a JEOL JEM-2100F TEM instrument at an accelerating voltage of 120 kV or a Hitachi H-7000 electron microscope. 1H NMR spectra were acquired using a Bruker Avance 300 MHz spectrometer, and XPS data were collected using a Kratos Axis Ultra X-ray Photoelectron Spectrometer.

Polarized optical microscopy (POM) images were taken using an Olympus BX51-P microscope in conjunction with a Linkam LS350 heating/cooling stage, a Leica SD6 Microscope, or an Ortholux II Pol-BK microscope (Leica). In the latter case, for illumination, a halogen lamp (XENOPHOT, Osram) with interference filter for 542 nm was used. The LC test cells used were planar cells (cell gap: 4.0 µm) with antiparallel polyimide alignment layers and 1° to 3° pre-tilt (LC Vision). For all POM imaging, the LC

mixtures were heated above the isotropic/nematic phase transition temperature (T_{NI}) and cooled at a rate of 1 °C min^{-1} until the desired temperature below T_{NI} was reached. FCPM images were obtained using a Nikon LV 100D-U upright microscope coupled with a Nikon Eclipse C1 Plus scanner/controller using a 488 nm laser to excite the dichroic dye *N,N'*-bis(2,5-di-*tert*-butylphenyl)-3,4,9,10-perylenedicarboximide (obtained from Sigma-Aldrich) used at 0.002wt%.

Electro-optic parameters were measured using two different setups. One setup included an LCAS I automated liquid crystal analyzer (LC Vision, LLC), a second one is described below. All test cells were positioned under an angle of 45° between crossed polarizers and the light intensity passing through the cell was measured using a photomultiplier tube (Oriel). A Linkam LTS350 heating stage with TMS94 controller was used for temperature control. Before measurement, all samples were heated up to the isotropic phase and then cooled down to 58°C with a cooling rate of 1 °C min^{-1}. Capacitance measurements were performed simultaneously to transmission measurement on an HP 4284A LCR bridge, varying the sine test signal level by using AC voltages from 0.05 Vrms to 19.95 Vrms to reorient the LC. The test signal frequency was 1 kHz. Analysis or interpretation of the data is performed based on the single-cell method described by Wu et al.[55]

The mixtures of the **Au NP$_{SiI}$** particles in **LC1** were prepared by weighing accurate amounts of the solid LC using a microbalance and dissolving it in a known amount of toluene. The as-prepared solutions of the respective NP was then combined in a V-vial® with the LC solution to produce the exact concentration of the NPs in **LC1**. The solvent was then allowed to evaporate under a steady stream of dry N_2 at ~70 °C for about 24 to 48 h followed by sonication.

The synthesis of the silanized gold NPs (**Au NP_{Sil}**) was carried out using a procedure adopted from a method reported elsewhere.[56] Briefly, a 10 ml solution of $HAuCL_4$ in toluene (0.01M) was prepared in the presence of an equimolar amount of DDAB using five minutes sonication. Next, 200 µl of a toluene solution of MPS (0.1M) was added under stirring followed by addition of 1 ml toluene solution of TBAB and DDAB (30 mg of TBAB and 27 mg of DDAB). The reaction solution turned immediately black and changed then slowly to pink. After one hour, 100 µl of TMODS and 230 µl of NaOH (1.0M) were added to the reaction mixture and stirring was continued for 15 h. Finally, the solvent was evaporated, and the collected particles were washed several times with chloroform and *iso*-propanol.

4.3 Results and Discussions

To enhance both thermal and chemical stability of Au NPs used as additives in LCs and circumvent thiol desorption and migration issues that could potentially falsely contribute as free thiol ligands to some of the observed effects, we here present a new robust type of hydrophobic Au NPs prepared using a simple, versatile silane conjugation approach, first reported by Jana and co-workers for hydrophilic thiol-capped Au NPs.[56] In this two-step silanization, the first step delivers 3-mercaptotrimethoxysilane (MPS)-capped Au NPs. These NPs, after isolation and purification, then undergo a silane conjugation step (i.e. hydrolysis and dehydration condensation under basic conditions) with a second, long chain alkytrimethoxysilane (here: $H_{37}C_{18}Si(OCH_3)_3$), which results in Au NPs that are thermally and chemically robust, survive extensive sonication without decomposition or

thiol desorption, and are well dispersible in both organic solvents and nematic LCs featuring aliphatic side chains such as **LC1** used in this study (**Figure 4.1**). We systematically characterized the NPs synthesized using the above-described silane conjugation approach by ^{1}H NMR (Figure B4.1) in the supplementary information presented in Appendix B), UV-vis spectrophotometry, x-ray photoelectron spectroscopy (XPS), and transmission electron microscopy (TEM). Batches of the same NPs kept at elevated temperatures and under prolonged sonication gave identical ^{1}H NMR spectra, visible absorption spectra, and TEM images, which confirms their exceptional stability.

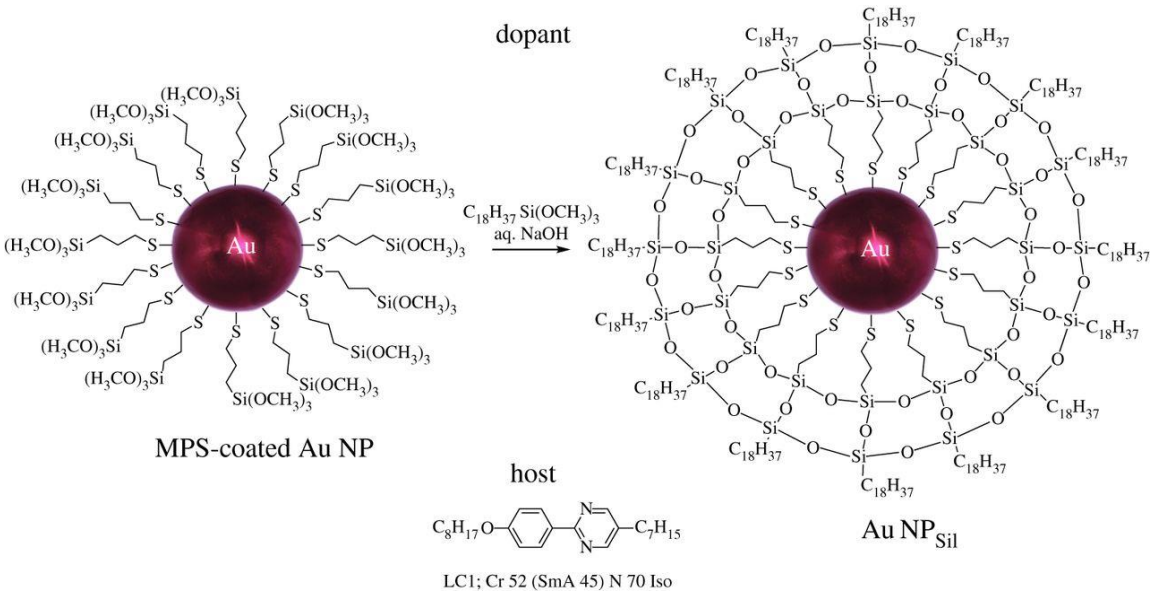

Figure 4.1 Silane conjugation synthesis and schematic representation of the silanized, hydrophobic Au NPs, and structure as well as phase transition temperatures of the Felix-2900-03 nematic liquid crystal host (LC1).

A visible absorption spectrum in hexane and a representative high-resolution TEM image are shown in **Figure 4.2**. TEM image analysis provided an average NP size of 4.1 ±

0.7 nm, and XPS confirmed the formation of a silica shell around the Au NP core (Table B4.1 in Appendix B). More detailed information about the characterization of these NPs are given in the supplementary information (Appendix B).

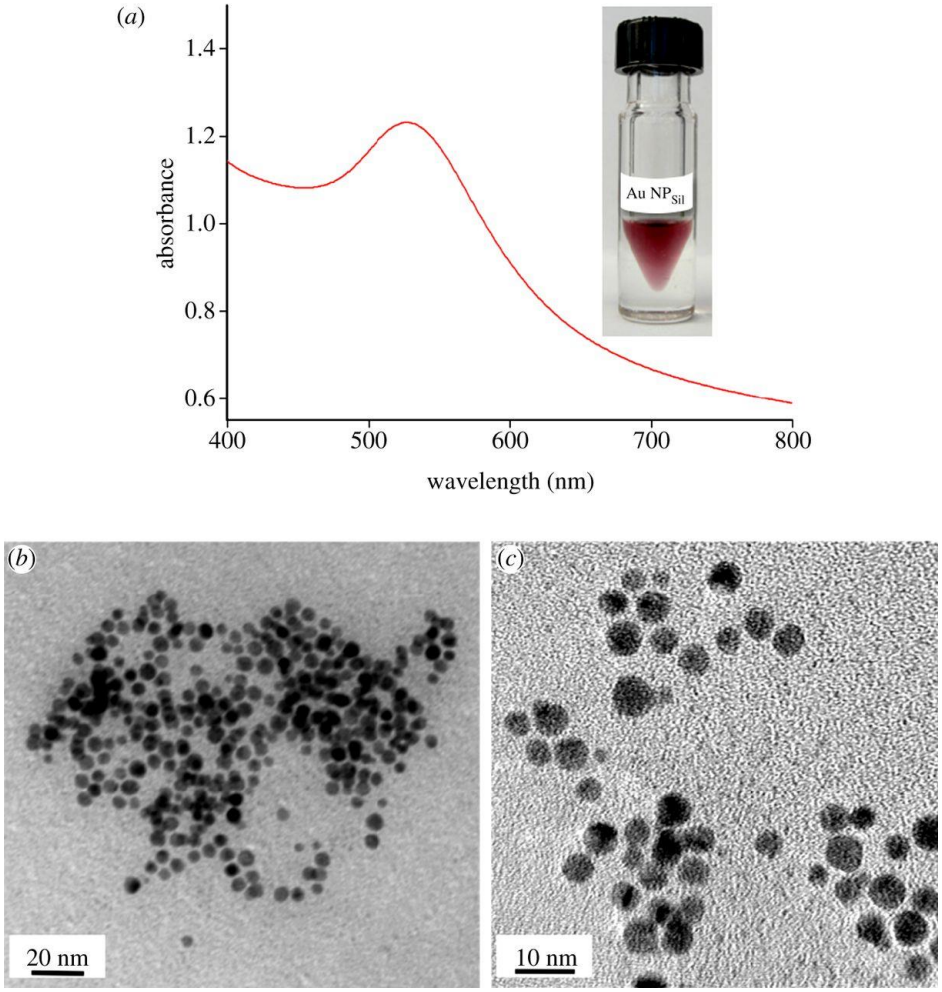

Figure 4.2 Visible absorption spectrum of Au NP_{Sil} in hexane (a) as well as TEM and high-resolution TEM images (b, c) of Au NP_{Sil}.

Based on protocols for investigating NP-doped nematic LCs established in our laboratory,[38] we tested seven different concentrations of the silanized Au NP in Felix-2900-

03 (**LC1**) from 0.25 to 7.5wt% covering an extended range from low to high NP loadings. The same nematic LC has been used for several studies in the past,[38, 57-59] which will allow us to compare current with prior test results later. Following the sample preparation protocol outlined in the Experimental Section provided the first visual clues that these silanized NPs are able to form stable suspensions in nematic solvents such as **LC1**. After complete solvent evaporation with the vial placed on a hotplate adjusted to a temperature below the isotropic to nematic phase transition (T_{NI}), all seven mixtures of **Au NP$_{Sil}$** in **LC1**, even up to 7.5wt%, appeared homogeneous, showed no signs of NP settling, and displayed a continuous color intensity increase based on the surface plasmon resonance (SPR) frequency of the NPs in **LC1** (**Figure 4.3**).

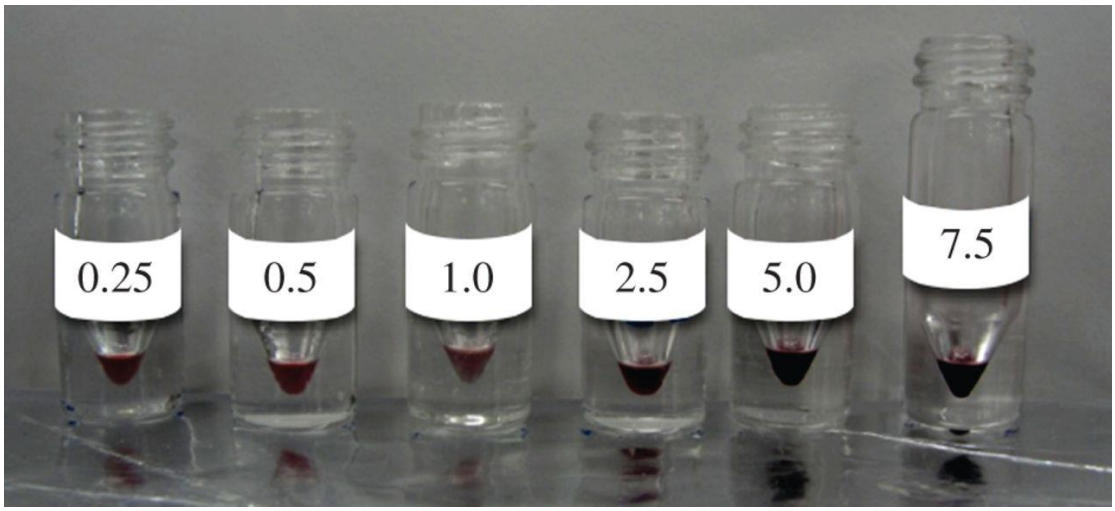

Figure 4.3 Photograph showing the quality of dispersion of Au NP$_{Sil}$ in LC1 in solid glass V-vials after complete solvent evaporation; vials are placed on a hotplate with the NP/LC1 dispersions in the nematic phase at $T_{NI} - T = 2$ °C (left to right: concentration ranging from 0.25 to 7.5wt%). One can clearly see the color of the SPR of the Au NP$_{Sil}$ increasing in intensity as the concentration is raised from 0.25 to 7.5 wt%. No settling or macroscopic aggregation is visible.

Thin films of the LC colloids between plain, un-treated glass slides were first investigated by polarized optical microscopy (POM) to test alignment and thermal properties. Predominantly at NP loadings ranging from 0.25 to 2.5wt% in **LC1**, large domains of NP-induced homeotropic alignment due to partial segregation of NPs to both glass substrates are observed. These homeotropic domains surround birefringent stripe features (see **Figure 4.4**a – c) frequently observed for many other types of Au NPs and quantum dots.[60, 61]

We recently investigated these textural features in more detail using fluorescence confocal polarizing microscopy (FCPM) and established both the director field within the stripes and the segregation of NPs causing the induced homeotropic alignment.[60] Two additional striking features were observed by POM both in untreated glass slides and rubbed polyimide-coated ITO-glass cells (cell gap: 4 μm). First, at NP concentrations exceeding 2.5wt% an increasing number of isotropic domains persist well below T_{NI} of the mixture on cooling.

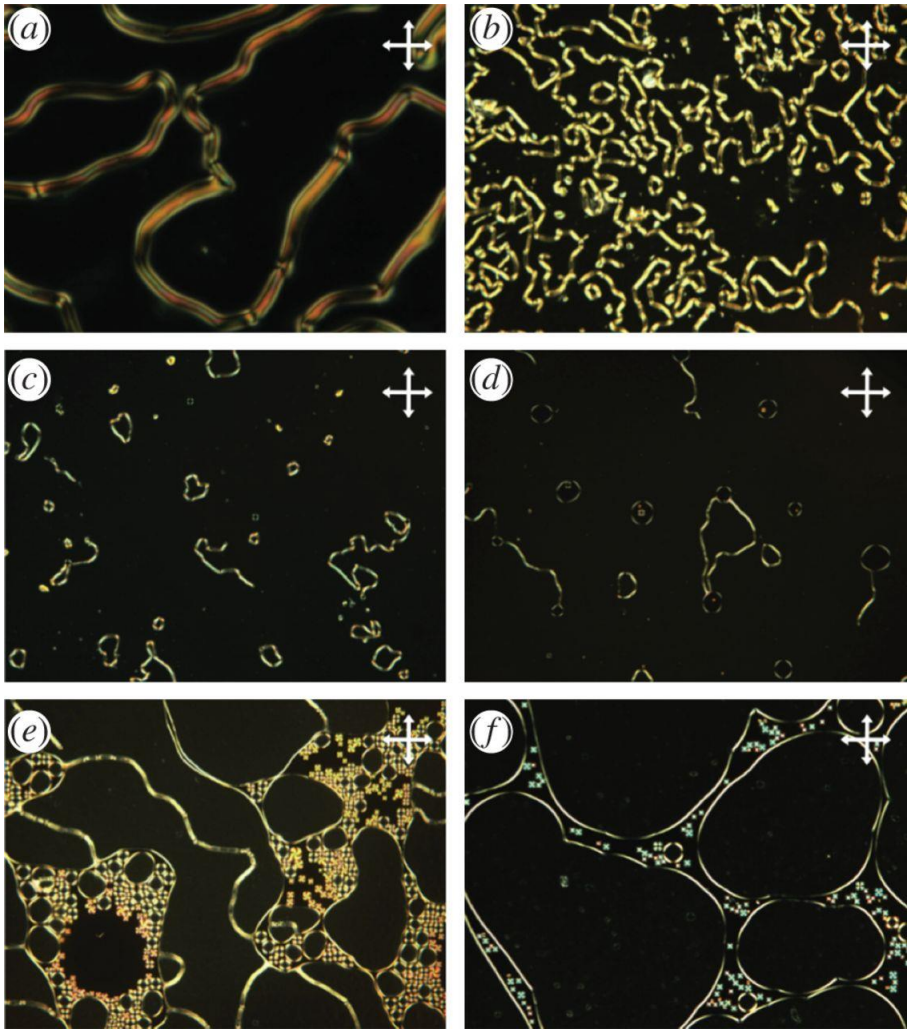

Figure 4.4 POM photomicrographs (crossed polarizers) of LC1 doped with Au NP_{Sil} at T_{NI} – T = 5 °C between plain glass slides; (a) 0.25wt%, (b) 0.5wt%, (c) 1.0wt%, (d) 2.5wt%, (e) 5.0wt%, and (f) 7.5wt%.

Coexistence ranges observed for all mixtures by POM on cooling are plotted in **Figure 4.5**. A very similar trend was also observed on heating. Second, and noticeable from the temperature plot in **Figure 4.5**, mixtures in the mid-concentration range (from 0.5 to 2.5 wt%) show an apparent stabilization of the nematic phase on heating from the solid state and on cooling from the isotropic liquid. To confirm these optical microscopy results, we performed differential scanning calorimetry (DSC) studies on all mixtures. DSC does not

register the biphasic behavior (coexistence of nematic and isotropic phase), but measures the bulk thermal behavior of these samples. Nevertheless, the DSC data show the same phase transitions temperature trends as noticed by POM (**Figure 4.6**). The bar diagrams show the measured phase transition temperatures on heating (**Figure 4.6a**) and cooling (**Figure 4.6b**) taken at a heating/cooling rate of 10 °C min^{-1}. Practically identical DSC traces were observed during the first and second heating/cooling run. Notably, not only the nematic, but also the monotropic smectic-A phase is stabilized (higher $T_{N\text{-}SmA}$) for all and especially in the lower to mid-concentration range mixtures (0.25 to 2.5 wt%), which we were able to confirm by POM. The full series of DSC traces can be found in the supplementary information.

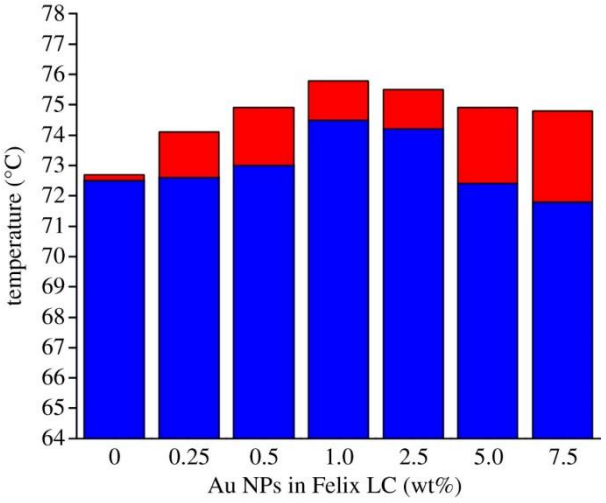

Figure 4.5 Plot of the phase transition temperatures (T_{NI} and biphasic N/Iso regions) of all mixtures of LC1 doped with Au NP_{Sil} observed by POM on cooling at a rate of 1 °C min^{-1} (plain glass and LC test cells). Red color denotes nematic-isotropic phases; blue color, nematic phase.

This thermal phase stabilization by about 1.5 to 2.0 °C for the nematic and about 3.5 °C for the smectic-A phase (at 0.5 to 1.0wt% of the NPs; far above the experimental error)

is a very surprising and stimulating result. We have not observed such stabilizing effect for any of the other NPs we tested in **LC1** until that time including similar sized Au NPs or CdSe quantum dots capped with alkylthiols, amines or carboxylic acids featuring similar hydrocarbon chain lengths.[57] Any other NP doped into a nematic or smectic mixture showed either no or a slight phase destabilizing effect. While some of the silanized **Au NP$_{SiI}$** appear to segregate to the interfaces inducing homeotropic alignment between plain glass slides, these NPs appear to enhance the overall order parameter of the nematic and the smectic-A phase. Similar drastic stabilizing effects have so far only been described for anisometric NP inclusions such as carbon nanotubes[62] or polar ferroelectric NPs[63]. In general terms, a mesophase stabilizing effect by NP inclusions is believed to be caused by weak interactions between NP and LC host or by NPs that are well compatible with (well dispersed in) a given nematic LC host.[64]

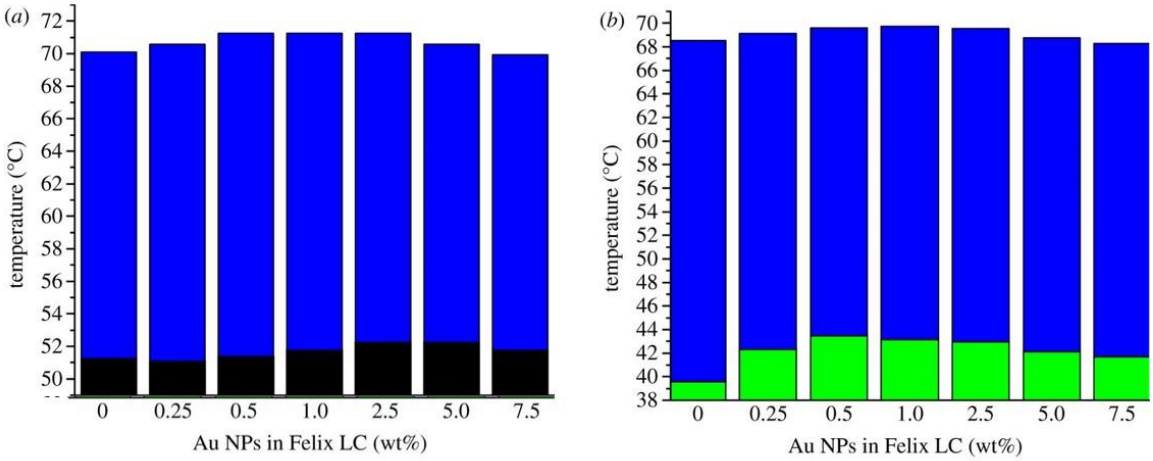

Figure 4.6 Plots of the phase transition temperatures measured by DSC at a rate of 10 °C min^{-1}: (a) on heating highlighting the stabilization of the nematic phase (blue, nematic; black, crystalline), and (b) on cooling demonstarting the stabilization of both the enantiotropic nematic (blue) and the monotropic smectic-A (green) phases.

The next step, alignment of the doped samples in rubbed polyimide coated ITO-glass cells was studied. Such cells were independently prepared in both participating laboratories, and the images in **Figure 4.7** and **Figure 4.8** show the polarized optical microscopy results with respect to alignment and biphasic behavior. All mixtures in the cells align perfectly planar without the formation of birefringent stripe defects or homeotropic domains as observed for other Au NPs in prior work. The cells only show the afore-mentioned isotropic domains, even 'deep' into the nematic phase on cooling (see **Figure 4.7e, f** and **Figure 4.8f, g**).

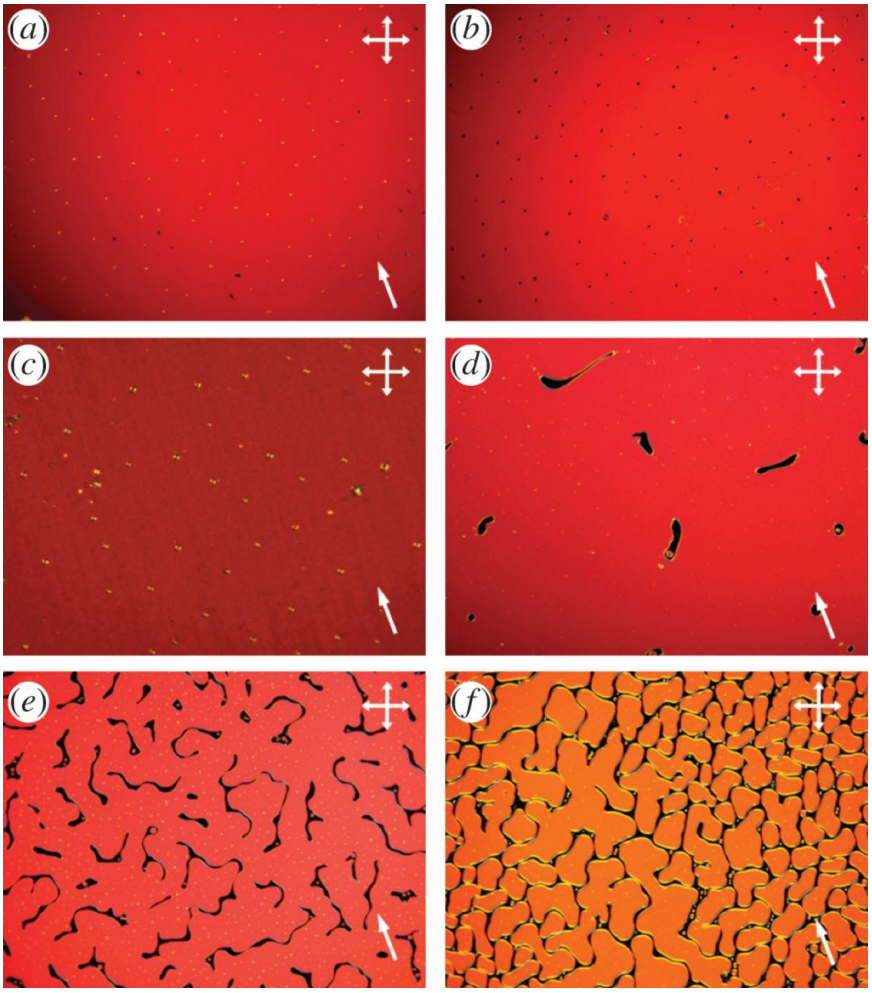

Figure 4.7 POM photomicrographs (crossed polarizers) of **LC1** doped with **Au NP$_{SII}$** at $T_{NI} - T = 5$ °C in planar cells (cell gap: 4μm) – a selected, representative section is shown; (a) 0.25wt%, (b) 0.5wt%, (c) 1.0wt%, (d) 2.5wt%, (e) 5.0wt%, and (f) 7.5wt% (arrows in bottom right indicate rubbing direction; small dots in these images are the spacers of the 4μm cells).

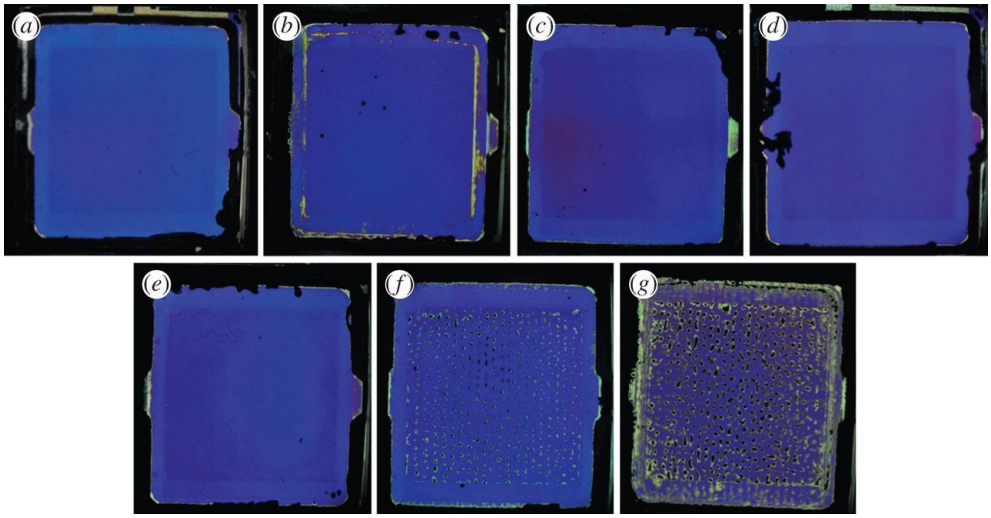

Figure 4.8 POM photomicrographs (crossed polarizers) of **LC1** doped with **Au NP$_{SII}$** at $T_{NI} - T$ = 5 - 7 °C in planar cells (cell gap: 4μm) – entire cell is shown; (a) 0.25wt%, (b) 0.5wt%, (c) 1.0wt%, (d) 2.5wt%, (e) 5.0wt%, and (f) 7.5wt% (tilting of the sample indicates the isotropic nature of the dark spots – coexistence of nematic and isotropic even 7 °C below T_{NI}).

FCPM tests using a dichroic dye (see Experimental Section) with a much better solubility in the isotropic liquid phase of **LC1** confirm the isotropic or biphasic nature of these domains (**Figure 4.9**). In addition, between uncrossed, parallel polarizers the locally elevated concentration of the Au NPs is clearly visible (dark spot-like regions in **Figure 4.9c**). This is not surprising for two reasons. First, NPs are in general better soluble in the isotropic liquid phase of an LC host, and secondly, the concentration ≥ 5wt% in these mixtures is far above the typical solubility limit of NPs in nematic phases; only a limited number of reports claims higher well-dispersed NP loads.[65]

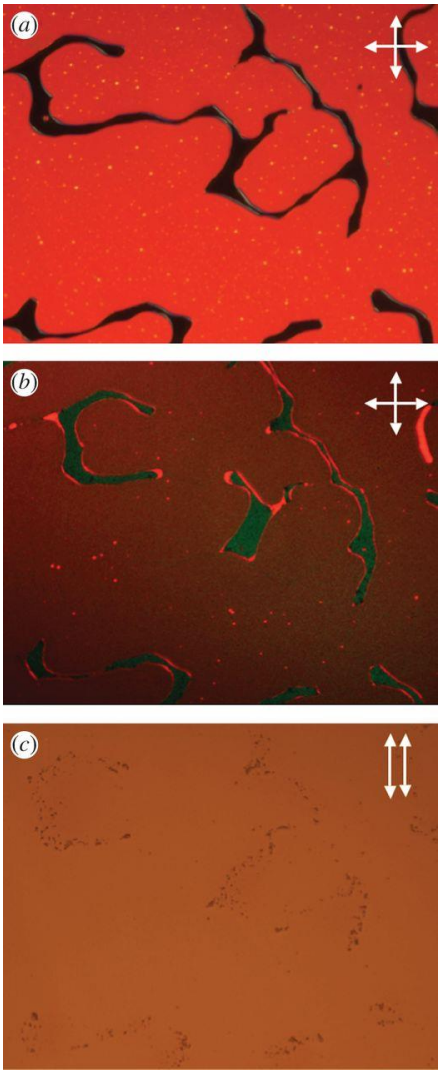

Figure 4.9 Photomicrographs showing the 5wt% **Au NP$_{SII}$** in **LC1** mixture at $T_{NI} - T = 5$ °C in a planar cell: (a) POM image (crossed polarizers) – see **Figure 4.7e**, (b) combined POM/FCPM image (both polarized transmission = red channel and fluorescence confocal = green channel) showing the larger concentration of the dye in the isotropic domains, and (c) POM image under identical conditions with parallel, un-crossed polarizers showing the larger concentration of NPs in these isotropic regions.

Electro-optic measurements were subsequently performed on all mixtures. Earlier studies on alkylthiol-capped metal NPs (dodecanethiol-capped Au NPs with core diameter of 5.4 nm[38] as well as hexanethiol-capped Ag NPs with a core diameter of 4.2 nm[40]) showed a tremendous reduction of V_{th} despite much reduced values for the dielectric anisotropy

($\Delta\varepsilon$). In contrast to the **Au NP$_{Sil}$** described here, these NPs induced homeotropic alignment in both untreated glass slides as well as rubbed polyimide-coated planar ITO-glass cells. For these NPs we always observed the dual and reverse electro-optic mode (switching from homeotropic to planar for a nematic LC with positive $\Delta\varepsilon$, particularly at low field frequencies)[38, 58] that was not observed in the current mixtures. The robustness of the current **Au NP$_{Sil}$**, allowing for the preparation of much-improved homogeneous and stable dispersion in **LC1** appears to be responsible for the diminished NP segregation to interfaces, and hence the lack of homeotropic alignment in planar cells.

V_{th} was determined from capacitance and transmittance measurements. However, transmittance measurements are sometimes more stable than capacitance measurements, as the capacitance plateau in latter can occasionally exhibit significant deviations. In addition, transmission measurements can selectively choose small regions from the cell for data acquisition, while the capacitance is always measured over the complete electrode area. In previous experiments using for example quantum dots, we were able to show that different areas within one cell can show different behavior: when a slight surface coverage of particles occurs due to NP segregation, the surface energy is changed and the threshold gets lost. For the calculation of threshold, the transmission data are transformed into phase retardation data, using Equation 4.2:

$$I_{det} = \frac{1}{2} \times I_0 \times sin(2\varphi)^2 \times \sin\left(\frac{\emptyset}{2}\right)^2 \qquad \text{(Eq. 4.2)}$$

where I_{det} and I_0 are the detector and initial intensity, respectively, φ the polar angle (45°) and ϕ the phase retardation (Equation 4.3):

$$\phi = \frac{2\pi\Delta n_{eff}}{\lambda} \qquad \text{(Eq. 4.3)}$$

where d is the thickness of the sample, Δn_{eff} the effective birefringence, and λ the wavelength of the used light source. Plots of V_{th} vs. temperature and vs. reduced temperature $T - T_{NI}$ are collected in **Figure 4.10**.

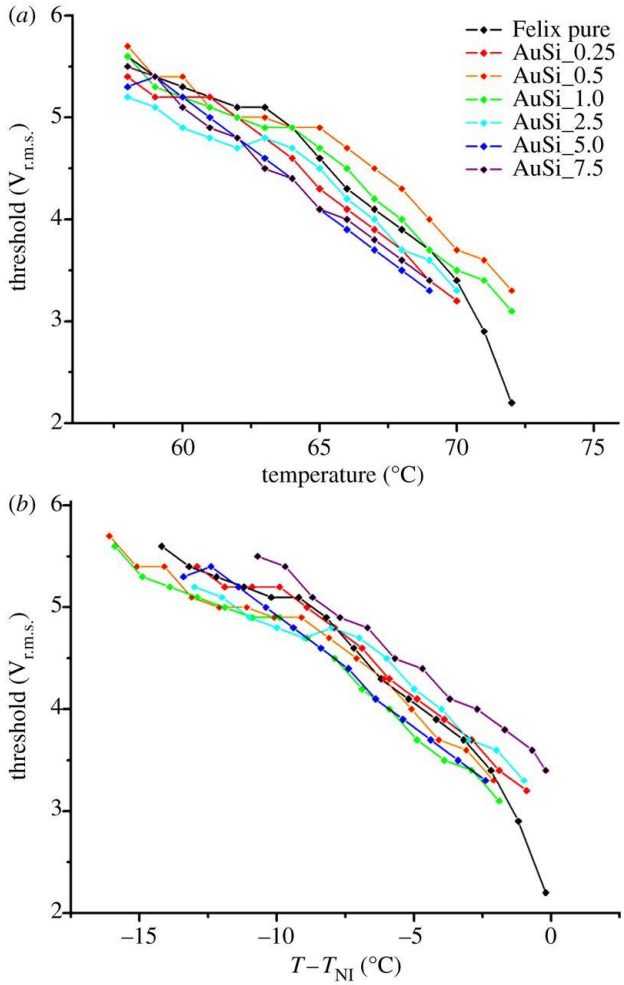

Figure 4.10 Plots of the theshold voltage (V_{th}): (a) vs. temperature and (b) vs. reduced temperature $T - T_{NI}$.

In general, a slight decrease of threshold with increasing particle concentration was found. Neglecting the mixtures with coexistence of nematic and isotropic domains (5 and 7.5wt%), the mixture with a concentration of 0.5, 1.0 and 2.5wt% of **Au NP$_{SII}$** in **LC1** show the lowest values for V_{th} in the V_{th} vs. reduced temperature plots (which are corrected for the difference in clearing point between mixtures). Maybe not surprisingly, the mixtures showing the most significant stabilization of the nematic and the monotropic smectic-A phase (0.5 and 1.0wt%) are the mixtures with the overall lowest V_{th} (**Figure 4.10b**). The

slope in each set of plots remains approximately identical, also in comparison to pure **LC1**, hence we conclude that the temperature dependence of V_{th} is not affected by the presence of suspended NPs. Accordingly, the same mixtures of 0.5 and 1.0wt% **Au NP$_{Sil}$** in **LC1** also show among the highest values for $\Delta\varepsilon$ in the investigated series (**Figure 4.11**). For both of these values, V_{th} and $\Delta\varepsilon$, the mixture containing 0.25wt% of the silanized NPs appears to show almost identical values to pure **LC1** within experimental error. It appears that this concentration is the lower threshold for electro-optic alterations in the current series, while concentrations around 5wt% and higher represent the upper useful limit.

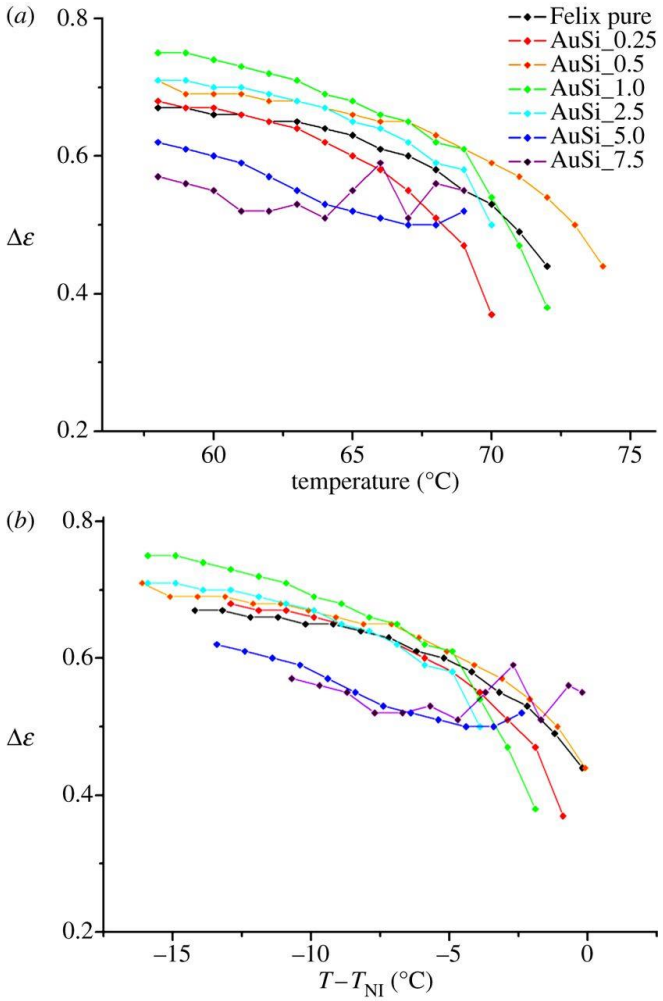

Figure 4.11 Plots of the dielectric anisotropy ($\Delta\varepsilon$): (a) vs. temperature and (b) vs. reduced temperature $T - T_{NI}$. The plots for the mixtures containing 5 and 7.5wt% of **Au NPs$_{Sil}$** (AuSi_5.0 and AuSi_7.5) show lower values for $\Delta\varepsilon$ because of defects originating due to isotropic domains.

Lastly, we also measured the switching times of all mixtures; both rise time (γ) and decay time (τ_{off}). For all tested cells, we found an increase of τ_{off} with increasing temperature. Obvious concentration dependencies were hard to find. Nevertheless, almost all NP-doped samples show lower decay times, increasingly so as we depart from T_{NI} on cooling at $T - T_{NI} < -10$ °C. Interestingly, the mixture doped with only 0.25wt% shows the lowest values for τ_{off} in this series at $T - T_{NI} < -5$ °C (**Figure 4.12**). Similar trends were

also observed for the rise time. The NP-doped mixtures show lower rise times far from the isotropic-nematic phase transition on cooling ($T - T_{NI} < -10$ °C) and slower rise times closer to the clearing point of the mixture. Overall, however, an increase in γ with increasing NP concentration can be seen in **Figure 4.13**.

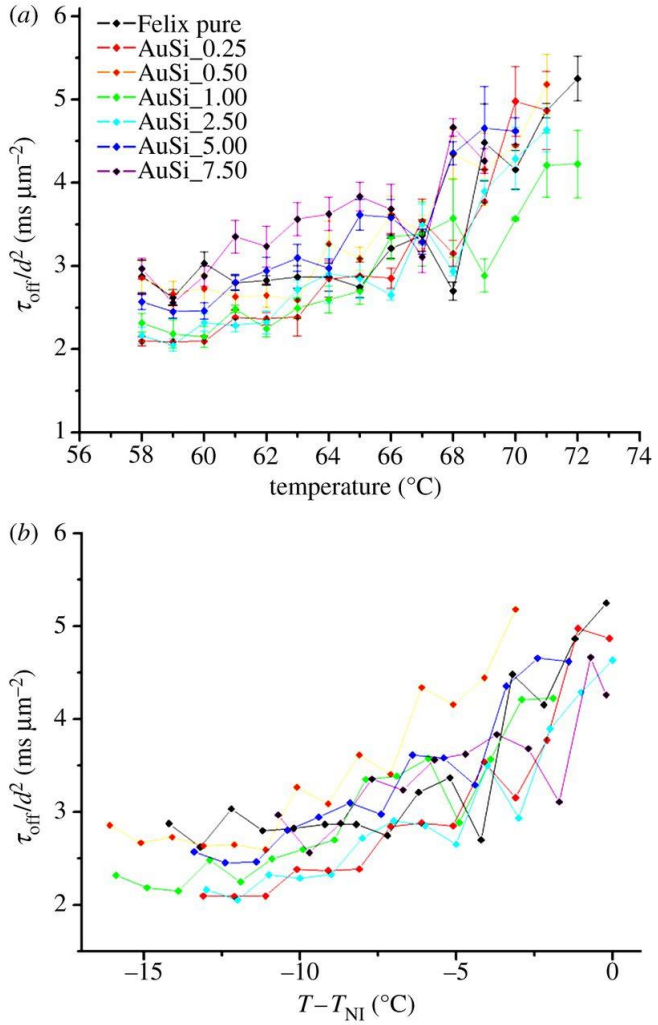

Figure 4.12 Plots of the decay time (τ_{off}): (a) vs. temperature and (b) vs. reduced temperature $T - T_{NI}$. At temperatures closer to T_{NI}, values of the τ_{off} significantly scatter, making a clear interpretation of trends with respect to NP concentration at higher temperatures somewhat difficult.

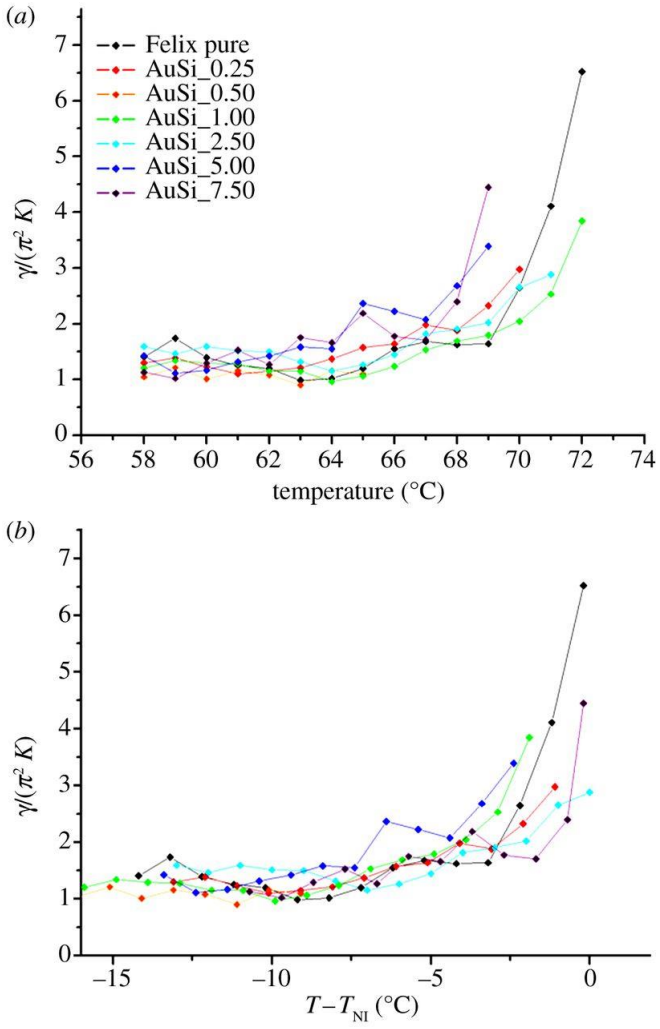

Figure 4.13 Plots of the rise time (γ): (a) vs. temperature and (b) vs. reduced temperature $T - T_{NI}$.

4.4 Conclusions

For the first time, we have been able to prepare and test truly robust Au NPs as additives in a nematic LC host. The silane conjugation chemistry used to synthesize these NPs provides access to chemically and thermally stable Au NPs without the risk of thiol desorption from or thiol migration on the Au NP surface. In addition, NP ripening or

sintering at elevated temperatures in the LC solvent during sample preparation and testing is also prevented by the stable siloxane corona around the NP. In this way, exceedingly reliable optical, thermal as well as electro-optic data of nematic mixtures containing these Au NPs could be collected. The nematic LC host is structurally characterized by a 2-phenylpyrimidine rigid core flanked by two terminal hydrocarbon chains, which, based on past and current experiments, enhance the dispersibility of alkyl monolayer-capped Au NPs. The **Au NP$_{Sil}$** particles used in this study, however, are much easier to disperse in the same nematic host used in numerous prior studies (**LC1**). Considering calculated molecular parameters, this enhanced dispersibility is most likely due to the larger, fixed distance between neighboring alkyl chains provided by the siloxane framework around the NP. Considering a homeotropic anchoring of the LC molecules to the NP surface, such larger distance may well provide better access for the LC molecules of the host, but could also mean weaker anchoring. In any event, the robustness imparted by the siloxane network allows for extended sonication times that help ensure well-dispersed LC colloidal samples.

Thermal characterization revealed that these silanized Au NPs induce a NP concentration-dependent LC phase stabilizing effect of up to 2.0 °C to the enantiotropic nematic phase and up to 3.5 °C to the monotropic smectic-A phase of the LC host, which one would only expect in this magnitude from anisometric, magnetic or ferroelectric NP inclusions. The exact nature of this stabilizing effect is somewhat unclear at the moment, but additional experiments with modified alkyl chain lengths of the alkyltrimethylsilane used to conjugate the MPS-coated Au NPs are pursued to shine more light onto this phenomenon. The mixture containing exactly 1wt% of the suspended NPs shows the largest thermal stabilization effect. The same mixture also shows the lowest values for the

threshold voltage and the highest values for the dielectric anisotropy, which indicates that thermal and electro-optic effects are to some extent connected. Finally, all NP doped nematic samples show faster optical switching (both rise and decay time) particularly at lower temperatures away from the isotropic-nematic phase transition on cooling.

In conclusion, the chemically and thermally robust, silanized Au NPs presented here are ideal candidates for studies of NPs in LCs and applications of such composites in devices based on the manipulation of optical and electro-optic properties. With the option to translate this approach to other NP platforms, silanization appears as ‘the way to go’.

Acknowledgement

This work was financially supported by the Natural Science and Engineering Research Council (NSERC) of Canada, the Canada Foundation for Innovation (CFI), the Manitoba Research and Innovation Fund (MRIF), the Deutsche Forschungsgemeinschaft (DFG, KI 411), and the European Science Foundation (ESF-EUROCORES, SONS II program, LCNANOP project). We are grateful to K. McEleney for his valuable assistance with and M. S. Freund for access to XPS measurements. We also thank A. Dufresne for help and assistance with TEM imaging. TH thanks the Government of Ohio's Third Frontier Program (Ohio Research Scholar Program).

4.5 References

1. Berkovic, G.; Krongauz, V.; Weiss, V. *Chem. Rev.* **2000,** 100, (5), 1741-1753.
2. Ikeda, T. *J. Mater. Chem.* **2003,** 13, (9), 2037-2057.
3. Pieraccini, S.; Masiero, S.; Ferrarini, A.; Spada, G. P. *Chem. Soc. Rev.* **2011,** 40, (1), 258-271.
4. Pieraccini, S.; Ferrarini, A.; Spada, G. P. *Chirality* **2008,** 20, (5), 749-759.
5. Lemieux, R. P. *Chem. Soc. Rev.* **2007,** 36, (12), 2033-2045.
6. Lemieux, R. P. *Soft Matter* **2005,** 1, (5), 348-354.
7. Lemieux, R. P. *Acc. Chem. Res.* **2001,** 34, (11), 845-853.
8. Choi, H.; Kim, J.; Nishimura, S.; Toyooka, T.; Araoka, F.; Ishikawa, K.; Wu, J. W.; Takezoe, H. *Adv. Mater.* **2010,** 22, (24), 2680-2684.
9. Wang, C. T.; Lin, T. H. *J. Appl. Phys.* **2010,** 107, (12).
10. Cao, W. Y.; Munoz, A.; Palffy-Muhoray, P.; Taheri, B. *Nat. Mater.* **2002,** 1, (2), 111-113.
11. Lyu, J. J.; Sohn, J.; Kim, H. Y.; Lee, S. H. *J. Display Technol.* **2007,** 3, (4), 404-412.
12. Hong, H.; Shin, H.; Chung, I. *J. Display Technol.* **2007,** 3, (4), 361-370.
13. Zhang, T.; Zhong, C.; Xu, J. *Jpn. J. Appl. Phys.* **2009,** 48, (5), 055002.
14. Umadevi, S.; Mirzaei, J.; Feng, X.; Sharma, A.; Moreira, P.; Hegmann, T. *Liq. Cryst.* **2011,** 38, (11-12), 1495-1514.
15. Qi, H.; Hegmann, T. *Liq. Cryst. Today* **2011,** 20, (4), 102-114.
16. Qi, H.; Hegmann, T. *J. Mater. Chem.* **2008,** 18, (28), 3288-3294.
17. Hegmann, T.; Qi, H.; Marx, V. M. *J. Inorg. Organomet. P.* **2007,** 17, (3), 483-508.

18. Stamatoiu, O.; Mirzaei, J.; Feng, X.; Hegmann, T. *Top. Curr. Chem.* **2012,** 318, 331-394.

19. Leys, J.; Glorieux, C.; Thoen, J. *Phys. Rev. E* **2008,** 77, (6), 061707.

20. Cordoyiannis, G.; Kralj, S.; Nounesis, G.; Kutnjak, Z.; Zumer, S. *Phys. Rev. E* **2007,** 75, (2), 021702.

21. Rozanski, S. A.; Sinha, G. P.; Thoen, J. *Liq. Cryst.* **2006,** 33, (7), 833-840.

22. Sinha, G.; Leys, J.; Glorieux, C.; Thoen, J. *Phys. Rev. E* **2005,** 72, (5), 051710.

23. Roshi, A.; Iannacchione, G. S.; Clegg, P. S.; Birgeneau, R. J.; Neubert, M. E. *Phys. Rev. E* **2005,** 72, (5), 051716.

24. Zakharov, A. V.; Thoen, J. *Eur. Phys. J. E* **2005,** 17, (4), 447-453.

25. Leys, J.; Sinha, G.; Glorieux, C.; Thoen, J. *Phys. Rev. E* **2005,** 71, (5), 051709.

26. Feldman, D. E.; Pelcovits, R. A. *Phys. Rev. E* **2004,** 70, (4), -.

27. Sinha, G.; Oka, A.; Glorieux, C.; Thoen, J. *Liq. Cryst.* **2004,** 31, (8), 1123-1129.

28. Roshi, A.; Iannacchione, G. S.; Clegg, P. S.; Birgeneau, R. J. *Phys. Rev. E* **2004,** 69, (3), 031703.

29. Clegg, P. S.; Birgeneau, R. J.; Park, S.; Garland, C. W.; Iannacchione, G. S.; Leheny, R. L.; Neubert, M. E. *Phys. Rev. E* **2003,** 68, (3), 031706.

30. Clegg, P. S.; Stock, C.; Birgeneau, R. J.; Garland, C. W.; Roshi, A.; Iannacchione, G. S. *Phys. Rev. E* **2003,** 67, (2), 021703.

31. Iannacchione, G. S.; Park, S.; Garland, C. W.; Birgeneau, R. J.; Leheny, R. L. *Phys. Rev. E* **2003,** 67, (1), 011709.

32. Jamee, P.; Pitsi, G.; Thoen, J. *Phys. Rev. E* **2002,** 66, (2), 021707.

33. Bellini, T.; Buscaglia, M.; Chiccoli, C.; Mantegazza, F.; Pasini, P.; Zannoni, C. *Phys. Rev. Lett.* **2000,** 85, (5), 1008-1011.

34. Haga, H.; Garland, C. W. *Phys. Rev. E* **1997,** 56, (3), 3044-3052.

35. Kreuzer, M.; Tschudi, T.; Dejeu, W. H.; Eidenschink, R. *Appl. Phys. Lett.* **1993,** 62, (15), 1712-1714.

36. Kreuzer, M.; Tschudi, T.; Eidenschink, R. *Mol. Cryst. Liq. Cryst.* **1992,** 222, 219-227.

37. Eidenschink, R.; Dejeu, W. H. *Electron Lett.* **1991,** 27, (13), 1195-1196.

38. Qi, H.; Kinkead, B.; Hegmann, T. *Adv. Funct. Mater.* **2008,** 18, (2), 212-221.

39. Marx, V. M.; Girgis, H.; Heiney, P. A.; Hegmann, T. *J. Mater. Chem.* **2008,** 18, (25), 2983-2994.

40. Qi, H.; Kinkead, B.; Hegmann, T. *Proc. SPIE* **2008,** 6911, 691106.

41. Nie, Z. H.; Petukhova, A.; Kumacheva, E. *Nat Nanotechnol* **2010,** 5, (1), 15-25.

42. Brust, M.; Bethell, D.; Schiffrin, D. J.; Kiely, C. J. *Adv. Mater.* **1995,** 7, (9), 795-797.

43. Brust, M.; Fink, J.; Bethell, D.; Schiffrin, D. J.; Kiely, C. *J. Chem. Soc., Chem. Comm.* **1995**, (16), 1655-1656.

44. Brust, M.; Walker, M.; Bethell, D.; Schiffrin, D. J.; Whyman, R. *J. Chem. Soc., Chem. Comm.* **1994**, (7), 801-802.

45. Hou, W. B.; Dasog, M.; Scott, R. W. J. *Langmuir* **2009,** 25, (22), 12954-12961.

46. Dasog, M.; Scott, R. W. J. *Langmuir* **2007,** 23, (6), 3381-3387.

47. Shon, Y. S.; Chuc, S.; Voundi, P. *Colloids and Surfaces. A: Physicochem. Eng. Aspects* **2009,** 352, (1-3), 12-17.

48. Ristau, R.; Tiruvalam, R.; Clasen, P. L.; Gorskowski, E. P.; Harmer, M. P.; Kiely, C. J.; Hussain, I.; Brust, M. *Gold Bull.* **2009,** 42, (2), 133-143.

49. Joseph, Y.; Besnard, I.; Rosenberger, M.; Guse, B.; Nothofer, H. G.; Wessels, J. M.; Wild, U.; Knop-Gericke, A.; Su, D. S.; Schlogl, R.; Yasuda, A.; Vossmeyer, T. *J. Phys. Chem. B* **2003,** 107, (30), 7406-7413.

50. Ionita, P.; Volkov, A.; Jeschke, G.; Chechik, V. *Anal. Chem.* **2008,** 80, (1), 95-106.

51. Gentilini, C.; Franchi, P.; Mileo, E.; Polizzi, S.; Lucarini, M.; Pasquato, L. *Angew. Chem. Int. Edit.* **2009,** 48, (17), 3060-3064.

52. Lucarini, M.; Pasquato, L. *Nanoscale* **2010,** 2, (5), 668-676.

53. Dass, A.; Holt, K.; Parker, J. F.; Feldberg, S. W.; Murray, R. W. *J. Phys. Chem. C* **2008,** 112, (51), 20276-20283.

54. Dass, A.; Stevenson, A.; Dubay, G. R.; Tracy, J. B.; Murray, R. W. *J. Am. Chem. Soc.* **2008,** 130, (18), 5940-5946.

55. Wu, S. T.; Coates, D.; Bartmann, E. *Liq. Cryst.* **1991,** 10, (5), 635-646.

56. Jana, N. R.; Earhart, C.; Ying, J. Y. *Chem. Mater.* **2007,** 19, (21), 5074-5082.

57. Mirzaei, J.; Urbanski, M.; Yu, K.; Kitzerow, H. S.; Hegmann, T. *J. Mater. Chem.* **2011,** 21, (34), 12710-12716.

58. Urbanski, M.; Kinkead, B.; Qi, H.; Hegmann, T.; Kitzerow, H. S. *Nanoscale* **2010,** 2, (7), 1118-1121.

59. Kinkead, B.; Hegmann, T. *J. Mater. Chem.* **2010,** 20, (3), 448-458.

60. Urbanski, M.; Kinkead, B.; Hegmann, T.; Kitzerow, H. S. *Liq. Cryst.* **2010,** 37, (9), 1151-1156.

61. Kinkead, B.; Urbanski, M.; Qi, H.; Kitzerow, H. S.; Hegmann, T. *Proc. SPIE-Int. Soc. Opt. Eng.* **2010,** 7775, 77750C1-77750C11.

62. Duran, H.; Gazdecki, B.; Yamashita, A.; Kyu, T. *Liq. Cryst.* **2005,** 32, (7), 815-821.

63. Lopatina, L. M.; Selinger, J. V. *Phys. Rev. Lett.* **2009,** 102, (19), 197802.

64. Khatua, S.; Manna, P.; Chang, W. S.; Tcherniak, A.; Friedlander, E.; Zubarev, E. R.; Link, S. *J. Phys. Chem. C* **2010,** 114, (16), 7251-7257.

65. Milette, J.; Toader, V.; Reven, L.; Lennox, R. B. *J. Mater. Chem.* **2011,** 21, (25), 9043-9050.

Appendix B

Appendix B: Supplementary Information for Chapter 4

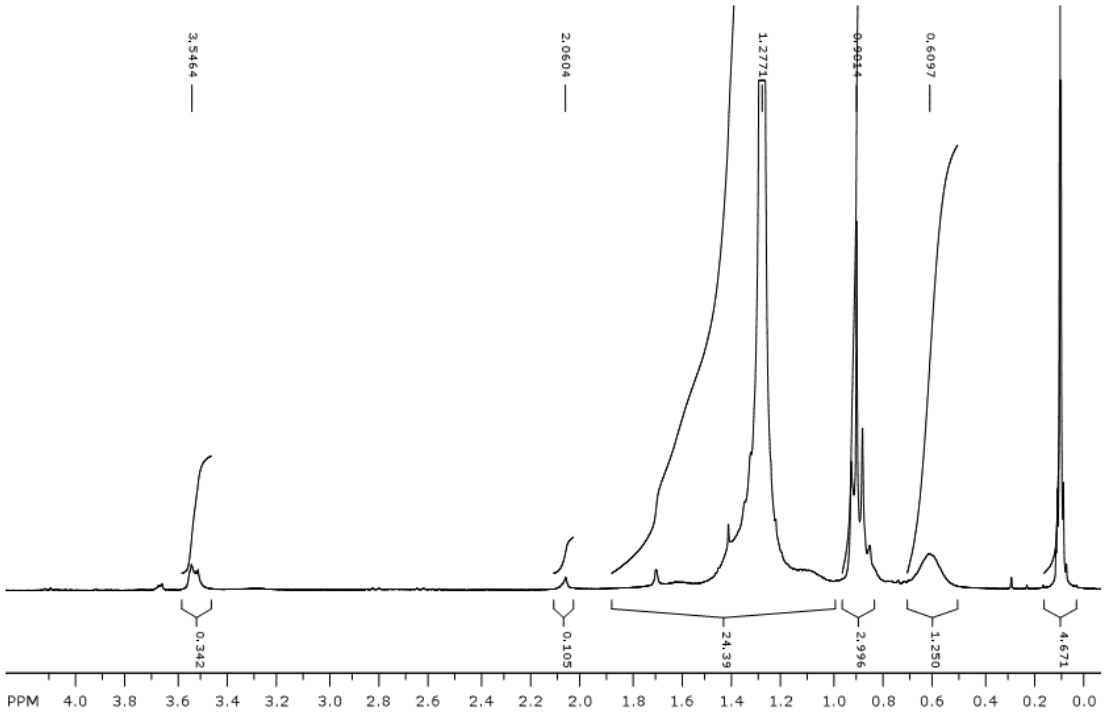

Figure B4.1 ^{1}H NMR spectrum of Au NP_{Sil} particles in $CDCl_3$ (typical broad peaks).

Table B4.1 XPS data of Au NP_{Sil} particles

Peak	Type	Position BE (eV)	FWHM (eV)	Raw Area (cps eV)	RSF	Atomic Mass	Atomic Conc %	Mass Conc %
C 1s	Reg	285.017	1.26	51353.5	0.278	12.011	66.05	51.99
O 1s	Reg	532.417	1.172	46690.5	0.78	15.999	18.96	19.88
Si 2p	Reg	102.317	1.333	12791.4	0.328	28.086	14.94	27.5
Au 4f	Reg	84.717	1.576	790.7	6.25	196.967	0.05*	0.63*

(*possibly shielded by the dense aliphatic layer and siloxane ‘belt’)

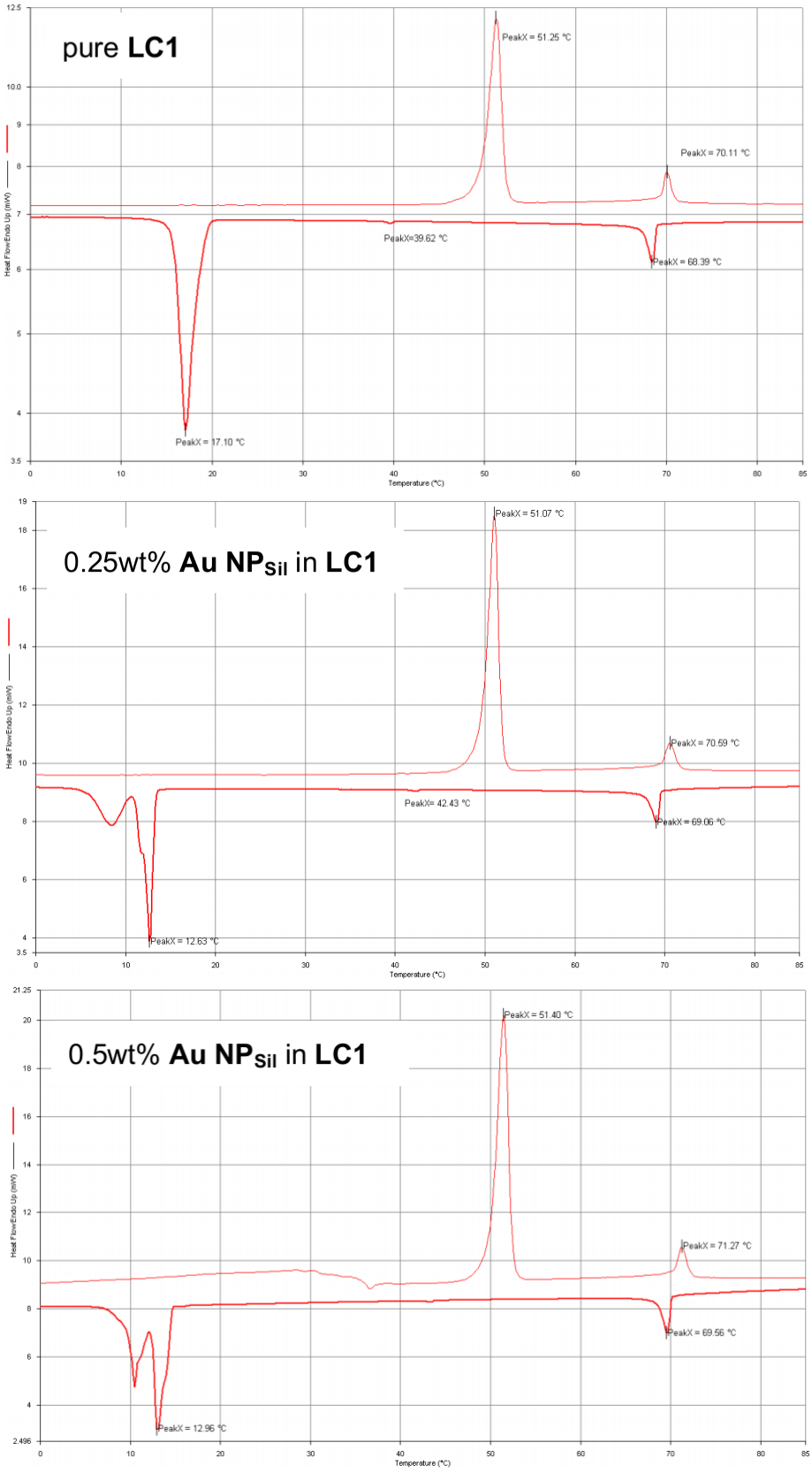
pure LC1
PeakX = 51.25 °C
PeakX = 70.11 °C
PeakX=39.62 °C
PeakX = 68.39 °C
PeakX = 17.10 °C
Heat Flow Endo Up (mW)
Temperature (°C)
0.25wt% Au NPSil in LC1
PeakX = 51.07 °C
PeakX = 70.59 °C
PeakX= 42.43 °C
PeakX = 69.06 °C
PeakX = 12.63 °C
Heat Flow Endo Up (mW)
Temperature (°C)
0.5wt% Au NPSil in LC1
PeakX = 51.40 °C
PeakX = 71.27 °C
PeakX = 69.56 °C
PeakX = 12.96 °C
Heat Flow Endo Up (mW)
Temperature (°C)

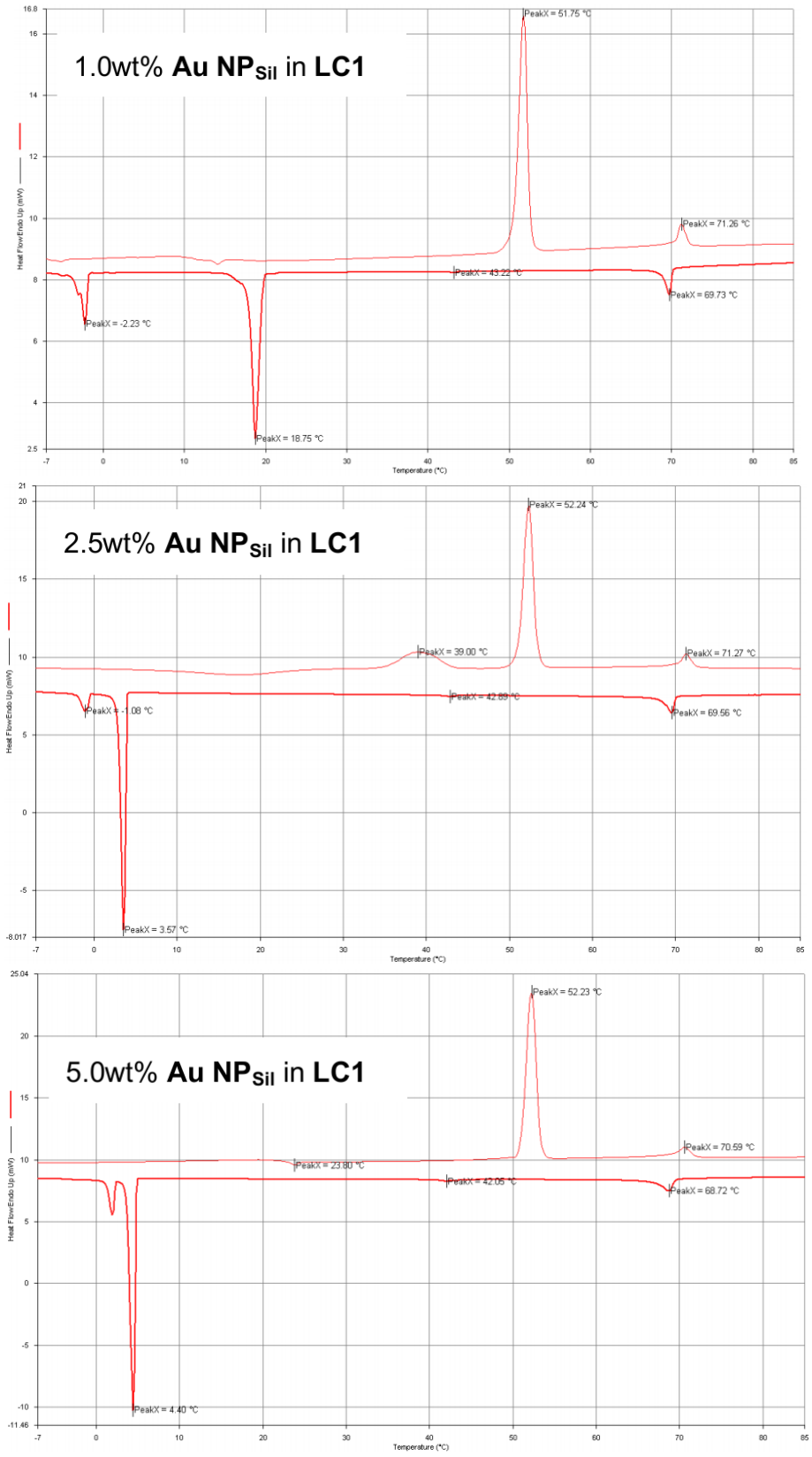
1.0wt% Au NPSil in LC1
PeakX = 51.75 °C
PeakX = 71.26 °C
PeakX = 43.22 °C
PeakX = 69.73 °C
PeakX = -2.23 °C
PeakX = 18.75 °C
Heat Flow Endo Up (mW)
Temperature (°C)
2.5wt% Au NPSil in LC1
PeakX = 52.24 °C
PeakX = 39.00 °C
PeakX = 71.27 °C
PeakX = 42.89 °C
PeakX = 69.56 °C
PeakX = -1.08 °C
PeakX = 3.57 °C
Heat Flow Endo Up (mW)
Temperature (°C)
5.0wt% Au NPSil in LC1
PeakX = 52.23 °C
PeakX = 70.59 °C
PeakX = 23.80 °C
PeakX = 42.05 °C
PeakX = 68.72 °C
PeakX = 4.40 °C
Heat Flow Endo Up (mW)
Temperature (°C)

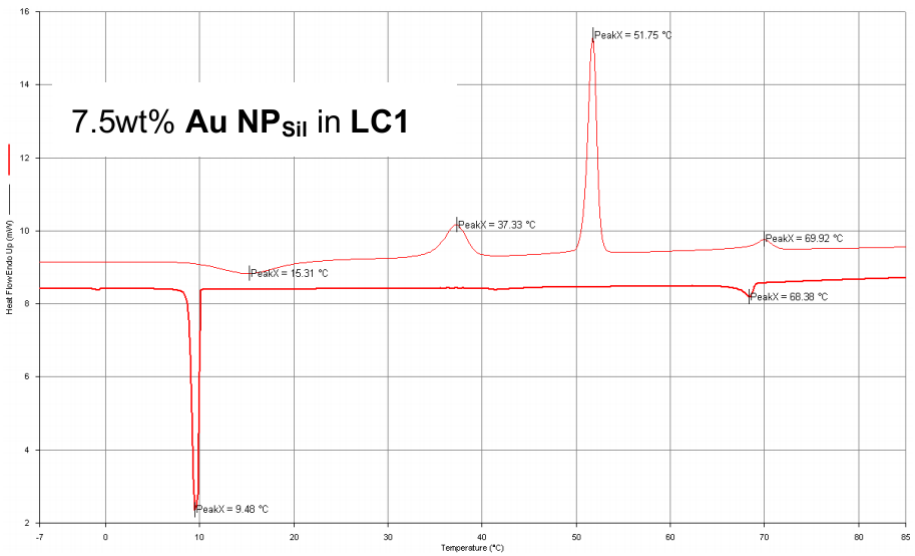

Figure B4.2 DSC traces of the Au NP_{Sil} /LC1 mixtures

Connecting Text for Chapter 5

Chapter 4 described the synthesis of silanized Au NP featuring hydrophobic aliphatic chains and their nematic nanocomposites. The data obtained by optical and electro-optical characterization of these doped nematic composites showed improved stability and miscibility of the silanized NP dopants and encouraged us to prepare Au NP dopants with ligands similar or structurally similar to nematic LC molecules using silane conjugation chemistry. In Chapter 5, we present the synthesis of three types of LC silane-functionalized Au NPs and their impact on the optical and electro-optical properties of nematic LC hosts. The results obtained from each Au NP dopant are discussed with respect to the structure of the ligand as well as the size of NP and the surface coverage. Finally, a theoretical model for the interaction of LC molecules and the liquid crystalline ligands on the NP dopants is proposed.

One of the Au NP studied in Chapter 5 showed the strongest effect on the electro-optical parameters. In view of the importance of these observations and to better understand the mechanism of LC-NP interactions, the nematic dispersions of this NP and a previously reported CdSe were chosen for complimentary theoretical studies and numerical simulations, which we present in the second appendix of Chapter 5.

Chapter 5

Synthesis of Liquid Crystal Silane-Functionalized Gold Nanoparticles and Their Effects on Optical and Electro-Optic Properties of a Structurally Related Nematic Liquid Crystal

Synthesis of Liquid Crystal Silane-Functionalized Gold Nanoparticles and Their Effects on Optical and Electro-Optic Properties of a Structurally Related Nematic Liquid Crystal

Javad Mirzaei[a], Marin Urbanski[b], Heinz-S. Kitzerow[b] and Torsten Hegmann[a,c,d]

[a] Department of Chemistry, University of Manitoba, Winnipeg, MB, R3T 2N2 Canada

[b] Department of Chemistry, University of Paderborn 33098 Paderborn, Germany

[c] *C*hemical Physics Interdisciplinary Program & Liquid Crystal Institute, Kent State University, Kent, OH 44242 USA

[d] Department of Pharmacology and Therapeutics, University of Manitoba, Winnipeg, MB, R3T 2N2 Canada

Reproduced with permission from *ChemPhysChem*, **2014,** 15, (7), 1381-1394.

Abstract

Chemically and thermally robust liquid crystal silane-functionalized gold nanoparticles (AuNP1-AuNP3) were synthesized via silane conjugation. Colloidal dispersions of these particles with mesogenic ligands structurally identical (AuNP1, AuNP2) or compatible (AuNP3) with molecules of the nematic liquid crystal host (N-LC) showed superior colloidal stability and dispersibility. The thermal, optical and electro-optic behavior of the N-LC composites at different concentrations of each gold nanoparticle was investigated. All dispersions showed lower values for the rotational viscosity and elastic constant, but only AuNP3 with a dissimilar structure between nanoparticle ligand and host displayed the most drastic thermal effects and overall strongest impact on the electro-optic properties of the host. The observed results were explained considering both the structure and the density of surface ligands of each gold nanoparticle.

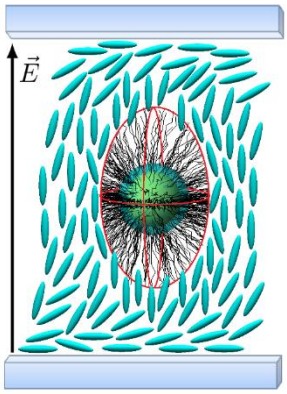

Graphical abstract

5.1 Introduction

Considering advances in nanoscience and nanotechnology over the past decade, incorporation of functional nanoparticles (NPs) in liquid crystals (LCs) has emerged as a promising approach to create LC nanocomposites with synergistic properties of both components.[1-7] Research on LC nanocomposites mainly focuses on LC-guided self-assembly and alignment of NPs as well as on modulating the properties of different LC phases using small quantities of a nanoscale additive. The bulk of research on the latter is devoted to nematic LC (N-LCs), because of their use in display and other optical and electro-optical technologies[8-10] such as optical antennas or optical shutters.[11]

It has been shown that doping N-LCs with low concentrations of NPs is an efficient way to tune the optical and electro-optic properties.[4, 12] For example, doping N-LCs with metallic NPs such as Au [13-17] or Ag NPs[18] capped with alkyl thiolate groups or semiconducting NPs also known as quantum dots (QDs), namely CdSe[18-21] and CdTe[19] can alter the properties of the host in a unique fashion. It is frequently observed that textures observed by polarized optical microscopy of these nematic nanocomposites containing less than 5 wt% of NPs capped with aliphatic ligands show birefringent stripes of equal width surrounded by homeotropic domains due to homeotropic orientation of the nematic director imposed by the NPs residing at the substrate/N-LC after the N-LC expelled the initially well-suspended NPs.[15, 17] Many electro-optic studies of such composites in ITO-coated cells with rubbed alignment layer confirmed altered (in part improved) electro-optical parameters including lower threshold voltage (V_{th}), larger dielectric anisotropy ($\Delta\varepsilon$), and faster response time.[17-20] Colloidal LC dispersions are not limited to metallic NPs.

Different other types of NPs including magnetic,[22, 23] ferroelectric,[24, 25] semiconductor[3] have also been found effective additives to alter properties such as bulk ordering, phase transition temperatures, birefringence, dielectric anisotropy, and response to external fields in N-LCs. Recently, substantially altered properties of ferroelectric LCs (FLCs) doped with metallic, semiconductor and metal oxide NPs were reported as well.[26-32] These experimental findings suggest that NPs are also uniquely able to alter electro-optic, dielectric, even luminescent properties and memory effects in FLCs.[26-34]

Despite all prospects and potential applications for the field, LC-NP composite research has been suffering from an apparent insufficiency of knowledge about the mechanism of interactions between LC molecules and NPs or their organic corona. In order to understand these mechanisms better, it seems urgent to primarily tackle two major obstacles facing LC nanocomposites. The first obstacle is the low miscibility or dispersibility of NPs in LCs that is exacerbated in the absence of compatible functional groups on surface of NPs. It is worth noting here that dispersibility of NPs in any liquid crystalline phase is expected to be lower than in the isotropic liquid by virtue of intrinsic limited miscibility in any partially ordered medium. The tendency of NPs to aggregate can also be viewed as the compensation of the system for distortions in the local order parameter in the presence of NPs smaller than 100 nm.[35] The second obstacle is the weak stability of NPs in LC composites arising from the lack of robust capping agents or inadequate coverage on the surface of NPs.

This limited stability can essentially increase the risk of NP aggregation causing irreversibly phase-separated (segregated) NP-LC system from the nano- to the macro-scale. Both of these obstacles have links to surface chemistry of the NP and therefore any attempt

to achieve well-dispersed and stable colloidal LCs should be addressed together. It is proven that when the surface of NPs is covered with organic ligands or surfactants featuring mesogenic or pro-mesogenic motifs close or comparable to those of host LC molecules, interactions of NPs with the LC matrix will be more specific.[5, 36] A mixed ligand shell (i.e. longer functional and shorter aliphatic) or more space between functional ligands would essentially enable insertion of organic ligands and host LC molecules (inter-digitation) in order to minimize the disturbance of the local director in the LC phase caused by presence of the NPs.[37] For example, Au NPs functionalized with mixed monolayer of alkyl thiolates and pro-mesogenic cyanobiphenyl,[38, 39] bent-core LC[40] or mesogenic triphenylene-based ligands[41] result in a larger impact on the LC properties because of the compatibility with the LC host molecules. It has been shown that Au NPs functionalized with LC or pro-mesogenic moieties can form mesophases and show rather unique multi-level self-assembly behavior.[42-49] Apart from Au NPs, there are several reports on other types of liquid crystalline NPs featuring TiO_2[50], Fe_2O_3[51, 52], CdSe[53], ZnO[54] and CdSe/ZnS[37] cores decorated with (pro-)mesogenic groups.

However, dispersions of LC-decorated NPs are still limited to very low concentrations and the LC or self-assembly properties of such NPs may vanish due to a lack of long-term stability.[5, 37] This is when LC dispersions are being challenged by the second obstacle; i.e. instability of NPs. Au NPs are the most frequently used particles in colloidal LCs. Apart from our interest in the unique size-dependent characteristics; Au NPs are relatively easy to make following the Brust-Schiffrin method.[55, 56] Moreover, Au-thiol ligand interactions are probably the best understood, and it is feasible to partially or completely remove

thiols[57, 58] or other stabilizers such as phosphines[59, 60] and amines[61-63] in situ or via place exchange reactions for further functionalization.

Nevertheless, it has been shown that the bonds between Au-atoms on the surface of NPs and the S-atoms of thiols experience dynamic binding and unbinding processes.[64, 65] This phenomenon increases the risk of NP aggregation as a result of the chemical vulnerability of thiolate-capped Au NPs towards oxidation[66], chemicals such as halides[67] or alkaline metal ions,[68] and elevated temperatures. The latter has been shown by thermogravimetric analysis (TGA) and temperature-dependent X-ray photoelectron spectroscopy (XPS). In fact, alkyl thiolate capping agents start to or completely desorb from the Au NP surface at temperatures between 90 °C and 160 °C depending on the length of the thiol alkyl chain.[69, 70] It should be noted that the thermal stability of Au NPs plays an important role in the overall stability of colloidal LCs, particularly when LC phases persist at higher temperatures and sample preparation requires annealing and slow cooling from the isotropic liquid phase. Another consequence of thiol migration on Au NP surfaces can be seen in sintering of particles. Sintering or coarsening is often observed for smaller Au NPs that tend to grow and form larger particles, an effect occurring rapidly at elevated temperatures (250 °C); but noticeably already at room temperature.[70, 71] Silica coating or silanization was found to be a prominent way to increase the stability of NPs and potentially avoid all of the aforementioned consequences.[72, 73] In a prior study, we utilized a versatile silane conjugation approach to synthesize hydrophobic Au NPs based on a method reported by Jana and co-workers.[74] The as-synthesized, silanized Au NPs bearing aliphatic $C_{18}H_{37}$ chains allowed for the preparation of homogenous N-LC dispersions even with high concentrations of NPs up to 5 wt% along with exceptional thermal and chemical stability.[16]

The motivation for the current study was to evaluate the effect of functionalizing such silane shell, that has proven to give stable nematic nanocomposites with (pro-)mesogenic ligands. Herein, we report the synthesis and mesogenic functionalization of a series of Au NPs (**AuNP1** − **AuNP3**) via silane conjugation, and experimental results of optical/electro-optical measurements in dispersions with the nematic Felix-2900-03 (**LC1**, **Figure 5.1**). As discussed earlier, by addressing both obstacles, these nematic dispersions give us a reliable platform to evaluate influences of NPs on N-LCs and shed more light on the complex mechanism of interactions of NPs with host LC molecules.

5.2 Experimental

Materials and methods

Hydrogen tetrachloroaurate(III) trihydrate was purchased from Alfa Aesar. Didodecyldimethylammonium bromide (DDAB), and tetrabutylammonium borohydride (TBAB), (3-mercaptopropyl)trimethoxysilane (MPS), 8-bromo-1-octene, 11-bromo-1-undecene, and platinum(0)-1,3-divinyl-1,1,3,3-tetramethyldi-siloxane complex solution (Karstedt's catalyst) were purchased from Sigma-Aldrich. Pure **LC1** (Felix 2900-03), 2-(4'-hydroxyphenyl)-5-*n*-heptylpyrimidine and 4-(6-acryloyloxy-hex-1-yl-oxy)phenyl, and 4-(hexyloxy)benzoate were purchased from Synthon Chemicals GmbH. All chemicals were used without further purification. All solvents used for the synthesis and purification were Aldrich purification grade purified via a PureSolv solvent purification system (Innovative Technology Inc.). Millipore water (18 MΩ) was used to rinse glassware and vials used for sample preparation. In addition, all glassware and vials used for synthesis,

sample handling, and mixing NPs with the LC host were cleaned with aqua regia and thoroughly rinsed with DI water. ^{1}H NMR spectra were recorded on a Bruker Avance 300 MHz spectrometer using deuterated chloroform ($CDCl_3$). Tetramethylsilane (TMS) was used as an internal standard. UV-vis-NIR absorption spectra were obtained by a Varian Cary 5000 UV-vis-NIR spectrophotometer using a quartz cell (1 cm path). HR-TEM images were recorded on a Jeol ultra-high resolution FEG-T/STEM operating at an accelerating voltage of 200 kV. The samples were prepared by drop casting a 5 μL dispersion of the Au NP toluene solution on carbon-coated copper grids (400 mesh) and dried for one hour under ambient conditions. XPS analysis of the Au NP samples was performed using a Kratos AXIS ULTRA spectrometer with a 300 W monochromated Al Kα source and a delay line detector. The survey and high-resolution scans were recorded with pass energies of 160 and 40 eV, respectively. All spectra were collected at 90° take-off angle and referenced to the C 1s peak set at 285 eV. The background pressure in the analyzer chamber was ~10^{-9} Torr. For quantitative analysis, sensitivity factors supplied by the instrument manufacturer were used. Melting points, phase transition temperatures, and the corresponding enthalpy values of all final LC-AuNP mixtures were determined by means of a Perkin-Elmer Pyris Diamond differential scanning calorimeter (DSC), obtained based on two cycles of heating and cooling at a rate of 10 °C min^{-1}. Thermogravimetric analysis experiments were carried out with a Linseis L81 thermobalance. The Au NP samples (~ 10 mg) were heated from 25 to 1000 °C in argon flows and then cooled to room temperature in static air at a rate of 20 °C min^{-1}. Experiments were conducted in alumina crucibles with an empty crucible as the reference. The buoyancy correction was carried out with an empty crucible in the sample position for all the samples.

Synthesis of silanes 3a-b

For the synthesis of the phenylpyrimidine derivatives **3a-b** commercially available 2-(4'-hydroxyphenyl)-5-*n*-heptylpyrimidine was alkylated with appropriate commercially available bromoalkenes to yield LC compounds **2a-b** containing a hydrocarbon chain with terminal vinyl group at one side. The terminal alkenes of **2a-b** were converted to a trimethoxysilane end group by a hydrosilylation reaction. The experimental details are given in the supplementary information (Appendix C). While compounds **3a-b** are not showing liquid crystalline behavior, POM confirms the formation of enantiotropic SmA and N phases and monotropic SmC phases for LCs **2a-b** with the phase transition temperatures matching with those previously reported[75] (for further experimental details see supplementary information in Appendix C).

Synthesis of LC silane 5

The terminal alkene-substituted nematic LC **4** is commercially available from Synthon Chemicals GmbH. Compound **4** shows a N-phase with the following phase transition temperatures: Cr 54 N 67 Iso. Similar to a method described elsewhere,[76] the terminal alkene of **4** was converted to silane in **5** by hydrosilylation reaction.

Synthesis of LC-decorated Au NPs

The synthesis of silanized NPs in one step starts from hydrogen tetrachloroaurate trihydrate as gold precursor, MPS and trialkoxysilane as capping ligands, and DDAB and TBAB as phase transfer catalyst and reducing agent, respectively. The general method for making all three **AuNP1-AuNP3** includes: A 10 mL solution of $HAuCL_4$ in toluene (0.01M) was prepared in the presence of an equimolar amount of DDAB using 5 min sonication. Next, 1 mL of a toluene solution of 3-mercaptopropyltrimethoxysilane MPS (0.1M) was added

under stirring followed by addition of 1 mL toluene solution of TBAB and DDAB (27 mg of TBAB and 25 mg of DDAB). The reaction solution turned immediately black and changed slowly to pink indicating formation of Au NPs coated with MPS. After 30 minutes without isolating the initial NPs, a 1.5 mL toluene solution of the second silane bearing a trimethoxysilane group (0.2M) (compounds **3a**, **3b**, or **5**) was added to the reaction mixture followed by 200 μL of an aqueous solution of NaOH (1.0M) for the silane conjugation step. This step comprises hydrolysis of alkoxysilanes to silanol groups under basic conditions followed by co-condensation of the two silanol groups. After stirring for 7 h solvent was evaporated, and the collected particles were washed several times with chloroform and isopropanol**.** The process of precipitation and re-dispersion was repeated several times until the last supernatant was free from any residual non-bound silane/siloxane as confirmed by ^{1}H NMR. The as-synthesized Au NPs (**AuNP1-AuNP3**) were dispersed in toluene and filtered through a 0.45 μm syringe filter (PTFE, Whatman) and then characterized by UV-vis, TEM, XPS and NMR spectroscopy.

Au NPs dispersion in nematic LC

The mixtures of the Au NPs in **LC1** were prepared by weighing accurate amounts of each Au NP and LC using a micro-balance and dissolving it in a known amount of dry toluene. Colloidal solutions of Au NPs were sonicated for about 15 minutes (water-bath sonication; f=37 KHz power). Then toluene solutions of each of **AuNP1**, **AuNP2** and **AuNP3** were combined in a V-vial® with the LC solution to produce the exact concentration of the Au NPs in **LC1** for each Au NP (0.5, 1, 2.5 & 5 wt% mixtures) and final solutions were sonicated for another 1 h. The solvent was then allowed to evaporate under a steady stream of dry N_2 at ~ 70 °C for about 48 h followed by sonication.

Optical and electro-optical characterization methods

Polarized optical microscopy (POM) images were taken using an Olympus BX51-P polarized optical microscope in conjunction with a Linkam LS350 heating/cooling stage with the samples sandwiched between untreated microscope glass slides. Electro-optic (EO) analysis was performed using an LCAS1 automated liquid crystal analyzer (LC Vision). EO data were obtained using the single-cell method built into the LCAS 1 software as originally described by Wu *et al.*[77] The LC test cells used were planar 4.0 µm cells with antiparallel polyimide alignment layers and 1° to 3° pre-tilt (LC Vision). Loading of the cells with LC-NP mixtures was performed by capillary force with the LC in the isotropic liquid phase (74-78 °C). For all POM imaging and EO measurements, the LC mixtures were heated above the Iso/N phase transition temperature ($T_{\text{Iso-N}}$) and cooled at a rate of 1 °C min^{-1} until the desired temperature below $T_{\text{Iso-N}}$ was reached. The average of all values and standard deviations of each electro-optic parameter were calculated from at least five or up to ten measurements at any given temperature for the each mixture (also using different cells).

In addition, simultaneous measurements were performed by light transmittance in a polarizing microscope to obtain threshold voltages, dielectric anisotropy, and switching times. The test cells were positioned under an angle of 45° between crossed polarizers within a Linkam LTS350 heating stage with TMS94 controller for temperature control. All samples were at first heated to 76 °C at a heating rate of 8 °C min^{-1}, followed by cooling procedure at 1 °C min^{-1} until the first measuring temperature of 48 °C or 58 °C, respectively, is reached. All measurements were performed on an Ortholux II Pol-BK microscope (Leica) using a halogen lamp (Xenophot, Osram) with DC stabilized power

supply. For monochromatic light, an interference filter with a transmission maximum at 542 nm (FWHM 10.8 nm) was used. Simultaneously, the cell capacitance was measured on an HP 4284A LCR bridge, varying the sine test signal level from 0.05 V_{rms} to 19.95 V_{rms} at a test signal frequency of 1 kHz. The blind capacitance (cable parasitic capacitance) of the setup due to wires, contacts etc. was determined to be 4.125 pF. The electro-optical analysis was done both on cooling and heating. Measurement on heating allows the determination of threshold voltages even at higher temperatures, as the temperature regime with a coexistence of nematic and isotropic phase was smaller on heating than on cooling. The results are not affected by the different sign of the temperature gradient. We showed that for a dispersion containing 0.5 wt% of AuNP3 in LC1, the dielectric properties or the threshold voltage are similar on heating and cooling (see supplementary information, Appendix C Figure C5.11). The switching times were recorded on a PicoScope3206A at a sampling rate of 100k samples/second. The driving frequency was 10 kHz, and the intensity signal was filtered by a 10 kHz low-pass filter to eliminate intensity fluctuations due to the driving frequency.

5.3 Results and Discussions

Nanoparticle Characterization

Characterization of the as-synthesized Au NPs using silane conjugation method started with collecting UV-visible spectra and high-resolution transmission electron microscopy (HR-TEM) images to obtain information about their optical behavior and physical dimension (average diameter and size uniformity). As shown in **Figure 5.2**, the visible

absorption spectrum in toluene for each Au NP showed the presence of the surface plasmon resonance (SPR) band at 530, 540 and 538 nm **AuNP1**, **AuNP2**, and **AuNP3**, respectively.

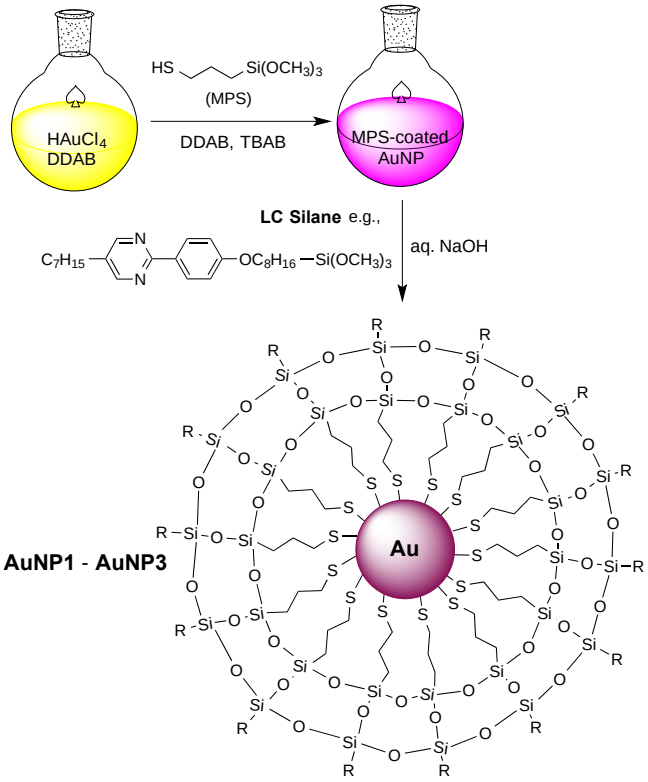

Au NP	R =
AuNP1	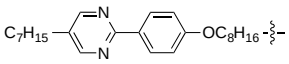
AuNP2	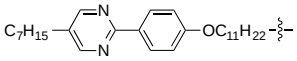
AuNP3	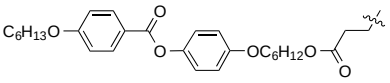

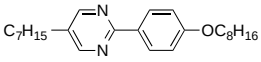

LC1; phase sequence: Cr 52 (SmA 45) N 70 Iso

Figure 5.1 Schematic synthesis and idealized structure of the Au NPs (**AuNP1 - AuNP3**) featuring either phenylpyrimidine or phenylbenzoate (pro-)mesogenic ligands. The most likely deviations from this idealized 2D schematic structure of the NP corona are shown in the SI. Abbreviations: MPS = (3-mercaptopropyl)-trimethoxysilane, DDAB = didodecyldimethylammonium bromide, and TBAB = tetrabutylammonium borohydride.

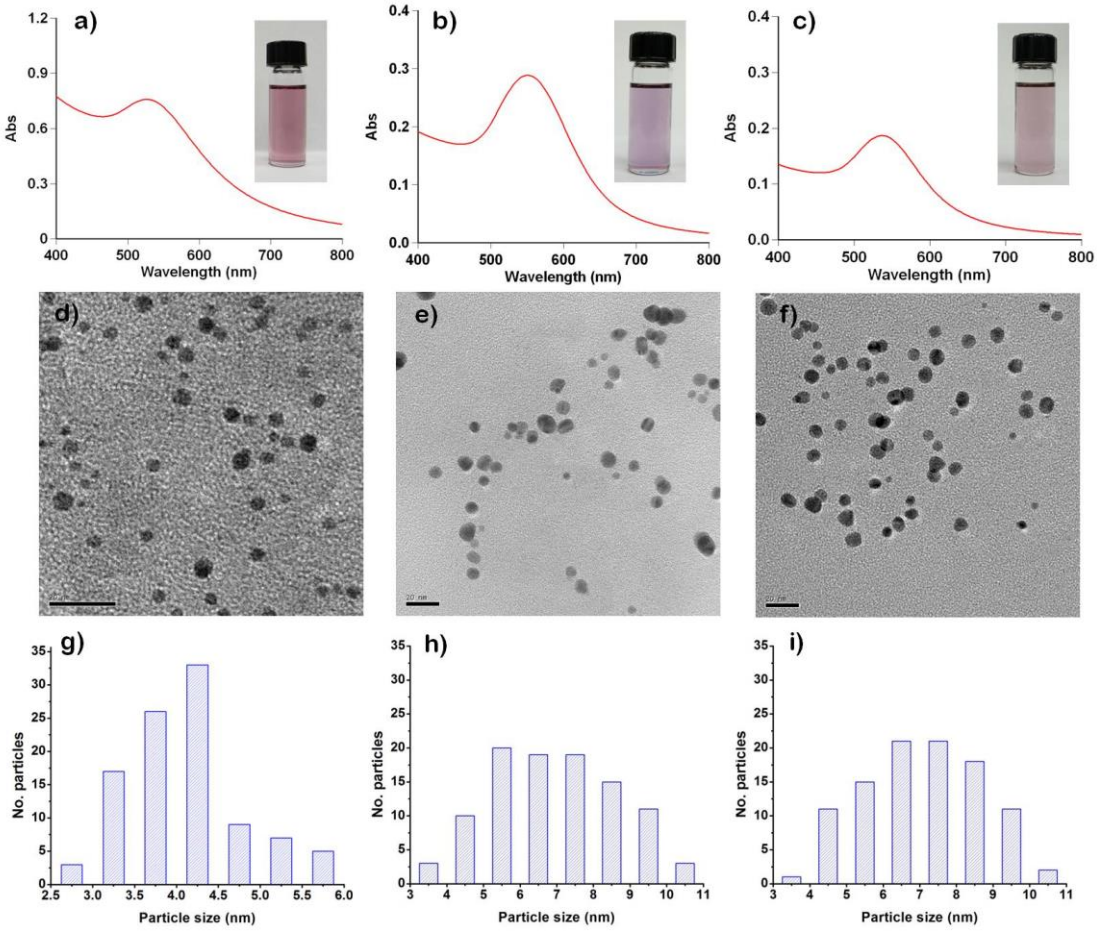

Figure 5.2 UV-vis spectra, HR-TEM image (scale bars: 20 nm) and size distribution histograms for **AuNP1** (a, d, g), **AuNP2** (b, e, h), and **AuNP3** (c, f, i). Inset in each absorption spectrum shows the colloidal solution of **AuNP1−3** in toluene.

The shift in the SPR band maximum in **AuNP2** and **AuNP3** compared to **AuNP1** is primarily due to larger particle size, and the size distribution analyses from TEM images confirm this (**Figure 5.2d-f**). **AuNP1** with the average NP size of 4.09 ± 0.7 nm is smaller than batches of **AuNP2** and **AuNP3** with average sizes of 6.9 ± 1.7 nm and 7.07 ± 1.6 nm, respectively. Since the synthetic conditions for all three types of Au NP were kept identical,

except of course for the trialkoxysilane LC ligand, this difference in average size can only be due to the different structure or chemical reactivity of this second trialkoxysilane LC ligand in the hydrolysis and condensation steps in the preparation of each of these Au NPs. The size histograms in **Figure 5.2g-i** are depicting the size distribution of **AuNP1−3**. ^{1}H NMR spectra of each of the NPs confirmed the presence of silane-conjugated ligands and that all impurities and non-reacted ligands were removed. XPS data confirm the formation of the silane shell around the Au NPs (for NMR and XPS data see supplementary information). In XPS, **AuNP2** and **AuNP3** are not showing any peak for Au 4f, which may be due to the presence of the longer silane-capping agents considering an instrumentally limited penetration depth.

To test the thermal stability of these NPs, batches of each type were kept at elevated temperatures (190 °C) under prolonged sonication. The silanized NPs after these conditions showed good re-dispersibility in non-polar solvents with identical UV-visible absorption spectra and TEM images indicating their exceptional stability. To prove and compare their superior thermal stability, we also synthesized dodecanethiol-capped Au NP, heated the dry NPs to 190 °C as well, and kept the sample at this temperature for 30 minutes following a procedure reported elsewhere.[78] The TEM of these particles before and after thermal treatment (**Figure 5.3a-b**) confirmed that the particle size increases from an average of 2.3 nm to about 7.2 nm, which is consistent with data reported earlier.[78] Interestingly, but not surprisingly, when we performed a similar thermal treatment for **AuNP1** (representative for all three silane conjugation-capped Au NPs described here), the average size showed only a negligible increase, bringing the average to 4.4 ± 0.9 nm (see **Figure 5.3c-d**).

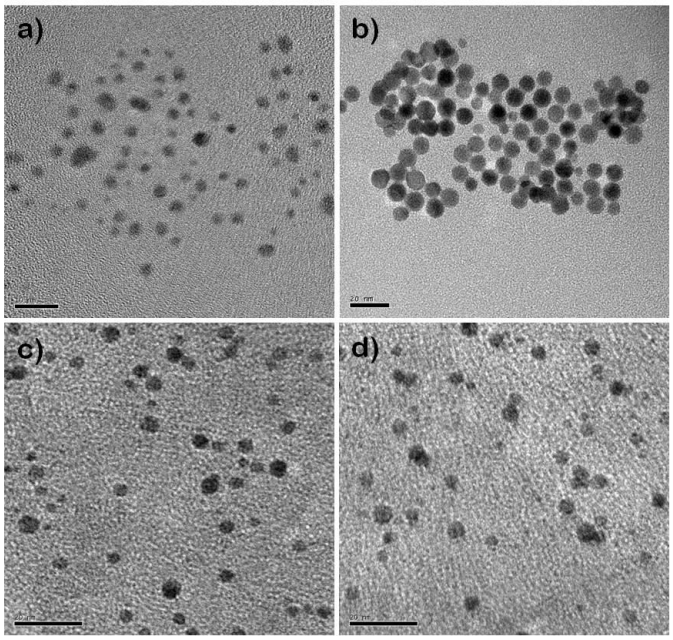

Figure 5.3 HR-TEM of dodecanethiol-capped Au NPs before (a) and after (b) thermal treatment at 190 °C (Note the increase in size of the thiol-capped Au NPs). In comparison, TEM of AuNP1 before (c) and after (d) similar thermal treatment – no increase in size (scale bars: 10 nm for (a) and 20 nm for (b-d)).

To ascertain the NP surface coverage with organic LC ligands, we performed TGA experiments and implemented the results and average NPs size obtained from TEM in a series of calculations according to a spherical particle model developed by Imahori et al.[79] **Table 5.1** summarizes the result of geometric calculations for each type of Au NP including volume and number of Au atoms in each particle. We also calculated the volume of organic corona and total volume for each particle by assuming the orthogonal orientation of the ligand molecules and using their molecular lengths obtained by MOPAC simulations. These calculations together with TGA data helped us estimate the density (coverage) of the organic corona for each **AuNP1−3** (**Table 5.1**). The obtained results, although approximate, can sufficiently provide a scale for comparing the amount and density of

organic ligands in each type of NP. As presented in **Table 5.1**, **AuNP2** has the densest organic corona, about three-times higher than **AuNP1** and **AuNP3**, which have almost equal density. However, for **AuNP1** and **AuNP3** if we take the number of ligands per nanoparticle into account, we will notice 2602 ligands for **AuNP3**, which is three and a half-higher than for **AuNP1**. It should be mentioned that as there is a network formed by two silanes in the organic corona; the number of ligands represents an approximate total number of both silane types (fully conjugated with the LC silane and just MPS) and does not necessarily mean ligands attached to the surface gold atoms. Using the aforementioned result, we also estimated the number of particles per unit volume of **LC1** for the three NP tested (**Table 5.1**). A representative sample calculation for **AuNP1** is given in the supplementary information (Appendix C).

Table 5.1 Determination of the density of ligands covering the surface of the Au NPs, and number of particles per unit volume in **LC1**.[a]

AuNP	Average NP size (nm)	Length of ligand (nm)	Number of Au atoms per NP	Number of Surface Au atoms	Total Volume of each NP (nm^3)	Volume of organic corona (nm^3)	Number of ligands per NP	Density of organic corona (g/cm^3)	Number of NPs per unit volume in **LC1** ($1/cm^3$)	M_w of Au NP (g/mol)
1	4.09	2.39	2077	630	366.95	331.15	728	2.22[b]	7.13×10^{15}	852306
2	6.90	2.62	9973	1906	937.26	765.35	4538	6.40	1.23×10^{15}	4910955
3	7.07	3.18	10728	2005	1270.5	1085.6	2602	2.83[b]	1.53×10^{15}	3986970

[a] For details on these calculations, see SI. [b] The lower density for **AuNP1** and **AuNP3** are likely the result of incomplete conjugation with the LC silane in step 2 of the synthesis shown in Figure 1; i.e. the ligand shell is not as complete as indicated in the cartoon.

Optical and Thermal Characterization

After the detailed characterization of the Au NPs, composites with the N-LC Felix-2900-03 (**LC1**) and **AuNP1–AuNP3** were prepared on the basis of protocols for investigating NP-doped N-LCs established in our laboratory and described in the Experimental Section.

We chose **LC1** as a structure for the ligand (initially for **AuNP1** and **AuNP2**, and a structurally different ligand for **AuNP3** to allow comparison) and the N-LC host because we used this N-LC for several studies in the past. This allowed us to compare current results with previous findings.[14, 16, 19, 20, 80] In these earlier studies, we noticed that the minimum and maximum NP loading with noticeable and positive doping effects was primarily between 0.5 and 5 wt %. After the preparation of the NP-doped samples, the quality of the dispersions was initially examined visually by inspecting the quality of the dispersion of the silanized NPs in the nematic phase (N phase) of LC1 at temperatures close to the nematic-to-isotropic phase-transition temperature ($T_{N\text{-}Iso}$). The absence of NP settling or color changes in the V vials as well as a continuous color intensity on the basis of the SPR and the concentration of the NPs in LC1 all suggested homogeneous and stable dispersions for all three types of Au NPs in LC1 at concentrations of 0.5, 1, 2.5, and 5 wt % (**Figure 5.4** shows LC1–AuNP2 mixtures; images for AuNP1 and AuNP3 are collected in Figure C5.7 and Figure C5.7 in the supplementary information presented in Appendix C).

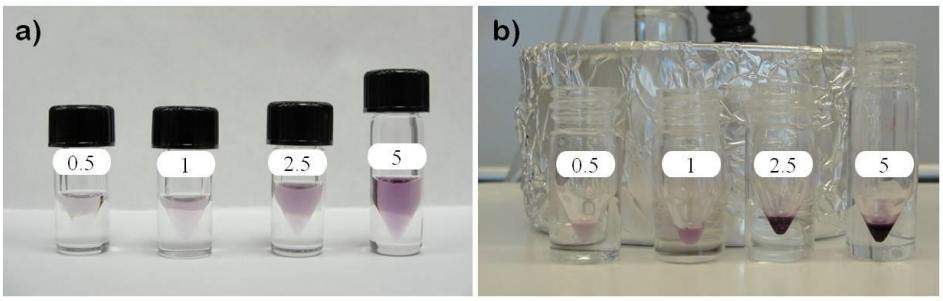

Figure 5.4 Figure 4. Mixtures of LC1 doped with **AuNP2**: a) in toluene and b) after solvent evaporation right below the Iso/N phase transition temperature (70 °C).

Polarized optical microscopy (POM) textures of thin films between plain, untreated glass slides offer first clues on the alignment and thermal properties of NP-doped **LC1** and further guide electro-optical measurements. All doped **LC1** samples studied showed temperature-dependent alignment; that is, starting with homogenous or planar orientation of the nematic molecules and slowly transforming into homeotropic alignment with the appearance of birefringent stripe textures. This texture was frequently observed by our group in the past for nematic mixture doped with comparable NPs.[13-16] NPs residing at LC/glass interface impose homeotropic anchoring of the nematic director.[15] The origin of the birefringent stripes, which are in fact π walls extending almost through the entire nematic film, for which the rodlike N-LC molecules follow the long axis of these stripes as described in our earlier work using fluorescence confocal polarizing microscopy (FCPM)[81] was found to be network of particles gathered in isotropic domains surrounded by forming nematic droplets upon cooling from the isotropic to the N phase.[82]

Again, NPs are normally more soluble in the isotropic LC than in the N phase. **Figure 5.5** depicts the POM images collected for **AuNP1** at different concentration at 58 °C upon cooling, these images show that an increasing concentration of the Au NPs (demonstratively for **AuNP1**) leads increasingly to vertical alignment. **Figure 5.6** and **Table 5.2** are together presenting optical textures and the temperatures at which the average planar alignment in the **LC1-AuNP1** nanocomposites start to transform into homeotropic at each concentration of **AuNP1**. The temperatures obtained for this alignment switching suggest a concentration-dependent effect, that is, dispersions with higher concentration of NPs tend to change alignment at higher temperatures. However,

we did not see any noticeable aggregation by increasing the NP load, as supported by microscopy images with uncrossed polarizers.

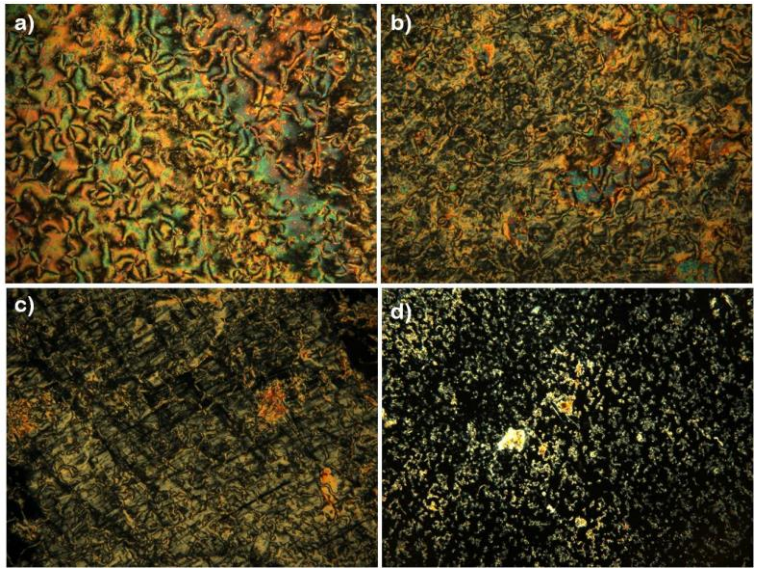

Figure 5.5 POM micrographs (crossed polarizers) of **LC1** doped with **AuNP2** at 58 °C: a) 0.5, b) 1, c) 2.5 and d) 5 wt% on cooling at a rate of 1 °C min^{-1}.

For mixtures of nematic **LC1** and **AuNP2**, POM micrographs of composites between untreated glass slides also confirmed the presence of homeotropic alignment of the N-LC molecules. For 0.5 and 1 wt%, the optical textures were initially randomly planar and then they transformed into a homeotropic orientation upon slow cooling, whereas at higher concentrations of 2.5 and 5 wt% of **AuNP2** in **LC1**, homeotropic alignment was observed upon cooling from the isotropic phase to the N phase and remained so until cooled to the smectic A phase (**Figure 5.7**). The temperatures at which the initial planar alignment for 0.5 and 1 wt% **AuNP2** doped samples turned to homeotropic were 63.5 and 65 °C, respectively. These temperatures are similar to those observed for the 2.5 and 5 wt%

AuNP1 dispersions, which indicates that size, ligand density, or both play a role in this change in LC orientation upon cooling.

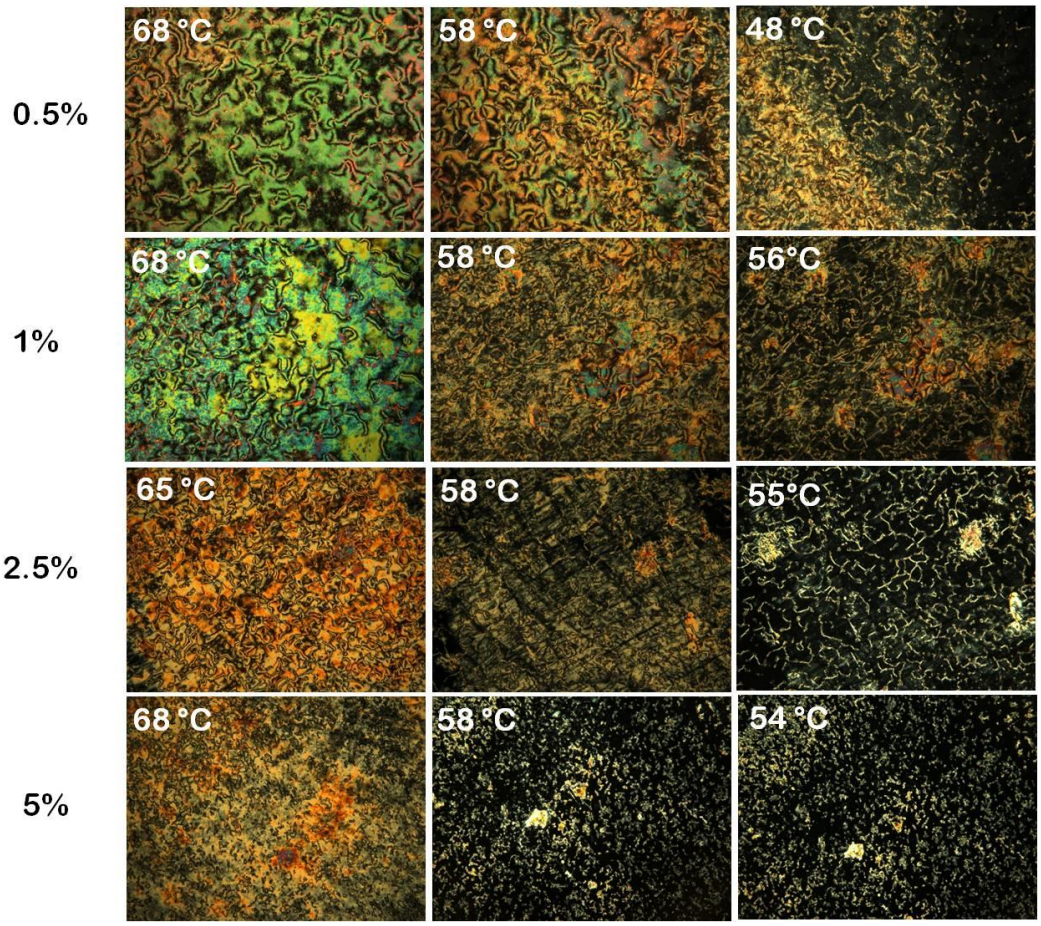

Figure 5.6 POM photomicrographs (crossed polarizers) of the temperature-dependent alignment of nematic phase of **LC1** doped with **AuNP1** (Every row showing similar area on cooling at a rate of 1 °C min^{-1})

Table 5.2 Temperature of alignment change from planar to homeotropic with some birefringent stripes for **LC1** doped with **AuNP1** (sandwiched thin film samples between plain, non-treated microscopy glass slides).

AuNP1 concentration wt%	Planar to homeotropic switch (°C)
0.5	52
1	59
2.5	61-60
5	62-61

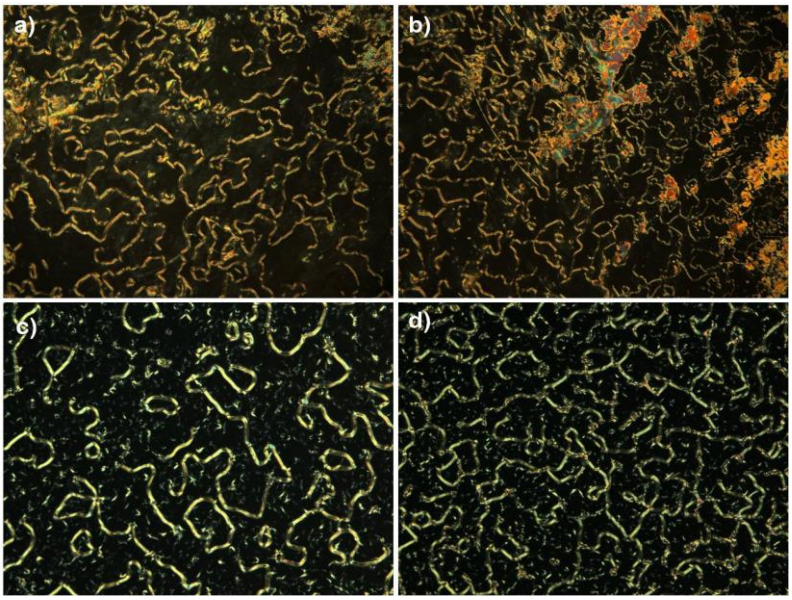

Figure 5.7 POM micrographs (crossed polarizers) of **LC1** doped with **AuNP2** at 58 °C: a) 0.5, b) 1, c) 2.5 and d) 5 wt% on cooling at a rate of 1 °C min^{-1}.

For LC1 doped with **AuNP3**, as depicted in **Figure 5.8**, with a structurally different ligand on the surface of the NP, similar optical patterns were observed. In terms of changing the alignment mode from planar to homeotropic, these changes also occurred at temperatures similar to those for the **AuNP1** dispersions (52, 58, and 60 °C for 0.5, 1, and 2.5 wt %, respectively), which is not surprising given the similar density of the ligand corona, as shown in **Table 5.1**. The mixture of 5 wt % **AuNP3**, however, showed birefringent stripes and homeotropic domains right at the transition from the isotropic phase to the N phase. This mixture also showed a relatively wide range over which the isotropic and nematic phases coexisted upon cooling. This is to be explained in the studies of phase transitions by POM and differential scanning calorimetry (DSC).

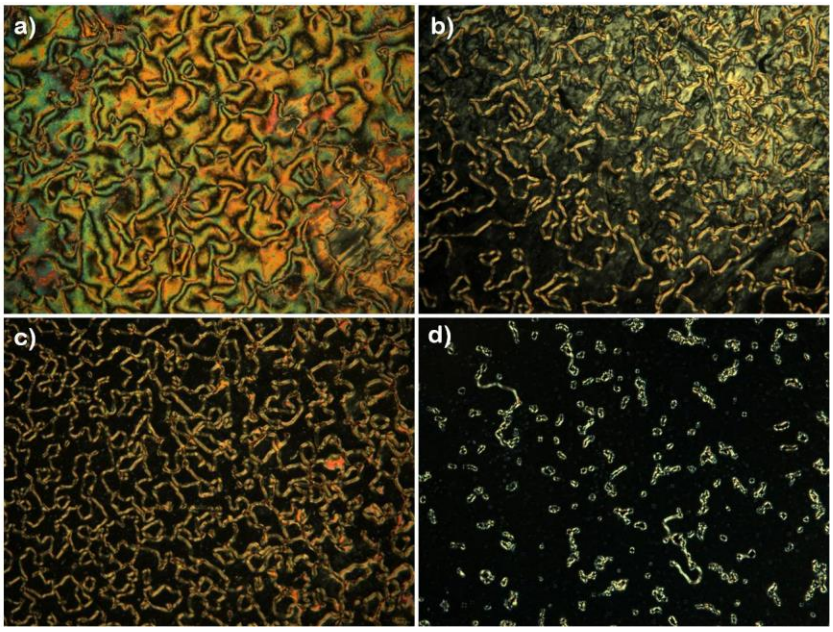

Figure 5.8 POM micrographs (crossed polarizers) of **LC1** doped with **AuNP3** at 58 °C: a) 0.5, b) 1, c) 2.5 and d) 5 wt% on cooling at a rate of 1 °C min^{-1}.

Analysis of the phase-transition temperatures observed by microscopy and DSC measurements revealed no increase in the phase-transition temperatures due to NP doping for **AuNP1**, **AuNP2**, and **AuNP3**. Higher concentrations of **AuNP2** and **AuNP3** even led to a slight decrease in the phase-transition temperatures and caused a rather broad temperature range over which the nematic and isotropic phases coexisted. This effect was very pronounced for 2.5 and 5 wt % **AuNP3**, which is in agreement with the phase-transition temperatures obtained by DSC. **Figure 5.9** shows the phase-transition temperatures for **LC1** and doped **LC1** samples at different concentrations of **AuNP1–AuNP3** obtained by DSC and POM upon heating. Notably, similar trends in the isotropic-to-nematic phase transitions were found during the cooling cycle with 5 wt % **AuNP2** and with all of the **AuNP3** samples, particularly 2.5 and 5 wt % **AuNP3**, which showed the

lowest isotropic-to-nematic transition temperatures, yet an almost identical N phase range to that of pure **LC1** (**Figure 5.10**).

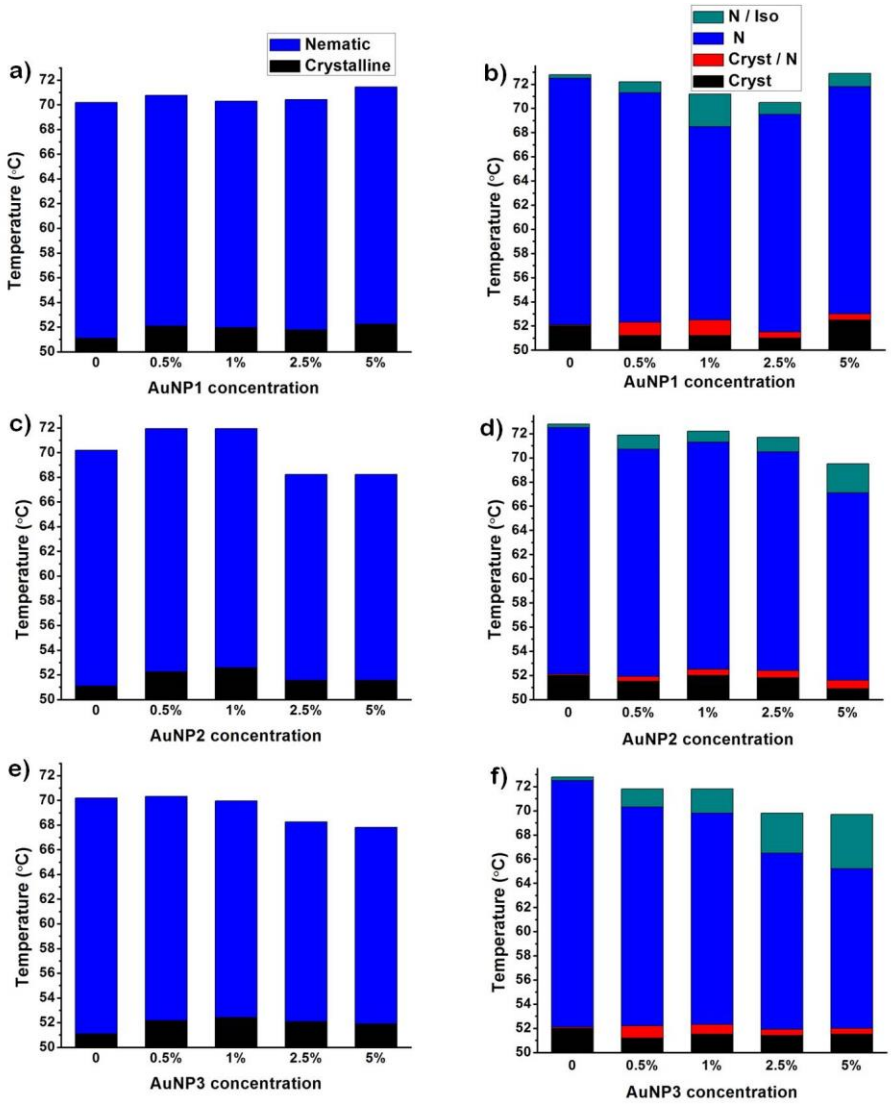

Figure 5.9 Phase-transition temperatures of pure **LC1** and dispersions containing various concentrations of NPs obtained by DSC upon heating at a rate of 10 °C min^{-1}: a) **AuNP1**, c) **AuNP2**, and e) **AuNP3**. Phase-transition temperatures and biphasic ranges of pure **LC1** and dispersions containing various concentrations of NPs obtained by POM upon heating at a rate of 2 °C min^{-1}: b) **AuNP1**, d) **AuNP2**, and f) **AuNP3**.

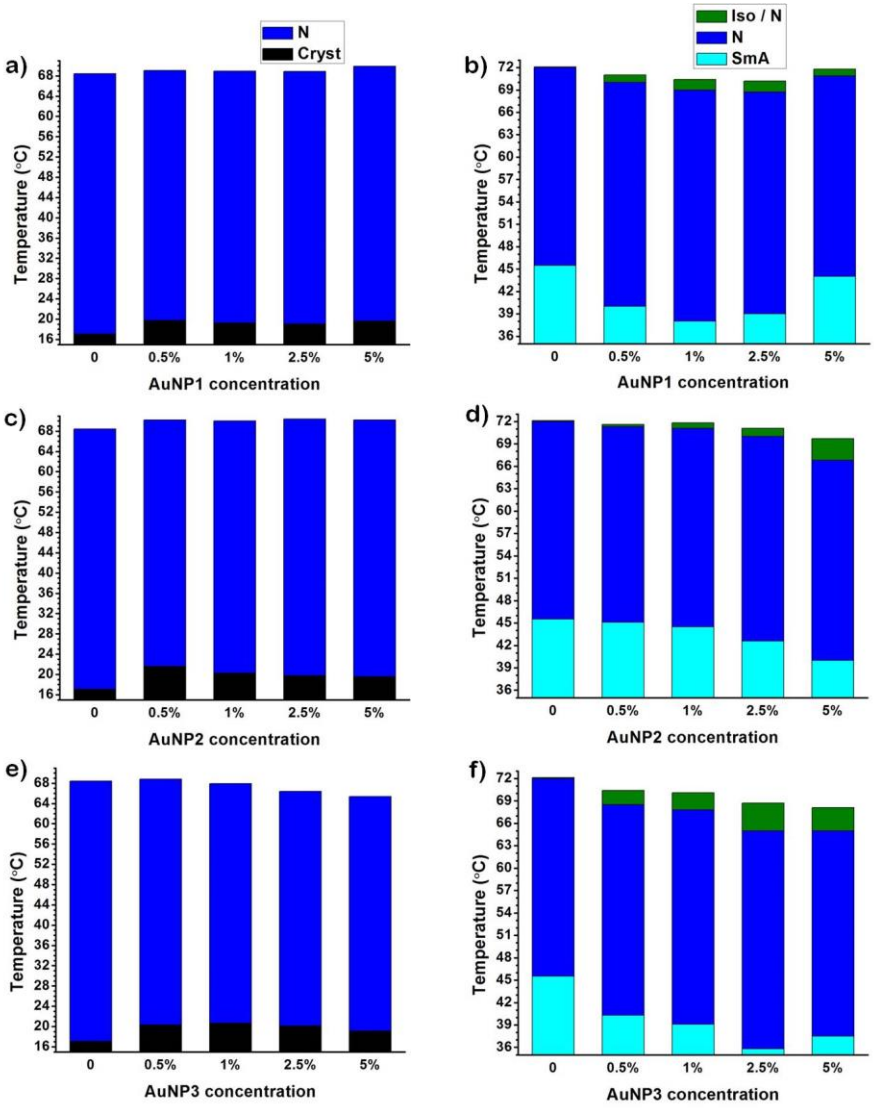

Figure 5.10 Phase-transition temperatures of pure **LC1** and dispersions containing various concentrations of nanoparticles obtained by DSC upon cooling at a rate of 10 °C min^{-1}: a) **AuNP1**, c) **AuNP2**, and e) **AuNP3**. Phase-transition temperatures and biphasic ranges of pure **LC1** and dispersions containing various concentrations of NPs obtained by POM upon cooling at a rate of 2 °C min^{-1}: b) **AuNP1**, d) **AuNP2**, and f) **AuNP3**.

The next step was to investigate the alignment and possible formation of defects for the NP-doped **LC1** in commercially available ITO-coated, antiparallel rubbed polyimide electro-optic (EO) cells favoring a planar alignment of the N-LCs. **Figure 5.11** shows

photomicrographs (crossed polarizers) at temperatures between 65 and 67 °C for **AuNP1–AuNP3** at different concentrations. The mixtures doped with **AuNP1** at all concentrations tested and with **AuNP2** at concentrations of 0.5 and 1 wt % showed fairly homogeneous planar textures expected from a rubbed polyimide cell inducing planar alignment (**Figure 5.11a-b**). The black area appearing for the **LC1** dispersion containing 2.5 wt % **AuNP1** is an inclusion of air, as tilting the sample between crossed polarizers as well as cooling to room temperature did not show any signs of birefringence, so that homeotropic alignment can be excluded. The optical textures of thin films of **LC1** doped with **AuNP2** and **AuNP3** in the EO cell at some concentrations appear to be different. As depicted in **Figure 5.11b-c**, **LC1** samples doped with 2.5 and 5 wt % **AuNP2** and with 1 wt % **AuNP3** and concentrations above started to induce inhomogeneities and optically isotropic domains in the N phase. This is not very surprising, as the phase-transition temperatures indicated a destabilized nematic phase and wider ranges of phase coexistence. These inhomogeneities were also observed in other **LC1** samples doped with another type of Au NP and were confirmed to be regions in which the nematic and isotropic phases coexist.[16] Although these domains become smaller upon decreasing the temperature, they do not disappear completely, and therefore, they always influence the dielectric characterization of these test cells. It was also found that these defects become smaller upon heating, after the samples are heated to the isotropic phase and subsequently cooled at 1 °C min^{-1} to 48 °C. Hence, all subsequent electro-optic measurements were performed both upon cooling and heating.

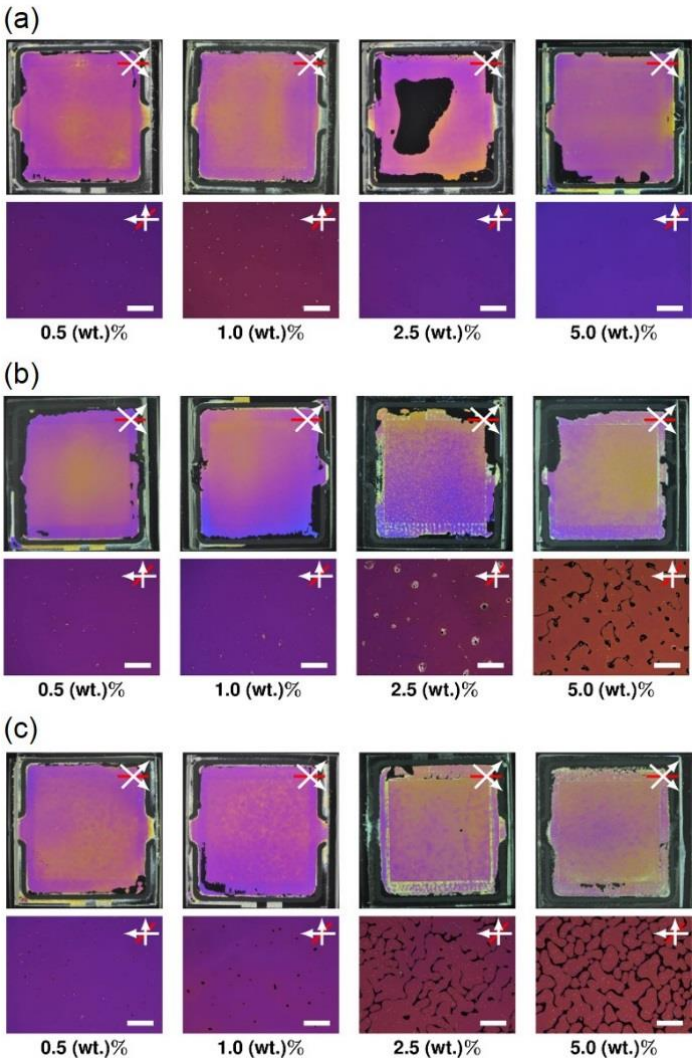

Figure 5.11 Top) Macroscopic images of the test cells containing a) **AuNP1**, b) **AuNP2**, and c) **AuNP3** in **LC1** between crossed polarizers at a temperature of 65–67 °C. Bottom, 100× magnification) POM images of the same test cells at a temperature of 65 °C after cooling from the isotropic phase. The white bar represents 200 μm, the gray bar represents the easy direction of the cells, and the crossed arrows represent the position of the polarizer and analyzer, respectively.

Electro-optic Characterization

Doping **LC1** with **AuNP1** slightly increased the Fréedericksz transition threshold voltage (V_{th}) of the doped samples relative to that of pure LC1, as shown in **Figure 5.12a**. For **LC1**

samples doped with **AuNP1**, the measured values of $\Delta\varepsilon$ as well as those of $\gamma/\Delta\varepsilon$ and γ/K_{eff}, in which γ is the rotational viscosity and K_{eff} is the effective elastic constant, were also plotted versus temperature and are shown in **Figure 5.12b-d**. The dielectric anisotropy ($\Delta\varepsilon$) was only slightly affected for lower particle concentrations. As shown in **Figure 5.11a**, the test cell containing 2.5 wt % NPs is not completely filled with dispersion as a result of the inclusion of air, which explains the significantly smaller dielectric anisotropy for this particular sample (**Figure 5.12b**). The slightly larger dielectric anisotropy for the dispersion containing 5 wt % **AuNP1** is caused by a larger value of the parallel dielectric permittivity ($\varepsilon_{\parallel}$) relative to that of the pure host, as indicated by dielectric permittivity measurements (for plots of the calculated permittivity values, see Figure C5.8 in the Appendix C). One possible explanation, among others (because the capacitance data would be strongly influenced by NPs residing at the interface), could be a higher order parameter (S) in the 5 wt % dispersion of **AuNP1** in **LC1**, which is also evident from the phase-transition temperatures (**Figure 5.9a-b**).

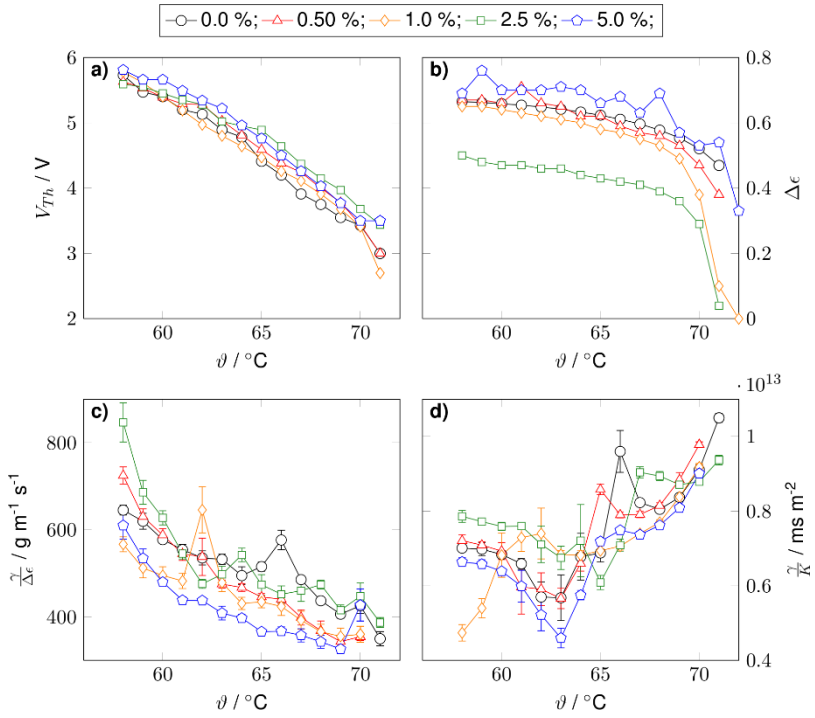

Figure 5.12 Plots of electro-optic data a) V_{th}, b) $\Delta\varepsilon$, c) $\gamma/\Delta\varepsilon$, and d) γ/K_{eff} versus temperature for dispersions of **AuNP1** in **LC1** at different particle concentrations.

AuNP2 in **LC1** slightly increases the value of V_{th} at low doping concentrations, whereas it decreases the value of V_{th} at high doping concentrations; the latter occurs due to their influence on the initial tilt angle. **Figure 5.13a** shows the plots of V_{th} versus temperature for all **AuNP2** dispersions. Plots of $\Delta\varepsilon$, $\gamma/\Delta\varepsilon$, and γ/K_{eff} versus temperature are shown in **Figure 5.13b-d**. Studying the values of the dielectric anisotropy versus temperature (**Figure 5.13b**) plot revealed the presence of a trend similar to that for V_{th}, that is, low concentrations of NPs lead to a slight increase in the value of $\Delta\varepsilon$, and high concentrations of NPs decrease the value of $\Delta\varepsilon$. Interestingly, both the perpendicular dielectric permittivity ($\varepsilon_\perp$) and the parallel dielectric permittivity ($\varepsilon_\parallel$) are enhanced for samples containing 0.5 and 1.0 wt % NPs. This cannot be explained by an increased order

parameter (S), as an increase in S should reduce $\varepsilon_\perp$ relative to the value of $\varepsilon_\perp$ for the pure host **LC1**.

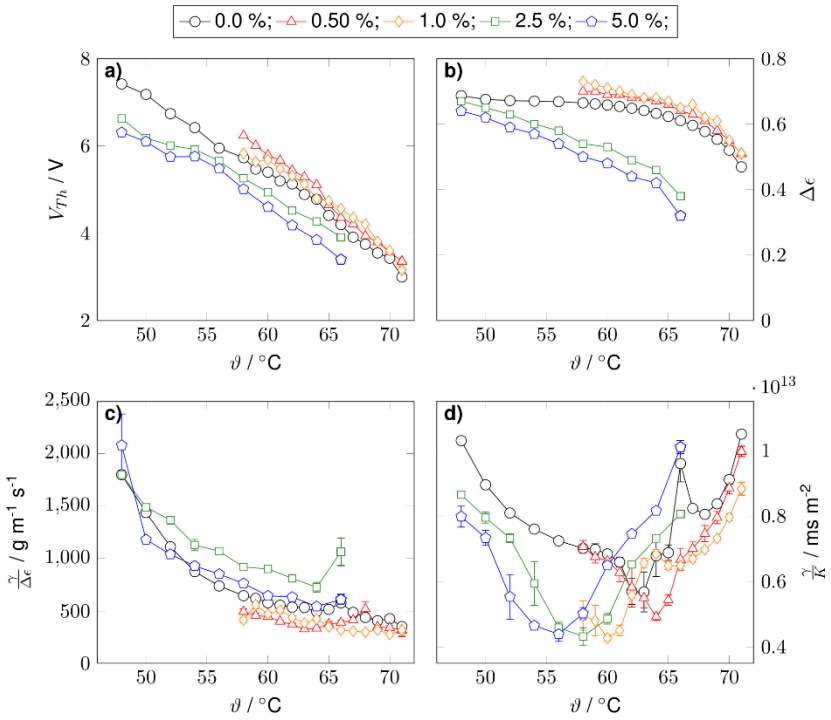

Figure 5.13 Plots of electro-optic data a) V_{th}, b) $\Delta\varepsilon$, c) $\gamma/\Delta\varepsilon$, and d) γ/K_{eff} versus temperature for dispersions of **AuNP2** in **LC1** at different particle concentrations.

The EO data for the **AuNP3** in **LC1** dispersions are plotted in **Figure 5.14**. As shown in the V_{th} versus temperature plot, all doped samples containing **AuNP3** exhibited lower V_{th} values than the pure host **LC1**. This improvement is unusual, as we initially expected that this type of particle with surface ligands less similar to those of the **LC1** host molecules should have a lower level of functionality and effect in **LC1** dispersions. However, the $\Delta\varepsilon$ values obtained for all concentrations of **AuNP3** in **LC1** are mostly lower than those for pure **LC1**, which does not confirm improved parameters for electro-optic switching. Another interesting observation was made for the test cell containing 2.5 wt % AuNP3, which showed a clear switch from tilted alignment at lower temperatures to

homogeneous planar alignment at higher temperatures. This can be derived from the field-dependent capacitance, as shown in **Figure 5.15**. At low temperatures, the light transmission changes continuously without exhibiting a threshold, but at a temperature of about 56 °C a threshold sets in. This implies the movement of the NPs from the surface to the bulk at higher temperatures, which causes a change in alignment from tilted to homogeneous planar. A similar effect can be observed for the field-dependent cell capacitance, for which an initial plateau and a threshold appear only above 56 °C. This process is reversible and presumably corresponds to a planar-to-homeotropic switch, which was observed in plain glass slides just by changing the temperature. However, except for a color change (white light illumination) or intensity change (monochromatic illumination) caused by the increased birefringence at lower temperatures, no other textural changes were observed by POM. With the easy direction of the polyimide alignment layers unchanged, we expect only minimal interface coverage with the NPs. Notably, the EO cell containing 5.0 wt % **AuNP3** in **LC1** at temperatures above 60 °C did not respond to an external field for unknown reasons, and response to an external field simply stopped during the measurement cycle at a voltage less than 10 V_{rms}. Microscopic investigation did not show any typical signs of a shortened cell or any similar issues.

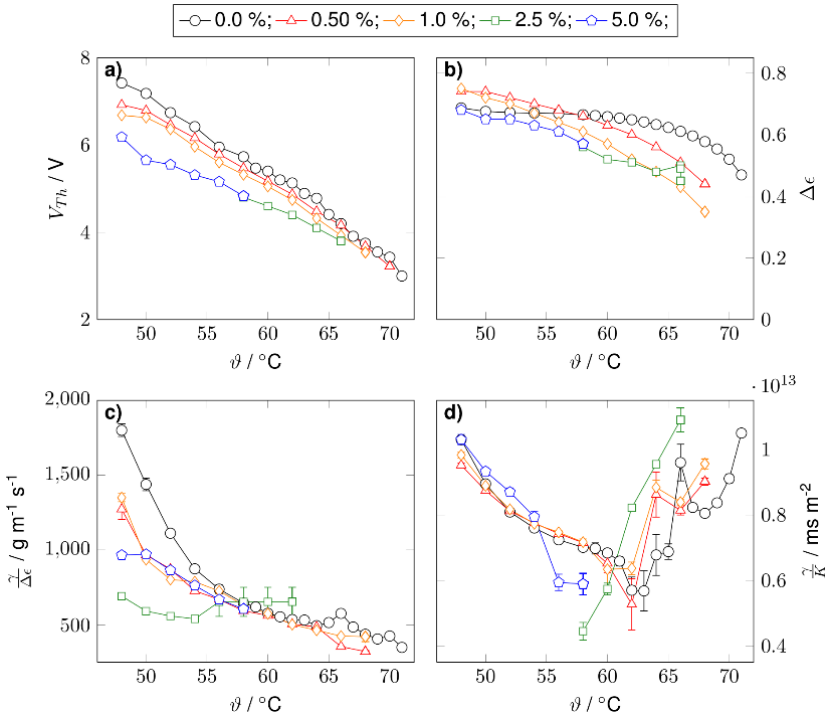

Figure 5.14 Plots of electro-optic data a) V_{th}, b) $\Delta\varepsilon$, c) $\gamma/\Delta\varepsilon$, and d) γ/K_{eff} versus temperature for dispersions of **AuNP3** in **LC1** at different particle concentrations.

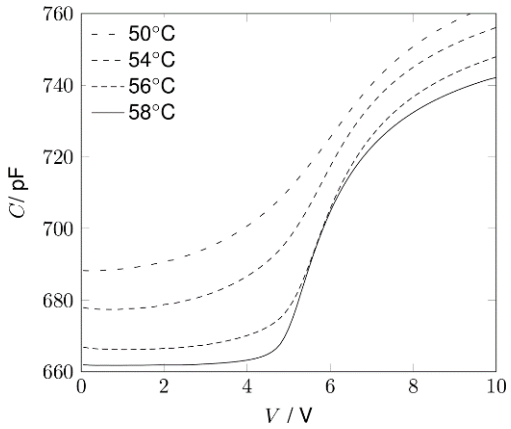

Figure 5.15 Plots of capacitance versus applied voltage of the test cell containing 2.5 wt % AuNP3 at different temperatures.

Further EO characterization was performed to calculate the rotational viscosity (γ_1) and effective elastic constant (K_{eff}) for all the **LC1** dispersions with **AuNP1–AuNP3** at

different temperatures. According to the rotational viscosity data plotted in **Figure 5.16**, doping seems to have led to a general decrease in the rotational viscosity. Especially for **AuNP3**, the decrease was found to be proportional to the doping concentration. As for the effective elastic constants, the calculated data was found to be lower for dispersions containing **AuNP1** or **AuNP3** (see the K_{eff} plot for dispersions of **AuNP1–AuNP3** in Figure C5.9; Appendix C). For **AuNP2**, slightly lower values of K_{eff} were only found at temperatures above 62 °C. This might also be indicative of NPs residing at the interface at lower temperatures and migrating to the bulk at higher temperatures as described above, and this would lead to a change in the elastic properties of the material.

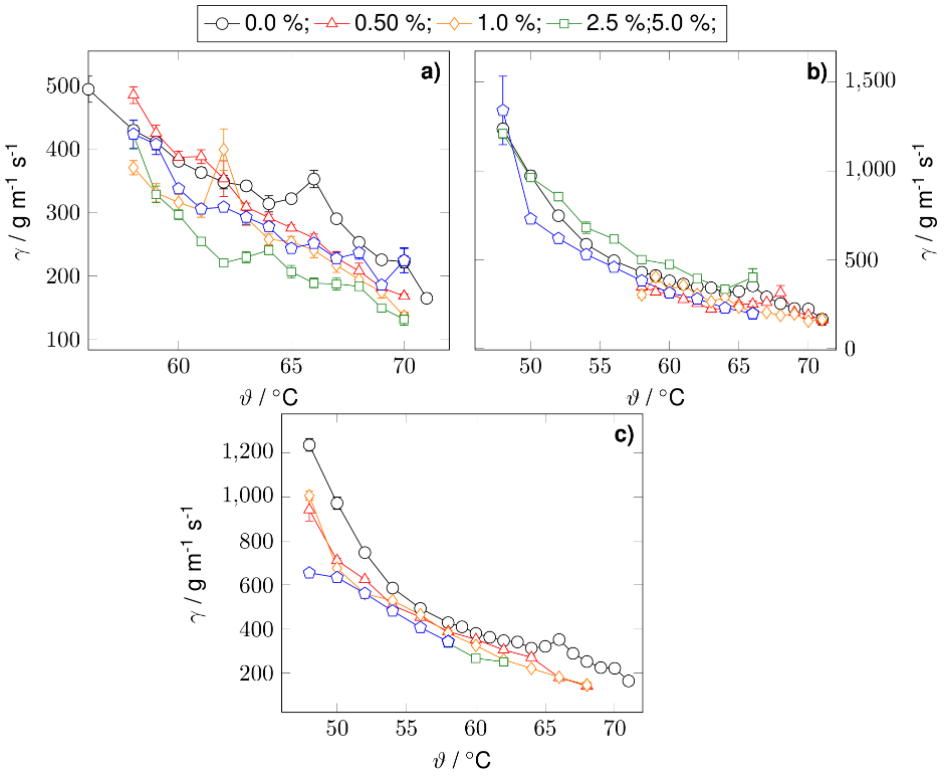

Figure 5.16 Plots of the calculated rotational viscosity (γ_1) for the three NP systems: a) **AuNP1**, b) **AuNP2**, and c) **AuNP3**

Calculation of the rotational viscosity and elastic constant as well as the interpretation of data relies on the correct analysis of the switching times. The switching experiments confirm, on the one hand, that the decay time τ_{decay} is independent of the applied voltage and, on the other hand, that the V_{th} values obtained by dynamic measurements match very well with the V_{th} data obtained by capacitance or light-transmission measurements. However, the dynamic data do not fully correspond to the observed switching behavior. With the calculated values of K_{eff} and $\Delta\varepsilon$, it is possible to calculate a threshold voltage ($V_{th,calcd}$) by using Equation 5.1:

$$V_{th,calc} = \pi \sqrt{\frac{K_{eff}}{\varepsilon_0 \Delta\varepsilon}} \qquad \text{(Eq. 5.1)}$$

To verify the coherency of the measured data, $V_{th,calcd}$ values were compared to the experimentally measured values, $V_{th,meas}$. We found that the calculated values were on average 1.8 times higher than the measured values (see plot of the $V_{th,calcd}/V_{th,meas}$ ratio in the Appendix C, Figure C5.10). This discrepancy is independent of the type of NP or NP concentration and is, therefore, a measure of the accuracy of the electro-optical analysis. One basic drawback is that the determination of threshold, rotational viscosity, and elastic constant strongly depends on the boundary conditions. Hence, a director tilt as well as weak boundary conditions should be minimized for higher accuracy in dynamic measurements. This prerequisite, however, can hardly be achieved if the NPs reside at the interface and influence the polyimide alignment layer.

Interpretation of Interaction of NPs with Host LC

Analyzing the alignment of all **AuNP1** dispersions in polyimide-coated EO cells (**Figure 5.11a**) revealed that doping **LC1** with **AuNP1** did not affect the alignment of the LC molecules and did not cause biphasic regions. Similarly, samples of **LC1** doped with **AuNP1** between plain glass slides at higher temperature did not cause homeotropic alignment of the nematic phase, except for 5 wt %. This is indicative of a good dispersion with minimum distortions in the local order parameter. The determined phase-transition temperatures upon cooling and heating confirm this. None of the doped samples showed considerably altered temperatures in comparison to pure **LC1** (**Figure 5.9a** and **Figure 5.10a**). Comparing the numbers obtained by DSC is even more convincing considering the bulk-phase transition temperatures. The only slight exception is the 5 wt % sample, and to some extent the 2.5 wt % sample, which even showed a minor stabilizing effect of the NP inclusions on the N phase. This observation can perhaps be explained by the ligand structure and density. Studying the parameters listed in **Table 5.1** revealed that **AuNP1** is the smallest NP (with maximum curvature) with the lowest density of the organic corona. These together will allow extended interaction between the surface ligands of AuNP1 and the host LC1 molecules, which will allow the nematic-to-isotropic phase transition to be stabilized a few degrees.[83] However, **AuNP1** dispersions in **LC1**, in general, are not effective in influencing the EO properties except at the highest concentrations. It is rather surprising to see that fairly well-dispersed colloidal LC samples are less effective in modulating the EO parameters than those noticeably impacting both alignment and local ordering.

Dispersions of **AuNP2** and **AuNP3** in **LC1**, however, affect the alignment of the N phase whether in plain glass or planar cells, and this causes numerous defects, especially at concentrations of 2.5 and 5 wt %. These defects are not found to be distortions in the director field, but rather optically isotropic domains that persist even upon cooling well below the biphasic behavior observed by POM and DSC. Moreover, these samples (**AuNP2** and **AuNP3** at 2.5 and 5 wt %) exhibited reductions in the phase-transition temperatures along with very broad biphasic temperature regions. For **AuNP2**, reduced interaction between the surface ligands and the **LC1** host molecules are probably due to the larger size of the particles, which results in a lower surface curvature, that is, denser ligand coverage compared to **AuNP1** (≈three times higher, as shown by the estimated values in **Table 5.1**). Otherwise, the surface ligands in **AuNP2** are structurally very close to those of **AuNP1** and the **LC1** molecules. For **AuNP3**, the observed thermal effects could be attributed to the larger size, the slightly higher ligand coverage, and the structural mismatch between the ligand and host. Together, these observations imply that dispersions with more significant thermal and alignment effects appear to have the strongest impact on the electro-optic properties of the N-phase of **LC1**. High doping concentrations for both **AuNP2** and **AuNP3** at all concentrations decreased the value of V_{th} for **LC1**, but apparently for different reasons. Nevertheless, dispersions of **AuNP3** in **LC1** at low concentrations (0.5 and 1.0 wt %) show no alignment or texture defects, no agglomeration, only a minimal decrease in the isotropic-to-nematic phase-transition temperature, but the most significant decrease in the value of V_{th}.

The dielectric anisotropy values of **LC1** doped with **AuNP2** and **AuNP3** at low concentrations and lower temperatures were larger than those for pure **LC1**. In general, the

dielectric properties of several test cells indicate a change in the bulk of the NP-doped nematic LC with increasing temperature. Although at low temperatures, higher parallel dielectric permittivity ($\varepsilon_{\parallel}$) than for the pure host was found, with increasing temperature this effect disappears and the $\varepsilon_{\parallel}$ values become smaller. The temperature of this change roughly corresponds to the observed temperatures of changing from planar to homeotropic upon cooling between plain glass slides. A very clear example of this behavior is found for the sample containing 2.5 wt % **AuNP3**, which showed tilted alignment at low temperatures and planar alignment at higher temperatures. Therefore, these results might be evidence for the temperature-dependent movement of the particles from the surface to the bulk or vice versa.

The calculated rotational viscosities (γ_1) and elastic constants (K_{eff}) appear, in general, to be lowered by NP doping (**Figure 5.16**). To explain the reduced viscosity and elastic constant as well as reduced threshold voltage, we propose a model. On the basis of this model and the assumption that there is sufficient interaction between the LC molecules and the ligands of the NPs, the anisometric host will impose a tactoidal deformation of the ligand shell.[47] This anisometric shape presumably originates from ligand chains in the axial position of the NP that fold and coil, whereas ligands in the equatorial region fully extend or unfold (**Figure 5.17**). Upon applying external electric fields, small distortions in the surrounding director field could induce a flip in the equatorial and axial orientation, for which coils unfold and unfolded ligands fold up. In this manner, the reorientation of the host molecules is facilitated by the presence of the NPs even without a rotation of the NP core by anisometric interactions of the ligands and the host molecules. This model would best explain the reduced V_{th} values and the reduced γ_1 values in dispersions with AuNP3

and high concentrations of **AuNP2**. It seems that for the latter particles, although the surface ligands are fairly compatible with the host molecules, for reasons such as larger NP size and higher density of organic ligands this compatibility is not sufficient to cause similar EO effects as **AuNP3**.

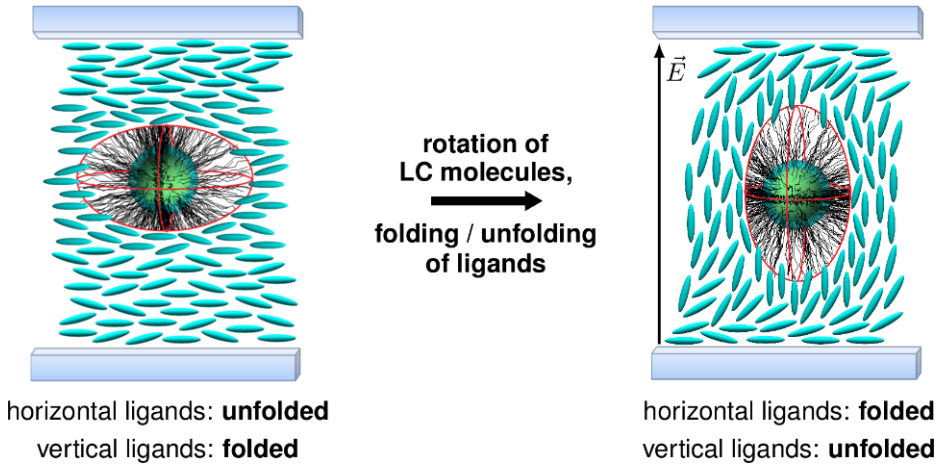

Figure 5.17 Schematic drawings of the expected mechanism of facilitated switching due to NP doping. Left) The ligand shell is deformed to a tactoidal shape due to anisometric interactions with the LC host. Right) Upon applying an electric field, the LC molecules rotate, whereas the particle remains unrotated. The previously folded ligands unfold, and the previously unfolded ligands fold.

Hence, the easier it is to achieve a distorted ligand shell, the more likely it will be to observe an altered EO response. We can interpret this as a dynamic feedback system, in which the effectiveness of a NP to alter the EO response depends on how it can be affected by the LC host. Notably, this model of anisotropic interactions comes along with an increase in the order parameter *S*, which could only be confirmed for lower temperatures considering the permittivity data. This is somewhat contradictory, as at lower

concentrations the NPs were found to affect the alignment and are therefore expected to be located at the interface.

5.4 Conclusions

Our studies suggest that LC-functionalized Au NPs prepared through silane conjugation have superior stability than other Au NPs functionalized by other methods, including ligand exchange. The as-synthesized particles in colloid form and in LC dispersions easily survived harsh conditions, such as high temperatures and prolonged sonication. In addition to enhanced chemical and thermal stability, the presence of LC-compatible surface ligands indeed allowed us to explore nematic dispersion with relatively high concentrations of NPs without any considerable aggregation. For example, **LC1** doped with **AuNP1** up to 5 wt% showed no signs of aggregation at the microscale or noticeable destabilization of the nematic phase. Preliminary experiments with the use of a laboratory-based small-angle X-ray scattering instrument showed no formation of periodic NP arrays or chains, but might need brighter synchrotron sources, as described recently by Hirst and co-workers for dispersions of quantum dots in a N-LC host.[84] Considering frequently reported colloidal LC mixtures with a NP loading limit of 0.5 to 1 wt%, our current results are promising. Thorough optical and electro-optic characterization of doped LC1 nematic mixtures, along with estimated values for ligand coverage for each Au NP obtained from theoretical calculations and TGA data, enabled us to study the effects of parameters such as size and concentration of the NPs, as well as the structure and density of the surface ligands. Each of these parameters, in part, can impact the quality of the NP dispersions in N-LCs, in

addition to the electro-optic properties of the N-LCs. It appears that although the presence of robust surface ligands with a structure similar to that of the host LC molecules is necessary to realize stable dispersions, optimization of the electro-optic properties of the N-LCs requires balancing of all aforementioned parameters involved in NP–LC interactions. Our proposed model also explains the plausible mechanism of interaction of the NPs with the LC molecules and also explains how the observed lower rotational viscosity and elastic constant values in the doped LC1 samples likely affect the overall and local order parameters.[85] Finally, AuNP3 proved to have the strongest effect on the electro-optic parameters, although at high concentrations there were some signs of nematic phase destabilization. In view of the importance of these results and to understand better the role and mechanism of NPs in a LC medium, complimentary experimental studies and theoretical simulations for dispersions of AuNP3 in LC1 were performed and the results are summarized in the supplementary information (Appendix D).

Acknowledgements

This work was financially supported by the Natural Sciences and Engineering Research Council (NSERC) of Canada, the Canada Foundation for Innovation (CFI), the Manitoba Research and Innovation Fund (MRIF), the Deutsche Forschungsgemeinschaft (DFG, KI 411), and the European Science Foundation (ESF-EUROCORES, SONS II program, LCNANOP project). We are grateful to Dr. K. McEleney for his valuable assistance with the XPS measurements and to Prof. M. S. Freund for access to these measurements. For access to a TGA instrument and assistance in performing measurements we are thankful to Prof. M. Bieringer and J. Lussier. We also thank Dr. A. Khan for help and assistance with HRTEM imaging. T.H. thanks the Government of Ohio's Third Frontier Program (Ohio Research Scholar Program).

5.5 References

1. Hegmann, T.; Qi, H.; Marx, V. M. *J. Inorg. Organomet. P.* **2007,** 17, (3), 483-508.
2. Stamatoiu, O.; Mirzaei, J.; Feng, X.; Hegmann, T. *Top. Curr. Chem.* **2012,** 318, 331-93.
3. Mirzaei, J.; Reznikov, M.; Hegmann, T. *J. Mater. Chem.* **2012,** 22, (42), 22350-22365.
4. Shivakumar, U.; Mirzaei, J.; Feng, X.; Sharma, A.; Moreira, P.; Hegmann, T. *Liq. Cryst.* **2011,** 38, (11-12), 1495-1514.
5. Saliba, S.; Mingotaud, C.; Kahn, M. L.; Marty, J. D. *Nanoscale* **2013,** 5, (15), 6641-6661.
6. Bisoyi, H. K.; Kumar, S. *Chem. Soc. Rev.* **2011,** 40, (1), 306-319.
7. Gardner, D. F.; Evans, J. S.; Smalyukh, I. I. *Mol. Cryst. Liq. Cryst.* **2011,** 545, 1227-1245.
8. HyungKi, H.; HyunHo, S.; InJae, C. *J. Display Technol.* **2007,** 3, (4), 361-370.
9. Lyu, J.-J.; Jiwon, S.; Kim, H. Y.; Seung Hee, L. *J. Display Technol.* **2007,** 3, (4), 404-412.
10. Bocharov, Y. V.; Gurova, I. N.; Kapustina, O. A.; Remizova, E. I.; Reshetov, V. N. *Mol. Cryst. Liq. Cryst.* **1991,** 209, 19-30.
11. Clark, N. A.; Lagerwall, S. T. *Appl. Phys. Lett.* **1980,** 36, (11), 899-901.
12. Qi, H.; Hegmann, T. *J. Mater. Chem.* **2008,** 18, (28), 3288-3294.
13. Qi, H.; Hegmann, T. *J. Mater. Chem.* **2006,** 16, (43), 4197-4205.
14. Qi, H.; Kinkead, B.; Hegmann, T. *Adv. Funct. Mater.* **2008,** 18, (2), 212-221.
15. Qi, H.; Hegmann, T. *ACS Appl. Mater. Inter.* **2009,** 1, (8), 1731-1738.

16. Mirzaei, J.; Urbanski, M.; Kitzerow, H.-S.; Hegmann, T. *Phil. Trans. R. Soc. A* **2013,** 371, (1988), 20120256.

17. Qi, H.; Hegmann, T. *Liq. Crys. Today* **2011,** 20, (4), 102 - 114.

18. Qi, H.; Kinkead, B.; Hegmann, T. *Proc. SPIE-Int. Soc. Opt. Eng.* **2008,** 6911, 691106.

19. Kinkead, B.; Hegmann, T. *J. Mater. Chem.* **2010,** 20, (3), 448-458.

20. Mirzaei, J.; Urbanski, M.; Yu, K.; Kitzerow, H.-S.; Hegmann, T. *J. Mater. Chem.* **2011,** 21, (34), 12710-12716.

21. Qi, H.; Kinkead, B.; Hegmann, T. *Proce, SPIE, Emerging Liq. Cryst. Technol.* **2008,** 6911, 91106.

22. Podoliak, N.; Buchnev, O.; Bavykin, D. V.; Kulak, A. N.; Kaczmarek, M.; Sluckin, T. J. *J. Colloid Interf. Sci.* **2012,** 386, 158-166.

23. Hu, W.; Zhao, H. Y.; Shan, L. K.; Song, L.; Cao, H.; Yang, Z.; Cheng, Z. H.; Yan, C. Z.; Li, S. J.; Yang, H. A.; Guo, L. *Liq. Cryst.* **2010,** 37, (5), 563-569.

24. Copic, M.; Mertelj, A.; Buchnev, O.; Reznikov, Y. *Phys. Rev. E* **2007,** 76, (1), 011702.

25. Kaczmarek, M.; Buchnev, O.; Nandhakumar, I. *Appl. Phys. Lett.* **2008,** 92, (10), 103307.

26. Kaur, S.; Singh, S. P.; Biradar, A. M.; Choudhary, A.; Sreenivas, K. *Appl. Phys. Lett.* **2007,** 91, (2), 023120.

27. Rozic, B.; Jagodic, M.; Gyergyek, S.; Drofenik, M.; Kralj, S.; Jaglicic, Z.; Kutnjak, Z. *Ferroelectrics* **2012,** 431, 150-153.

28. Liang, H. H.; Xiao, Y. Z.; Hsh, F. J.; Wu, C. C.; Lee, J. Y. *Liq. Crys.* **2010,** 37, (3), 255-261.

29. Singh, D. P.; Gupta, S. K.; Pandey, K. K.; Yadav, S. P.; Varia, M. C.; Manohar, R. *J. Non-cryst. Solids* **2013,** 363, 178-186.

30. Kumar, A.; Biradar, A. M. *Phys. Rev. E* **2011,** 83, (4), 041708.

31. Kumar, A.; Tripathi, S.; Deshmukh, A. D.; Haranath, D.; Singh, P.; Biradar, A. M. *J. Phys. D* **2013,** 46, (19), 195302.

32. Singh, D. P.; Gupta, S. K.; Srivastava, A.; Manohar, R. *J. Lumin* **2013,** 139, 60-63.

33. Joshi, T.; Kumar, A.; Prakash, J.; Biradar, A. M. *Appl. Phys. Lett.* **2010,** 96, 253109.

34. Prakash, J.; Choudhary, A.; Kumar, A.; Mehta, D. S.; Biradar, A. M. *Appl. Phys. Lett* **2008,** 93, (11), 112904.

35. Chernyshuk, S. B.; Lev, B. I.; Yokoyama, H. *Phys. Rev. E* **2005,** 71, (6), 062701.

36. Nealon, G. L.; Greget, R.; Dominguez, C.; Nagy, Z. T.; Guillon, D.; Gallani, J. L.; Donnio, B. *Beilstein J. Org. Chem.* **2012,** 8, 349-370.

37. Prodanov, M. F.; Pogorelova, N. V.; Kryshtal, A. P.; Klymchenko, A. S.; Mely, Y.; Semynozhenko, V. P.; Krivoshey, A. I.; Reznikov, Y. A.; Yarmolenko, S. N.; Goodby, J. W.; Vashchenko, V. V. *Langmuir* **2013,** 29, (30), 9301-9309.

38. Qi, H.; Kinkead, B.; Marx, V. M.; Zhang, H. R.; Hegmann, T. *ChemPhysChem* **2009,** 10, (8), 1211-1218.

39. Milette, J.; Cowling, S. J.; Toader, V.; Lavigne, C.; Saez, I. M.; Lennox, R. B.; Goodby, J. W.; Reven, L. *Soft Matter* **2012,** 8, (1), 173-179.

40. Marx, V. M.; Girgis, H.; Heiney, P. A.; Hegmann, T. *J. Mater. Chem.* **2008,** 18, (25), 2983-2994.

41. Kumar, S.; Pal, S. K.; Kumar, P. S.; Lakshminarayanan, V. *Soft Matter* **2007,** 3, (7), 896-900.

42. Dintinger, J.; Tang, B.-J.; Zeng, X.; Liu, F.; Kienzler, T.; Mehl, G. H.; Ungar, G.; Rockstuhl, C.; Scharf, T. *Adv. Mater.* **2013,** 25, (14), 1999-2004.

43. Yu, C. H.; Schubert, C. P.; Welch, C.; Tang, B. J.; Tamba, M. G.; Mehl, G. H. *J. Am. Chem. Soc.* **2012,** 134, (11), 5076-9.

44. Kanie, K.; Matsubara, M.; Zeng, X. B.; Liu, F.; Ungar, G.; Nakamura, H.; Muramatsu, A. *J. Am. Chem. Soc.* **2012,** 134, (2), 808-811.

45. In, I.; Jun, Y. W.; Kim, Y. J.; Kim, S. Y. *Chem. Commun.* **2005**, (6), 800-801.

46. Lewandowski, W.; Constantin, D.; Walicka, K.; Pociecha, D.; Mieczkowski, J.; Gorecka, E. *Chem. Commun.* **2013,** 49, (71), 7845-7847.

47. Draper, M.; Saez, I. M.; Cowling, S. J.; Gai, P.; Heinrich, B.; Donnio, B.; Guillon, D.; Goodby, J. W. *Adv. Funct. Mater.* **2011,** 21, (7), 1260-1278.

48. Mang, X.; Zeng, X.; Tang, B.; Liu, F.; Ungar, G.; Zhang, R.; Cseh, L.; Mehl, G. H. *J. Mater. Chem.* **2012,** 22, (22), 11101-11106.

49. Lewandowski, W.; Jatczak, K.; Pociecha, D.; Mieczkowski, J. *Langmuir* **2013,** 29, (10), 3404-3410.

50. Belaissaoui, A.; Cowling, S. J.; Goodby, J. W. *Liq. Cryst.* **2013,** 40, (3), 421-427.

51. Buluy, O.; Burseva, D.; Hakobyan, M. R.; Goodby, J. W.; Kolosov, M. A.; Reznikov, Y.; Hakobyan, R. S.; Slyusarenko, K.; Prodanov, M. F.; Vashchenko, V. *Mol. Cryst. Liq. Cryst.* **2012,** 560, 149-158.

52. Demortiere, A.; Buathong, S.; Pichon, B. P.; Panissod, P.; Guillon, D.; Begin-Colin, S.; Donnio, B. *Small* **2010,** 6, (12), 1341-1346.

53. Kaur, S.; Liu, H.; Addis, J.; Greco, C.; Ferrarini, A.; Goertz, V.; Goodby, J. W.; Gleeson, H. F. *J. Mater. Chem. C* **2013,** 1, (40), 6667-6676.

54. Kaur, S.; Addis, J.; Greco, C.; Ferrarini, A.; Goertz, V.; Goodby, J. W.; Gleeson, H. F. *Phys. Rev. E* **2012,** 86, (4).

55. Brust, M.; Walker, M.; Bethell, D.; Schiffrin, D. J.; Whyman, R. *J. Chem. Soc. Chem. Comm.* **1994**, (7), 801-802.

56. Brust, M.; Fink, J.; Bethell, D.; Schiffrin, D.; Kiely, C. *J. Chem. Soc., Chem. Comm.* **1995,** (16), 1655-1656.

57. Kassam, A.; Bremner, G.; Clark, B.; Ulibarri, G.; Lennox, R. B. *J. Am. Chem. Soc.* **2006,** 128, (11), 3476-3477.

58. Zhou, J.; Ralston, J.; Sedev, R.; Beattie, D. A. *J. Colloid Interf. Sci.* **2009,** 331, (2), 251-262.

59. Shem, P. M.; Sardar, R.; Shumaker-Parry, J. S. *Langmuir* **2009,** 25, (23), 13279-13283.

60. Weare, W. W.; Reed, S. M.; Warner, M. G.; Hutchison, J. E. *J. Am. Chem. Soc.* **2000,** 122, (51), 12890-12891.

61. Gandubert, V. J.; Lennox, R. B. *Langmuir* **2005,** 21, (14), 6532-6539.

62. Rucareanu, S.; Gandubert, V. J.; Lennox, R. B. *Chem. Mater.* **2006,** 18, (19), 4674-4680.

63. de la Presa, P.; Multigner, M.; de la Venta, J.; Garcia, M. A.; Ruiz-Gonzalez, M. L. *J. Appl. Phys.* **2006,** 100, (12).

64. Love, J. C.; Estroff, L. A.; Kriebel, J. K.; Nuzzo, R. G.; Whitesides, G. M. *Chem. Rev.* **2005,** 105, (4), 1103-1169.

65. Ji, X.; Copenhaver, D.; Sichmeller, C.; Peng, X. *J. Am. Chem. Soc.* **2008,** 130, (17), 5726-5735.

66. Hou, W. B.; Dasog, M.; Scott, R. W. J. *Langmuir* **2009,** 25, (22), 12954-12961.

67. Dasog, M.; Scott, R. W. J. *Langmuir* **2007,** 23, (6), 3381-3387.

68. Shon, Y. S.; Chuc, S.; Voundi, P. *Colloids and Surfaces. A: Physicochem. Eng. Aspects* **2009,** 352, (1-3), 12-17.

69. Ristau, R.; Tiruvalam, R.; Clasen, P. L.; Gorskowski, E. P.; Harmer, M. P.; Kiely, C. J.; Hussain, I.; Brust, M. *Gold Bull.* **2009,** 42, (2), 133-143.

70. Joseph, Y.; Besnard, I.; Rosenberger, M.; Guse, B.; Nothofer, H. G.; Wessels, J. M.; Wild, U.; Knop-Gericke, A.; Su, D. S.; Schlogl, R.; Yasuda, A.; Vossmeyer, T. *J. Phys. Chem. B* **2003,** 107, (30), 7406-7413.

71. Teranishi, T.; Hasegawa, S.; Shimizu, T.; Miyake, M. *Adv. Mater.* **2001,** 13, (22), 1699-1701.

72. Guerrero-Martinez, A.; Perez-Juste, J.; Liz-Marzan, L. M. *Adv. Mater.* **2010,** 22, (11), 1182-1195.

73. Yang, P.; Li, X.; Zhang, R.; Liu, N.; Zhang, Y. *J. Nanosci. Nanotechnol.* **2013,** 13, (3), 1784-1788.

74. Jana, N. R.; Earhart, C.; Ying, J. Y. *Chem. Mater.* **2007,** 19, 5074-5082.

75. Kelly, S. M. *Liq. Cryst.* **1993,** 14, (3), 675-698.

76. Umadevi, S.; Feng, X.; Hegmann, T. *Ferroelectrics* **2012,** 431, (1), 164-175.

77. Wu, S. T.; Coates, D.; Bartmann, E. *Liq. Cryst.* **1991,** 10, (5), 635-646.

78. Shimizu, T.; Teranishi, T.; Hasegawa, S.; Miyake, M. *J. Phys. Chem. B* **2003,** 107, (12), 2719-2724.

79. Imahori, H.; Arimura, M.; Hanada, T.; Nishimura, Y.; Yamazaki, I.; Sakata, Y.; Fukuzumi, S. *J. Am. Chem. Soc.* **2001,** 123, (2), 335-336.

80. Urbanski, M.; Kinkead, B.; Qi, H.; Hegmann, T.; Kitzerow, H. S. *Nanoscale* **2010,** 2, (7), 1118-1121.

81. Urbanski, M.; Kinkead, B.; Hegmann, T.; Kitzerow, H. S. *Liq. Cryst.* **2010,** 37, (9), 1151-1156.

82. Soule, E. R.; Milette, J.; Reven, L.; Rey, A. D. *Soft Matter* **2012,** 8, (10), 2860-2866.

83. Milette, J.; Toader, V.; Reven, L.; Lennox, R. B. *J. Mater. Chem.* **2011,** 21, (25), 9043-9050.

84. Rodarte, A. L.; Pandolfi, R. J.; Ghosh, S.; Hirst, L. S. *J. Mater. Chem. C* **2013,** 1, (35), 5527-5532.

85. Singh, U. B.; Dhar, R.; Dabrowski, R.; Pandey, M. B. *Liq. Cryst.* **2013,** 40, (6), 774-782.

Appendix C

Appendix C: Supplementary Information for Chapter 5

Synthesis of silanes

5-heptyl-2-(4-(oct-7-en-1-yloxy)phenyl)pyrimidine (2a)

Potassium carbonate (0.45 g, 3.3 mmol) was added to a solution of 2-(4'-hydroxyphenyl)-5-*n*-heptylpyrimidine (**1**) (0.3 g, 1.1 mmol) and 8-bromo-1-octene (0.33 mL, 1.9 mmol) in methyl ethyl ketone (10 mL). The resulting mixture was stirred at 75 °C for 24 h. The reaction mixture was filtered; then solvent was removed by evaporation under reduced pressure. The product was purified using column chromatography with a hexane/ethyl acetate (5/1) mixture as eluent and finally was recrystallized from ethanol to yield pure product (0.23 g, 55%). ^{1}H NMR (300 MHz, $CDCl_3$) δ (ppm): 0.9 (t, 3H, CH_3), 1.2-1.6 (m, 16H, -CH_2-, overlapping peaks), 1.8 (q, 2H, -O-CH_2-CH_2-CH_2-), 2.09 (q, 2H, -CH_2-CH_2-CH=), 2.6 (t, 2H, -CH_2-Ar), 4.04 (t, 2H, -O-CH_2-CH_2), 5 (d, 2H, -CH_2=CH-), 5.8 (m, 1H, -CH_2-CH=CH_2), 6.9 (d, 2H, Ar-H), 8.3 (d, 2H, Ar-H), 8.6 (s, 2H, Ar-H). IR (KBr) ν_{max}: 2925, 2850, 1639, 1600, 1584, 1540, 1425, 1252, 915, 850, and 790 cm^{-1}. 5-heptyl-2-(4-(undec-10-en-1-yloxy)phenyl)pyrimidine (**2b**) has been prepared following the same method described above using 11-bromo-1-undecene.

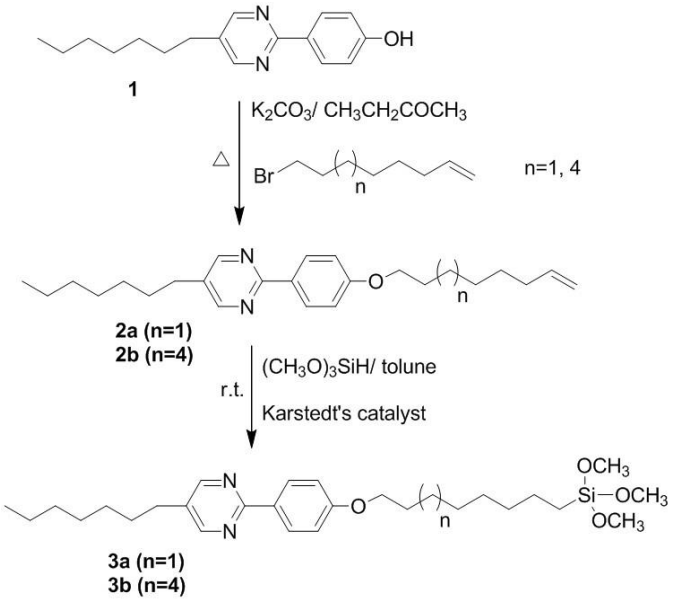

Figure C5.1 Schematic synthesis of silanes 3a-b

5-heptyl-2-(4-((8-(trimethoxysilyl)octyl)oxy)phenyl)pyrimidine (3a):

A typical procedure followed to obtain silane **3a** from compound **2a** is described below (**Figure C5.1**). Compound **2a** (0.13 g, 0.34 mmol) was dissolved in dry toluene (10 mL) and trimethoxysilane (0.45 mL, 3.4 mmol) added under nitrogen atmosphere and stirred for 30 min. To this solution, platinum(0)-1,3-divinyl-1,1,3,3-tetramethyldisiloxane complex (Karstedt's catalyst) in xylene 40 µl was added and stirring continued for further 48 hours maintaining the nitrogen atmosphere. The solvent and excess trimethoxysilane was removed under vacuum resulting in a light brown residue. Attempts to purify the silane from this residue using column chromatography (both silica and alumina) were unsuccessful; however, TLC and NMR of the final product showed purity of product with no sign of vinlyic or allylic hydrogens which could emerge in the presence of starting

material (**2a**) or isomerized starting material with double bond migrated from terminal position (vinyl → allyl). ^{1}H NMR (300 MHz, $CDCl_3$) δ (ppm): 0.66 (t, 2H, -CH_2-Si-(OCH_3)$_3$), 0.88 (t, 3H, -CH_3), 1.2-1.8 (m, 22H, -CH_2-, overlapping peaks), 2.6 (t, 2H, -CH_2-Ar), 3.6 (s, 9H, -Si-(OCH_3)$_3$), 4.0 (t, 2H, -O-CH_2-CH_2), 6.9 (d, 2H, Ar-H), 8.3 (d, 2H, Ar-H), 8.5 (s, 2H, Ar-H). IR (KBr) ν_{max}: 2925, , 2853, 1607, 1584, 1428, 1250, 1189, 1166, 1078, 884, 796, 723, 653, 613 and 445 cm^{-1}. The other ligand 5-heptyl-2-(4-((11-(trimethoxysilyl)undecyl)oxy)phenyl)-pyrimidine (**3b**) was synthesized similarly using corresponding alkene-terminated LC (**3a**).

4-((6-((3-(trimethoxysilyl)propanoyl)oxy)hexyl)oxy)phenyl-4-(hexyloxy)benzoate (5): The terminal alkene-substituted nematic LC **4** is commercially available from Synthon Chemicals GmbH. As described above, the terminal alkene of **4** was converted to compound **5** a trimethoxysilane derivative by similar hydrosilylation reaction. (**Figure C5.2**) ^{1}H NMR (300 MHz, $CDCl_3$) δ (ppm): 0.1 (m, 2H, -CH_2-Si-(OCH_3)$_3$), 0.89 (t, 3H, -CH_3), 1.24–1.50 (m, 12H, -CH_2-), 1.75–1.6 (m, 2H, -OCO-CH_2-*CH_2*), 1.84 (4H, m, -O-CH_2-*CH_2*), 2.3 (t, 2H, -OOC-CH_2), 3.6 (s, 9H, -Si-(OCH_3)$_3$), 4.10–3.95 (m, 4H, -O-CH_2), 4.16 (t, 2H, -OCO-CH_2), 7.0–6.9 (m, 4H, Ar-H), 7.1 (d, 2H, Ar-H), 8.15 (d, 2H, Ar-H). IR (KBr) ν_{max}: 3078, 2918, 2851, 1738, 1719, 1601, 1512, 1472, 1410, 1312, 1251, 1202, 1163, 1122, 1053, 1021, 885, 838, 750, 691, 652, and 632 cm^{-1}.

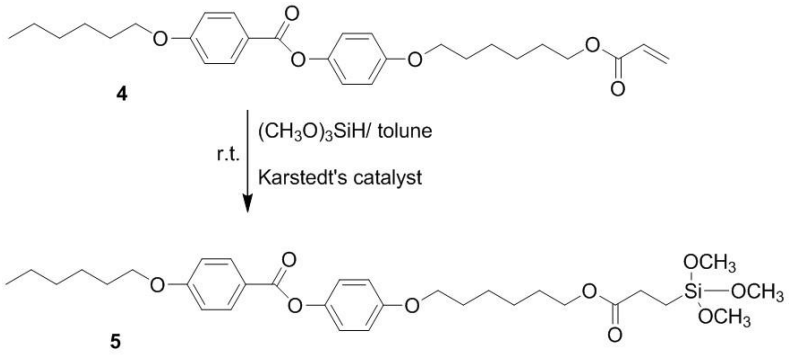

Figure C5.2 Schematic synthesis of silane 5

XPS of AuNP1-AuNP3

AuNP1:

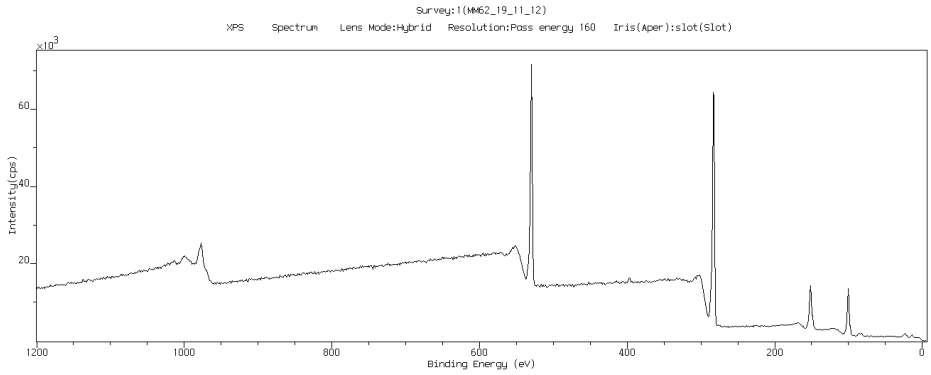

Peak	Position BE (eV)	FWHM (eV)	Raw Area (cps eV)	RSF	Atomic Mass	Atomic Conc (%)	Mass Conc (%)
C 1s	284.995	1.302	8334.8	0.278	12.011	76	64.59
O 1s	532.295	1.358	5183.1	0.78	15.999	15.07	17.06
Si 2p	102.495	1.521	1033.7	0.328	28.086	8.88	17.65
Au 4f	84.495	1.203	108.8	6.25	196.967	0.05	0.7

AuNP2:

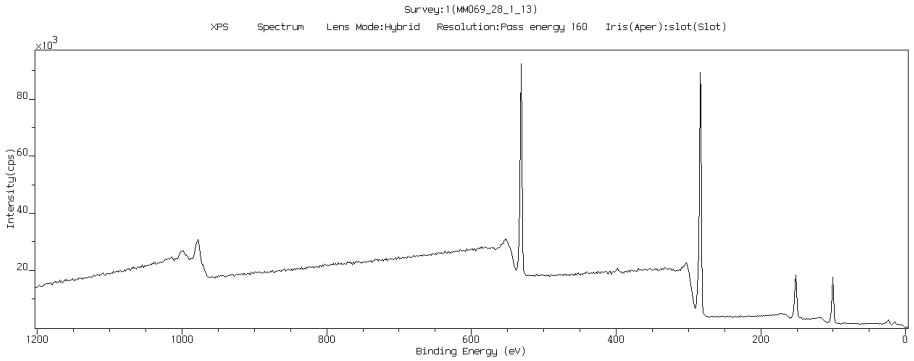

Peak	Position BE (eV)	FWHM (eV)	Raw Area (cps eV)	RSF	Atomic Mass	Atomic Conc (%)	Mass Conc (%)
C 1s	284.954	1.165	9637.3	0.278	12.011	70.32	57.98
O 1s	532.454	1.157	7872.9	0.78	15.999	18.31	20.11
Si 2p	102.354	1.274	1652.6	0.328	28.086	11.37	21.91

AuNP3:

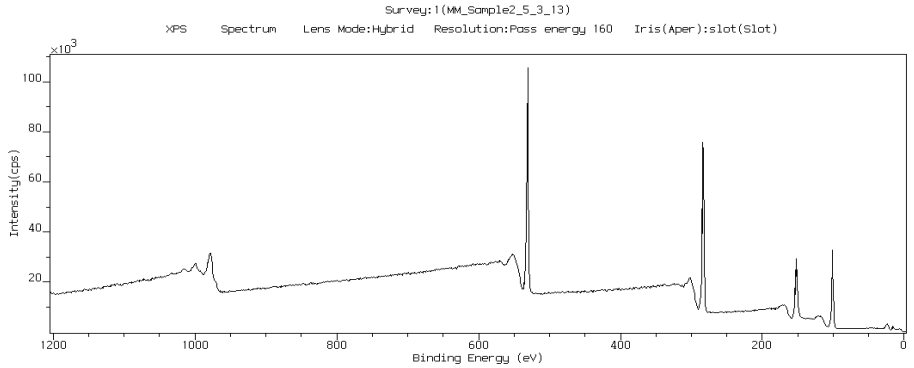

Peak	Position BE (eV)	FWHM (eV)	Raw Area (cps eV)	RSF	Atomic Mass	Atomic Conc (%)	Mass Conc (%)
C 1s	284.958	1.08	6757	0.278	12.011	56.58	41.57
O 1s	532.558	1.058	8188.6	0.78	15.999	21.86	21.39
Si 2p	102.458	1.23	2731.8	0.328	28.086	21.56	37.04

The percentage of Au atom is low in **AuNP1** probably due to the formation of silanized coating the Au NP core and in **AuNP2** and **AuNP3** with larger diameter this effect limits detection of gold by XPS.

TGA analysis of AuNP1-3

An initial weight gain is observed for all three **AuNP1**-**AuNP3** samples at almost the same temperature range (**Figure C5.3**). Although the exact reason is unknown, it is probably be due to an adsorption of substance present in the argon gas used for analysis, at higher temperatures. However, since the effect was almost identical for all three **AuNP1**-**AuNP3**, the weight loss was calculated based on the original weight. In order to investigate this observation, TGA experiment was repeated only for **AuNP2** sample (representative for all) due to scarcity of the other two Au NP. This time oxygen gas was used for analysis and almost identical weight loss to the first run was observed for **AuNP2** with the absence of the initial weight gain in the curve (**Figure C5.3**).

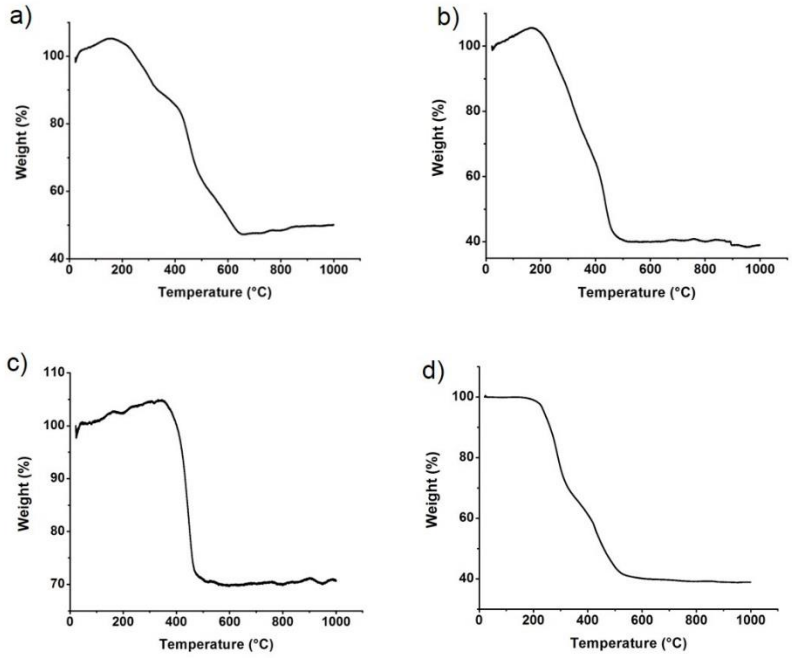

Figure C5.3 Plots of weight loss percentage vs. temperature obtained by TGA analysis (analysis gas: argon) a) **AuNP1**, b) **AuNP2** c) **AuNP3** and d) **AuNP2** (second run; analysis gas: oxygen)

Sample Calculation of nanoparticle weight and number of ligands for AuNP1

Average size: 4.09 nm

R = 2.045 nm

Volume of each NP: $\frac{4}{3} \times 3.14 \times (2.045)^3 = 35.80\ nm^3$

Assuming the density of hexagonal-close-packed gold is 58.01 atom per 1 nm^3

Total number of gold atoms in each NP: 35.80 × 58.01 = 2077 atoms

Radius of the core of NP: R_{NP}-$R_{gold\ atom}$: 2.045 - 0.145 = 1.9 nm

Surface area of the core of NP: $4 \times 3.14 \times (1.9)^2 = 45.34\ nm^2$

Number of gold atoms on the surface of NP assuming the number of gold atoms per unit area on the surface is 13.89 nm^{-2}: 45.34 × 13.89 = 630 atoms

From TGA analysis the weight loss due to loss of organic ligands is 48%. So from 6.7 mg of sample analyzed 3.48 mg is the total weight of organic ligands and 3.22 mg is related to the gold atoms:

3.22 mg gold: $\frac{0.00322}{196.97} \times 6.02 \times 10^{23} = 9.84 \times 10^{18}$ total number of gold atoms

$\frac{9.84 \times 10^{18}}{2077} = 4.73 \times 10^{15}$ total number of NPs

For finding the total weight of organic corona for each NP:

$\frac{0.00348}{4.73 \times 10^{15}} = 7.36 \times 10^{-19}$ (g) weight of organic corona for each NP

Total molecular weight for surface ligands is approximately 607.9 (g/mol) so:

$\frac{7.36 \times 10^{-19}}{607.9} = 1.21 \times 10^{-21}$ (mol) $\times 6.02 \times 10^{23} = 728$

Volume (total) = $\frac{4}{3} \times 3.14 \times (2.045 + 2.397)^3 = 366.95$ nm^3

Volume (organic corona) = Volume (total) - V (core gold) = 366.95 -35.80 = 331.15 nm^3

Density values:

Weight of core gold of each NP: $\frac{0.00322}{4.73 \times 10^{15}} = 6.80 \times 10^{-19}$ g

Density (*d*; of core gold) = $\frac{m}{v} = \frac{6.80 \times 10^{-19}}{3.58 \times 10^{-20}} = 18.99$ g/cm^3

d (of organic corona) = $\frac{7.36 \times 10^{-19}}{3.31 \times 10^{-19}} = 2.22$ g/cm^3

d (of core + corona) = $\frac{1.41 \times 10^{-18}}{3.66 \times 10^{-19}} = 3.86$ g/cm^3

Number of **AuNP1** in 1% mixture

For making 1 wt% dispersion of **AuNP1** in LC1, 0.15 mg of **AuNP1** in 14.85 mg **LC1** were used.

$\frac{0.00015}{1.41 \times 10^{-18}} = 1.06 \times 10^{14}$ of nanoparticles

Assuming **LC1** has a density of 1 g/cm^3:

$\frac{1.06 \times 10^{14}}{0.01485} = 7.13 \times 10^{15}$ NPs per unit volume of LC1 ($\frac{1}{cm^3}$)

Deviations from the idealized structure shown in Figure 5.1

As indicated in the experimental part: "The process of precipitation and re-dispersion was repeated several times until the last supernatant was free from any residual non-bound silane/siloxane as confirmed by ^{1}H NMR."

The resulting sticky nanoparticle samples always showed considerable amounts of solvent from the washing steps, which make integration really difficult and almost useless. Key signatures (in the aromatic section) for the LC ligands are discernible, and in principle the sharp singlets indicating free Si-OCH_3 groups at around 3.5 ppm are absent.

In addition, the peaks of almost all hydrogen atoms are very broad and "smeared out" because all ligands are to some extent all linked via silane conjugation (Si-O-Si linkages in three dimensions). This is in agreement with the much simpler spectra of other silane-conjugated nanoparticles. This also means that some linkages are not active, i.e. some simply hydrolyzed without condensation causing various deviations from the idealized structure shown in **Figure 5.1**. Some of these structures are summarized in the **Figure C5.4**.

For the above reasons, both TGA and XPS measurements were performed. In addition, spectra of the silanes used for the conjugation step – silanes 1 to 3 were collected (silanes **3a**, **3b** and **5** in the manuscript; for the synthesis of **AuNP1** – **AuNP3**, respectively).

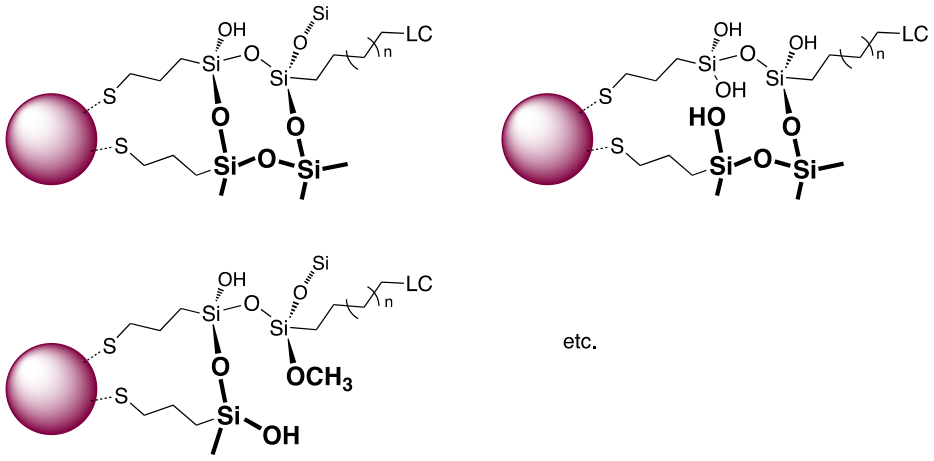

Figure C5.4 Other possible and likely structures of Au NP deviated from perfect/idealized silane shell

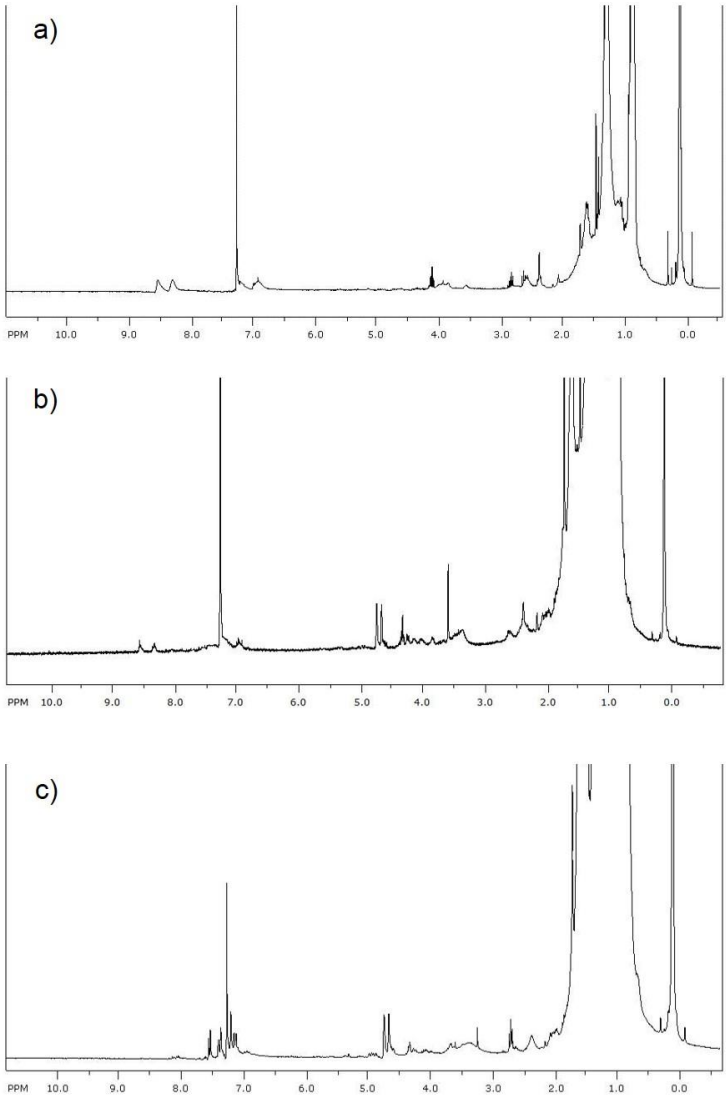

Figure C5.5 ^{1}H NMR of **AuNP1** (a), **AuNP2** (b) and **AuNP3** (c). Due to extensive washing of Au NPs with solvents in purification step, solvent peaks are visible. Enlarged intensity of the signals is necessary for Au NP samples due to weak signals as a result of scarcity of the samples for NMR.

Au NP-doped LC samples

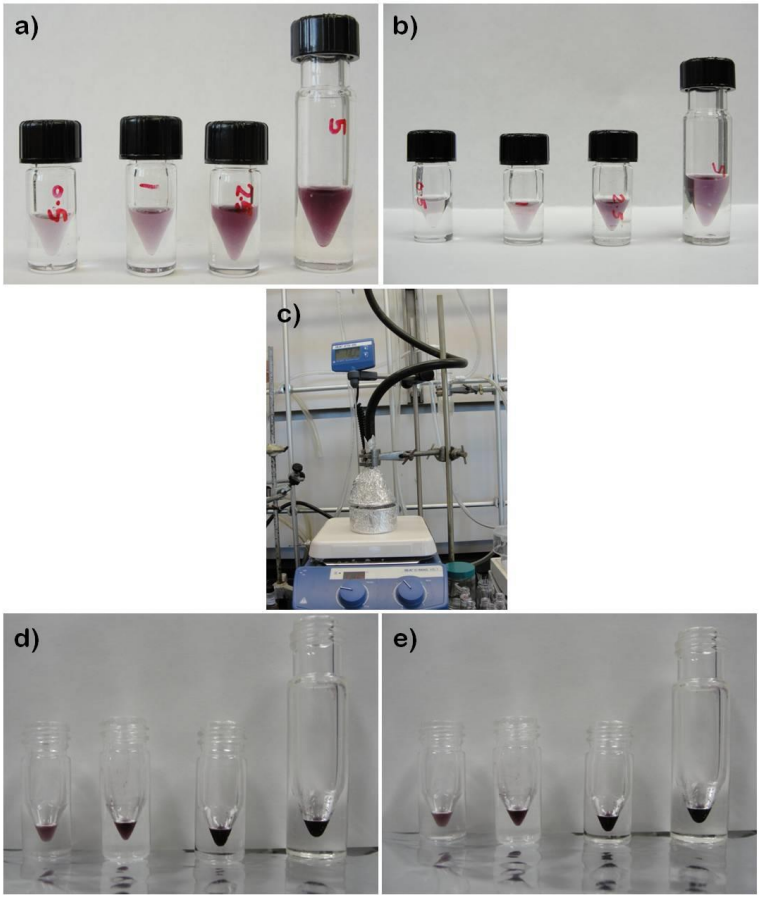

Figure C5.6 AuNP1-LC1 in V-vials (0.5, 1, 2.5 and 5 wt%) in toluene: a) before and d) after solvent evaporation at 73 °C using a hotplate and a steady stream of dry N2 (as in c). **AuNP3-LC1** in V-vials at 0.5, 1, 2.5 and 5 wt% in toluene: b) before and e) after solvent evaporation at 73 °C.

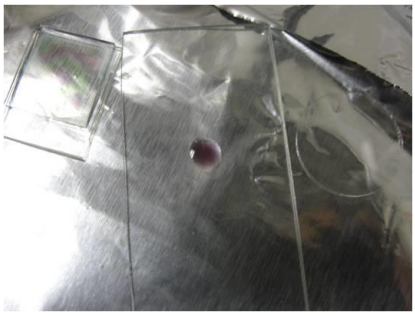

Figure C5.7 Sample preparation by placing a few drops of **LC1** doped with 5 wt% of **AuNP3** on a microscope slide at Iso-N temperature with no NP settling and turbidity.

Electro-optical measurements

Dielectric permittivity values

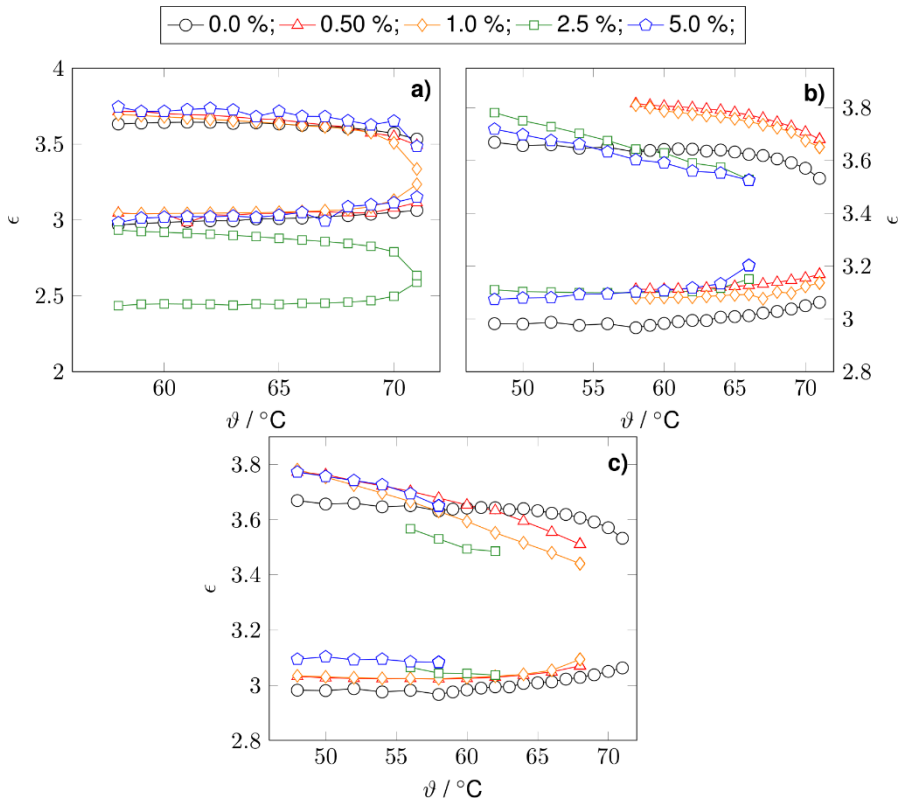

Figure C5.8 Plots of the calculated permittivity values $\varepsilon_{\perp}$ and $\varepsilon_{||}$ for the three nanoparticle systems **AuNP1** (a), **AuNP2** (b), and **AuNP3** (c).

Effective elastic constant K_{eff}

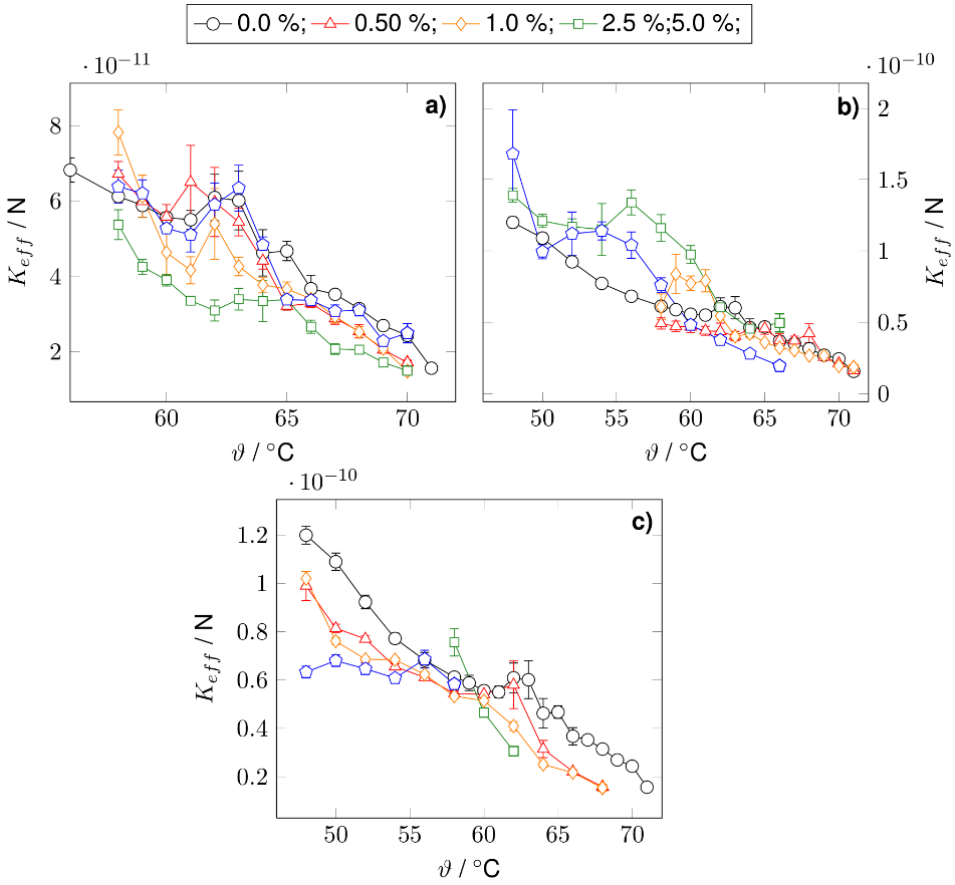

Figure C5.9 Plots of the calculated effective elastic constant K_{eff} for the three nanoparticle systems **AuNP1** (a), **AuNP2** (b) and **AuNP3** (c).

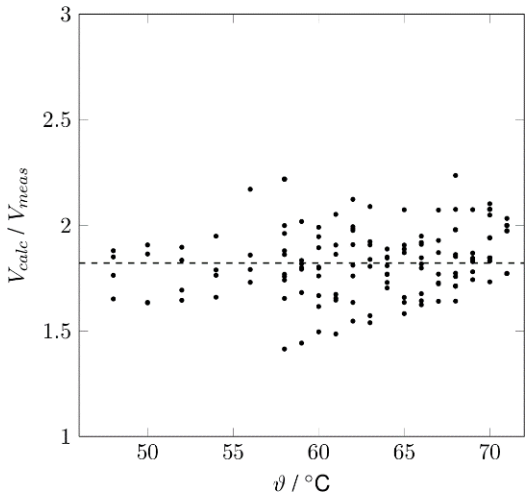

Figure C5.10 Plot of the ratio $V_{th,\,calc.}$ / $V_{th,\,meas.}$ of all measured samples. The ratio is found to be ca. 1.8 instead of 1.0, indicating some lack of accuracy in the experiments.

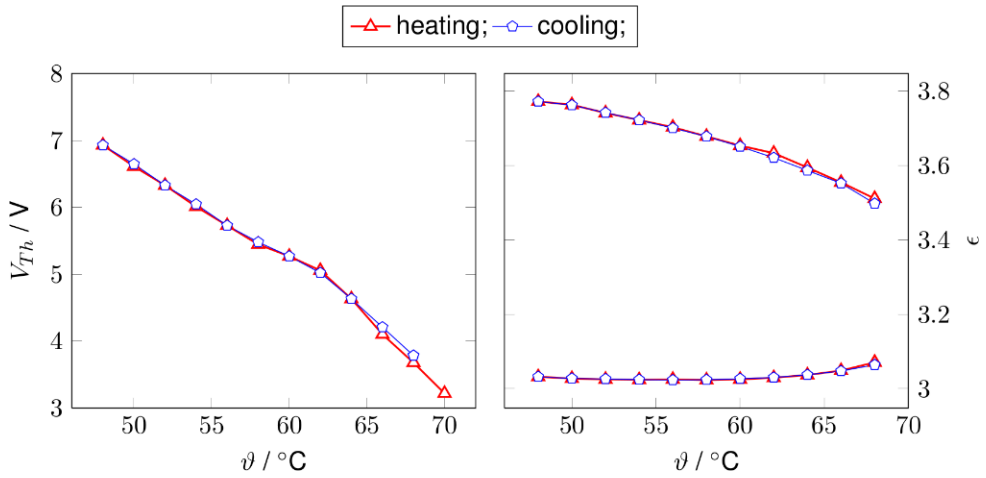

Figure C5.11 Comparison of electro-optic results obtained during heating (red lines) and cooling (blue lines) of a dispersion obtaining 0.5 wt% **AuNP3**. Left: Threshold voltage obtained by light transmission measurement. Right: Dielectric properties.

Appendix D

Appendix D: Surface and Bulk Effects by Numerical Simulations

Nanoparticle Doping in Nematic Liquid Crystals: Distinction Between Surface and Bulk Effects by Numerical Simulations

Nanoparticle Doping in Nematic Liquid Crystals: Distinction Between Surface and Bulk Effects by Numerical Simulations

Marin Urbanski[a], Javad Mirzaei[b], Torsten Hegmann[b,c,d] and Heinz-S. Kitzerow[a]

[a] Department of Chemistry, University of Paderborn 33098 Paderborn, Germany

[b] Department of Chemistry, University of Manitoba, Winnipeg, MB, R3T 2N2 Canada

[c] Chemical Physics Interdisciplinary Program & Liquid Crystal Institute, Kent State University, Kent, OH 44242 USA

[d] Department of Pharmacology and Therapeutics, University of Manitoba, Winnipeg, MB, R3T 2N2 Canada

Reproduced with permission from *ChemPhysChem*, **2014**, 15, (7), 1395-1404.

Abstract

Doping nematic liquid crystals with small amounts of nanoparticles can significantly alter the electro-optic response of the nematic host. Some of these effects result from nanoparticles influencing on the liquid crystal / substrate interface, while other effects are caused by nanoparticles in the bulk. So far, little attention has been paid to the influence of surface interactions on the determination of bulk properties. In the present study, these effects are investigated experimentally and confirmed by numerical simulations. The splay-type Fréedericksz-transition of the nematic liquid crystal 5CB doped with CdSe quantum dots is investigated, as these dispersions are known from earlier studies to affect the initial alignment layers. In comparison, dispersions of chemically and thermally stable silanized gold nanoparticles in the apolar nematic host FELIX-2900-03 are analyzed, which are expected to be bulk active only. A data fitting routine is presented which allows a distinction between bulk and surface effects of nanoparticle doping. For the quantum dots, an increase of pretilt angle proportional to the doping concentration is found, as well as a slight decrease of the anchoring energy of molecules at the confining substrates. The silanized gold particles show no influence on the boundary conditions up to doping concentrations of 2.5 wt%. For higher concentrations an increase of pretilt angle is reported.

Introduction

A relatively young research field of increasing interest is doping of liquid crystals with nanoparticles. It is known that ferroelectric nanoparticles can enhance the dielectric anisotropy[1] and the orientational order[2] of nematic liquid crystals. Dispersions of ultra-small magnetic needles[3] or platelets[4] result in ferromagnetics, which can be reoriented by weak magnetic fields and allow threshold-less optical switching in electric fields.[5] Carbon nanotubes are found to be compatible with nematic hosts due to their anisometric shape.[6] All these examples utilize nanoparticles with additional special physical properties, such as ferroelectricity, magnetism or anisotropic shape. Since the pioneering work of Qi et al.[7] it is known that doping nematic liquid crystals with spherical nanoparticles made of gold or semiconductors can also significantly change the electro-optical properties of the host. These dispersions are particularly interesting as they allow investigating pure interactions between dopant and host, without overlaying additional effects. However, even in the simplest case of nanoparticle doping, occurring surface and bulk effects can interfere and make proper data interpretation difficult. In the present study we show different possibilities of nanoparticle / host interactions, and utilize numerical simulations to distinguish these effects.

It has been reported several times over the past few years that doping a nematic liquid crystal with a small quantity of functionalized nanoparticles can influence the initial alignment of liquid crystal cells and induce homeotropic alignment. This phenomenon is reported for alkylthiol-capped gold particles,[8] for mesogenic functionalized gold particles,[9] for hexadecylamine functionalized CdSe particles[10, 11] as well as for myristic acid capped

magic-sized CdSe quantum dots.[12] Other groups made similar observations, like da Cruz et al. for γ-Fe_2O_3 in 5CB[13] and Bezrodna et al. by investigating montmorillonite clay in 5CB.[14] The underlying mechanism of this alignment change can be explained by nanoparticles residing on the interface and thereby superimposing the effects of any underlying alignment layer. An insufficient miscibility between the nematic host and the organic ligand shell leads to agglomeration of particles and to an expulsion of particles from the liquid crystal phase. This gives rise to the observed accumulation of particles close to the confining substrates and therefore may strongly affect the boundary conditions. As shown by Qi et al.[8], preloading liquid crystal test cells with nanoparticles and subsequent filling with a nematic liquid crystal also leads to homeotropic alignment. Fluorescence confocal microscopy on a CdSe-quantum dot doped sample revealed evidence for the accumulation of particles at the substrate interfaces of the test cell as well as signs of agglomeration (see **Figure D5.1** and the discussion reported elsewhere[15]). Hegmann et al. recently introduced ink-jet printed nanoparticle alignment layers as a versatile tool in the production of patterned alignment layers.[16] As shown by Mehl et al. gold nanoparticles with side-on functionalized mesogenic units show a typical schlieren texture and do not induce homeotropic alignment.[17] In general, the alignment of nematic nanoparticle dispersions strongly depends on the chemical modification of the surface of particles, the solubility of particles in the host, and the properties of the confining substrates.

In addition to effects on the surface, nanoparticles can also influence the bulk properties of the nematic guest phase. For example, formation of electro-convection rolls at low-frequency electric fields have been shown.[15] This electro-convection effect results from the combination of homeotropic alignment at the surface and nanoparticle induced

charges in the bulk of nematic nanocomposites.[15] As a result, a reverse switching is observed, where a liquid crystal with positive dielectric anisotropy switches from a homeotropic dark state to a birefringent bright state between crossed polarizers. With an increase of dielectric anisotropy and a decrease in threshold voltage, pure bulk effects have recently been published by Mirzaei et al.[18] where the authors investigated gold nanoparticles with stabilizing silane shell. A systematic study by Prodanov et al. recently showed the importance of an optimized interaction between ligand shell and host to yield stable dispersions.[19]

When the presence of nanoparticles influences both the surface and bulk properties of a nematic test cell, several difficulties occur: The common methods used to determine the bulk properties of a nematic material require known and well-defined boundary conditions, which are usually achieved by high quality alignment layers, e.g. rubbed polyimide.[20] However, when nanoparticles reside on the initial alignment layers, the well-defined boundary conditions might get obscured and the theoretical approach does no longer match the experimental conditions.

In this work, we aim to investigate the effect of nanoparticles on the boundary conditions with respect to pretilt angle θ_0 and polar anchoring energy (W). We use numerical simulation routines which enables us to determine the elastic constants K_{11} and K_{33}, the dielectric permittivities $\varepsilon_\perp$ and $\varepsilon_\parallel$, the initial pretilt angle θ_0 and the polar anchoring energy coefficient W by fitting simulation data to corresponding experimental data. This allows us to distinguish nanoparticle-induced effects on the anchoring conditions and effects of nanoparticles on the liquid crystal bulk properties. In order to investigate the effect of nanoparticles on the boundary conditions, dispersions of hexadecylamine-capped

CdSe quantum dots (**NP1**) in the host 4-cyano-4'-pentylbiphenyl (**LC1**, see **Figure D5.2**) are studied, as these dispersions are known for strong surface interactions.[10] In contrast, dispersions of silanized gold particles (**NP2**) in the nematic host 5-n-heptyl-2-(4-n-octyloxy-phenyl)pyrimidine (**LC2**) are investigated, which are expected to show only little or no surface effects. This expectation is based on previous work with similar nanoparticles, as reported previously.[18]

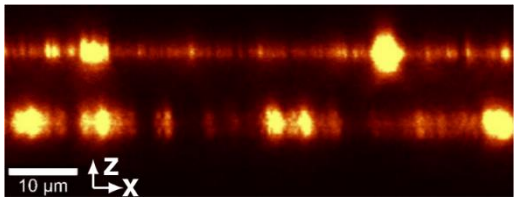

Figure D5.1 Confocal fluorescence microscopy image obtained from a sample of 1 wt% **NP1** in **LC2**. The intensity distribution in the (x, z)-plane strongly indicates that the luminescent nanoparticles are residing at the liquid crystal / substrate interface. The directions for x and z correspond to the definitions in Figure D5.3.

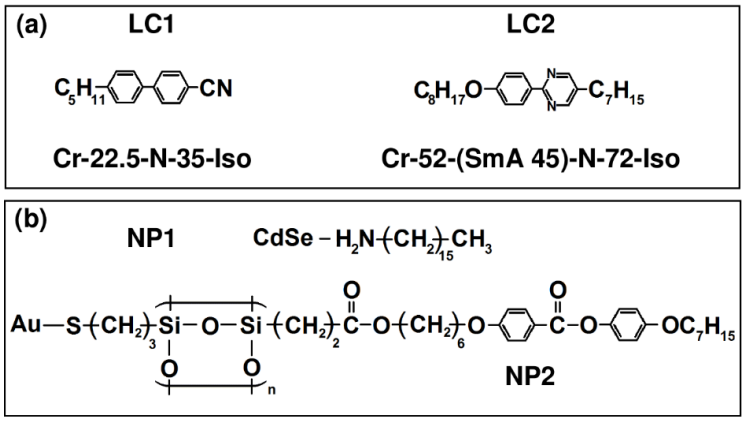

Figure D5.2 Chemical structures and phase transition temperatures of the liquid crystalline hosts **LC1** and **LC2** (a) and chemical structures of nanoparticles **NP1** and **NP2** (b).

Experimental and Methods

Materials

The hexadecylamine-capped CdSe nanoparticles **NP1** were purchased from Sigma-Aldrich as Lumidot^{TM} CdSe quantum dots with core sizes between 4.7-5.2 nm and a fluorescence emission maximum at 610 nm. Dispersions of **NP1** were prepared in the host **LC1** (4-cyano-4'-pentylbiphenyl, 5CB) by adding suitable amounts of the quantum dots dissolved in toluene (5 mg/ml) to a small amount of liquid crystal in toluene. The solvent was then removed under mechanical stirring and reduced pressure of $p < 5.0\times10^{-3}$ Pa at a temperature of 60-70°C for 36 hours. For electro-optic characterization, the dispersions were filled in polyimide coated test cells (E.H.C Co., Ltd, Japan) with 10 µm cell gap and antiparallel rubbing. In this work, results for dispersions containing 0.5 %, 1.0 % and 2.5 wt% of nanoparticles are shown. Higher doping concentrations induce homeotropic alignment and therefore cannot undergo a Fréedericksz transition.

Liquid crystal-decorated gold nanoparticles **NP2** with an average diameter of 7 nm were synthesized via a modified silane conjugation method descried elsewhere.[21] Pure **LC2** (5-n-heptyl-2-(4-n-octyloxy-phenyl)pyrimidine, FELIX-2900-03) was purchased from Synthon Chemicals GmbH and used without further purification. Dispersions of **NP2** in **LC2** were prepared by weighing accurate amounts of particles and **LC2** using a micro-balance and dissolving them separately in a known amount of toluene. Colloidal solutions of **NP2** were sonicated for about 15 minutes (water bath sonication, f=37 kHz power). Then accurate amounts of solutions of each **NP2** and **LC2** were combined in a V-vial to produce colloidal dispersions with particle concentrations of 0.5, 1.0, 2.5 and 5.0 wt%. These

mixtures were sonicated for another 1 h. Then toluene was allowed to evaporate under a steady stream of N_2 at about 70°C for about 48 h followed my 1 minute sonication. The test cells used for these dispersions exhibit antiparallel polyimide alignment layers for planar alignment (1°-3° pretilt) and a thickness of 4.0 µm (LC Vision, USA). Loading of cells with LC-NP mixtures was performed by capillary force with the liquid crystal in the isotropic phase at temperatures between 74°C and 78°C.

Methods

The characterization of test cells follows the Single-Cell-Method as described by Wu et al.[22] with additional simultaneous measurement of light transmittance in a polarizing microscope. The test cells were positioned under an azimuthal angle of φ=45° with respect to the optical axis between crossed polarizers within a Linkam LTS350 heating stage with TMS94 controller for temperature control. Samples of **LC2** were first heated up to 76°C at a heating rate of 8°C/min, followed by a cooling procedure at 1°C/min until the first measuring temperature of 48°C is reached. Samples of **LC1** were heated up to 40°C at a heating rate of 8°C/min and cooled at 1°C/min to the first measuring temperature of 25°C. All measurements were performed on an Ortholux II Pol-BK microscope (Leica) using a halogen lamp (Xenophot, Osram) with DC stabilized power supply. For monochromatic light an interference filter with a transmission maximum at 542 nm (FWHM 10.8 nm) was used. Simultaneously, the cell capacitance was measured on an HP 4284A LCR bridge by varying the sine test signal level from 0.05 V to 19.95 V at a test signal frequency of 1 kHz. The blind capacitance of the setup due to wires, contacts etc. was determined to be 4.125 pF. POM images were obtained on a Leica DM4500 P microscope using a Leica DFC295 digital camera.

Experiments for determining the bulk properties of liquid crystalline materials are well-known and have been refined over the last decades to enhance precision. Two of the most established methods are the capacitance measurement and the birefringence measurement during a Fréedericksz-transition. The Single-Cell geometry reported by Clark et al.[23] and refined by Wu[22, 24] allows a full determination of elastic and dielectric properties in a single experiment and has been implemented in automatic liquid crystal testers like the ALCT from Instec, Inc (USA) or the LCAS by LC Vision (USA). The basic principle of these techniques is the determination of elastic constants by finding the threshold of the Fréedericksz-transition and the determination of the dielectric properties by measuring the capacitance of the test cell in the planar and homeotropic state. However, this well-established method requires good knowledge about the anchoring conditions at the substrate boundaries. For liquid crystals with positive dielectric anisotropy ($\Delta\varepsilon = \varepsilon_{\parallel} - \varepsilon_{\perp} > 0$), usually test cells with opposing electrodes and a high-quality alignment layer for inducing planar alignment are used. In this case, a splay-type Fréedericksz-transition can be observed and used for data evaluation. A schematic drawing of the respective cell geometry is given in **Figure D5.3**.

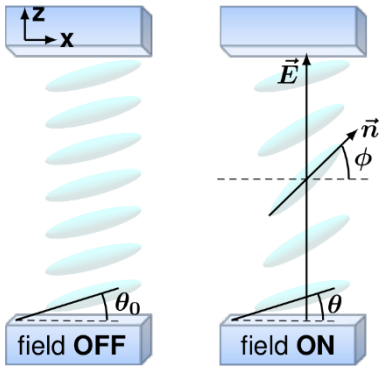

Figure D5.3 Illustration of cell geometry in the field OFF state (*left*) and under the influence of an external electric field (*right*).

The threshold V_{Th} of the Fréedericksz-transition is given by the onset of director deformations when the electric torque overcomes the restoring elastic torque of the nematic material, and can be expressed by the relation $V_{Th} = \pi\sqrt{K_{11} / \varepsilon_0 \Delta\varepsilon}$. Here, K_{11} represents the elastic constant for the splay deformation. During the measurement, a certain change of director field is required to detect this onset, which is chosen rather arbitrarily to be a change of 5 % in capacitance *C* or phase retardation *R*. Therefore, by this simple but widely used approach the experimentally determined threshold slightly overestimates the elastic constant for the splay deformation, as illustrated in **Figure D5.4**. The threshold V_{Th} can be only defined in a strict sense for zero pretilt angle ($\theta_0 = 0$). The polyimide test cells commonly used for electro-optical experiments exhibit, depending on the manufacturer, pretilt angles between 1° and 3° (LC Vision) or $0° < \theta_0 < 1°$ (EHC), respectively. Therefore only a quasi-threshold behavior is observed within these cells. As the pretilt is still small, the aforementioned overestimation is compensated and good results are yielded. Any larger pretilt angle leads to a deformation of the director field at lower field strengths compared to zero pretilt, and in consequence to lower quasi-threshold voltages. This causes a significant decrease of apparent threshold $V_{Th,app}$ for large pretilt angles, as shown in **Figure D5.5**. Additionally, a finite pretilt angle increases the cell capacitance in the field-off state, which seemingly decreases the dielectric anisotropy of the nematic material.

The polar anchoring energy *W* at the confining substrates of a liquid crystal test cell also influences the Fréedericksz transition of the cell. Weaker anchoring energy leads to smaller threshold voltages V_{Th}, although the bulk elastic properties K_{11} and K_{33} remain unaffected. Therefore the relation $V_{Th} = \pi\sqrt{K_{11} / \varepsilon_0 \Delta\varepsilon}$ can be used to estimate the splay

elastic constant for strong anchoring only. In the case of weak anchoring this equation no longer holds. Commercial electro-optic test cells with rubbed polyimide alignment layer as used in this work are designed to yield strong anchoring conditions. However, the effect of nanoparticles on the anchoring strength when residing at the interface has not been investigated yet. As a nanoparticle-induced change from planar to homeotropic alignment is frequently observed in literature (see references given in the introduction) and the anchoring energy of homeotropic alignment layers is typically two magnitudes smaller compared to alignment layers for planar anchoring,[25] the influence of nanoparticles on the anchoring strength of nematic nanoparticle dispersions is discussed in the following section.

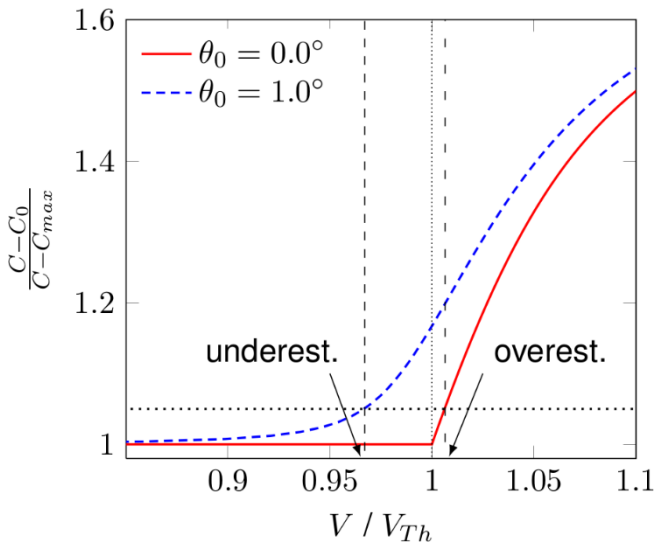

Figure D5.4 Simulation of the onset of director deformation for **LC2** at T-T_{NI} = -25 °C with (dashed curve) and without (solid line) pretilt angle θ_0. While in the case of no pretilt angle the threshold V_{Th} is slightly overestimated, a finite pretilt angle leads to an underestimation of V_{Th}.

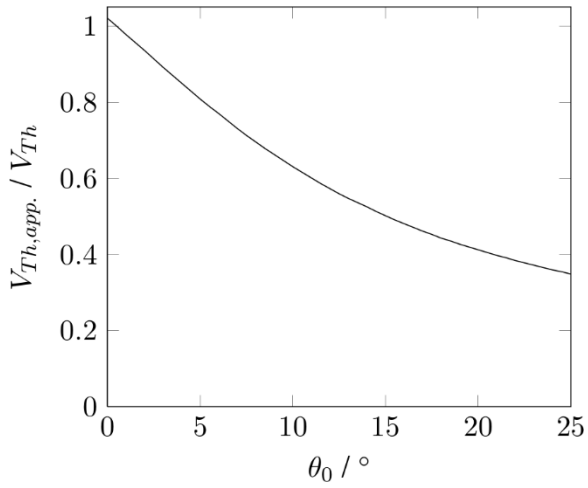

Figure D5.5 Dependence of apparent threshold $V_{\mathrm{Th,app}}$ compared to $V_{Th} = \pi\sqrt{K_{11}/\varepsilon_0\Delta\varepsilon}$ with increasing pretilt angle θ_0 when using an onset of capacitance change for experimentally determining the threshold voltage.

Anchoring energy (*W*)

Several experimental techniques are discussed in literature in order to measure the anchoring strength at a nematic liquid crystal / substrate interface.[26] We follow the high field approach introduced by Yokoyama and van Sprang.[27] The precipitation of particles from the bulk to the surface cannot be quantitatively controlled yet, which makes it impossible to prepare identical conditions on different substrates or test cells. However, with the high field approach by Yokoyama and van Sprang we can determine the bulk properties as well as the boundary conditions within the same test cell, and therefore under identical experimental conditions. The method is based on measuring changes in the cell capacitance *C* and phase retardation *R* at high electric fields, where the director in the bulk of the test cell is fully reoriented and additional changes of the director distribution occur only in the vicinity of the confining substrates. To fulfil this condition, Yokoyama and van

Sprang suggest a lower voltage limit for the measurement of surface energies given by the inequality $V > V_{min} > 6\ V_{Th}$. A second restriction for the observable voltage range is given by the condition that the surface reorientation is small. Assuming a Rapini-Papoular potential for the anchoring energy[25], the surface energy density f_s can be estimated by using Equation (1):

$$f_s = \frac{1}{2} W \sin^2\left(\theta - \theta_0\right) \tag{1}$$

For zero pretilt and $\Delta\theta = \theta\text{-}\theta_0 < 0.3$, this relation can be simplified to $f_s = ½ \times W \times (\Delta\theta)^2$. In case of finite pretilt angle, this simplification is valid only for $\Delta\theta = 0.1$.[26] The maximum voltage V_{max} which still hold this requirement is found to be proportional to the product $\Delta\theta W d$, whereas a higher accuracy is obtained for thicker cells. As shown by Lavrentovich et al.,[28] the cell thickness should be at least 200 times larger than the surface extrapolation length $b = K_{11}/W$ to obtain reliable results. This condition is clearly fulfilled in 10 µm polyimide coated test cells (E.H.C Co., Ltd, Japan) filled with **LC1** as used in our experiments.

As the surface coverage of nanoparticles residing on the alignment layers of the electro-optical test cells is not necessarily homogeneous over the complete electrode area, it is undesirable to perform capacitance measurements for determining *W*. Instead, the RV-routine developed by Lavrentovich et al.[28] is preferred, requiring field-dependent phase retardation data only. According to this approach, the experimental data is plotted using Equation (2):

$$\frac{R\left(V - \bar{V}\right)}{R_0} = \tilde{J}_0 - \frac{2K_{11}}{Wd}\left(1 + \kappa y_p\right)\left(V - \bar{V}\right) \tag{2}$$

with $\kappa = \left(K_{33} - K_{11}\right)/K_{11}$, $y_p = \sin^2\theta_0$, the cell thickness d, the intercept $\tilde{J}_0$ depending on the material parameters of the nematic material (for details see reference [28]), and Equation3 (3) and (4):

$$\bar{V} = \alpha \frac{\Delta\varepsilon}{\varepsilon_{\square}} V_{Th} \tag{3}$$

and

$$\alpha = \frac{1}{\pi}\int_{y_p}^{1} \sqrt{\frac{(1+\gamma)(1+\kappa\gamma)}{y(1+\gamma y)}}\,dy\,. \tag{4}$$

The phase retardation R is obtained by light transmission measurements using Equation (5):

$$I_{\det} = \frac{1}{2}\sin^2(2\vartheta)\sin^2\left(\frac{R}{2}\right) \tag{5}$$

Where ϑ=45° represents the azimuthal angle between the optical axis of the liquid crystal and the crossed polarizers. Equation (2) gives a linear relation where the slope is proportional to the anchoring energy W.

One fundamental drawback of this approach is that the determination of α requires knowledge about the parameters K_{11}, K_{33}, $\varepsilon_{\parallel}$, $\varepsilon_{\perp}$ and θ_0 of the dispersion, which are not known a priori. A fitting routine, however, requires knowledge of the anchoring energy W to yield proper results. To solve this problem, it is assumed that nanoparticle coverage might affect the anchoring energy, but will not cause drastic changes. Then in a first step, a numerical simulation is performed assuming W=∞, and in a second step the obtained parameters for K_{11}, K_{33}, $\varepsilon_{\parallel}$, $\varepsilon_{\perp}$, and θ_0 are used to determine the anchoring energy W. This

value can then be used to refine the fitting parameters. This procedure is repeated, until the change in the surface correlation length *b* between two iterations is less than 0.01 µm.

Results and Discussion

Simulation results for **NP1** nanoparticles in **LC1** are shown in **Figures D5.6** and **Figure D5.7**. It is found that **NP1** nanoparticles strongly influence the elastic constants K_{11} and K_{33}, the tilt angle θ_0 as well as the polar anchoring energy W. The decrease of the elastic constants is in agreement with earlier observations.[10] A possible explanation model is given previously,[9] where the authors report a tactoidal deformation of the ligand shell surrounding the metal core. Thereby, a field-induced reorientation of the nematic host is facilitated by folding and unfolding of ligands without rotating the nanoparticle itself. With increasing particle concentration, an increase in θ_0 and a decrease of anchoring strength W is found. This observation confirms the expectation of an intermediate state of nanoparticle surface covering between planar and homeotropic alignment. As the anchoring strength has to be regarded in comparison with the bulk elastic properties, the respective measure is the surface correlation length $b = K_{11}/W$ (see **Figure D5.6**a). Doping concentrations of ≥5 % by weight induced homeotropic alignment in polyimide coated test cells and are therefore not investigated in this work.

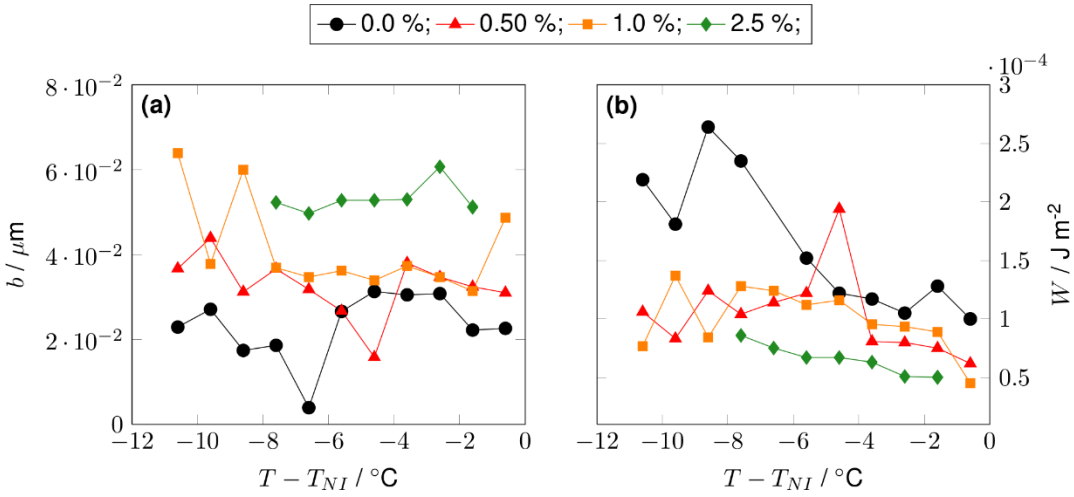

Figure D5.6 (a) Anchoring extrapolation length $b = K_{11}/W$ for dispersions of **NP1** nanoparticles in **LC1**. (b) Calculated surface energy coefficients W for the same dispersions. Although nanoparticle doping leads to a decrease of surface energy and an increase of anchoring extrapolation length, the changes are small compared to the cell thickness and therefore can be neglected.

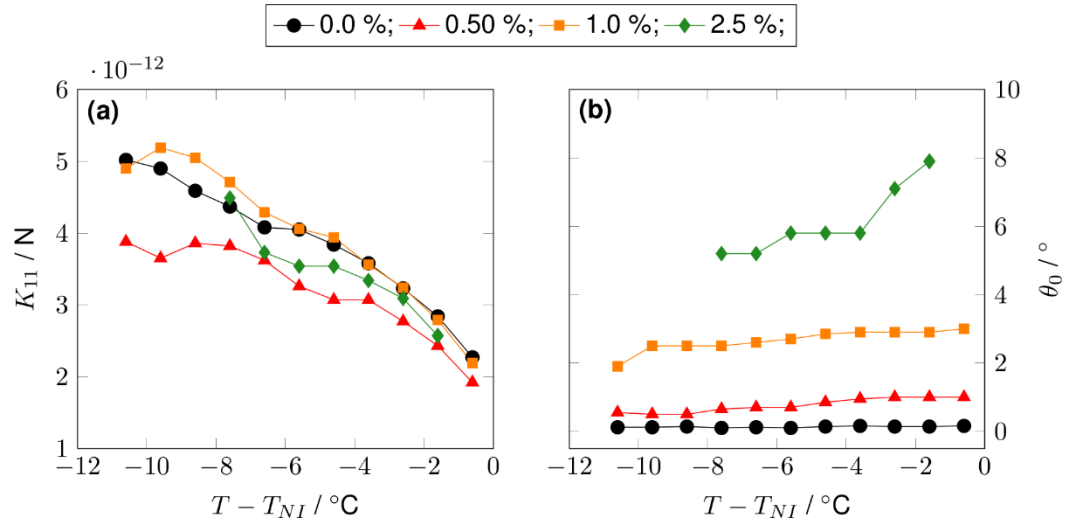

Figure D5.7 Simulation results for **NP1** nanoparticles in **LC1**. (a) Elastic constant K_{11} for splay deformations. (b) Initial tilt angle θ_0. Nanoparticle doping leads to a slight decrease of elastic constant, which is in accordance to earlier observations. Additionally, a clear increase of initial tilt angle is found, which is presumably caused by nanoparticles residing at the initial alignment layers of the test cell.

In order to answer the question whether surface effects have to be considered or not for dispersions of **NP1** in **LC1**, the effective cell thickness $d^* = d + 2b$ is compared to the physical cell thickness d.[26] Although for the dispersions investigated here nanoparticle doping clearly leads to an increase of the effective cell thickness, the deviation is still smaller than 1% compared to the cell thickness, so the assumption $d^* \approx d$ holds. The anchoring strength W of strong anchoring conditions is usually found to be in the range of $10^{-4} - 10^{-3}\,\mathrm{J/m^2}$ which is fulfilled for all samples investigated here.[28] Numerical simulations with the simplifying assumption $W=\infty$ yield values for K_{11} which are under 10% higher than values obtained for finite anchoring strength. The self-consistent algorithm described above gives stable values for K_{11} and W after 3-4 iterations. In summary it is found that **NP1** particles do affect the polar anchoring energy W, but this effect is small and negligible for the cell thicknesses investigated here. A change of initial tilt angle θ_0 however is significant and has to be considered in the simulation models used to estimate the dispersions bulk properties.

In a second set of experiments, dispersions of **NP2** nanoparticles in the host **LC2** are investigated. The determination of anchoring strength for these dispersions was not successful, as the RV-routine gives negative anchoring energy coefficients W for the nematic host **LC2**, and therefore fails to produce meaningful values for W. This is presumably caused by deviations of the director field deformation from the one-dimensional theoretical approach at high field strengths.[28] However, earlier experimental results with silanized gold nanoparticles indicate that this group of nanoparticles yields stable dispersions without signs of surface interactions on polyimide alignment layers.[18] A simplified simulation model with five parameters (K_{11}, K_{33} , $\varepsilon_{\parallel}$, $\varepsilon_{\perp}$ and W) following the

Welford-Sambles approach[29] is found to be sufficient to reproduce the measured capacitance responses for pure and doped samples with high accuracy. An influence of particles on the polar anchoring energy coefficient W therefore is excluded. The initial pretilt angle θ_0 of the pure compound is found to be 1.4°-1.7° in LC Vision test cells. This confirms the data provided by the manufacturer. The dispersions containing 0.5 % and 1.0 wt% of nanoparticles show no effect on the pretilt angle (**Figure D5.8**a).

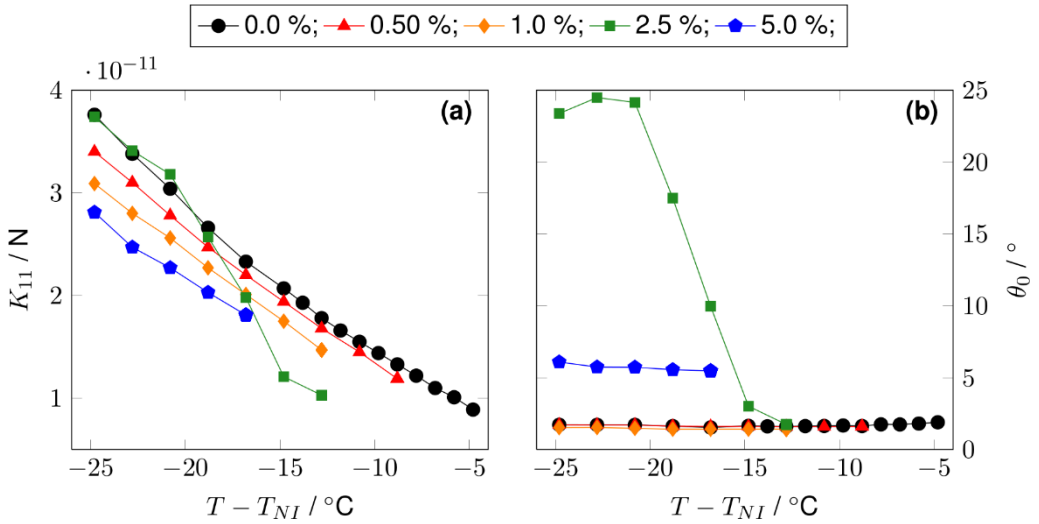

Figure D5.8 Simulation results for **NP2** particles in **LC2** showing the splay elastic constant K_{11} (a) and the initial tilt angle θ_0 (b). Nanoparticle doping is found to decrease the elastic constant. At low doping concentrations the nanoparticles do not affect the initial tilt angle θ_0, while higher doping concentrations increase θ_0. For the sample containing 2.5 wt% of nanoparticles, a correlation between the increase of pretilt angle and the decrease of elastic constant is found: When at low temperatures the tilt angle is high, the elastic constant of the dispersion is comparable to the values of the pure compound. With decreasing tilt angle at higher temperatures the elastic constant also decreases, which indicates a movement of particles from the interface to the bulk.

For the highest doping concentration of 5.0 wt% an average pretilt angle of 5.7° is found. The dispersion containing 2.5 wt% of nanoparticles reproducibly shows very large

pretilt angles above 20° for low temperatures, while at high temperatures no change of pretilt compared to the pure compound is found. The respective data can be found in **Figure D5.8**b. The analysis of elastic constants reveals a general decrease with increasing doping concentration, as shown in **Figure D5.8**a and **Figure D5.9**a. A similar effect of nanoparticle doping has recently been reported elsewhere.[18] However, in this case there seems to be a correlation between the decrease in the K_{11} elastic constant and the pretilt angle θ_0: When dispersed in the bulk, **NP2** particles lead to a decrease of the splay elastic constant of the dispersion compared to the pure compound. When residing at the interface, the particles have an effect on the tilt angle but no longer on the bulk properties. This can clearly be seen for the dispersion containing 2.5 wt% of nanoparticles, where an increase of pretilt angle correlates to an increase of splay elastic constant, yielding values of the pure compound. There is evidence for a temperature dependent shift of particles from the surface to the bulk in a polyimide coated test cell. Similar observations have been reported so far only for plain glass substrates in other references.[8, 10]

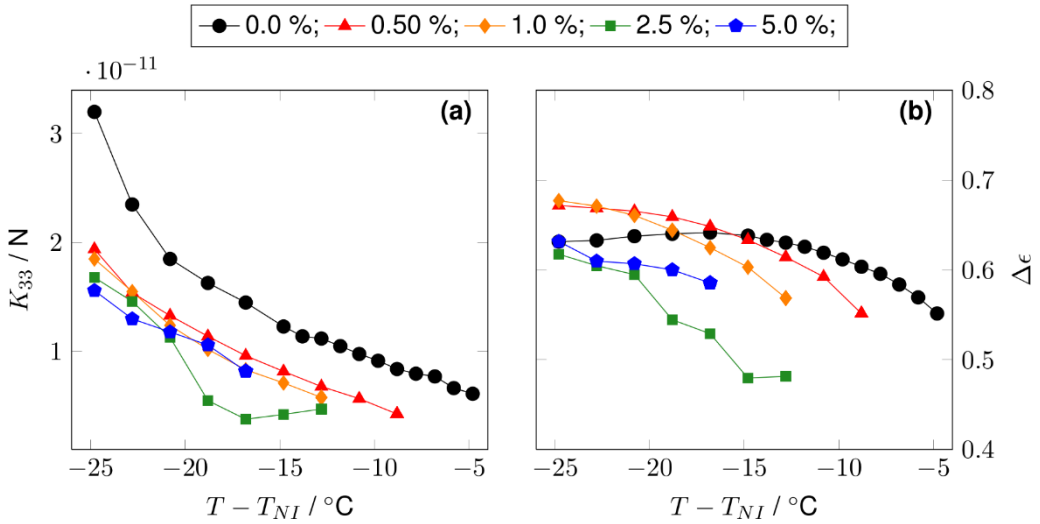

Figure D5.9 Simulation results for **NP2** dispersions in **LC2** showing the bend elastic constant K_{11} (a) and the dielectric anisotropy $\Delta\varepsilon$ (b). Nanoparticle doping with **NP2** decreases the bend elastic constant, while a clear trend for the dielectric anisotropy is not found.

Numerical simulations

The theoretical director field distribution within the test cell is simulated using the well-known theory of the Fréedericksz-transition,[29] and the fitting parameters of the respective model are varied until the mean square difference between theoretical capacitance response and measured capacitance data is minimized.

The theoretical calculation of director field distributions follows the idea of minimizing the total free energy F of the liquid crystal. This total free energy F of a nematic liquid crystal under an external electric field is given by Equation (6):

$$F = \int_V \left(f_e + f_E\right) dv + \int_S f_s \, ds \qquad (6)$$

Where f_e, f_E and f_s represent the bulk elastic free energy density, the electric field energy density and the surface anchoring energy density, respectively.[30] According to the Frank-Oseen theory, the elastic free energy density is given by Equation (7):

$$f_e = \frac{1}{2}K_{11}(\nabla \cdot n)^2 + \frac{1}{2}K_{22}\left(n \cdot \nabla \times n - q_0\right)^2 + \frac{1}{2}K_{33}(n \times \nabla \times n)^2 + \frac{1}{2}(K_{24} - K_{22})\left[\nabla \cdot (n\nabla \cdot n \times \nabla \times n)\right] \quad (7)$$

For the case studied here (nonchiral nematics, splay type Fréedericksz-transition), the elastic free energy density f_e only depends on the one-dimensional angle-dependency ϕ(Z) given by equation (8).

$$f_e = \frac{1}{2}\left(\frac{d\phi}{dz}\right)^2 \left(K_{11}\cos^2\phi + K_{33}\sin^2\phi\right) \quad (8)$$

The electric field energy density f_E in this geometry is then given by Equation (9):

$$f_E = -\frac{1}{2}\varepsilon_0 E^2 \left(\varepsilon_{\parallel}\sin^2\phi + \varepsilon_{\perp}\cos^2\phi\right) \quad (9)$$

The minimum in the total free energy F is obtained by using first order variations, leading to Equation (10):

$$\left(K_{33} - K_{11}\right)\sin\phi\cos\phi\left(\frac{d\phi}{dz}\right)^2 + \left(K_{11}\cos^2\phi + K_{33}\sin^2\phi\right)\frac{d^2\phi}{dz^2} + \varepsilon_0\Delta\varepsilon E^2\sin\phi\cos\phi = 0 \quad (10)$$

A very commonly used simplification of equation (10) is the One-constant-approximation[25] by assuming $K_{11} = K_{33} = K$. This simplified approach yields reliable results for the threshold V_{Th} as well as the permittivities $\varepsilon_{\perp}$ and $\varepsilon_{\parallel}$ only under the condition of small initial tilt angles θ_0<2° and strong anchoring(W=∞). For larger angles θ_0, the fit condition of minimizing the mean square difference between experimental data and simulation

requires a consideration of two independent elastic constants for the splay and bend deformation. Therefore in this work only an extended model is used.

For liquid crystals with large dielectric anisotropy $\gamma = \Delta\varepsilon/\varepsilon_\perp$, the reorientation of molecules causes a non-negligible change of permittivity and therefore affects the local electric field. The electric field distribution through the cell can be obtained by solving the Laplace equation [Equation (11)]:

$$\nabla \cdot \boldsymbol{\varepsilon} \cdot \nabla u = 0 \tag{11}$$

where u represents the potential and $E = -\nabla u$ In the one-dimensional case observed here, Equation (11) leads to Equation (12):

$$2\Delta\varepsilon \sin\phi\cos\phi \frac{d\phi}{dz}\frac{du}{dz} + \left(\varepsilon_\perp + \Delta\varepsilon \sin^2\phi\right)\frac{d^2u}{dz^2} = 0 \tag{12}$$

Equations (10) and (12) represent a system of coupled second-order differential equations, which can be linearized and solved using numerical solving routines, e.g. the bvp4c solver implemented in Matlab software (TheMathworks, Inc).

For the assumption of strong anchoring of molecules at the surfaces of the test cell, the set of equations can be solved using Dirichlet boundary condition by using $\theta_0 = \theta$. In the general case of arbitrary anchoring strength W, Neumann boundary conditions have to be used, allowing the director at the surface to change its orientation under the influence of electric fields. As shown by Yokoyama and van Sprang[26], the torque balance at the surface is given by Equation (13):

$$\frac{df_s(\theta)}{d\theta} = \left(K_{11}\cos^2\phi + K_{33}\sin^2\phi\right)\frac{d\phi}{dz}\bigg|_{z=0} \tag{13}$$

The angle θ at the interface is then given by Equation (14):

$$\theta = \frac{df_s(\theta)}{d\theta} + W\left[\sin(\Delta\theta)\cos(\Delta\theta)\right] \tag{14}$$

For the case of strong boundary conditions and small dielectric anisotropies, another numerical approach is more convenient, as the aforementioned system of coupled differential equations might cause instable solutions at high fields when using the described commercial solvers. The numerical algorithm follows the approach by Welford and Sambles given in another reference[31] and is based on the work of Deuling[32] with extension to arbitrary initial tilt angles θ_0 In a first step, the voltage V required to yield a maximum tilt angle ϕ_m in the middle of the test cell is calculated by means of Equation (15):

$$V = \sqrt{\frac{K_{11}}{\varepsilon_0 \Delta\varepsilon} \cdot (1 + Y(1+\gamma))} \cdot \int_{Q_l}^{\infty} \sqrt{\left[\frac{(1+Y)(1+Q)+\kappa YQ}{\left[(1+Y)(1+Q)+\gamma YQ\right](1+Y+Q)(1+Q)Q}\right]} dQ \tag{15}$$

With $Y = \tan^2\phi_m$, $Q = \tan^2\psi$, $\sin\psi = \sin\phi/\sin\phi_m$, $\gamma = \Delta\varepsilon/\varepsilon_\perp$ and $\kappa = (K_{33} - K_{11})/K_{11}$. The lower limit of the integral depends on the initial tilt angle θ_0 and is given by Equation (16):

$$Q_l = \tan^2\left[\sin^{-1}\left(\frac{\sin\theta_0}{\sin\phi_m}\right)\right] \tag{16}$$

The spatial angle distribution along the z-direction is given by Equation (17):

$$\frac{z}{L} = \frac{\int_{Q_l}^{\infty} Z dQ}{2\int_{Q_l}^{Q_h} Z dQ} \tag{17}$$

With Equation (18):

$$Z = \sqrt{\left[\frac{\left[(1+Y)(1+Q)+\kappa YQ\right](1+Y)(1+Q)+\gamma YQ}{(1+Y+Q)(1+Y)(1+Q)Q}\right]} \cdot \frac{1}{1+Q} \tag{18}$$

The upper limit in the integral is given by Equation (19):

$$Q_h = \frac{\tan^2\phi(1+Y)}{Y-\tan^2\phi} \tag{19}$$

The cell capacitance for a given spatial angle distribution is then given by a calculated permittivity profile along the *z*-direction of the cell. As shown in **Figure D5.10**, this approach yields very good results for dispersions of **NP2** nanoparticles in the host **LC2**. The mean deviation between experiment and simulation is less than 0.1 pF.

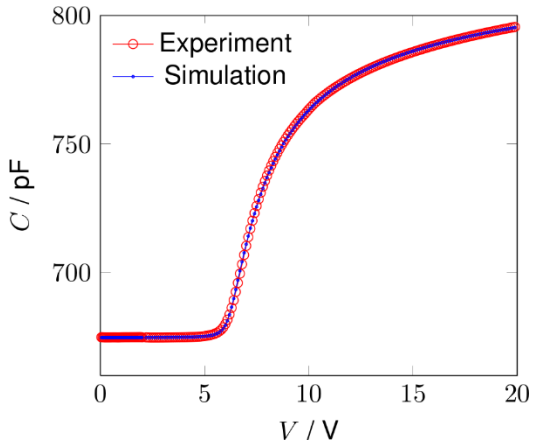

Figure D5.10 Comparison of experimental and simulated data for 0.5% (w) of **NP2** in **LC2** using the approach by Welford and Sambles.[31] As the dielectric anisotropy of the host **LC2** is small ($\Delta\varepsilon \approx 0.5$) changes of the permittivity tensor ε during director redistribution can be neglected. The mean deviation between experiment and simulation is less than 0.1 pF.

Conclusion

Based on experimental and numerical results with nanoparticle dispersions, the anchoring conditions require additional attention when investigating the properties of nematic nanoparticle dispersions. Nanoparticles residing at the liquid crystal / substrate interfaces can affect the anchoring energy W and the tilt angle θ_0 to varying degrees. We distinguish three general cases of surface interactions (**Figure D5.11**).

In the case of no surface interactions or negligible surface coverage of nanoparticles on the alignment layers, the initial alignment layers ensure strong boundary conditions with sufficiently small director tilt from the planar surface. In this case the standard techniques for investigation nematic liquid crystals work very well, and the Single-Cell-Method as described by Clark and Wu yield reliable results.

In the case of high surface coverage, a switching from planar alignment to homeotropic alignment can occur. According to the explanation model established in literature and based on own experiments, this switching is caused by nanoparticles residing at the interfaces and superimposing the effects of the initial alignment layers. As has been reported several times in literature and is in accordance with our own observations, the surface coverage can be dependent on temperature or external electric fields. In any case reported, the surface coverage is proved by homeotropic alignment in POM images. No Fréedericksz-like switching can be observed for liquid crystals with positive dielectric anisotropy and homeotropic alignment in test cells with opposing electrodes, where the electric field is perpendicular to the substrates. Therefore, the standard methods for determining bulk properties cannot be performed.

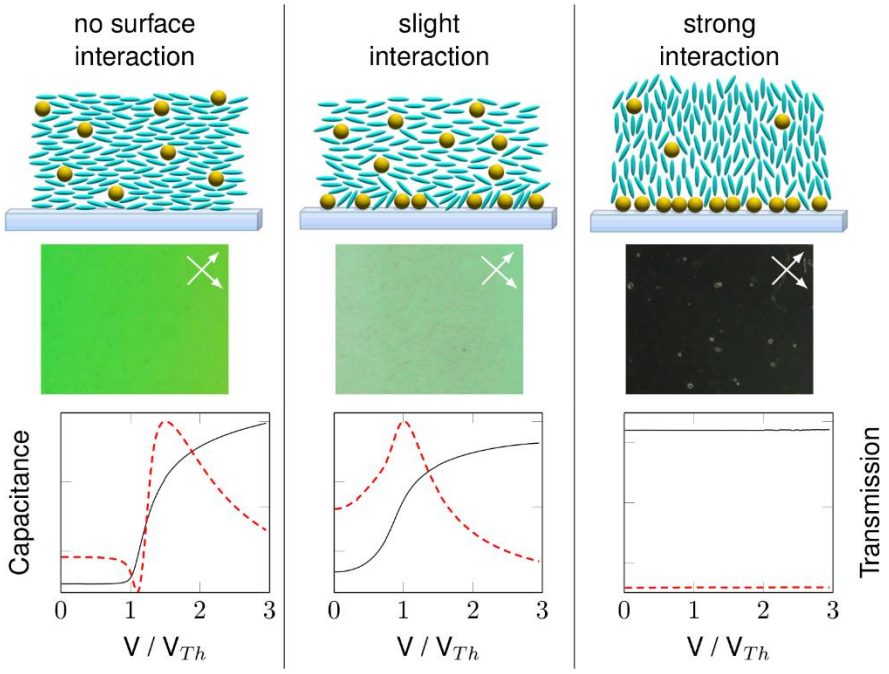

Figure D5.11 Illustration of three possible degrees of surface interactions of nanoparticles with the alignment layers. *Left:* No surface coverage of particles, therefore no influence on the initial alignment layers. The bulk properties can be determined using simple models. *Center:* Slight surface coverage might influence the initial tilt angle θ_0 and anchoring strength. The determination of bulk properties via Fréedericksz-transition is possible, but requires additional numerical simulations. *Right:* Strong surface coverage can induce homeotropic alignment. For materials with positive dielectric anisotropy no Fréedericksz-like switching is possible, therefore the bulk properties cannot be measured by the methods used in this paper

An intermediate surface coverage on the substrates may have an effect on the initial tilt angle θ_0 and the anchoring energy W, but is still not sufficient to induce homeotropic alignment. In this case a Fréedericksz-transition can be observed, and therefore the Single-Cell-Methods could in principle be applied. However, influences of tilt angle and weak boundary conditions have to be considered during data evaluation, as these parameters strongly affect the threshold voltage V_{Th}, the permittivity of the field-OFF state and thus on the estimation of elastic constants.

In this work we proved the influence of nanoparticles on the initial tilt angle θ_0 as well as on the anchoring energy W. However, for the dispersions investigated here we also showed that the change in anchoring energy W is small and negligible. On the other side, the influence of nanoparticles on the initial tilt angle θ_0 can be significant and requires consideration during data evaluation. By numerical fitting routines we succeeded in determining the surface parameters θ_0 and W as well as the bulk properties K_{11}, K_{33}, $\varepsilon_{\parallel}$ and $\varepsilon_{\perp}$. We showed that nanoparticle doping can influence the apparent threshold voltage $V_{\mathrm{Th,app}}$ not only by changing the bulk properties, but also by affecting the boundary conditions on the substrates. Finally our results confirm earlier experimental studies on nanoparticle dispersions concerning a reduction of elastic constants and a slight decrease of dielectric anisotropy.

References

1. Ouskova, E.; Buchnev, O.; Reshetnyak, V.; Reznikov, Y.; Kresse, H. *Liq. Cryst.* **2003,** 30, (10), 1235-1239.
2. Li, F. H.; Buchnev, O.; Il Cheon, C.; Glushchenko, A.; Reshetnyak, V.; Reznikov, Y.; Sluckin, T. J.; West, J. L. *Phys. Rev. Lett.* **2006,** 97, 147801.
3. Rault, J.; Cladis, P. E.; Burger, J. P. *Phys. Lett. A* **1970,** A 32, (3), 199-200.
4. Hayes, C. F. *Mol. Cryst. Liq. Cryst.* **1976,** 36, (3-4), 245-253.
5. Liang, B. J.; Chen, S. H. *Phys. Rev. A* **1989,** 39, (3), 1441-1446.
6. Dierking, I.; Scalia, G.; Morales, P. *J. Appl. Phys.* **2005,** 97, (4), 044309.
7. Qi, H.; Hegmann, T. *J. Mater. Chem.* **2006,** 16, (43), 4197-4205.

8. Qi, H.; Hegmann, T. *ACS Appl. Mater. Inter.* **2009,** 1, (8), 1731-1738.
9. Draper, M.; Saez, I. M.; Cowling, S. J.; Gai, P.; Heinrich, B.; Donnio, B.; Guillon, D.; Goodby, J. W. *Adv. Funct. Mater.* **2011,** 21, (7), 1260-1278.
10. Kinkead, B.; Hegmann, T. *J. Mater. Chem.* **2010,** 20, (3), 448-458.
11. Urbanski, M.; Kinkead, B.; Hegmann, T.; Kitzerow, H.-S. *Liq. Cryst.* **2010,** 37, (9), 1151-1156.
12. Mirzaei, J.; Urbanski, M.; Yu, K.; Kitzerow, H. S.; Hegmann, T. *J. Mater. Chem.* **2011,** 21, (34), 12710-12716.
13. Da Cruz, C.; Sandre, O.; Cabuil, V. *J. Phys. Chem. B* **2005,** 109, (30), 14292-14299.
14. Bezrodna, T.; Chashechnikova, I.; Gavrilko, T.; Puchkovska, G.; Shaydyuk, Y.; Tolochko, A.; Baran, J.; Drozd, M. *Liq. Cryst.* **2008,** 35, (3), 265-274.
15. Urbanski, M.; Kinkead, B.; Qi, H.; Hegmann, T.; Kitzerow, H. S. *Nanoscale* **2010,** 2, (7), 1118-1121.
16. Reznikov, M.; Sharma, A.; Hegmann, T. *Part. Part. Syst. Charact.* **2014,** 31, (2), 257-265.
17. Cseh, L.; Mehl, G. H. *J. Mater. Chem.* **2007,** 17, (4), 311-315.
18. Mirzaei, J.; Urbanski, M.; Kitzerow, H.-S.; Hegmann, T. *Phil. Trans. R. Soc. A* **2013,** 371, 20120256.
19. Prodanov, M. F.; Pogorelova, N. V.; Kryshtal, A. P.; Klymchenko, A. S.; Mely, Y.; Semynozhenko, V. P.; Krivoshey, A. I.; Reznikov, Y. A.; Yarmolenko, S. N.; Goodby, J. W.; Vashchenko, V. V. *Langmuir* **2013,** 29, (30), 9301-9309.
20. Jerome, B. *Rep. Prog. Phys.* **1991,** 54, (3), 391-451.

21. Mirzaei, J.; Urbanski, M.; Kitzerow, H.-S.; Hegmann, T. *ChemPhysChem* **2014,** 15, (7), 1381-1394.

22. Wu, S. T.; Coates, D.; Bartmann, E. *Liq. Cryst.* **1991,** 10, (5), 635-646.

23. Clark, M. G.; Raynes, E. P.; Smith, R. A.; Tough, R. J. A. *J. Phys. D* **1980,** 13, (11), 2151-2164.

24. Wu, S. T.; Wu, C. S. *Phys. Rev. A* **1990,** 42, (4), 2219-2227.

25. Blinov, L. M.; Chigrinov, V. G. *Electrooptic Effects in Liquid Crystal Materials*, Springer, New York, **1994**, pp.118-120.

26. Yokoyama, H. *Mol. Cryst. Liq. Cryst.* **1988,** 165, 265-316.

27. Yokoyama, H.; Vansprang, H. A. *J. Appl. Phys.* **1985,** 57, (10), 4520-4526.

28. Nastishin, Y. A.; Polak, R. D.; Shiyanovskii, S. V.; Bodnar, V. H.; Lavrentovich, O. D. *J. Appl. Phys.* **1999,** 86, (8), 4199-4213.

29. Demus, D.; Goodby, J. W.; Gray, G. W.; Spiess, H. W.; Vill, V. *Handbook of Liquid Crystals, Part 1: Fundementals,* Wiley-VCH, Weinheim, **1998**, pp. 270-272.

30. Wang-Yang Li; Shu-Hsia Chen. *Jpn. J. Appl. Phys.* **1999,** 38, (3R), 1482-1487.

31. Welford, K. R.; Sambles, J. R. *Mol. Cryst. Liq. Cryst.* **1987,** 147, 25-42.

32. Deuling, H. J. *Mol. Cryst. Liq. Cryst.* **1974,** 27, (1-2), 81-93.

Chapter 6

Summary, Future Work and Outlook

6.1 Summary

The research presented in this thesis shines new light on the complex interactions between the host N-LC molecules and NPs with regard to the role of size, core composition, type and density of surface ligands of the NPs. In view of the importance of the chemical and thermal stability of NPs in thermotropic nematic LC composites, silanization of Au NPs has been developed to provide robust and easy-to-functionalize surface coating for metal NPs. Silanized Au NPs are proven to be more finely dispersed in the nematic medium with superior thermal/chemical stability as showcased by means of optical and electro-optical studies of the nematic composites.

In this thesis, the impacts of NP doping on the physical properties of N-LCs such as alignment, phase transition temperatures, stability of the mesophase and important electro-optical parameters, were investigated by detailed POM studies and electro-optical measurements. Investigations on optical textures obtained by POM were used as strong evidence for the alignment and formation of defects in the liquid crystalline host, placed between plain glass slides or in polyimide-rubbed electro-optic test cells. In addition, POM studies coupled with DSC measurements were used to study the phase transition temperatures and the influence of NPs on stabilizing/destabilizing mesophases as well as on inducing biphasic behavior in doped samples.

In order to obtain reliable results from EO measurements, two techniques of capacitance and transmittance were applied to detect and measure field-induced permittivity and birefringence changes in the pure and doped nematic samples. The nanocomposites studied in this thesis covered metallic Au NPs and semiconducting CdSe

QDs of different diameters up to 10 nm and with different hydrophobic organic functionalized ligands.

Insights into the role of core composition and differences on NP surface defect states were obtained by studying nematic nanocomposites with three types of monodisperse CdSe quantum dots similar in size and capping agent (myristic acid), but slightly different in surface defect states and core composition (using a type of CdSe doped with Zn). We were able to show that small compositional and subsequent surface defect state differences in NPs can influence their impacts on the nematic LC properties. Additionally, FCPM was used to study the distribution of photoluminescent QDs within nematic dispersions and to confirm the director field distribution in particle induced-disclination lines observed in the POM textures.

In all the LC-NP composites, whether with small semiconductor QDs or metallic Au NPs that were tested in this thesis, it was found that the NP surface ligands play a critical role in the interaction of the NPs with the nematic LC molecules; and, consequently, in the final quality of dispersions. Surface passivation of NPs with robust organic ligands and functional groups compatible with those of LC molecules are prerequisites for chemically and thermally stable LC-NP composites. Such hybrid systems ultimately provide a better understanding and control of structure-property relationships between LCs and NPs. Numerous experiments performed in this thesis led to the development of syntheses of Au NPs with robust and functionalized coatings for colloidal LC dispersions by utilizing silane conjugation chemistry. Silanized Au NPs with a siloxane network, are proven to have superior thermal and chemical stability due to the low or eliminated tendency of ligand dissipation and thiol migrations compared with alkylthiolate-capped Au NPs. Surviving

long extended sonication times and high temperatures, silanized Au NPs as nematic LC dopants, provide access to higher concentrations of doping without considerable NP settling.

Silanized Au NPs studied in this thesis were either functionalized with long aliphatic chains ($-C_{18}H_{37}$) or liquid crystalline groups. Detailed optical and electro-optical measurements were utilized to investigate the influence of such particles on the nematic medium. Different N-LC properties were discussed with respect to the concentration and size of NP dopant, as well as with the chemical structure and coverage density of surface ligand molecules.

It is shown in this thesis that a mesogenic ligand shell has the potential to provide better miscibility of NPs in the LC medium, and facilitates a tactoidal deformation of the ligand shell which can be assumed accountable for the improved EO responses such as lower V_{th} values and shorter rise times in doped nematic samples. However, studies and characterizations performed on these nematic nanocomposites with silanized aliphatic- or LC-functionalized Au NPs, in comparison with the results from previously-studied nanocomposites with alkylthiolate- or amine-capped Au NPs and QDs, strongly indicate that achieving ideal dispersions not only requires stability of the surface ligands and their compatibility with host LC molecules, but also needs an optimization of the coverage density and molecular length of the surface ligands, in order to provide maximum penetration of the host LC molecules into the ligand layer.

The key information summarized in this thesis and analysis of previous results, allow the conclusion that particle size influences the LC-NP composites, considering the fact that different sizes result in different surface curvature in NPs which can then determine the

density of ligand coverage. It is therefore conceivable that relatively smaller particles with a higher curvature allow for better interdigitation between ligands and host molecules. However, this effect seems to be less pronounced for the particles in the size regime of less than 10 nm, like those studied in this thesis, where NPs often show a relatively broad size distribution.

Throughout these studies, no general difference between Au and CdSe particles with different core compositions was found in terms of their impacts on the physical properties of colloidal nematic dispersions. A possible explanation may be related to the high density of ligands on the surface of the NPs, which may prevent a direct interaction between core material and host molecules. As a result, in colloidal dispersion of NPs in N-LCs by changing the core materials, the quality of the composite and its physical properties should not change noticeably providing all the other parameters such as surface ligand and size remain identical. Despite the fact that the synthesis of well-defined clusters with various surface functional groups and different core compositions may be very challenging, following such an avenue in LC-NP studies, appears to be a promising continuation of this thesis.

All nematic nanocomposites investigated in this work showed homeotropic alignment within untreated glass slides due to NP migration and agglomeration at the LC/substrate interface. As was shown, this phenomenon is more pronounced with NPs lacking sufficient chemical compatibility of their surface ligand shell with the N-LC host molecules. In electro-optical test cells deposition of NPs over the surface can superimpose the initial alignment layers for planar alignment and can, therefore, cause some disruptions in standard planer boundary condition required for the EO measurements of nematics using

the single-cell method. By numerical simulations we were able to investigate the bulk and surface effects NPs and have shown how partial surface coverage of NP at the LC/substrate interface, may cause changes in the initial tilt angel (θ_0) and surface anchoring energy (W).

6.2 Future Work and Outlook

Silanization is without a doubt a prominent method for the synthesis and functionalization of NPs, maintaining the stability and compatibility required for the homogeneous dispersion of NPs in LC media. It has been shown recently that NPs with mixed layers of both aliphatic and mesogenic surface ligands obtained by ligand exchange methods yield homogeneous LC dispersions.[1, 2] The silanization chemistry may be applied to prepare NPs with mixed mesogenic and aliphatic ligands. According to the results of this thesis, such new NPs are expected to further improve the miscibility and stability of LC nanocomposites, therefore leading to new LC mixtures with superior electro-optical properties.

Future research should also focus on the development of feasible synthetic methods that provide more benign NPs using cheaper reactants and allow large scale preparations. In recent years, carbon NPs also known as “carbon dots” (C-dots), have attracted significant attention due to their unique properties. Carbon dots possess distinct advantages, such as chemical inertness, a lack of optical blinking, low cytotoxicity, and excellent biocompatibility, especially as fluorescent labels compared to organic dyes and other semiconductor QDs with heavy metal cores.[3, 4] In view of the unique properties of C-dots and the prospects of their applications in LC phases, synthesis of hydrophobic C-dots

was initiated in this thesis. There are numerous methods for the synthesis of C-dots, including chemical or thermal oxidation of carbonaceous compounds.[3] However, most of these methods provide hydrophilic particles that are not suitable for LC applications in which there is a need for compatibility of C-dots with non-polar LC molecules. As shown in **Figure 6.1**, the synthesis of a series of hydrophobic carbon dots (C-dot1-3) and organosilanes-functionalized carbon dots (SiC-dot), have been accomplished by making modifications to previously reported methods.[5, 6] Preliminary results related to the characterization of the colloidal C-dots (TEM, PL of only C-dot2 are shown) and composites of nematic LC Felix-2900-03 with C-dot2 are summarized in **Figure 6.2**. Our collaborators are currently conducting further optical and electro-optical studies of nematic composites doped with C-dots.

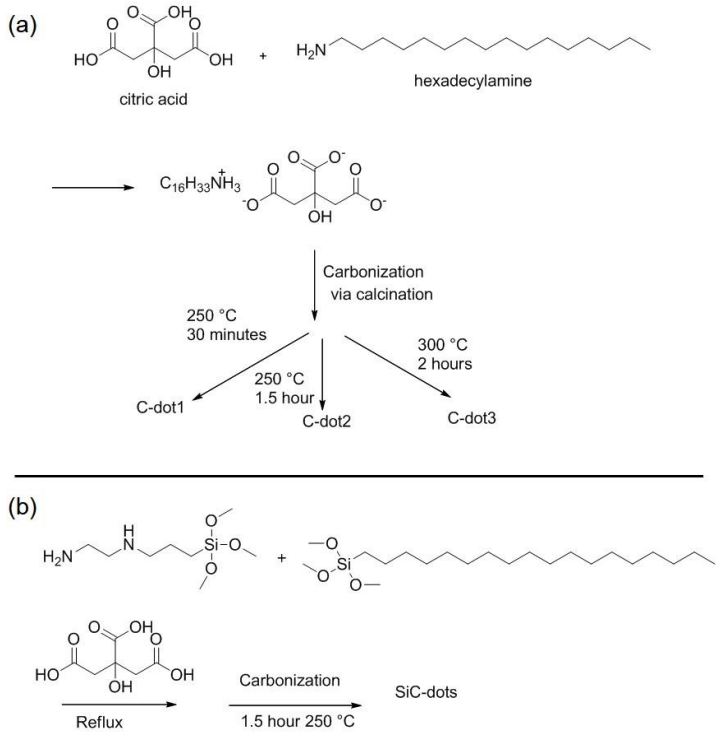

Figure 6.1 Schematic diagram for the syntheses of carbon dots. (a) Hydrophobic C-dot1-3 and (b) hydrophobic organosilanes-functionalized carbon dots (SiC-dot).

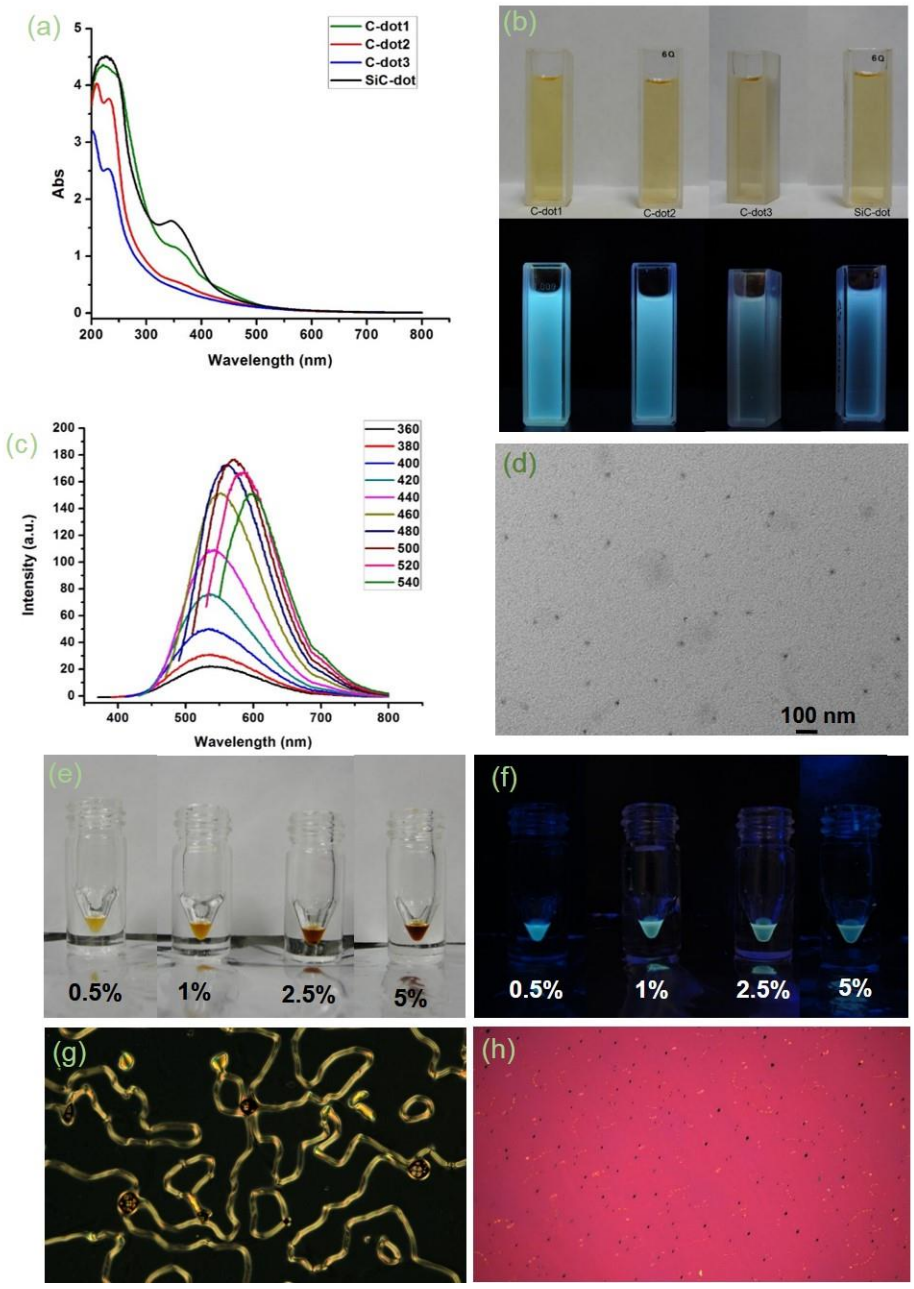

Figure 6.2 (a) Absorption spectra of purified C-dots1-3 and SiC-dot; (b) colloidal dispersion of C-dots in hexanes, under ambient light (top) and 366 nm illumination (bottom) indicating bright photoluminescent of C-dots; (c) PL spectra of purified C-dot2 at different excitation wavelengths from 360 nm to 540 nm increasing at 20 nm intervals; (d) TEM image of C-dot2; (e-f) vials containing nematic Felix-2900-03 doped with different concentrations of C-dot2 after solvent evaporation under ambient light and illumination of 366 nm; (g-h) POM micrographs of the nematic composites doped with 1wt% of C-dot2 in plain glass slides (g) and polyimide rubbed test cell (h).

Despite significant advancement in the preparation and characterization of NPs and significant interest in the development and application of LC nanocomposites, there remain several challenges that need to be overcome by the scientific community in the LC nanoscience field. These challenges encompass various aspects, including the following:

1) Design of 1D-nanomaterials with anisometric properties such as carbon nanotube, and nanorods of different core materials with optimized surface functionalities for LC dispersions.
2) Gaining deeper insights into the mechanisms of the interaction between NPs and LC molecules by obtaining the capability to visualize the location of NPs in nematic hosts, (current efforts are focused on using polymerizable nematic mixtures that can be isolated as thin films and sectioned for TEM or using FCPM technique on QD-doped liquid crystalline materials).
3) Conducting a more extensive and systematic study of the electro-optic properties of LC-NP composites in conjunction with industry partners interested in incorporation of nanotechnology into LCD devices.

Liquid crystal-nanoparticle composites have become one of the most exciting areas of research within the LC community, as evidenced by global research in this field. The outcomes of every research on a particular type of nanomaterial and LC phase, may benefit the other LC nanocomposites of various nanostructures and mesophases. With the current progress in modulating electro-optical properties of various LC phase by nanoscale additives, emergence of new flat panel displays with high energy efficiency and stunning image quality based on this new technology is not far from becoming a reality. In addition,

advances in LC-directed assembly of NPs into well-ordered arrays that can be manipulated by electric fields or temperature, will lead to the creation of novel types of materials with applications in devices such as tunable lasers, sensors and more.[7-9]

6.3 References

1. Prodanov, M. F.; Pogorelova, N. V.; Kryshtal, A. P.; Klymchenko, A. S.; Mely, Y.; Semynozhenko, V. P.; Krivoshey, A. I.; Reznikov, Y. A.; Yarmolenko, S. N.; Goodby, J. W.; Vashchenko, V. V. *Langmuir* **2013,** 29, (30), 9301-9309.
2. Draper, M.; Saez, I. M.; Cowling, S. J.; Gai, P.; Heinrich, B.; Donnio, B.; Guillon, D.; Goodby, J. W. *Adv. Funct. Mater.* **2011,** 21, (7), 1260-1278.
3. Li, H. T.; Kang, Z. H.; Liu, Y.; Lee, S. T. *J. Mater. Chem.* **2012,** 22, (46), 24230-24253.
4. Luo, P. G.; Sahu, S.; Yang, S.-T.; Sonkar, S. K.; Wang, J.; Wang, H.; LeCroy, G. E.; Cao, L.; Sun, Y.-P. *J. Mater. Chem. B* **2013,** 1, (16), 2116-2127.
5. Bourlinos, A. B.; Stassinopoulos, A.; Anglos, D.; Zboril, R.; Karakassides, M.; Giannelis, E. P. *Small* **2008,** 4, (4), 455-458.
6. Wang, F.; Xie, Z.; Zhang, H.; Liu, C.-y.; Zhang, Y.-g. *Adv. Funct. Mater.* **2011,** 21, (6), 1027-1031.
7. Rippa, M.; Mormile, P.; Capasso, R.; Zanella, M.; Petti, L. *Mol. Cryst. Liq. Cryst.* **2013,** 573, (1), 18-25.
8. Jia, D.; Yang, C.; Li, X.; Peng, Z.; Liu, Y.; Cao, Z.; Mu, Q.; Hu, L.; Li, D.; Yao, L.; Lu, X.; Xiang, X.; Zhang, H.; Xuan, L. *Liq. Cryst.* **2014,** 41, (2), 207-213.

9. Khoo, I. C. *Prog. Quant. Electron.* **2014,** 38, (2), 77-117.